eman ta zabal zazu

Universidad del País Vasco
Euskal Herriko Unibertsitatea

Department of Analytical Chemistry

# Development of novel procedures for the preservation of archaeological irons and mural paintings

Report to compete for the International PhD degree

**Marco Veneranda**

July 2017

# ACKNOWLEDGMENTS

Marco Veneranda is grateful to the Ministry of Innovation and Competitiveness (MINECO) for his pre-doctoral fellowship (from February 2013 to January 2017) as well as, to its research group of the Department of Analytical Chemistry, Ikerkuntza eta Berrikuntza Analitikoa (IBeA).

This PhD work has been developed thanks to the financial support received from:

- Global Change and Heritage UFI project (Ref UFI 11-26 UPV-EHU), founded by UPV/EHU.
- DISILICA-1930 project (ref. BIA 2014-59124P) founded by Spanish Ministry of Economy and Competitiveness (MINECO) and the European Regional Development Fund (FEDER).
- Punta Begoña project (ref 3171.16REGB) founded by Getxo City Council.
- CTP projects (ref CTP09-P04 and CTP12-P10) founded by Working Community of the Pyrenees, Basque Government.

Special thanks deserve Dr. Xabier Murelaga (Department of Stratigraphy and Palaeontology of the University of the Basque Country), Dr. Iñaki Garcia Camino and Laura Garcia (Archaeological Museum of Bizkaia) and Dr. Massimo Osanna (Superintendency of Pompeii), for their relevant contribution in this research, through their support, their facilities and their knowledge.

My thankfulness goes also to the technical support and knowledge provided by Dr. Alfredo Sarmiento (in the Singular Coupled Multispectroscopy Laboratory, LASPEA) and Dr. Javier Sanguesa (in the X-Ray Service of Rocks and Minerals Unit), from the Research General Services of the UPV/EHU (SGIKER). Dr. Torsten Paarup, from the Bioanalytical Techniques Unit from the Higher Council of Scientific Research (CSIC) is also gratefully acknowledged.

I would also like to express my sincere gratitude to:

- MONARIS research group from the University of Pierre et Marie Curie (UPMC, Paris, France), especially to Dr. Ludovic Bellot-Gourlet and Dr. Philippe Colomban, for welcoming me in their laboratories in order to develop part of this PhD work.

- Institute of Electronic Structure & Laser from the Foundation for Research & Technology (IESL-FORTH, Heraklion, Greece), especially to Dr. Demetrios Anglos, for welcoming me during my stay in its laboratory.
- Luo laboratory from the University of Connecticut (Connecticut, USA), especially to Dr. Yangchao Luo for giving me the opportunity to perform an important part of the research in his group.

I would like to thank Dr. Danilo Bersani. for introducing me in the IBeA research group, Dr. Juan Manuel Madariaga for giving me the opportunity to do this PhD, and my supervisor Dr. Kepa Castro for all the effort to carry out this work.

Finally, I would also like to thank all professors and researchers forming part of the IBeA group, for the key role they have played in the development of this research.

# INDEX

# CHAPTER 1:
# INTRODUCTION

## 1.1 *Cultural Heritage* definition

The term *Cultural Heritage* encompasses the material and immaterial testimonies of civilization, history and culture developed by communities and passed on from one generation to the next one as an integral part of their identity.

*Cultural Heritage* can be described as a dynamic concept since the recognition of the cultural significance of an asset does not depend solely on its intrinsic value, but rather on the value conferred to it by the community as a mean representative of their traditions and beliefs [1]. The *Cultural Heritage* of a community is irreplaceable, inimitable and needs to be preserved and enhanced as part of the world heritage of mankind as a whole.

The preservation of *Cultural Heritage* is not merely threatened by environmental degradation pathways, but also by the social, economic and political context where the asset to be protected is located. For this reason, it is incumbent on the international community to identify the exact boundaries of *Cultural Heritage* and establish an effective international system for its safeguard. In recent decades,

many efforts have been made to achieve this purpose. The first official international recognition of *Cultural Heritage* occurred in 1954 through the ratification of the *Convention for the Protection of Cultural Property in the Event of Armed conflict* (also known as *Hague Convention*) [2].

However, the most significant legislative innovation on this subject was the *Convention Concerning the Protection of the World Cultural and Natural Heritage,* adopted by the *United Nations Educational, Scientific and Cultural Organization* (UNESCO, a specialized agency of the United Nations) in 1972 [3]. The convention introduced a list of the assets to be considered as *Cultural Heritage*. The list included several movable and immovable properties such as sculptures, paintings, monuments and archaeological sites, having a widely recognized historical, artistic, scientific, aesthetic or anthropological value. Furthermore, the concept of *Natural Heritage* was also presented, which refers to natural areas, as well as geological and physiographical formations, having an universally recognized aesthetic and/or scientific value.

This document, adopted by all member states, was flanked in 2003 by the *Convention for the Safeguarding of the Intangible Cultural Heritage* [4]. This convention introduced the concept of *Intangible Cultural Heritage* and its indivisible link with *Cultural* and *Natural Heritage* [5]. As described in Article 2, *Intangible Cultural Heritage* includes "*practices, representations, expressions, knowledge, skills – as well as the instruments, objects, artefacts and cultural spaces associated therewith – that communities, groups and, in some cases, individuals recognize as part of their Cultural Heritage*".

The two juridical instruments were complimented in 2005 by the UNESCO *Convention on the Protection and Promotion of the Diversity of Cultural Expressions,* which aimed at protecting the diversity of cultural expressions and reaffirming the indissoluble bond between culture and development for all countries [6].

The three conventions constitute the main legislative instruments for the recognition and safeguarding of *Tangible* and *Intangible Heritage*. In addition to these, many other declarations have been introduced by international, national and regional organizations with the specific aim of better identify and preserve *Cultural Heritage*, for instance, the *Convention on the Protection of the Underwater Cultural Heritage* [7], the *Yamato Declaration on Integrated Approaches for Safeguarding Tangible and Intangible Cultural Heritage* [8] and the *European Landscape Convention* [9].

Based on international, national and regional legislation guidelines, *Cultural Heritage* can be organized as displayed in Figure 1.1:

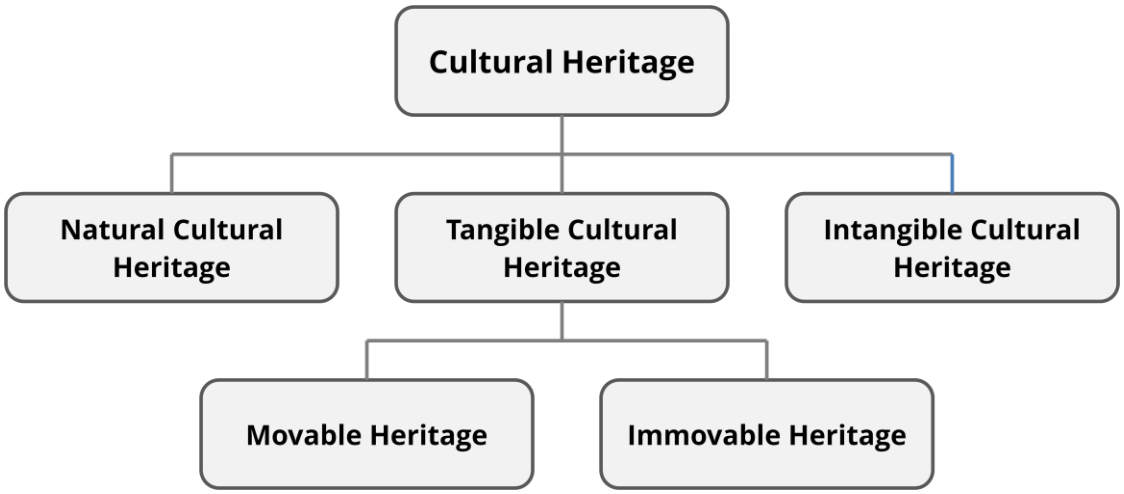


*Figure 1.1: Schematic classification of Cultural Heritage based on international legislation guidelines.*

## 1.2 *Tangible Cultural Heritage*

As this PhD project has been focused on the analytical study of different kinds of properties produced by mankind, a more thorough description of *Immovable* and *Movable Cultural Heritage* is needed.

### *a) Immovable Cultural Heritage*

*Immovable Cultural Heritage* encompasses buildings, group of buildings, engineering structures and monumental works of art outstanding for a distinguished artistic or historic value and having an indissoluble bond with the territory where they are located. As described by the *Convention Concerning the Protection of the World Cultural and Natural Heritage* [3], the *Immovable Cultural Heritage* can be organized in three different sub-categories:

1) *Monuments*: all architectures, monumental sculptures and other artworks which are of outstanding historical, scientific or artistic value [10].

2) *Groups of buildings:* groups of architectures connected by a common value recognized on their homogeneity, their style or their place in the landscape.

3) *Sites*: natural landscapes linked to specific historic events or molded through human intervention as well as excavated and unexcavated archaeological sites.

*b) Movable Cultural Heritage*

*Movable Cultural Heritage* refers to all kind of artwork and artefacts that can be moved from place to place without compromising their integrity or their cultural value [11]. According to their nature and/or primary function, assets can be classified as follows:

1) *Works of art:* all movable artworks, made in any material support, primarily developed as carriers of an aesthetic or symbolic message, for instance, paintings, sculptures, drawings, photographs, specific jewelry, ceramics and other ornamental objects [12].
2) *Archaeological artefacts:* utensils, artefacts and other objects remains crafted by mankind, recovered through archaeological excavation and having a cultural or historical value [13].
3) *Historic assets*: all kind of objects which are firmly bonded to people or events of recognized importance. This category includes, for instance, artefacts, tools, weapons, musical instruments and specific documents.
4) *Scientific heritage:* artefacts related to scientific and technical activities as well as the tools produced for dissemination and didactic purposes, for instance, ancient collections, scientific instruments, industrial tools, manuscripts and books [14].

## 1.3 Conservation of *Tangible Cultural Heritage*

The conventions mentioned in section 1.1 clearly underline that the establishment of a widely shared concept of *Cultural Heritage* has the main purpose of safeguarding and preserve the properties from degradation and ensuring the transmission of their cultural and historical values to future generations.

In this light, conservation/restoration activities play a key role in the process of *Tangible Cultural Heritage* protection. The concept of conservation has acquired various meanings over time. Each of them has been forged by the social and the political trends of its historical context, often resulting in the development of

contrasting thought flows [15]. In this regard, modern conservation theories are the result of a slow process of evolution that took its first step in the Classic Age.

The ancient testimonies come down to us confirm that, in the heyday of the Greek civilization, artworks and monuments restoration was an activity widely practiced. In that epoch, conservation works were conducted by artists (painters, sculptors or architects) and mainly aimed at restoring the original appearance of the property and its sympathetic relationship with nature and the gods. This interpretation of *Cultural Heritage* conservation was closely linked to the Greek ideals of beauty and harmony, regarded as canons of perfection to be followed in every aspect of the society (art, religion, politics and ethics) [16].

In Roman times in contrast, restoration was regarded as a reshaping process aimed at renewing their significance and/or utility according to religious and political needs [16].

Since the fall of the Roman Empire until the 17$^{th}$ century, it was maintained the practice according to which the conservation/restoration of a property was often accompanied by a renewal of the decorative style.

However, during the 18$^{th}$ century, the discovery of the archaeological sites of Hercolaneum (1738) and Pompeii (1748) gave birth throughout Europe to a renewed interest in the historical and archaeological study of ancient heritage. This interest was further fuelled, at the end of the century, by the archaeological discoveries protracted by Napoleon during the French Campaign in Egypt and Syria [17]. Accordingly, intense debates concerning the ethics principles of conservation brought to the development of new restoration theories [18].

Two contrasting thought flows arose in the 19$^{th}$ century. These two approaches, conceived to be applied to all kind of *Cultural Heritage*, found in the *Immovable Heritage* restoration the most critical divergences. On the one hand, Eugène-Emmanuel Viollet-le-Duc (1814-1879, Figure 1.2a) conceived the theory of stylistic restoration [19]. According to this school of thought, restoration means "*to reestablish* (the property) *to a finished state, which may in fact never have actually existed at any given time*". In practical terms, this theory was based on the assumption that, to achieve a proper restoration, the asset had to reacquire the style and completeness as it was conceived by its creator. Thus, the stylistic restoration was aimed at deleting the signs of the passing of time by reconstructing the "original" elements and removing those added at later dates.

Opposed to the thought flow conceived by Viollet-Le-Duc, John Ruskin (1819-1900 Figure 1.2b) asserted that the cultural value of an ancient property mainly lies in the traces marked by its history [20]. Accordingly, interventions should be focused on the preservation of the historical marks shown by the asset rather than to the recovery of its original aesthetic appearance.

Furthermore, the Ruskin's theory had a significant influence on the distinction between conservation and restoration, being the last one "*the most total destruction which a building can suffer: a destruction out of which no remnants can be gathered: a destruction accompanied with false description of the thing destroyed*" [20].

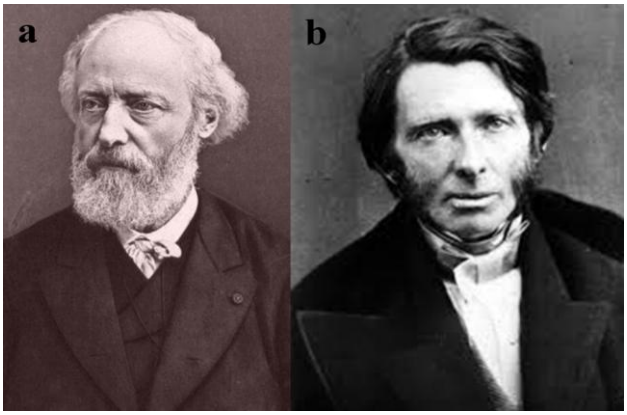


*Figure 1.2: a) Eugène-Emmanuel Viollet-le-Duc (1814-1879); b) John Ruskin (1819-1900).*

Over time, the Ruskin's theory has been reworked by numerous other authors, including Gustavo Giovannoni (1873-1947) that, at the beginning of the 20$^{th}$ century, introduced for the first time the concept of *scientific restoration*. In opinion of Giovannoni, the proper conservation of a property passes through the knowledge of its history, its materials and its conservation problems. Under these requirements, the figure of the conservator must be flanked by experts proceeding from other fields of knowledge [21].

Hence, it was born the concept of interdisciplinary approach in the *Cultural Heritage* conservation field: architects, archaeologists, chemists, biologists and physicists collaborate with conservators with the purpose of characterizing the property, implementing the conservation process and establishing the best conditions for its preservation. From here on out, all modern conservation theories have been based on the concept of interdisciplinarity.

As a matter of fact, this concept is reflected on the several regional and international conventions that, starting from the 20th century, have been dedicated to the preservation and protection of *Cultural Heritage*. Among them, it must be underlined the importance of the *Athens Charter for the Restoration of Historic Monuments*, drafted in 1931 [22]. This document firmly recommended that "*architects and curators of monuments should collaborate with specialists in the physical, chemical and natural sciences with a view to determining the methods to be adopted in specific cases*".

In the wake of the massive damages caused by the First and Second World War, conservation and restoration of *Cultural Heritage* became a theme of primary importance worldwide. Indeed, it was drafted, in 1964, the *International Charter for the Conservation and Restoration of Monuments and Sites* (also known as *Venice Charter*) [23]. This document recovered and emphasized the importance of the interdisciplinary approach recommended in the *Athens Charter* by establishing that conservation and restoration works "*must have recourse to all the sciences and techniques which can contribute to the study and safeguarding of the architectural heritage*".

In recent years, this concept has been implemented in further regulations such as the *Declaration of Amsterdam* (1975) [24], the *Charter for the Conservation of Historic Towns and Urban Areas* (also known as *Washington charter*, 1987) [25] and the *Charter of Krakow* (2000) [26]. All modern international, national and regional charters and conventions clearly emphasize that the preservation of *Cultural Heritage* is an interdisciplinary/transdisciplinary commitment in which the above mentioned scientific disciplines, have a steadily increasing importance.

Today, the practice according to which researchers from different scientific fields offer their contribution to properly preserve *Cultural Heritage* assets is widespread. Indeed, from the chemical evaluation of materials to the development of novel technologies, each scientific aspect supporting *Cultural Heritage* identification, conservation and enhancement is nowadays universally recognized as part of a specific and integrated scientific network that takes the name of *Conservation Science*.

## 1.4 The role of *Conservation Science*

The term *Conservation Science* encloses all kind of scientific activities devoted to the study of *Cultural Heritage* [27]. As represented in Figure 1.3, *Conservation*

*Science* is a broad field that supports the conservation of *Cultural Heritage* by crossing the boundaries between several fields of scientific knowledge.

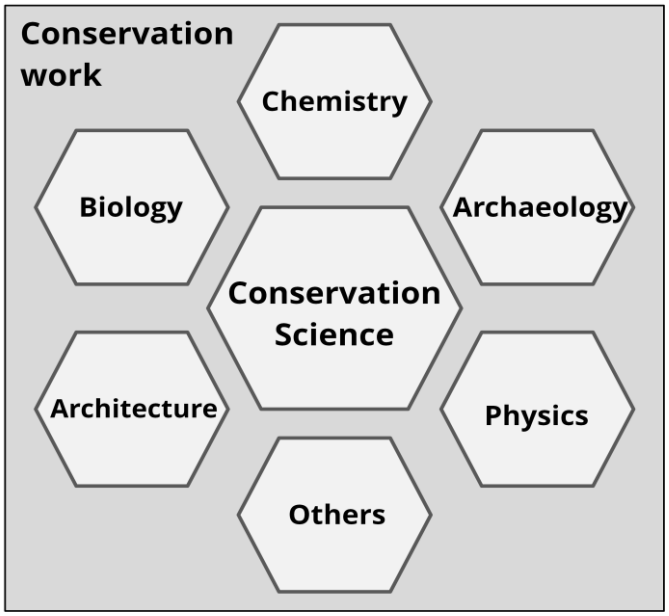


*Figure1.3: Schematic representation of the main scientific disciplines supporting the work of conservators in the field of Cultural Heritage.*

The disciplines summarized in Figure 1.3 play a crucial role in the preservation of *Cultural Heritage*. In fact, through the interdisciplinary collaboration among researchers from different scientific fields it is possible to:

a) Identify the original (and eventually restoration) materials composing the property under analysis;

b) Characterize the degradation processes threatening its conservation and identify their origin;

c) Develop and/or optimize novel methodologies and products to support the preservation of *Cultural Heritage*;

Even though these three main objectives are pursued for each kind of *Movable* and *Immovable Cultural Heritage* asset, it is important to underline that both, professional profiles and analytical techniques needed for their accomplishment, can vary greatly depending on the kind of asset under analysis.

As this manuscript concerns with the study of mural paintings and metallic archaeological artefacts, this section evaluates the main contributions of *Conservation Science* on the conservation of these specific items.

### *1.4.1 Characterization of original materials*

The knowledge of the materials constituting a *Cultural Heritage* asset is of paramount importance to guarantee its proper integrity. The information obtained through the analytical characterization of original materials facilitates the work of conservators and deepen the knowledge about the origins and the history of the property [28].

*a) Mural paintings*

Wall paintings represent one of the oldest artistic expressions of mankind. From cave paintings to modern graffiti, this artistic expression has showed a constant evolution over the centuries. Accordingly, the evolution of this visual art has been constantly accompanied by the establishment of new painting techniques and the use of new and advanced materials.

In this field of study, one of the primary contributions of *Conservation Science* is to identify the painting technique used to produce the artwork. Indeed, optical and spectroscopic systems have been successfully employed with the purpose of identifying the technique used to fix the pigments on the support [29-35]. In this context, the first distinction that can be made is whether the mural painting was produced by using a "*fresco*" or "*secco*" technique.

In the first case, the pigment is fixed to the wall thanks to a carbonation reaction [36]. To perform a "*fresco*" painting, the pigment is dispersed in water and applied on a layer of wet slaked lime (calcium hydroxide, $Ca(OH)_2$). The water contained in the slaked lime allows the pigment to penetrate into the substrate, becoming one with it. Afterwards, the chemical interaction between the substrate and the carbon dioxide ($CO_2$) contained in the air, progressively led to the formation of calcium carbonate ($CaCO_3$) according to the reaction described below (reaction 1.1):

$$Ca(OH)_2 + CO_2 \rightarrow CaCO_3 + H_2O \qquad \text{Reac. 1.1}$$

The carbonation reaction ends with the formation of a solid layer of calcium carbonate that fixes the pigment grains, making them extremely stable and long lasting (see Figure 1.4a).

In the case of "*secco*" techniques, the pigment is laid out on a dry substrate (Figure 1.4b). Therefore, the pigments are fixed to the mural surface through the use of specific binders. Depending on the epoch of the painting and the implemented technique, different kinds of binders (of organic nature such as oils, albumen, animal glues and casein) have been used [37].

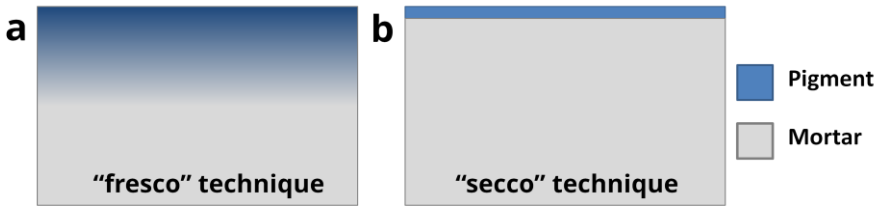


*Figure 1.4: a) In the "fresco" technique, pigments penetrate into the fresh layer of slaked lime plaster and are fixed to the substrate through a carbonation reaction; b) In the "secco" technique, pigments are applied upon a dried plaster and are fixed to it by means of specifics binders.*

Binders' characterization provides important data to conservators, helping them to identify the painting technique to select the most indicated approach for preservation works. As a matter of fact, chromatographic and spectroscopic techniques have been effectively applied in several cases of study with the specific purpose of characterizing the used binders [34, 38-43].

In this context, the work of E. Tomassini et al. (2016) [44] presents a case of study in which fragments of mural paintings from the Andean church of Our Lady (Copacabana de Andamarca, Bolivia) were sampled and analyzed with the purpose of identifying the binders used to fix the pigment to the substrate. To identify binder materials, the collected samples were first subjected to an extraction process which separates lipids and proteins fractions. Afterwards, the extracted organic compounds were characterized by means of Gas Chromatography (GC) and Gas Chromatography-Mass Spectrometry (GC-MS) techniques. With regards to lipidic fraction, chromatographic analyses proved the presence of azelaic acid and cholesterol, which are indicatives of linseed oil and egg yolk respectively. On the other side, chromatograms collected from the analysis of proteinaceous fraction displayed the presence of glycine and proline,

characteristic compounds of animal glues. GC-MS results, supported by Raman and Fourier Transform Infrared Spectroscopy (FTIR) analyses of mortars and pigments, helped to shed light on the paint technique used by the artist. Indeed, it was deduced that animal glue was used as preparatory coating, while the pigments were fixed (using the *secco* technique) by mixing them with a binder composed of egg and oil.

With regard to pigments and dyes, it is important to highlight that the colour palette available to the artists has been constantly evolving [45]. As shown in Figure 1.5, the palette has been remarkably expanded during the modern era. Indeed, starting from the industrial revolution, the scientific progress led to the synthesis of several novel pigments (for instance mars red, titanium white and chrome orange) capable of ensuring greater stability and opacity compared to some natural ones.

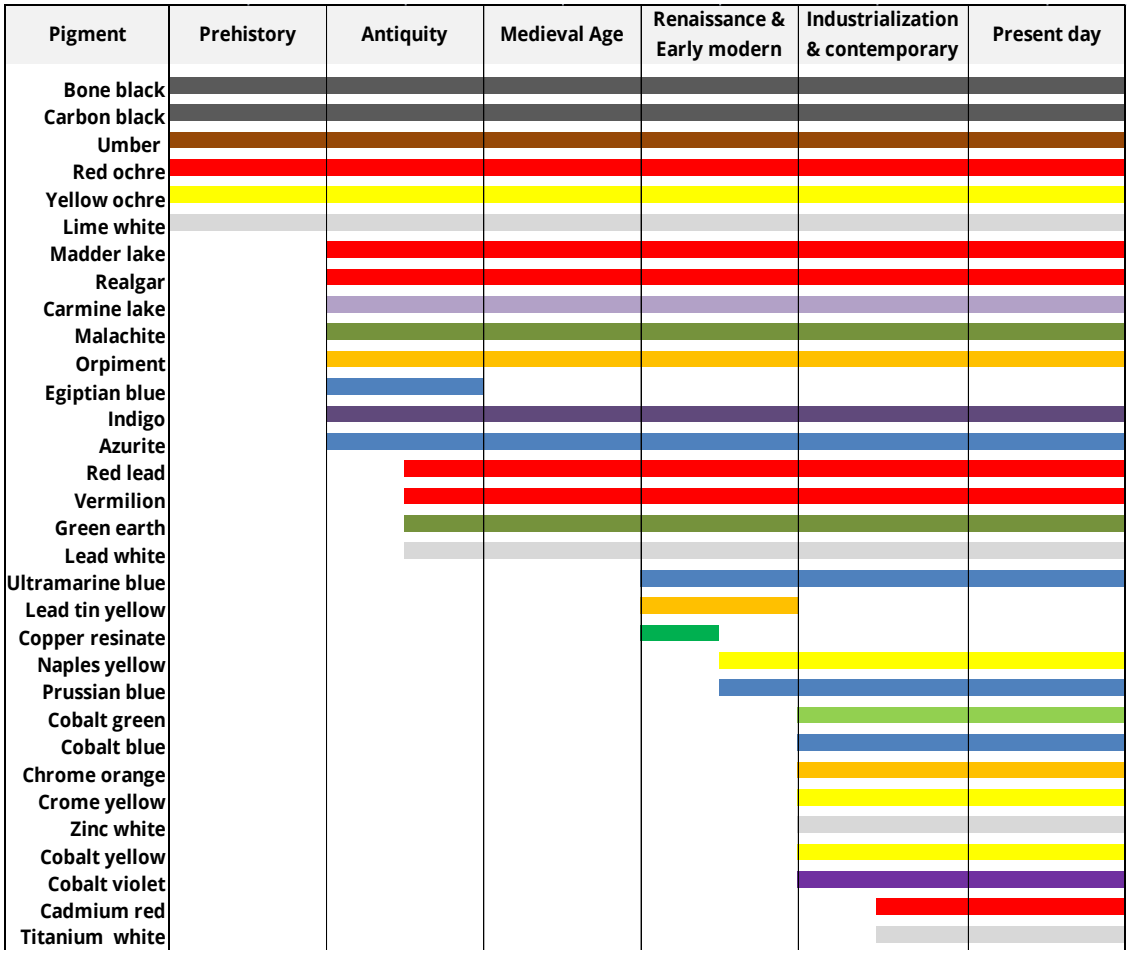


*Figure 1.5: Timeline (from prehistory to the present day) showing the epoch of discovery/synthesis of the main pigments used in Cultural Heritage.*

In this context, the role of conservation scientists is to characterize the pigments composing the paintings. As proved by several research works, this information enables to assess the originality of the artwork and to identify the presence of previous restorations [46,47].

For example, in the case of the study presented by D. Bersani and co-workers (2009) [48], Raman spectroscopy was selected as the main analytical technique to characterize the colour palette of two mural paintings (16$^{th}$ century) conserved in the church of San Giovanni Evangelista (Parma, Italy). Molecular analyses enabled the detection of several pigments consistent with the age of the paintings, such as goethite (FeO(OH)), hematite ($Fe_2O_3$), malachite ($Cu_2CO_3(OH)_2$), brochantite ($Cu_4SO_4(OH)_6$), azurite ($Cu_3(CO_3)_2(OH)_2$) and lead white ($(PbCO_3)_2 \cdot Pb(OH)_2$). However, both artworks also revealed the additional presence of chrome yellow ($PbCrO_4$) and anatase ($TiO_2$). Considering that those two compounds were introduced as pigments in the 19$^{th}$ and 20$^{th}$ century respectively, it was deduced that both *frescoes* were subjected to an undocumented restoration work.

*b) Metallic archaeological artefacts*

This term refers to all kind of metallic objects (such as artworks, jewels, war materials and tools used in daily life) crafted by mankind and recovered from archaeological endeavours. The analytical study of archaeological artefacts plays a crucial role towards a better understanding of our historical past. Indeed, through the characterization of materials and production techniques, it is possible to achieve significant inferences about several social, economic and dynamic aspects of ancient societies [49]. Through the work of Conservation scientists, it is therefore possible to reconstruct the unwritten history of human civilizations and communities.

Analytical researches devoted to characterize artefacts' composition and the implemented manufacture processes are included in the broader field of *archaeometallurg*y [50].

In this light, it must be emphasized that the art of *metallurgy*, understood as the set of technologies used to extract and process metals, has shown a slow but progressive evolution over the centuries. From the Chalcolithic Age (6$^{th}$-5$^{th}$ millennium BC) to the modern era, the evolution of *metallurgy*, which has been constantly promoted by the discovery of new metallic elements and the

development of novel manufacture methods, has resulted in the production of an uncountable number of different alloys with many different properties [51].

For that reason, each alloy has specific conservation issues and one of the main roles of *Conservation Science* consists in characterizing the elemental composition of the artefacts, their crystalline structure and mechanical properties. Under these requirements, several analytical techniques are commonly used for the study of metal-based archaeological artefacts. For instance, elemental techniques such as X-Ray Fluorescence (XRF), Laser Induced Breakdown Spectroscopy (LIBS) and Proton Induced X-Ray Emission (PIXE) have been extensively used with the purpose of identifying the metals and the alloys used to forge the artefacts [52-56].

All these techniques provide elemental data that helps to define the metal/alloys used to forge the object under analysis as well as provide useful information for cataloguing and conservation purposes. Furthermore, they can also provide important clues to deepen the knowledge on many other aspects of the object such as manufacturing procedures and metal provenance.

A clear example is given by the work of M. Martinón-Torres et al. (2012) [57] who, by XRF analyses, reconstructed the production organization behind the bronze arrows of the Terracotta Army in the First Emperor's Mausoleum, Xi'an, (China). Of the approximately 40,000 arrows preserved in the archaeological site, the work was focused on metric and elemental characterization of the 278 quivers containing 90 arrows or more. On the one hand, the comparative study proved that these objects were produced in a limited number of crucibles. On the other hand, by plotting lead and tin contents of the arrowheads as a scatter plot it was proved that each arrow bundle would leave the workshop as a finished item. In conclusion, thanks to elemental analyses, it was clarified that the manufacture of the arrows was organized according to a cellular production of finished bundles in semiautonomous units rather than a single flow line of production and assembly (Figure 1.6).

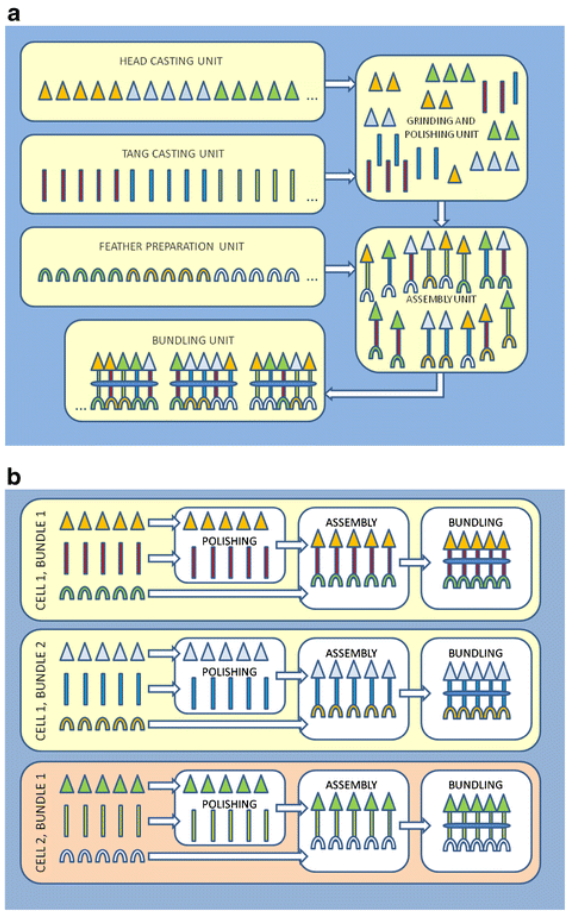


*Figure 1.6: Schematic representation of arrows production models and their predicted effects in the distribution of chemical batches. Each colour represents a different batch.* a) *A single flow line of production and assembly; b) Cellular production of finished bundles in semi-autonomous units (source: M. Martinón-Torres et al. 2012 [57]).*

As evidenced by several works focused on this topic, elemental analyses of archaeological artefacts are often complemented by metallographic observations. *Metallography* is based on the sampling of metal fragments from the object, which is polished and analyzed by means of a metallographic microscope with the purpose of characterizing its polycrystalline microstructure. Through metallographic studies, relevant information can be obtained, such as the implemented manufacturing technique, the temperatures reached during crafting and the ores used for metal production and smelting [58-65].

For example, S. Scrivano and co-workers (2017) [66] performed a very interesting experimental work aimed at identifying the microstructural and compositional fingerprints produced by ancient soldering methods. To do so, the three most

used soldering procedures known in the pre-roman epoch to produce gold-based jewels (brazing, solid-state diffusion with copper salt and autogenous welding) were reproduced in the laboratory and then analyzed by means of Scanning Electron Microscopy-Energy Dispersive X-Ray Spectroscopy (SEM-EDS), X-Ray Fluorescence (XRF), Particle-Induced X-Ray Emission (PIXE) and metallographic techniques. Thanks to the multianalytical approach it was demonstrated that brazing soldering technique was recognizable for a dendritic-porous microstructure (see Figure 1.7) and for an increase of Ag and Cu elements in the joining zone. In contrast, solid state diffusion with copper showed a crystal hexagonal structure and an increase of Cu content. The autogenous welding, instead, did not show any change in the metallographic structure and in the elemental content. By comparing the obtained results, the researcher finally demonstrated that, by means of elemental and metallographic analyses, it is possible to identify the metal-joining method employed to forge ancient artefacts and jewels.

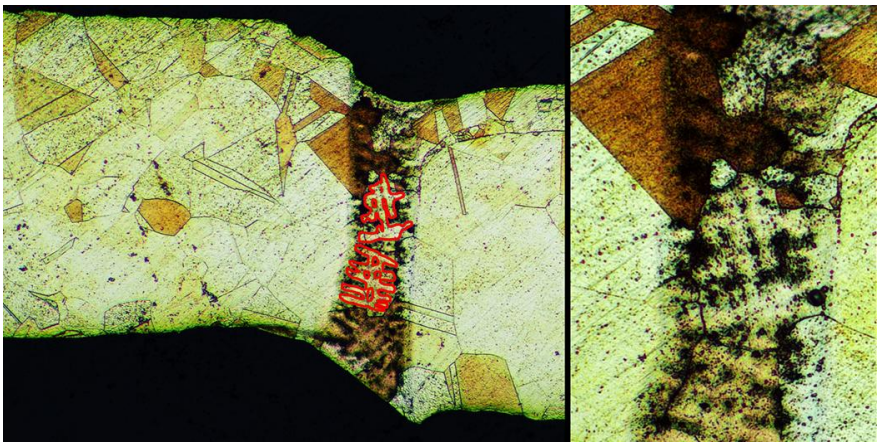

*Figure 1.7: Metallographic analysis of the crystalline structure of two alloy-M brazed foils. The red lines highlight the dendritic structure of the soldering area (source S. Scrivano et al. (2017) [66].*

In addition to elemental and metallographic analyses, further techniques can be used to deepen the knowledge of the archaeological artefacts under study. For example, the geological origin of the raw material used to forge a metallic object can be identified through isotopic analyses. As proved by several works, the method is generally based on Thermal Ionization Mass Spectrometry (TIMS) and Multicollector Inductively Coupled Plasma Mass Spectrometry (MC-ICP-MS) techniques, which are used to analyze and compare the isotope ratio of the

metals composing the object under analysis with the isotopic composition of ores in mineral deposits [67-74].

For example, the analytical work carried out by M. Bode et al. (2009) [75] traced the lead sources used to forge several metal objects proceeding from Roman archaeological sites located near the river Rhine, in Germany. The collected data proved that the lead isotopic ratio of most of the artefacts had strong similarities with the Augusta-Tiberian lead ore deposits located in north of Germany, proving that were locally produced.

*1.4.2 Study of degradation processes*

The degradation pathways capable of inducing the decay of *Cultural Heritage* materials are manifold. For this reason, one of the main tasks of conservation scientists is to characterize the degradation forms and identify the causes behind their formation.

*a) Mural paintings*

The main degradation forms capable of jeopardizing the conservation of mural paintings can be traced to anthropogenic, environmental and biological factors.

**Anthropogenic factors**

Nowadays, no less than in the past, human activity represents one of the main factors endangering the conservation of mural paintings. Anthropogenic degradations have many forms and can be either intentional or not. Among them, one of the most common one is vandalism, understood as the whole of activities (such as scratches, inscriptions and incisions) dedicated to the deliberate destruction of the *Cultural Heritage* [76,77]. In some cases, the voluntary mutilation of wall paintings is driven by precise political and religious reasons. A clear example is the so-called *iconoclasm*, a religious movement occurred in the Byzantine Empire ($8^{th}$ century AD) which, asserting its contrariety to the veneration of icons, provoked the deliberate destruction of a large number of religious representations [78]. In other cases, the anthropogenic degradation also resulted as a side effect of national and international conflicts. For example, during the Second World War hundreds of ancient churches and other buildings were destroyed by bombing, which resulted in the irreversible loss of the artworks therein conserved [79]. In recent years, one of the most dramatic examples of the damages that conflicts can produce to *World Heritage* are the

painted Buddha statues of Bāmiyān, which were destroyed in 2001 by Taliban during the war in Afghanistan [80,81].

However, anthropogenic deterioration of *Cultural Heritage* can also be induced in an unintentionally way. It often occurs during the application of restoration works and is mainly related to the use of inappropriate methods and materials that, not being compatible with the original compounds, trigger their degradation. For example, several pathologies can rise from the application of protective synthetic and organic coatings on the paint surface. This practice, widely used in the past, often led to the onset of aesthetic and chemical damages such as chromatic variations (darkening and yellowing), dirt retention and permeability modification [82]. In this context, chromatographic and spectroscopic techniques can be effectively employed to identify the composition of these protective layers [83-85]. In addition, it must be highlighted that most of these coatings fluoresce when excited by UV-light (see Figure 1.8). Thus, by using UV-lamps, conservator scientists can reveal the treated areas and guide conservators towards a targeted intervention [85-87].

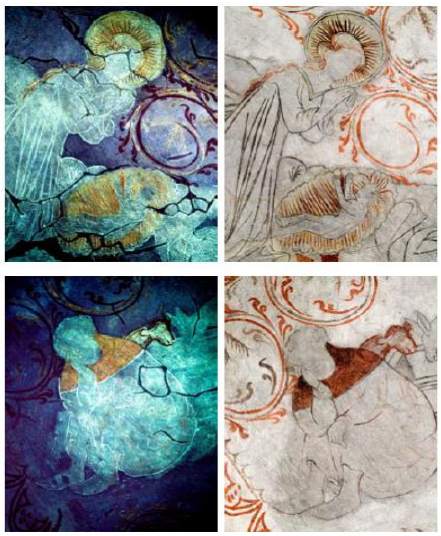

*Figure 1.8: Mural paintings from Undløse Church (Undløse, Denmark) exposed to UV-light (left) and VIS-light (right). Fluorescent areas reveal the presence of organic-based coatings applied in earlier restorations (source: H.S. Garreau (2007) [82]).*

**Environmental factors**

This group includes all the degradation forms produced either by the isolated or combined effects of environmental parameters such as temperature, humidity, components of rain, air and wind.

The most common pathologies are triggered by the natural and anthropogenic pollutants dispersed into the atmosphere. For example, the **particulate matter** (intended as the set of solid particles of micrometer scale contained in the air) carried by winds, tend to deposit on the artwork surfaces, producing dark patinas that comprise the appearance of the wall painting [88]. On the other side, **acid gases** such as $CO_2$, $SO_x$ and $NO_x$, which are mainly emitted from anthropogenic activities, such as industrial production and fuel combustion, can be dissolved in rainwater causing a critical reduction of its pH value [89]. This phenomenon is particularly harmful to the wall paintings directly exposed to the atmosphere, since acid rain can react with carbonated mortars and trigger the irreversible dissolution of the substrate. Aiming at corroborate their role in the onset of degradation pathways, many scientific works complemented the characterization of original and decay materials composing an artwork with the analytical study of the atmospheric pollutants of its surroundings [90,91].

In addition to those, the direct exposition of wall paintings to direct sun-light irradiation can produce critical physical pathologies. Indeed, strong daily and seasonal **thermal fluctuations** activate a cyclical phenomenon of expansion and contraction of the original materials. Considering that each material has a specific coefficient of volumetric thermal expansion [92], the expansion/contraction process can produce critical side effects such as decrease of compactness, cracks and loss of material. In order to prevent and/or limit those irreversible degradation forms, conservation scientists can play a key role by monitoring the environmental conditions of wall paintings through the implementation of environmental sensors [93-95].

For instance, the work of M.C. Pérez et al. (2013) [96] was focused on monitoring the microclimatic conditions of several rooms from the Ariadne's House (Archaeological site of Pompeii, Italy). The environmental study proved that the rooms protected by transparent rooftops had stronger daily and seasonal thermal fluctuations than those protected by opaque ones, which had significant adverse impacts on the conservation state of the mural paintings conserved beneath.

In addition to the stressor factors described above, one of the main degradation pathways produced by the interaction of a mural painting with its environmental context is the crystallization of **soluble efflorescence salts**. The accumulation of soluble salts in the wall is due to different sources (such as leaching of original

materials, infiltration waters, metabolite products of organisms and atmospheric deposits), being the capillary rise from the soil the most common one [97,98]. Indeed, soil moisture constantly enriches the walls with several kind of soluble anions (i.e., bicarbonates, sulphates, chlorides and nitrates) and cations (i.e., sodium, potassium, calcium, ammonium and magnesium). When the water evaporates, soluble salts tend to crystallize. If this process occurs in the external surface of the wall painting, the salt crystallization is called efflorescence. On the contrary, crypto-efflorescence is the term used to describe crystallizations that take place within the porous structure of the inner layers [99]. Since salt crystallization can lead to critical chemical and physical damages (see Figure 1.9), analytical studies are often carried out with the purpose of delivering to conservators important guidelines regarding their treatment [100-103].

For example, an interesting case of study was presented by J.M Madariaga and co-workers (2014) [104], who made use of portable analytical techniques to evaluate the composition of soluble efflorescence salts degrading Pompeian mural paintings. Concretely, thanks to the use of Raman and Energy Dispersive-X-Ray Fluorescence (ED-XRF) spectrometers, several nitrates and sulphates-based degradation compounds such as niter ($KNO_3$), thenardite ($Na_2SO_4$), mirabilite ($Na_2SO_4 \cdot 10H_2O$), epsomite ($MgSO_4 \cdot 7H_2O$) and gypsum ($Ca_2SO_4 \cdot 2H_2O$) were characterized. Furthermore, by considering the environmental context in which the walls are conserved, it was also deduced that the main reasons behind the accumulation of soluble salts were the direct exposition to rainfall and/or the infiltration of waters from the ground.

*Figure 1.9: Mural painting from the archaeological site of Pompeii (Italy) showing critical damages due to soluble salt crystallization (source: J.M. Madariaga et al. (2014) [104]).*

**Biological factor**

It is well known that several species of algae, bacteria, lichens and moods are able to colonize the painted surface, producing aesthetic, physical and chemical damages [105]. The aesthetic damage is mainly due to deposition of undesirable polychromatic patinas (see Figure 1.10) that cover the artwork and seriously compromise its aspect [106,107]. Moreover, as described in detail by K.L. Garg et al. (1995) [108], microorganisms also play an important role in the process of chemical weathering of paintings. On the one hand, the chemical reactions produced by most of biodeteriogens to assimilate the nutrients can affect the original compounds of the artwork (assimilation process). On the other hand, the high number of acids and enzymes produced by fungi and mosses during their metabolism can involve the transformation and disintegration of paint materials (dissimilation process).

Moreover, biodeteriogens colonization also involves the deposition of biomass, which transforms the wall painting surface in a fertile substrate for the growth of higher plants [109]. In this case, the main degradation problem is triggered by the penetration of the root system within the cracks and the porous of the murals. Thus, the identification of biodeteriogens in the early stages of colonization is essential to avoid or limit the occurrence of irreversible damages.

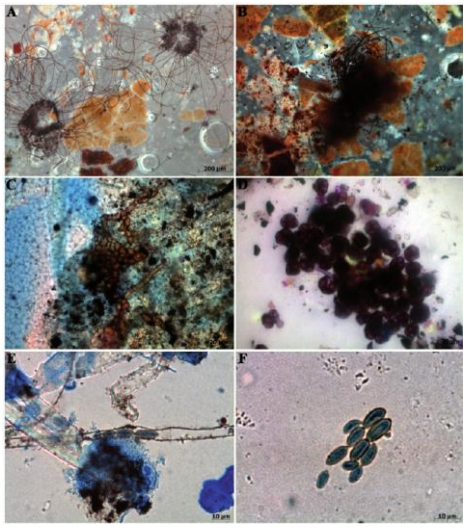

*Figure 1.10: Microbial community jeopardizing wall paintings from the Church of the Holy Ascension (Veliki Krčimir, Serbia). a,b) Chaetomium sp. perithecia; c) microcolonial fungi embedded in painted layer in the form of unbranched chains and d) spheroidal cell clusters; f) Cladosporium like conidia clustered and e) intertwined with cobweb (source: N. Unkovíc et al. (2015) [107]).*

In order to achieve this purpose, Raman spectroscopy has been widely used to identify biodeteriogens metabolics such as carotenoids, chlorophyll, scytonenemin and calcium oxalate [110-114]. In addition to spectroscopic techniques, the lidar fluorescence technique (which was first tested on monuments in 1995 by V. Raimondi et al. [115]) is increasingly used for the detection and characterization of photoautotrophic biodeteriogens (such as green algae and cyanobacteria) in the field of *Cultural Heritage* [116-118].

However, for a complete and reliable characterization of the biological strains producing biodeterioration, DNA-based approaches are needed. Among them, the most used strategy is the rRNA partial sequence analysis, which involves biodeteriogens isolation, DNA extraction and polymerase chain reaction (PCR) amplification [119-122]. A clear example of the advantages provided by the use of this method is displayed in the work of A.A Gurbushina et al. (2004) [123] which deal with the characterization of biodeteriogens threatening a mural painting from the 16$^{th}$ century (St. Martins church, Greene–Kreiensen, Germany). Indeed, thanks to the DNA extraction and PCR amplification of a few collected samples, the research team was able to isolate and characterize up to 32 fungal strains (including *Acremonium, Aspergillus, Cladosporium, Fusarium sp.*) and more than 20 different bacteria (mostly belonging to the *Bacillus sp*.).

*b) Metallic archaeological artefacts*

The set of chemical and electrochemical reactions arising from the interaction between a metal object and its environment leads to the onset of corrosion products [124]. In the case of archaeological artefacts, as summarized below, two main environmental conditions can be distinguished.

**Corrosion during burial**

During the phase of burial, corrosion processes start when the metal, losing electrons, produces positively charged ions that react with the burial matter [125]. This suggests that the characteristic ionization energy of the metals used to forge an artefact has a primary importance on the development of corrosion products. For instance, iron and tin have a low ionization energy (they yield electrons very easily), which promotes the activation of chemical reactions with the environment. On the other side, gold is the most stable among all metals (it does not yield electrons) and, being unable to interact with the surroundings, is almost immune to corrosion processes.

The onset of degradation processes during the burial phase is not exclusively influenced by the metallic composition of the artefact, but also by the intrinsic characteristics of the soil. Indeed, many different factors of the burial environment, such as the chemical composition, the pH value, the electrical resistivity, the amount of oxygen and the water content can play a key role in the development of specific corrosion processes [126].

Among them, the environmental parameters that most affect the corrosion dynamics during burial are the amount of oxygen (expressed as Redox potential) and the pH value. Indeed, specific diagrams (Pourbaix) are used with the aim of determining the corrosion behaviour of metals as a function of this two parameters [127]. As showed in Figure 1.11, the Pourbaix diagrams can be used to identify the stability region of a metal, as well as to estimate the corrosion product compositions at various pH and Redox potential combinations.

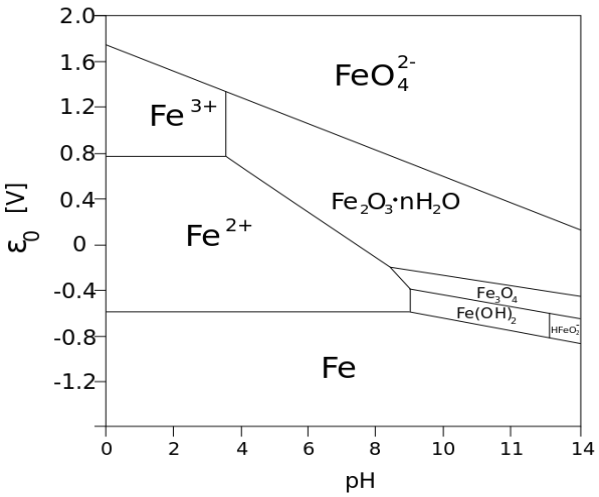


*Figure 1.11: Pourbaix diagram of iron.*

Whereas these values have a strong influence on the activation of corrosion processes, conservation scientists often combine the characterization of degradation processes with the assessment of burial soil parameters [128-130].

In addition to the pH and Redox potential, infiltration and accumulation of soluble salts from the soil is a fundamental parameter to take into account [131]. In fact, it is well known that salts are able to destabilize the object during the burial phase by providing highly conductive electrolytes that trigger accelerated corrosion processes [132]. Considering their influence in the formation of corrosion products, important inferences can be obtained from the analysis of the soluble salt content of burial soils. To achieve this purpose, analytical techniques such as

Ion Chromatography (IC) [133], Capillary Electrophoresis (CE) [134] and Inductively Coupled Plasma-Mass Spectrometry (ICP-MS) [135] can be used after extracting the soluble ions of the soil by water.

During the burial phase, artefacts corrosion can also be triggered by metabolites produced by microorganisms. As summarized by C. Remazeilles et al. (2009) [136], this process is often detected in anaerobic conditions (also in the case of marine environments) where sulphate-reducing bacteria (i.e. *Desulfovibrio vulgaris*) oxidize the hydrogen while creating hydrogen sulphide, a corrosive chemical agent that promotes pitting corrosion [137,138].

Owing to the set of environmental and biological factors influencing the degradation process, artefacts' corrosion systems are often composed of a mixture of many different phases [139,140]. Each of them has a specific repercussion on the conservation state of an object. Indeed, some corrosion products are stable compounds that protect the uncorroded core from further chemical reactions, while others are reactive phases that jeopardize the conservation of artefacts [141,142]. For this reason, one of the main roles of *Conservation Science* is to characterize the corrosion phases and their stratigraphic distribution with the purpose of estimate the stability of the object. To achieve this aim, conservation scientists generally make use of molecular analytical techniques such as Raman, Fourier Transform Infrared Spectroscopy (FTIR), Mössbauer and X-Ray Diffraction (XRD) techniques [143-146].

Recently, L. Ponti et al. (2015) [147] performed a multianalytical evaluation of several copper-based coins recovered from the archaeological site of Pompeii. In the first step, X-Ray Diffraction (XRD) and FTIR systems were employed for the characterization of crystalline and amorphous corrosion phases respectively. Then, Raman analyses were performed on cross-sectioned samples with the purpose of identifying the stratigraphic distribution of the detected degradation compounds. Molecular results, supported by elemental ED-XRF and SEM-EDS analyses, underlined that each coin was subjected to different corrosion processes, which was probably due to the specific environmental conditions experimented during burial.

**Corrosion after excavation**

Corrosion is an ongoing, dynamic process that often increases its rate after excavation. To understand the reasons of this phenomenon, it is important to

highlight that the indispensable condition for the preservation of metallic objects is the achievement of a chemical and physical equilibrium with their surroundings. When the artefact is recovered from archaeological endeavours its environmental context changes completely. In most of the cases, a metallic archaeological object exposed to the open air experiences a lower humidity and a higher oxygen concentration in comparison to the burial environment [148]. The change of those key parameters becomes especially dangerous in presence of soluble salts. For instance, recently excavated iron-based artefacts affected by chloride infiltration often experiment the sudden reactivation of corrosion processes and the subsequent formation of akaganeite ($FeO_{0.883}(OH)_{1.167}Cl_{0.167}$) [149]. The presence of chloride ions in the molecular structure of this iron phase (see Figure 1.12) increases the porosity of the corrosion layer, compromising its compactness and facilitating cracks and swellings phenomena [150-152].

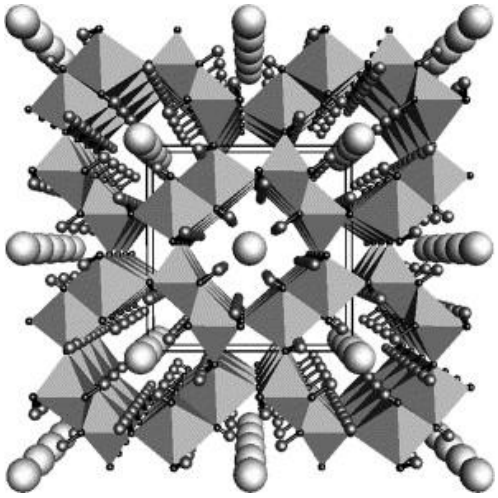

*Figure 1.12: The crystal structure of akaganeite viewed down the b-axis. Large spheres represent chlorides, small terminal spheres hydrogens (source: .K. Ståhl et al. (2003) [150])*

In order to prevent the reactivation of degradation processes, conservators need to apply specific desalination treatments soon after the recovery of the artefact. Nowadays, conservators can select from a wide range of methods for removal of salts from metallic artefacts [153]. Recognizing the needs of conservators, researchers can support their work by monitoring the effectiveness of the selected treatment. Based on the literature, several analytical techniques such as IC, ICP-MS, CE and ion selective electrodes have been widely used to periodically quantify the soluble salt extracted by desalination treatments and evaluate their efficacy [154-156]. Moreover, *Conservation Science* also provides further assistance

to conservator by monitoring the stability of metal artefacts after the application of preservation treatments. Indeed, spectroscopic techniques have been widely used to assess the transformation/stabilization of reactive corrosion products after desalination treatments [157,158].

For example, M. Rimmer et al. (2012) [159] performed an experimental work aimed at evaluating and comparing the desalination capability of three different treatments. To do so, 120 iron nails affected by chlorine infiltration were treated by 1) alkaline sulphite solution (0.1 M NaOH/0.05 M $Na_2SO_3$) at room temperature, 2) alkaline sulphite solution at 60 ºC and c) deoxygenated sodium hydroxide solution (0.1 M NaOH) at room temperature. After a period of time between 56 and 96 days (depending on the sample) treated nails were digested to measure their residual chloride content. Thanks to the collected data, the research team provided information of paramount importance to conservators, suggesting the employment of deoxygenated NaOH baths.

### *1.4.3 Technological development on conservation*

As previously explained, researchers also provide an important assistance to *Cultural Heritage* preservation by developing novel conservation products and improving the efficacy of the existing methods.

*a) Mural paintings*

In the case of mural paintings, one of the main contributions of *Conservation Science* is the design of novel products for the removal of undesired patinas from the artwork surface.

Indeed, many scientific works are nowadays devoted to the development and the application of micellar solutions [160]. Those products started to be widely applied in *Cultural Heritage* since their formulation allows removing a wide range of compounds that are difficult to remove by means of traditional cleaning methods [161]. For example, literature shows that micellar solutions and micro-emulsions can be successfully applied for the removal of undesirable synthetic polymer layers (which were largely applied in the past for conservation purposes) from mural paintings and other surfaces of cultural interest [162-165].

Beside synthetic polymers, several kinds of organic materials were used in past restorations in order to protect and consolidate wall paintings. As previously explained, most of these products (made of animal and vegetal glues, milk and

eggs proteins) are capable of modifying the physical-chemical properties of the substrate, often resulting in the development of degradation processes such as yellowing, detachments and loss of materials [82]. To address this issue, several researchers are experimenting with the use of innovative biological products capable of removing the organic compounds without damaging the painted surface. The need to find selective cleaning methods led to the use of bioactive molecules such as enzymes [166]. The first cleaning attempts with pure bioactive molecules on artworks can be dated back in the 80's, when F. Makes (1988) [167] applied a mixture of amylase and protease enzymes for the removal of an organic binder from a painting surface. In recent years, this enzyme-based method has also been successfully applied for the controlled removal of organic layers from mural paintings [168]. The most recent advances in this field have recently led to the use of living bacteria that produce very effective enzymes for the removal of unwanted organic materials. For example, in the work by P. Bosh-Roig et al. (2013) [169], the *Pseudomonas stutzeri* bacteria specie was used to remove a layer of animal glue applied in the past during the restoration of the *frescoes* from Santos Juanes Church (Valencia, Spain).

In addition, live bacterial cells can also be used for the removal of environmental degradation products. For example, sulphate-reducing bacteria (i.e. *Pseudomonas stutzeri* and *Desulfovibrio desulfuricans*) have been successfully used to remove black crusts from materials of cultural interest [170]. These results are consistent with other scientific works, proving that traditional (and often hazardous) restoration products can be replaced by new eco-friendly methods [171-173].

In this light, researchers are also experimenting with the possible use of essential oils (EOs) as novel conservation products against the biological colonization of *Cultural Heritage* materials. Those volatile and hydrophobic products, extracted from plants leafs, barks and fruits [174] by distillation or other techniques, contain a wide variety of antifungal and antibacterial constituents that have already found a reliable application in nutritional and medical fields [175,176]. In spite of the fact that their use has been just barely introduced in the field of *Cultural Heritage* conservation, the results obtained so far are very promising [177-179].

The contribution of *Conservation Science* is not only limited to the design of novel cleaning products but also focused on the development of innovative consolidation methods.

This is a topic of great interest for conservators since the wall paintings substrate, which for most of the cases is made of carbonate-based materials, can be weakened and damaged by several different degradation phenomena. Dry deposition, acid rain leaching, physical erosion, crypto-efflorescence crystallization and water freeze–thaw cycles are just some of the many processes leading to the disintegration of the painting substrate [180]. In this context, it has been recently developed a novel conservation method based on calcium hydroxide ($Ca(OH)_2$) nanoparticles that penetrate in the weakened substrate and consolidate it through a carbonation reaction using the atmospheric $CO_2$ (see Figure 1.13) [181,182]. This treatment is increasingly used (for *Cultural Heritage* conservation purposes) to consolidate calcium carbonate materials for its high penetration and reactivity features [183,184].

*Figure 1.13: Details of the mural paintings from the Acropolis of Chik-Naab (Calakmul, Mexico). Pictures on the left show the presence of sulphates over the surface and flaking phenomena damaging the paint layer; pictures on the right show the same detail six months after calcium-hydroxide consolidation treatment (source: R. Giorgi et al. (2010) [182]).*

*b) Metallic archaeological artefacts*

As previously explained, the degradation of metallic archaeological artefacts is a dynamic process that often increases its rate after excavation. One of the main

reasons lies in the presence of reactive ions (such as $Cl^-$) that, after excavation, often lead to the reactivation of corrosion processes due to the contact with atmospheric oxygen and ozone ($O_3$). In this context, conservation scientists research and develop new strategies to enchant the efficacy of desalination treatments.

Recently, the use of alkaline desalination baths applied in subcritical conditions of temperature and pressure has proved to be a promising option for the stabilization of iron objects of cultural interest [185-188]. As displayed in Figure 1.14, subcritical conditions are achieved when the treatment solvent media (generally ultrapure water) reaches a state above its critical pressure and critical temperature values.

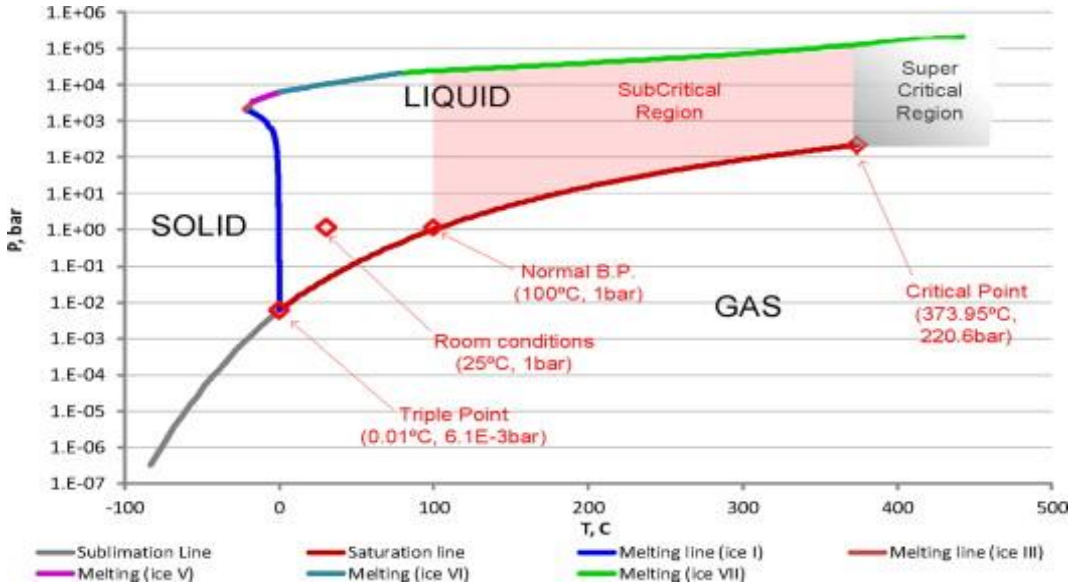


*Figure 1.14: Phase diagram of pure wate, showing pressure and temperature values needed to reach subcritical conditions (source: L.M.E. Näsänen et al. (2013) [188]).*

When these conditions are reached, the transport properties of the solvent media are between those of a liquid and a dense gas, which provides thermodynamic and kinetic options not viable under ambient conditions [189-191]. As proved in several works, the most significant advantage of this desalination method lies in a significant reduction of the treatment time.

In fact, as proved by L.M.E. Näsänen et al. [188], conventional desalination baths require an average of 150 days (depending on the composition and the nature of the object) to remove the majority of the ions. However, the time required to

stabilize the artefact can be reduced by more than 90% by applying the same desalination solution in subcritical conditions.

In addition to novel desalination treatments, specific methodologies have been developed with the aim of facilitating the removal of undesirable corrosion layers. In the past years, several researchers experimented with the low-pressure hydrogen gas plasma reduction method [192]. This procedure is based on the partial reduction of corrosion products by reactive species generated in hydrogen glow discharge plasma [193]. The hydrogen atoms generated by the plasma (below 400ºC) react with the corrosion products, thereby reducing them to a lower oxidation state. This reaction decreases the density of the rust layer without affecting the metallurgical structure of the metal core. As described by K. Schmidt-Ott et al. (2002) [194] low-pressure hydrogen gas plasma method considerably weakens the resistance of the treated corrosion, producing two important effects: 1) facilitate the mechanical cleaning of the artefact 2) speed-up the desalination process by alkaline baths. Although the first applications in the field of *Cultural Heritage* conservation are dating back to the 80's [195,196], only in recent years it has become an integral part of the conservation procedures for archaeological metallic objects [197-199].

Beside the low-pressure hydrogen gas plasma reduction method, some researchers have experimented with the potential use of short laser pulses as an alternative, selective and safe method for corrosion layers removal. First proposed in 1978 [200], laser cleaning has spread out only in recent times for the restoration of metal objects and surfaces of cultural interest [201-202].

The collaboration between researchers and conservators is also producing important advances in the development of novel coating materials. Those layers, applied after desalinization and cleaning procedures, have the purpose of protecting the metal surface from the interaction with the environment [203]. In recent years, several novel organic products based on polymers and self-assembled monolayers have been tested in substitution of commercial products (such as paraffin and microcrystalline waxes) to protect metals while preserving their aesthetic appearance [160].

Among them, one of the most interesting approaches is the self-assembled monolayer coating of carboxylate [204-206]. This method relies on the immersion of the artefact in an aqueous solution containing sodium carboxylate. In a preliminary step, the object surface is oxidized by the oxygen dissolved in the

solution. Afterwards, carboxylate anions react with the object by replacing the hydrogen of the hydroxyl (–OH) group with a metal cation. The fast reaction results in the self assembling of an ultra thin layer of carboxylate salt on the metal surface that inhibits corrosion processes [207].

The methods showed so far, are just a few example of the uncountable contributions of conservation scientists addressed to solve the conservation issues of *Cultural Heritage* materials. In this sense, the research work presented in this manuscript, developed in close collaboration with experienced conservators, represents a further contribution to this field as it will be described in the following chapters.

## 1.5 References

**[1]** J. Blake (2000) On Defining the Cultural Heritage. *The International and Comparative Law Quarterly*, 49, 61-85.

**[2]** UN Educational, Scientific and Cultural Organization (UNESCO) (1954) Convention for the Protection of Cultural Property in the Event of Armed conflict, available at: http://unesdoc.unesco.org/images/0008/000824/082464mb.pdf (May 28th 2017).

**[3]** UN Educational, Scientific and Cultural Organization (UNESCO) (1972) Convention Concerning the Protection of the World Cultural and Natural Heritage, available at: http://unesdoc.unesco.org/images/0011/001140/114044e.pdf#page=134 (May 28th 2017).

**[4]** UN Educational, Scientific and Cultural Organisation (UNESCO) (2003) Convention for the Safeguarding of the Intangible Cultural Heritage, available at: http://unesdoc.unesco.org/images/0013/001325/132540e.pdf (May 28th 2017).

**[5]** Y. Ahamad (2006) The Scope and Definition of Cultural Heritage, From Tangible to Intangible. *International Journal of Heritage Studies*, 12, 292-300.

**[6]** UN Educational, Scientific and Cultural Organisation (UNESCO) (2005) Convention on the Protection and Promotion of the Diversity of Cultural Expressions, available at: http://unesdoc.unesco.org/images/0014/001429/142919e.pdf (May 28th 2017).

**[7]** UN Educational, Scientific and Cultural Organisation (UNESCO) (2001) Convention on the Protection of the Underwater Cultural Heritage, available at: http://unesdoc.unesco.org/images/0012/001246/124687e.pdf#page=56 (May 28th 2017).

**[8]** Japanese Agency for Cultural Affairs and UN Educational, Scientific and Cultural Organisation (UNESCO) (2004) International Conference on The Safeguarding of Tangible and Intangible Heritage, available at: http://portal.unesco.org/culture/es/files/23863/10988742599Yamato_Declaration.pdf/Yamato_Declaration.pdf (May 28th 2017).

**[9]** Council of Europe, European Landscape Convention (2000) available at: https://rm.coe.int/CoERMPublicCommonSearchServices/DisplayDCTMContent?documentId=0900001680080621 (May 28th 2017).

**[10]** T. Darvill, A. Saunders, B. Startin (1987) A question of national importance: approaches to the evaluation of ancient monuments for the Monuments Protection Programme in England. *Antiquity*, 61, 393-403.

**[11]** Office of Parliamentary Counsel, Camberra, Australia (1986) Protection of Movable Cultural Heritage Act, available at: https://www.legislation.gov.au/Details/C2016C01056 (May 28th 2017).

**[12]** R. Stecker (1996) Artworks: definition, meaning, value. *Penn State Press*, *State College (USA)*, pp 334.

**[13]** W.Y. Adams, E.W. Adamns (1991) Archaeological typology and practical reality: a dialectical approach to artifact classification and sorting. *Cambridge University Press, Cambridge (UK),* pp 452.

**[14]** M.C. Lourenço, L. Wilson (2013) Scientific heritage: Reflections on its nature and new approaches to preservation, study and access. *Studies in History and Philosophy of Science*, 44, 744-753.

**[15]** N. Price, M.K. Talley, A.M.Vaccaro (2016) Historical and Philosophical Issues in the Conservation of Cultural Heritage. *Getty Publications*, *Los Angeles (USA),* pp 520.

**[16]** M.C. de Azevedo (1952) Conservazione e Restauro presso i Greci e i Romani. *Bollettino dell'Istituto Centrale del Restauro*, 9-10, 53-60.

**[17]** G. Neret (2007) Description of Egypt (Taschen 25t Anniversary). *Taschen, Cologne (Germany)*, pp 752.

**[18]** J. Jokilehto (2002) A History of Architectural Conservation. *Butterworth-Heinemann, Oxford (UK)*, pp 354.

**[19]** M.F. Hearn (1990) The architectural Theory of Viollet-le-Duc: Readings and Commentary. *The MIT Press*, *Boston (USA),* pp 306.

**[20]** S. Staniforth (2013) Historical Perspectives on Preventive Conservation. *Getty Conservation Institute*, *Los Angeles (USA),* pp 426.

**[21]** G. Zucconi, G. Giovannoni (2014) A Theory and a Practice of Urban Conservation. In: Change Over Time. *Penn press, Philadelphia (USA)*, 76-91.

**[22]** International Council on Monuments and Sites (ICOMOS) (1931) The Athens Charter for the Restoration of Historic Monuments, available at: http://www.icomos.org/en/charters-and-texts/179-articles-en-francais/ressources/charters-and-standards/167-the-athens-charter-for-the-restoration-of-historic-monuments (May 28th 2017).

**[23]** International Council on Monuments and Sites (ICOMOS) (1965) International Charter for the Conservation and Restoration of Monuments and Sites, available at: https://www.icomos.org/charters/venice_e.pdf (May 28th 2017).

**[24]** International Council on Monuments and Sites (ICOMOS) (1975) The Declaration of Amsterdam, available at: http://www.icomos.org/en/charters-and-texts/179-articles-en-francais/ressources-/charters-and-standards/169-the-declaration-of-amsterdam (May 28th 2017).

**[25]** International Council on Monuments and Sites (ICOMOS) (1987) Charter for the Conservation of Historic Towns and Urban Areas, 1987, available at: http://www.icomos.org/en/what-we-do/focus/179-articles-en-francais/ressources/charters-and-standards/159-charter-for-the-conservation-of-historic-towns-and-urban-areas (May 28th 2017).

**[26]** Cart of Cracow (2000) Principles for conservation and restoration of built heritage, available at: http://smartheritage.com/wp-content/uploads/2015/03/KRAKOV-CHARTER-2000.pdf (May 28th 2017).

**[27]** G. Artioli (2010) Scientific Methods and Cultural Heritage: An Introduction to the Application of materials science to archaeometry and conservation science. *Oxford University Press*, *Oxford (UK)*, pp 368.

**[28]** E.A. Varella (2012) Conservation Science for the Cultural Heritage: Applications of Instrumental Analysis. *Springer, Heidelberg (Germany),* pp 334.

**[29]** C. Miliani, F. Rosi, I. Borgia, P. Benedetti, B.G. Brunetti, A. Sgamelotti (2007) Fiber-Optic Fourier Transform Mid-Infrared Reflectance Spectroscopy: A Suitable Technique for in Situ Studies of Mural Paintings. *Applied Spectroscopy*, 61, 293-299.

**[30]** A.C. Felici, G. Fronterotta, M. Piacentini, C. Nicolais, S. Sciuti, M. Vendittelli, C. Vazio (2004) The wall paintings in the former Refectory of the Trinità dei Monti convent in Rome: relating observations from restoration and archaeometric analyses to Andrea Pozzo's own treatise on the art of mural painting. *Journal of Cultural Heritage*, 5, 17-25.

**[31]** L. Apollonia, D. Vaudan, V. Chatel, M. Aceto, P. Mirti (2009) Combined use of FORS; XRF and Raman spectroscopy in the study of mural paintings in the Aosta Valley (Italy). *Analytical and Bioanalytical Chemistry*, 395, 2005-2013.

**[32]** R. Mazzeo, E. Joseph, V. Minguzzi, G. Grillini, P. Baraldi, D. Prandstraller (2006) Scientific investigations of the Tokhung-Ri tomb mural paintings (408 A.D.) of the Koguryo era, Democratic People's Republic of Korea. *Journal of Raman Spectroscopy*, 37, 1086-1097.

**[33]** S. Daniilia, E. Minopoulou, K.S. Andrikopoulos, A. Tsakalof, K. Bairachtari (2008) From Byzantine to post-Byzantine art: the painting technique of St. Stephen's wall paintings at Meteora, Greece. *Journal of Archaeological Science*, 35, 2474-2485.

**[34]** M. Gil, M.L. Carvalho, A. Seruya, I. Ribeiro, P. Alves, A. Guilherme, A. Cavaco, J. Mirão, A. Candeias (2008) Pigment characterization and state of conservation of an 18th century fresco in the Convent of S. António dos Capuchos (Estremoz). *X-Ray Spectrometry*, 37, 328-337.

**[35]** M. Gil, V. Serrao, M.L. Carvalho, S. Longelin, L. Dias, A. Cardoso, A.T. Caldeira, T. Rosado, J. Mirao, A.E. Candeias (2013) Material and Diagnostic Characterization of 17th Century Mural Paintings by Spectra-Colorimetry and SEM-EDS: An Insight Look at Jose de Escovar Workshop at the CONVENT of N$^{a}$ Sr$^{a}$ da Saudacao (southern Portugal). *Color research and application*, 39, 288-306.

**[36]** G. Hale, S. O'Sheel (1966) Technique of Fresco Painting, *Dover Publications Inc.*, *Mineola (USA),* pp 69.

**[37]** M. Matteini, A. Moles (2007) La chimica nel restauro. *Nardini editore, Firenze, (Italy)*, pp 408.

**[38]** J. Romero-Pastor, A. Duran, A.B. Rodríguez-Navarro, R.V. Grieken, C. Cardell (2011) Compositional and Quantitative Microtextural Characterization of

Historic Paintings by Micro-X-ray Diffraction and Raman Microscopy. *Analytical Chemistry*, 83, 8420-8428.

**[39]** S. Sotiropoulou, Z.E. Papliaka, L. Vaccari (2016) Micro FTIR imaging for the investigation of deteriorated organic binders in wall painting stratigraphies of different techniques and periods. *Microchemical Journal*, 124, 559-567.

**[40]** F. Benedetti, G. Perra, D. Damiani, A. Atrei, N. Marchettini (2015) ToF-SIMS characterization of proteinaceous binders in the wall painting "Madonna and Child enthroned with Saints" by Ambrogio Lorenzetti in the St. Augustine Church (Siena, Italy). *International Journal of Mass Spectrometry*, 392, 111-117.

**[41]** E. Cheilakou, M. Troullinos, M. Koui (2014) Identification of pigments on Byzantine wall paintings from Crete (14th century AD) using non-invasive Fiber Optics Diffuse Reflectance Spectroscopy (FORS). *Journal of Archaeological Science*, 41, 541-555.

**[42]** D. Bersani, M. Berzioli, S. Caglio, A. Casoli, P.P. Lottici, L. Medeghini, G. Poldi, P. Zannini, (2014) An integrated multi-analytical approach to the study of the dome wall paintings by Correggio in Parma cathedral. *Microchemical Journal*, 114, 80-88.

**[43]** D. Fico, A. Pennetta, G. Rella, A. Savino, V. Terlizzi, G.E. De Benedetto (2015) A combined analytical approach applied to Medieval wall paintings from Puglia (Italy): The study of painting techniques and its conservation state. *Journal of Raman Spectroscopy*, 47, 321-328.

**[44]** E. Tomasini, D.C. Rodríguez, B.A. Gómez, D.L.A. de Faria, C.R. Landa, G. Siracusano, M.S. Maier (2016) A multi-analytical investigation of the materials and painting technique of a wall painting from the church of Copacabana de Andamarca (Bolivia). *Microchemical Journal*, 128, 172-180.

**[45]** B. Guineau, F. Delemare (2000) Colors: The Story of Dyes and Pigments. *Harry N. Abrams Inc., New York (USA)*, pp 160.

**[46]** I. Aliatis, D. Bersani, E. Campani, A. Casoli, P.P Lottici, S. Mantovan, I.G. Marino, F. Ospitali (2009) Green pigments of the Pompeian artists' palette. *Spectrochimica Acta Part A*, 73, 532-538.

**[47]** S. Daniilia, S. Sotiropoulou, D. Bikiaris, C. Salpistis, G. Karagiannis, Y. Chryssoulakis, B.A. Price, J.H. Carlson (2000) Panselinos' Byzantine wall paintings in the Protaton Church, Mount Athos, Greece: a technical examination. *Journal of Cultural Heritage*, 1, 91-110.

**[48]** D. Bersani G. Antonioli, P.P. Lottici, A. Casoli (2003) Raman microspectrometric investigation of wall paintings in S. Giovanni Evangelista Abbey in Parma: a comparison between two artists of the 16th century. *Spectrochimica Acta Part A*, 59, 2409-2417.

**[49]** E. May, M. Jones (2006) Conservation Science: Heritage Materials. *Royal Society of Chemistry*, *London (UK),* pp 376.

**[50]** S. Seetharaman (2005) Fundamentals of Metallurgy. *Elsevier, Amsterdam (Netherlands),* pp 578.

**[51]** R.F. Tylecote (1976) A history of metallurgy. *The metals Society, Ann Arbor (USA),* pp 182.

**[52]** K.O. Emeriewen, F.E. Oladugbagbe (2014) A characterization of selected precious metals artifacts from Benin city. *Inernational Journal of Conservation Science*, 5, 321-328.

**[53]** R.C. Fierascu, R.M. Ion, I. Fierascu (2015) Archaeometallurgical Characterization of Numismatic Artifacts. *Instrumentation Science and Technology*, 43, 107-114.

**[54]** J. Agresti, I. Osticioli, M.C. Guidotti, N. Kardjilov, S. Siano (2016) Non-invasive of bronze figurines using neutron, laser, and X-ray techniques. *Microchemical Journal*, 124, 765-774.

**[55]** G.C. Ezeh, E.I. Obiajunwa (2017) Multi-elemental analysis of colonial and post-colonial Nigerian coins by Proton Induced X-Ray Emission (PIXE) spectrometry. *Journal of Fundamental and Applied Sciences*, 9, 499-508.

**[56]** S. Calusi (2011) The External Ion Microbeam of the LABEC laboratory in Florence: Some Application to Cultural Heritage. *Microscopy and Microanalysis*, 15, 661-666.

**[57]** M. Martinón-Torres, X.J. Li, A. Bevan, Y. Xia, K. Zhao, T. Rehren (2014) Forty Thousand Arms for a Single Emperor: From Chemical Data to the Labor Organization Behind the Bronze Arrows of the Terracotta Army. *Journal of Archaeological Method and Theory*, 21, 534-562.

**[58]** L. Biggs, B. Bellina, M. Martinón-Torres, T.O. Pryce (2013) Prehistoric iron production technologies in the Upper Thai-Malay Peninsula: metallography and slag inclusion analyses of iron artefacts from Khao Sam Kaeo and Phu Khao Thong. *Archaeological and Anthropological Sciences*, 5, 311-329.

**[59]** A. Garbacz-Klempka, Z. Kwak, M. Perek-Nowak, M. Starski (2015) The Metallographic Characterization of Metal Artifacts Based on Late Medieval Examples. *Archives of Foundry Engineering*, 15, 29-34.

**[60]** A. Hauptmann, R. Lashimke, M. Burger. (2016) On the making of copper oxide ingots: evidence from metallography and casting experiments. *Archaeological and Anthropological Sciences*, 8, 751-761.

**[61]** M.R. Pinasco, M.G. Ienco, P. Piccardo, G. Pelatti, E. Stagno (2007) Metallographic Approach to the Investigation of Metallic Archaeological Objects. *Annali di Chimica*, 97, 553-574.

**[62]** G. Pagès, Ph. Dillmann, P. Fluzin, L. Long (2011) A study of the Roman iron bars of Saintes-Maries-de-la-Mer (Bouches-du-Rhône, France). A proposal for a comprehensive metallographic approach. *Journal of Archaeological Science,* 38, 1234-1252.

**[63]** M. Carl, M.L. Young (2016) Complementary analytical methods for analysis of Ag-plated cultural heritage objects. *Microchemical Journal*, 126, 307-315.

**[64]** F. Nocete, R. Sáez, M.R. Bayona, J.M. Nieto, A. Peramo, P. López, J.l. Gil-Ibarguchi, N. Inácio, S. García, J. Rodríguez (2014) Gold in the Southwest of the Iberian Peninsula during the 3rd Millennium BC. *Journal of Archaeological Science*, 41, 691-704.

**[65]** E. Figueiredo, R.J.C. Silva, M.F. Araúlo, J.C. Senna-Martinez (2010) Identification of ancient gilding technology and Late Bronze Age metallurgy by EDXRF, Micro-EDXRF, SEM-EDS and metallographic techniques. *Microchimica Acta*, 168, 283-291.

**[66]** S. Scrivano, B.G. Tubío, I. Ortega-Feliu, F.J. Ager, A. Paul, M.A. Respaldiza (2017) Compositional and microstructural study of joining methods in archaeological gold objects. *X-Ray Specrometry*, 46, 123-130.

**[67]** M.A. Beherec, T.E. Levy, O. Tirosh, M. Najjar, K.A. Knabb, Y. Erel (2016) Iron Age Nomads and their relation to copper smelting in Faynan (Jordan): Trace metal and Pb and Sr isotopic measurements from the Wadi Fidan 40 cemetery. *Journal of Archaeological Science*, 65, 70-83.

**[68]** B. Valentine, G.D. Kamenov, J. Krigbaum (2008) Reconstructing Neolithic groups in Sarawak, Malaysia through lead and strontium isotope analysis. *Journal of Archaeological Science*, 35, 1463-1473.

**[69]** S. Baron, C. Le-Carlier, J. Carignan, A. Ploquin (2009) Archaeological reconstruction of medieval lead production: Implications for ancient metal provenance studies and paleopollution tracing by Pb isotopes. *Applied Geochemistry*, 24, 2093-2101.

**[70]** J. Baker, S. Stos, T. Waight (2006) Lead isotope analysis of archaeological metals by multiple-collector inductively coupled plasma mass spectrometry. *Archaeometry*, 48, 45-56.

**[71]** Z.A. Stos-Gale, N.H. Gale (2009) Metal provenancing using isotopes and the Oxford archaeological lead isotope database (OXALID). *Archaeological and Anthropological Sciences*, 1, 195-213.

**[72]** Z.A. Stos-Gale, G. Maliotis, N.H. Fale, N. Annetts (1997) Lead isotope characteristics of the cyprus copper ore deposits applied to provenance studies of copper oxide ingots. *Archaeometry*, 39, 83-123.

**[73]** J. Ling, E. Hjärthner-Holdar, L. Grandin, K. Billström, P.O. Persson (2013) Moving metals or indigenous mining? Provenancing Scandinavian Bronze Age artefacts by lead isotopes and trace elements. *Journal or Archaeological Science*, 40, 291-304.

**[74]** J. Ling, Z. Stos-Gale, L. Grandin, K. Billström, E. Hjärthner-Holdar, P.O. Persson (2014) Moving metals II: provenancing Scandinavian Bronze Age artefacts by lead isotope and elemental analyses. *Journal of Archaeological Science*, 41, 106-132.

**[75]** M. Bode, A. Hauptmann, K. Mezger (2009) Tracing Roman lead sources using lead isotope analyses in conjunction with archaeological and epigraphic evidence-a case study from Augustan/Tiberian Germania. *Archaeological and Anthropological Sciences*, 1, 177-194.

**[76]** S. Sfarra, C. Ibarra-Castanedo, M. Tortora, L. Arrizza, G. Cerichelli, I. Nardi, X. Maldague (2016) Diagnostic of wall paintings: A smart and reliable approach. *Journal of Cultural Heritage*, 18, 229-241.

**[77]** P. Taruvinga, W. Ndoro (2013) The vandalism of the Domboshava rock painting site, Zimbawe: Some reflections on approaches to heritage management. *Conservation and Management of Archaeological Sites*, 6, 3-10.

**[78]** D. Gamboni (2013) The Destruction of Art: Iconoclasm and Vandalism since the French Revolution. *Reaktion Books, London (UK),* pp 416.

**[79]** D. Hapgood, D. Richardson (1984) Monte Cassino: The Story of the Most Controversial Battle of World War II. *Da Capo Press, Boston (USA,)* pp 320.

**[80]** F. Francioni, F. Lenzerini (2003) The destruction of the Buddhas of Bamiyan and international law. *European Journal of International Law,* 14, 619–651.

**[81]** A. Lluveras-Tenorio, R. Vinciguerra, E. Galano, C. Baensdorf, E. Emmerling, M.P. Colombini, L. Birolo, I. Bonaduce (2017) GC/MS and proteomics to unravel the painting history of lost Giant Buddas of Bāmiyān (Afghanistan). *Plos One*, 12: e0172990.

**[82]** H.S. Garreau (2007) Removal of Damaging Conservation Treatments on Mural Paintings. *Swedish National Heritage Broad, Stockholm (Sweden),* pp 72.

**[83]** A. Andreotti, I. Bonadulce, M.P. Colombini, G. Gautier, F. Modugno, E. Ribechini (2006) Combined GC/MS Analytical Procedure for the Caracterization of Glycerolipid, Waxy, Resinous, and Proteinaceous Materials in a Unique Paint Microsample. *Analytical Chemistry*, 78, 4490-4500.

**[84]** S. Prati, E. Joseph, G. Sciutto, R. Mazzeo (2010) New advances in the Application of FTIR Microscopy and Spectroscopy for the Characterization of Artistic Materials. *Account of Chemical Research*, 43, 792-801.

**[85]** P. Bosch-Roig, J.L. Regidor-Ros, P. Soriano-Sancho, R.M. Montes-Estelles (2013) Biocleaning of animal glue on wall paintings by Pseudomonas stuzeri. *Chemistry Today*, 31, 50-53.

**[86]** H. Liang (2016) Advances in multispectral and hyperspectral imaging for archaeology and art conservation. *Applied Physics A*, 106, 309-323.

**[87]** D. Comelli, G. Valentini, A. Nevin, A. Farina, L. Toniollo, R. Cubeddu (2008) A portable UV-fluorescence multispectral imaging system for the analysis of painted surfaces. *Review of Scientific Instruments,* 79: 086112.

**[88]** B. Horemans, C. Cardell, L. Bencs, V. Kontozova-Deutsch, K. De Wael, R.V. Grieken (2011) Evaluation of airborne particles at the Alhambra monument in Granada, Spain. *Microchemical Journal*, 99, 429-438.

**[89]** P. Ortiz, M.A. Vázquez, R. Ortiz, J.M. Martín, T. Ctvrtnickova, M.P. Mateo, G. Nicolas (2010) Investigation of environmental pollution effects on stone monuments in the case of Santa Maria La Blanca, Seville (Spain). *Applied Physics A*, 100, 965-973.

**[90]** A. Sarmiento, M. Maguregui, I. Martínez-Arkarazo, M. Angulo, K. Castro, M.A. Olazabal, L.A. Fernández, M.D. Rodríguez-Laso, A.M. Mujika, J. Gómez, J.M. Madariaga (2008) Raman spectroscopy as a tool to diagnose the impacts of combustion and greenhouse aced gases on properties of Built Heritage. *Journal of Raman Spectroscopy*, 39, 1042-1049.

**[91]** V. Kontozova-Deutsch, C. Cardell, M. Urosevic, E. Ruiz-Agudo, F. Deutsch, R.V. Grieken (2010) Characterization of indoor and outdoor atmospheric pollutants impacting architectural monuments: the case of San Jerónimo Monastery (Granada, Spain). *Environmental Earth Sciences*, 63, 1433-1445.

**[92]** M.J. Le Blas, A.L. Streckeisen (1991) The IUGS systematic of igneous rocks. *Journal of the Geological Society*, 148, 825-833.

**[93]** P. Merello, F.J. García-Diego, M. Zarzo (2012) Microclimate monitoring of Ariadne's house (Pompeii, Italy) for preventive conservation of fresco paintings. *Chemistry Central Journal*, 6, 145-161.

**[94]** M.I. Martínez-Garrido, D. Ergenç, R. Fort (2016) Wireless monitoring to evaluate the effectiveness of roofing systems over archeological sites. *Sensors and Actuators A: Physical*, 252, 120-133.

**[95]** M. Zarzo, A. Fernández-Navajas, F.J. García-Diego (2011) Long-Term Monitoring of Fresco Paintings in the Cathedral of Valencia (Spain) Through Humidity and Temperature Sensors in Various Locations for Preventive Conservation. *Sensors*, 11, 8685-8710.

**[96]** M.C. Pérez, F.J. García-Diego, P. Merello, P. D'Antoni, A. Fernández-Navajas, A. Ribera, I. Lacomba, L. Ferrazza, J. Pérez-Miralles, J.L. Baró, P. Merce, H. D'Antoni, J. Curiel-Esparza (2013) Ariadne's house (Pomeii, Italy) wall paintings: A multidisciplinar study of its present state focused on a future restoration and preventive conservation. *Materiales de Construcción*, 63, 449-467.

**[97]** E. Doehne, C. Price (2010) Stone conservation, an overview of current research. *The Getty conservation Institute*, *Los Angeles (USA)*, pp 164.

**[98]** C.M. Grossp, R.M. Esbert (1994) Las sales soluble en el deterioro de rocas monumentales. Revisión bibliográfica. *Materiales de Construcción*, 235, 15-30.

**[99]** F. Moreno, S.A.G. Vilela, A.S.G. Antunes, C.A.S. Alves (2006) Capillary-rising salt pollution and granitic stone erosive decay in the parish church of Torre de Moncorvo (NE Portugal)-implications for conservation strategy. *Journal of Cultural Heritage,* 7, 56-66.

**[100]** E. Rosina, A. Sansonetti, S. Erba (2017) Focus on soluble salts transport phenomena: The study cases of Leonardo mural paintings at Sala delle Asse (Milan). *Construction and Building Materials*, 136, 643-652.

**[101]** M. Irazola, M. Olivares, K. Castro, M. Maguregui, I. Martínez-Arkarazo, J.M. Madariaga (2012) In situ Raman spectroscopy analysis combined with Raman and SEM-EDS imaging to assess the conservation state of 16$^{th}$ century wall paintings. *Journal of Raman Spectroscopy*, 43, 1676-1684.

**[102]** M.L. Amadori, S. Barcelli, G. Poldi, F. Ferrucci, A. Andreotti, P. Baraldi, M.P. Colombini (2015) Invasive and non-invasive analyses for knowledge and conservation of Roman wall paintings of the Villa of the Papyri in Herculaneum. *Microchemical Journal,* 118, 183-192.

**[103]** S. Vettori, S. Bracci, E. Cantisani, C. Riminesi, B. Sacchi, F. D'Andria (2016) A multianalytical approach to investigate the state of conservation of the wall paintings of Insula 104 in Hierapolis (Turkey). *Microchemical Journal*, 128, 279-287.

**[104]** J.M. Madariaga, M. Maguregui, S. Fernández-Ortiz de Vallejuelo, U. Knuutinen, K. Castro, I. Martínez-Arkarazo, A. Giakoumaki, A. Pitarch (2014) In situ analysis with portable Raman and ED-XRF spectrometers for the diagnosis of the formation of efflorescence on walls and wall paintings of the Insula IX 3 (Pompeii, Italy). *Journal of Raman Spectroscopy*, 45, 1059-1067.

**[105]** T. Rosado, J. Mirão, A. Candeias, A.T. Caldeira (2014) Microbial communities analysis assessed by pyrosequencing-a new approach applied to conservation state studies of mural paintings. *Analytical and Bioanalytical Chemistry*, 406, 887-895.

**[106]** O. Ciferri (1999) Microbial Degradation of Paintings. *Applied and Environmental Microbiology*, 65, 879-885.

**[107]** N. Unkovíc, M.L. Grbić (2015) Biodeteriogenic and toxigenic agents on 17th century mural paintings and facade of the old church of the Holy Ascension (Veliki Krcimir, Serbia). *Indoor and Built Environment*, 25, 826-837.

**[108]** K.L. Garg, K.K. Jain, A.K. Mishra (1995) Role of fungi in the deterioration of wall paintings. *The Science of Total Environment*, 167, 255-271.

**[109]** Th. Dornieden, A.A. Gorbushina, W.E. Krumbein (2000) Biodecay of cultural heritage as a space/time-related ecological situation — an evaluation of a series of studies. *International Biodeterioration and Biodegradation*, 46, 261-270.

**[110]** T. Rosado, M. Gil, J. Mario, A. Candeias, A.T. Caldeira (2013) Oxalate biofilm formation on mural paintings due to microorganisms – A comprehensive study. *International Biodeterioration and Biodegradation,* 85, 1-7.

**[111]** S.E.J. Villar, H.G.M. Edwards, M.R.D. Seaward (2004) Lichen biodeterioration of ecclesiastical monuments in northern Spain. *Spectrochimica Acta Part A*, 60, 1229-1237.

**[112]** M. Maguregui, U. Knuutinen, J. Trebolazabala, H. Morillas, I. Martínez-Arkarazo, J.M. Madariaga (2012) Use of in situ and confocal Raman

spectroscopy to study the nature and distribution of carotenoids in brown patinas from a deteriorated wall painting in Marcus Lucretius House (Pompeii). *Analytical and Bioanalytical Chemistry*, 402, 1529-1539.

**[113]** M. Pérez-Alonso, K. Castro, I. Martínez-Arkarazo, M. Angulo, M.A. Olazabal, J.M. Madariaga (2004) Analysis of bulk and degradation inorganic products of stones, mortars and wall paintings by portable Raman microprobe. *Analytical and Bioanalytical Chemistry,* 379, 42–50.

**[114]** H.G.M. Edwards, N.C. Russell, M.R.D. Seaward (1997) Calcium oxalate in lichen biodeterioration studied using FT-Raman spectroscopy. *Spectrochimica Acta Part A*, 53, 99-105.

**[115]** V. Raimondi, L. Masotti, G. Cecchi, L. Pantani (1995) Remote sensing of cultural heritage: a new field for lidar fluorosensors. *In: Proceedings of 1st International Congress on Science and Technology for the Safeguard of Cultural Heritage in the Mediterranean Basin, Catania,* 935–938.

**[116]** V. Raimondi, G. Cecchi, D. Lognoli, L. Palombi, R. Grönlund, A. Johansson, S. Svanberg, K. Barup, J. Hällström (2009) The fluorescence lidar technique for the remote sensing of photoautotrophic biodeteriogens in the outdoor cultural heritage: A decade of in situ experiments. *International Biodeterioration and Biodegradation*, 63, 823-835.

**[117]** V. Raimondi, L. Palombi, G. Cecchi, D. Lognoli, M. Trambusti, I. Gomoiu, (2007) Remote detection of laser-induced autofluorescence of fungal and bacterial strains with a high-spectral resolution lidar system and their analysis with multivariate techniques. *Optics Communications*, 273, 219–225.

**[118]** D. Lognoli, G. Cecchi, I. Mochi, L. Pantani, V. Raimondi, R. Chiari, T. Johansson, P. Weibring, H. Edner, S. Svanberg (2003) Fluorescence lidar imaging of the cathedral and baptistery of Parma. *Applied Physics B*, 76, 457–465.

**[119]** M.E.F. Abdel-Haliem, A.A. Sakr, M.F. Ali, M.F. Ghaly, C. Sohlenkamp (2013) Characterization of Streptomyces isolates causing colour changes of mural paintings in ancient Egyptian tombs. *Microbiological Research*, 168, 428-437.

**[120]** M.Y. Lee, H.M. Park, Y.J. Chung (2015) Biochemical Characteristics and Growth Control for fungi isolated from mural painting of Tomb No.6 at Songsan-ri, Gongju. *Journal of Conservation Science*, 31, 227-241.

**[121]** M. Díaz-Herraiz, V. Jurado, S. Cuezva, L. Laiz, P. Palecchi, P. Tiano, S. Sánchez-Moral, C. Sáiz-Jiménez (2013) The Actinobacterial Colonization of Etruscan Paintings. *Scientific Reports*, 3: 1440.

**[122]** C. Schabereiter-Gurtner, C. Sáiz-Jiménez, G. Piñar, W. Lubitz, S. Rölleke (2002) Altamira cave Palaeolithic paintings harbour partly unknown bacterial communities. *Microbiology letters*, 211, 7-11.

**[123]** A.A Gorbushina, J. Heyrman, T. Dornieden, M. Gonzalez-Delvalle, W.E. Krumbein, L. Laiz, K. Petersen, C. Saiz-Jimenez, J. Swings (2004) Bacterial and fungal diversity and biodeterioration problems in mural painting environment of St. Martins church (Greene-Kreiensen, Germany). *International Biodeterioration and Biodegradation*, 53, 13-24.

**[124]** Ph. Dillmann, G. Beranger, P. Piccardo, H. Matthiessen (2007) Corrosion of Metallic Heritage Artefacts. *Woodhead Publishing, Sawston (UK),* pp 416.

**[125]** P.R. Roberge (2006) Corrosion Basics: An introduction. *Nace Press Book, Huston (USA),* pp 364.

**[126]** D. Neff, Ph. Dillmann, L. Bellot-Gurlet, G. Beranger (2005) Corrosion of iron archaeological artefacts in soil: characterization of the corrosion system. *Corrosion Science,* 47, 515-535.

**[127]** B. Beverskog, I. Puigdomenech (1996) Revised Pourbaix diagrams for iron at 25-300ºC. *Corrosion Science*, 38, 2121-2135.

**[128]** W. Gerwin, R. Baumhauer (2000) Effect of soil parameters on the corrosion of archaeological metal finds. *Geoderma*, 96, 63-80.

**[129]** V. Fell, J. Williams (2004) Monitoring of archaeological and experimental iron at Fiskerton, England. *National Museum of Australia Canberra* ACT, 4–8 October 2004, *Camberra (Australia)*.

**[130]** K. Tronner, A.G. Nord, G.Ch. Borg (1995) Corrosion of archaeological bronze artefacts in acidic soil. *Water, Air, and Soil Pollution*, 85, 2725-2730.

**[131]** M. Kibblewhite, G. Tóth, T. Hermann (2015) Predicting the preservation of cultural artefacts and buried materials in soil. *Science of the Total Environment,* 529, 249-263.

**[132]** A.G. Nord, E. Mattsson, K. Tronner (2005) Factors Influencing the Long-term Corrosion of Bronze Artefacts in Soil. *Protection of Metals*, 41, 309-316.

**[133]** K. Fitzpatrick Nieto, W.T. Frankenberger (1984) Single Column Ion Chromatography: I. Analysis of Inorganic Anions in Soils. *Soil Science Society of America Journal*, 49, 587-592.

**[134]** S.M. Valsecchi, S. Polesello (1999) Analysis of inorganic species in environmental samples by capillary electrophoresis. *Journal of Chromatography A*, 834, 363-385.

**[135]** C.A. Wilson, C.A. Davidson, M.S. Cresser (2008) Multi-element soil analysis: an assessment of its potential as an aid to archaeological interpretation. *Journal of Archaeological Science*, 35, 412-424.

**[136]** C. Remazeilles, D. Neff, F. Kergourlay, E. Foy, E. Conforto, E. Guilminot, S. Reguer, Ph. Refait, Ph. Dillmann (2009) Mechanisms of long-term anaerobic corrosion of iron archaeological artefacts in seawater. *Corrosion Science*, 51, 2932-2941.

**[137]** G. Cragnolino, O.H. Tuovinen (1984) The role of sulphate-reducing and sulphur-oxidizing bacteria on the localized corrosion of iron-base alloys - A review. *International Biodeterioration*, 20, 9-26.

**[138]** W.A. Hamilton (1994) Biocorrosion: the action of sulphate-reducing bacteria. In: Biochemistry of Microbial Degradation. *Kluwer, Minneapolis (USA),* 555-570.

**[139]** D. Neff, S. Reguer, L. Bellot-Gurlet, Ph. Dillmann, R. Bertholon (2004) Structural characterization of corrosion products on archaeological iron: an integrated analytical approach to establish corrosion forms. *Journal of Raman Spectroscopy*, 35, 739-745.

**[140]** G.M. Ingo, T. De Caro, C. Riccucci, E. Angelini, S. Grassini, S. Balbi, P. Bernardini, D. Salvi, L. Bousselmi, A. Cilingiroglu, M. Gener, V.K. Gouda, O. Al Jarrah, S. Khosroff, Z. Mahdjoub, Z. Al Saad, W. El-Saddik, P. Vassiliou (2006) A large scale investigation of chemical composition, structure and corrosion mechanism of bronze archeological artefacts from Mediterranean basin. *Applied Physics A*, 83, 513-520.

**[141]** D. Neff, L. Bellot-Gurlet, Ph. Dillmann, S. Reguer, L. Legrand (2006) Raman imaging of ancient rust scales on archaeological iron artefacts for long-term atmospheric corrosion mechanisms study. *Journal of Raman Spectroscopy*, 37, 1228-1237.

**[142]** J. Monnier, L. Legrand, L. Bellot-Gurlet, E. Foy, S. Reguer, E. Rocca, Ph. Dillmann, D. Neff, F. Mirambet, S. Perrin, I. Guillot (2008) Study of archaeological artefacts to refine the model of iron long-term indoor atmospheric corrosion. *Journal of Nuclear Materials*, 379, 105-111.

**[143]** G. Pingitore, T. Cerchiara, G. Chidichimo, M. Castriota, C. Gattuso, D. Marino (2015) Structural characterization of corrosion product layers on archaeological iron artifacts from VIgna Nuova, Crotone (Italy). *Journal of Cultural Heritage*, 16, 372-376.

**[144]** F.E. Wagner, R. Gebhard, W. Häusler, U. Wagner, P. Albert, H. Hess, Z. Révay, P. Kudejová, K. Kleszcz (2016) Study of archaeological iron objects by PGAA, Mössbauer spectroscopy and X-ray diffraction. Hyperfine Interactions, 237: 30.

**[145]** E. Angelini, S. Grassini, G. Solorzano, G.N. Campos, T. De Caro (2006) Integrated approach to the characterization and conservation of artefacts of the Brazilian colonial period. *Applied Physics A*, 83, 485-491.

**[146]** L. Robbiola, J.M. Blengino, C. Fiaud (2017) Morphology and mechanisms of formation of natural patinas on archaeological Cu-Sn alloys. *Corrosion Science*, 40, 2083-2111.

**[147]** L. Pronti, A.C. Felici, M. Alesiani, O. Tarquini, M.P. Bracciale, M.L. Santarelli, G. Pardini, M. Piacentini (2015) Characterisation of corrosion layers formed under burial environment of copper-based Greek and Roman coins from Pompeii. *Applied physics A*, 121, 59-68.

**[148]** L. Selwyn (2004) Overview of archaeological iron: the corrosion problem, key factors affecting treatment, and gaps in current knowledge (2004) *National Museum of Australia Canberra* ACT, 4–8 October 2004, *Camberra (Australia)*.

**[149]** S. Reguer, Ph. Dillmann, F. Mirabet (2007) Buried iron archaeological artefacts: Corrosion mechanisms related to the presence of Cl-containing phases. *Corrosion Science*, 49, 2726-2744.

**[150]** K. Ståhl, K. Nielsen, J. Jiang, B. Lebech, J.C. Hanson, P. Norby, J. van Lanschot (2003) On the akaganeite crystal structure, phase transformation and possible role in post-excavational corrosion of iron artifacts. *Corrosion Science*, 45, 2563-2575.

**[151]** K.E. García, C.A. Barrero, A.L. Morales, J.M. Greneche (2009) Magnetic structure of synthetic akaganèite: a review of Mossbauer data. *Revista Facultad de Ingeniería Universidad de Antioquia*, 49, 185–191.

**[152]** S. Reguer, F. Mirambet, E. Dooryhee, J.L. Hodeau, Ph. Dillmann, P. Lagarde (2009) Structural evidence for the desalination of akaganeite in the preservation of iron archaeological objects, using synchrotron X-ray powder diffraction and absorption spectroscopy. *Corrosion Science*, 51, 2795-2802.

**[153]** Ph. Dillmann, D. Watkinson, E. Angelini, A. Adriaens (2013) Corrosion and Conservation of Cultural Heritage Metallic Artefacts. *Woodhead Publishing*, *Sawston (UK),* pp 640.

**[154]** Q. Wang, S. Dove, F. Shearman, M. Smirniou (2008) Evaluation of methods of chloride ion concentration determination and effectiveness of desalination treatments using sodium hydroxide and alkaline sulphite solutions. *The conservator*, 31, 67-74.

**[155]** W. Carlin, D. Keith, J. Rodríguez (2001) Less is More: Measure of Chloride Removal from Wrought Iron Artifacts During Electrolysis. *Studies in Conservation*, 46, 68-76.

**[156]** E. Sangouard, E. Nordgren, R. Spohn, K. Brunke, D. Krop (2015) Evaluation of sodium nitrite as corrosion inhibitor for USS Monitor artifacts. *Studies in Conservation*, 60, 253-266.

**[157]** E. Guilminot, N. Huet (2008) Dechlorination of archaeological iron artefacts: dechlorination efficiency assessment assisted by physic-chemical analytical high-tech methods. *Metals*, 1, 435-443.

**[158]** S. Turgoose (1982) Post-excavation changes in iron antiquities. *Studies in Conservation*, 27, 97-101.

**[159]** M. Rimmer, D. Watkinson, Q. Wang (2012) The efficiency of chloride extraction from archaeological iron objects using deoxygenated alkaline solutions. *Studies in Conservation*, 57, 29-41.

**[160]** R. Giorgi, M. Baglioni, D. Berti, P. Baglioni (2010) New methodologies for the conservation of cultural heritage: micellar solutions, microemulsions, and hydroxide nanoparticles. *Accounts of Chemical Research,* 43, 695-704.

**[161]** P. Baglioni, D. Berti, M. Bonini, E. Carretti, L. Dei, E. Fratini, R. Giorgi. (2014) Micelle, microemulsions, and gels for the conservation of cultural heritage. *Advances in Colloids and Interface Science*, 205, 361-371.

**[162]** M. Baglioni, D. Rengstl, D. Berti, M. Bonini, R. Giorgi, P. Baglioni (2010) Removal of acrylic coatings from works of art by means of nanofluids: understanding the mechanism at the nanoscale. *Nanoscale*, 2, 1723-1732.

**[163]** M. Baglioni, R. Giorgi, D. Berti, P. Baglioni (2012) Smart cleaning of cultural heritage: a new challenge for soft nanoscience. *Nanoscale*, 4, 42-53.

**[164]** E. Carretti, L. Dei, P. Baglioni (2003) Solubilization of Acrylic and Vinyl Polymers in Nanocontainer Solutions. Application of Microemulsions and Micelles to Cultural Heritage Conservation. *Langmuir*, 19, 7867-7872.

**[165]** M. Baglioni, D. Berti, J. Teixeira, R. Giorgi, P. Baglioni (2012) Nanostructured Surfactant-Based Systems for the Removal of Polymers from Wall Paintings: A Small-Angle Neutron Scattering Study. *Langmuir*, 28, 15193-15202.

**[166]** F. Palla (2013) Bioactive molecules: innovative contributions of biotechnology to the restoration of cultural heritage. *Conservation Science in Cultural Heritage*, 13, 273-277.

**[167]** F. Makes (1988) Enzymatic consolidation of the portrait of Rudolf II with a multienzyme preparation isolated from Antarctic krill (Euphausia superbia). *Acta Universitatis Gothoburgensis - Götenburg Studies on Conservation, Götenburg (Sweden),* pp 49.

**[168]** S. Beutel, K. Klein, G. Knobbe, P. Konigfeld, K. Petersen, R. Ulber, T. Scheper (2002). Controlled Enzymatic Removal of Damaging Casein Layers on Medieval Wall Paintings. *Biotechnology and Bioengineering*, 80, 13-21.

**[169]** P. Bosh-Roig, J.L. Regidor-Ros, P. Soriano-Sancho, R.M. Montes-Estellés (2013) Biocleaning of animal glue on wall paintings by Pseudomonas stutzeri. *Biocides,* 31, 50-53.

**[170]** F. Cappitelli, L. Toniolo, A. Sansonetti, D. Gulotta, G. Ranalli, E. Zanardini, C. Sorlini (2007) Advantages of using microbial technology over traditional chemical technology in removal of black crusts from stone surfaces of historical monuments. *Applied and Environmental Microbiology*, 72, 5671-5675.

**[171]** G. Lustrato, G. Alfano, A. Andreotti, M.P. Colombini, G. Ranalli (2012) Fast biocleaning of medieval frescoes using viable bacterial cells. *International Biodeterioration and Biodegradation*, 69, 51-61.

**[172]** P. Antonioli, G. Zapparoli, P. Abbruscato, C. Sorlini, G. Ranalli, P.G. Righetti (2005) Art-loving bugs: The resurrection of Spinello Aretino from Pisa's cemetery. *Proteomics*, 5, 2453-2459.

**[173]** F. Cappitelli, E. Zanardini, G. Ranalli, E. Mello, I. Daffonchio, C. Sorlini (2006) Improved methodology for bioremoval of black crust on historical stone artworks by use of sulfate reducing bacteria. *Applied and Environmental Microbiology*, 72, 3733-3737.

**[174]** J. Gutiérrez, C. Barry-Ryan, P. Bourke (2008) The antimicrobial efficacy of essential oil combinations and interactions with food ingredients. *International Journal of Food Microbiology*, 124, 91-97.

**[175]** F.M. Pelissari, M.V.E. Grossman, F. Yamashita, E.A.G. Pineda (2009) Antimicrobial, Mechanical, and Barrier Properties of Cassava Starch-Chitosan Films Incorporated with Oregano Essential Oil. *Journal of Agricultural and Food Chemistry*, 57, 7499-7504.

**[176]** C.C. Liolios, O. Gortzi, S. Lalas, J. Tsaknis, I. Chinou (2009) Liposomal incorporation of carvacrol and thymol isolated from the essential oil of Origanum dictamnus L. and in vitro antimicrobial activity. *Food Chemistry*, 112, 77-83.

**[177]** M. Stupar, M.L. Grbić, A. Džamić, N. Unković, M. Ristić, A. Jelikić, J. Vukojević (2014) Antifungal activity of selected essential oils and biocide benzalkonium chloride against the fungi isolated from cultural heritage objects. *South African Journal of Botany*, 93, 118-124.

**[178]** A.A. Sakr, M.F. Ghaly, M.E.F. Abdel-Haliem (2012) The efficacy of specific essential oils on yeasts isolated from the royal tomb paintings at Tanis, Egypt. *International Journal of Conservation Science*, 3, 87-92.

**[179]** M.A. Rogerio-Candelera (2014) Science, Technology and Cultural Heritage. *CRC Press, Boca Ratón (USA)*, pp 514.

**[180]** D. Chelazzi, G. Poggi, Y. Jaidar, N. Toccafondi, R. Giorgi, P. Baglioni (2013) Hydroxide nanoparticles for cultural heritage: Consolidation and protection of wall paintings and carbonate materials. *Journal of Colloid and Interface Science*, 392, 42-49.

**[181]** A. Daehne, C. Herm (2013) Calcium hydroxide nanosols for the consolidation of porous building materials – result from EU-STONECORE. *Heritage Science*, 1: 11.

**[182]** R. Giorgi, M. Ambrosi, N. Toccafondi, P. Baglioni (2010) Nanoparticles for Cultural Heritage Conservation: Calcium and Barium Hydroxide Nanoparticles for Wall Painting Consolidation. *Chemistry-A European Journal,* 16, 9374-9382.

**[183]** L. Dei, P. Baglioni, M. Ambrosi, R. Giorgi, C. Neto (2001) Colloidal Particles of $Ca(OH)_2$: Properties and Applications to Restoration of Frescoes. *Langmuir,* 17, 4251-4255.

**[184]** L. Dei, B. Salvadori (2006) Nanotechnology in cultural heritage conservation: nanometric slaked lime saves architectonic and artistic surfaces from decay. *Journal of Cultural Heritage*, 7, 110-115.

**[185]** N.G. González, P. De Viviés, M.J. Drews, P. Mardikian (2004) Hunting free and bound chloride in the wrought iron rivets from the American Civil War submarine, H.L. Hunley. *Journal of American Institute for Conservation,* 43, 161–174.

**[186]** M. Bayle, P. De Viviés, J.B. Memet, E. Foy, Ph. Dillmann, D. Neff (2016) Corrosion product transformations in alkaline baths under pressure and high temperature: The sub-critical stabilisation of marine iron artefacts stored under atmospheric conditions. *Materials and Corrosion*, 67, 190-199.

**[187]** M.J. Drews, N.G. González-Pereyra, P. Mardikian, P. De Viviés (2013) The application of subcritical fluids for the stabilization of marine archaeological iron. *Studies in Conservation*, 58, 314-325.

**[188]** L.M.E. Näsänen, N.G. González-Pereyra, S.A. Cretté, P. De Viviés (2013) The applicability of subcritical fluids to the conservation of actively corroding iron artifacts of cultural significance. *The Journal of Supercritical Fluids*, 79, 289-298.

**[189]** P. Kritzer (2004) Corrosion in high-temperature and supercritical water and aqueous solutions: a review. *The Journal of Supercritical Fluids,* 29, 1–29.

**[190]** M.J. Drews, M. Williams, M. Barr (2000) A kinetic study of the SCWO of a sulfonated lignin waste stream. *Industrial and Engineering Chemistry Research,* 39, 4784–4793.

**[191]** W. Wagner, A. Pruß (2002) The IAPWS formulation 1995 for the thermodynamic properties of ordinary water substance for general and scientific use, *Journal of Physical and Chemical Reference Data*, 31, 387–535.

**[192]** P. Fojtíková, L. Řádková, D. Janová, F. Krčma (2015) Application of low-temperature low pressure hidrogen plasma: treatment of artificially prepared corrosion layers. *Open Chemistry*, 13, 362-368.

**[193]** V.D. Daniels, L. Holland, C. Pascoe (1979) Gas plasma reactions for the conservation of antiquities. *Studies in Conservation*, 24, 85–92.

**[194]** K. Schmidt-Ott, V. Boissonnas (2002) Low-pressure hydrogen plasma: an assessment of its application on archaeological iron. *Studies in Conservation*, 47, 81-87.

**[195]** S. Veprek, J. Patscheider, J. Elmer (1984) Restoration and Conservation of Ancient Artifacts: A New Area of Application of Plasma Chemistry. *Plasma Chemistry and Plasma Processing*, 5, 201-209.

**[196]** S. Veprek, Ch. Eckmann, J. Elmer (1988) Recent progress in the restoration of archaeological metallic artifacts by means of low-pressure plasma treatment. *Plasma Chemistry and Plasma Processing*, 8, 445-466.

**[197]** L. Radkova, P. Mikova, R. Prikryl, F. Krcma (2016) Plasma chemical reduction of model corrosion brass layers prepared in soil. *The European Physical Journal Applied Physics*, 75: 24717.

**[198]** F. Krčma, L. Blahová, P. Fojtíková, W.G. Graham, H. Grossmannová, L. Hlochová, J. Horák, D. Janová, C.P. Kelsey, Z. Kozáková, V. Mazánková, M. Procházka, R. Přikryl, L. Řádková, V. Sázavská, M. Vašíček, R. Veverková, M. Zmrzlý (2014) Application of low temperature plasmas or restoration/conservation of archaeological objects. *Journal of Physics: Conference Series*, 565: 012012.

**[199]** A. Masalles, E. Lehmann, D. Mannes (2015) Non-destructive Investigation of "The Violinist" a Lead Sculpture by Pablo Gargallo, Using the Neutron Imaging Facility NEUTRA in the Paul Scherrer Institute. *Physics Procedia*, 69, 636-645.

**[200]** J.F. Asmus (1978) Light cleaning: Laser technology for surface preparation in the arts. *Technology and Conservation*, 3, 14-18.

**[201]** O. Abdel-Kareem, A. Al-Zaharani, A. Khedr, M. Abdel Harith (2016) Evaluating laser cleaning of corroded archaeological silver coins. *Mediterranean Archaeology and Archaeometry*, 16, 135-143.

**[202]** B. Radojković, S. Ristić, S. Polić, R. Jančić-Heinemann, D. Radovanović (2017) Preliminary investigation on the use of the Q-switched Nd:YAG laser to clean corrosion products on museum embroidered textiles with metallic yarns. *Journal of Cultural Heritage*, 23, 128-137.

**[203]** E. Cano, D. Lafuente, D.M. Bastidas (2010) Use of EIS for the evaluation of the protective properties of coatings for metallic cultural heritage: a review. *Journal of Solid State Electrochemistry*, 14, 381–391.

**[204]** R.A. Grayburn, M.G. Dowsett, A. Adriaens (2016) Further advances in lead carboxylate coatings: coating unprimed heritage lead. *Heritage Science*, 4: 7.

**[205]** G.T. Hefter, N.A. North, S.H. Tan (1997) Organic Corrosion Inhibitors in Neutral Solutions; Part 1 – Inhibition of Steel, Copper, and Aluminium by Straight Chain Carboxylates. *Corrosion Engineering*, 53, 657-667.

**[206]** R.A. Grayburn, M.G. Dowsett, M. De Keersmaecker, D. Banerjee, S. Brown, A. Adriaens (2014) Towards a new method for coating heritage lead. *Heritage Science*, 2: 14.

**[207]** E. Rocca, J. Steinmetz (2001) Inhibition of lead corrosion with saturated linear aliphatic chain monocarboxylates of sodium. *Corrosion Science*, 43, 891-902.

# CHAPTER 2:

# OBJECTIVES

Since 2000, the IBeA research group of excellence (Ikerkuntza eta Berrikuntza Analitikoa) has been working in several research projects addressed to *Cultural Heritage* conservation and enhancement.

Since that year, the scientific production of the research team has led, among others, to the drafting of 10 doctoral theses and the publication of more than 100 research papers (in high impact index journals) related to this field of study.

According to the prior experience of the research group (fundamental in the process of learning the management of scientific instrumentation as well as the treatment and interpretation of analytical data), and in the framework of DISILICA-1930, CTP09-P04, CTP10-P12 and APUV research projects, the following overall objective was defined for this PhD work:

**"Development and optimization of innovative methodologies for the characterization and conservation of archaeological irons and mural paintings"**

As previously mentioned, this research work has been focused on the study of two different categories of *Cultural Heritage*, that is, metallic archaeological artefacts and ancient mural paintings. For each of them, specific particular objectives were outlined.

In the case of archaeological artefacts, the technological advances to pursue consisted in:

1. *To develop a new methodological approach for a fast and reliable evaluation of the stability of corrosion systems formed on iron-based archaeological artefacts.*

2. *To optimize the most used desalination method for the conservation of metallic archaeological objects with high chloride content*.

As regards to wall paintings, the purpose was:

1. *To evaluate the possible exploitation of biocide essential oils as a novel and eco-friendly conservation product to neutralize biodeteriogens colonization.*

Following the guidelines recommended by national and international conventions concerning the protection and safeguarding of *Cultural Heritage*, the research works presented in this manuscript have been carried out in close collaboration with *Cultural Heritage* conservators as well as with experts from several scientific disciplines included in the broad field of *Conservation Science* (such as biologists, physicists and archaeologists). By following this interdisciplinary approach, the novel preservation procedures described above respond to the needs of minimize/control specific degradation processes detected during the study of numerous examples of real archaeological artefacts and mural paintings.

Accordingly, the attainment of the overall PhD purpose passes through the achievement of the following operational objectives:

1. *To analyze the molecular and elemental composition of original materials and, in the case of wall paintings, distinguish them from the products applied in earlier conservation treatments.*

2. *To identify the degradation processes threatening the conservation of the artworks under analysis and, through the study of the environmental context, determine the causes leading to their development.*

3. *To evaluate the most controversial degradation pathways and propose specific research lines addressed at improving/flanking the current conservation methodologies.*

# CHAPTER 3:

# EMPLACEMENTS AND SAMPLES

## 3.1 Archaeological artefacts

As explained in section 1.4.1, the analytical characterization of archaeological artefacts has a paramount importance in deepen the knowledge of our historical past, in order to understand social, economic and dynamic aspects of ancient societies [1].

Indeed, through the study of metallic artefacts it is possible to attain valuable data about the level of technological development achieved by ancient settlements in the field of *metallurgy*. Moreover, by comparing these data with those proceeding from bordering regions, possible social and commercial connections can be identified, such as trade routes and technology transfer activity between communities.

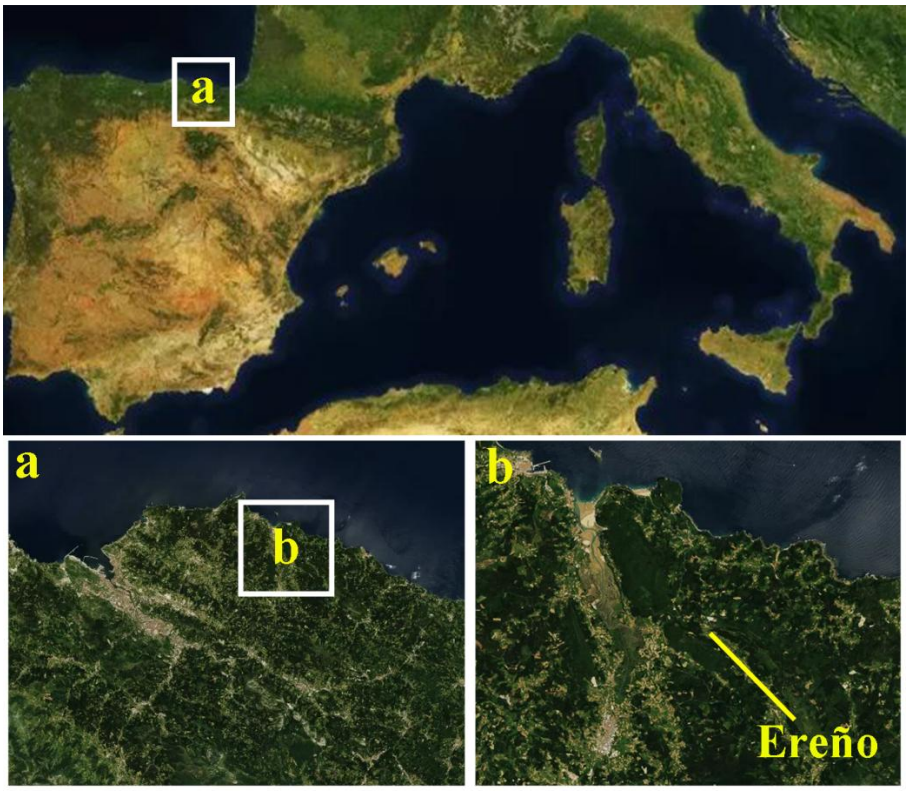


*Figure 3.1: Localization of the Archaeological site of Ereñozar (Spain).*

However, it must be highlighted that the conservation of metal artefacts is rather unusual in some regions. The intrinsic characteristics of the soils, the proximity to the coast, and the specific weather conditions of the area, favour the activation of aggressive degradation processes during the phase of burial, which often lead to the total destruction of metallic remains. Thus, the amount of metallic objects that are usually recovered from some archaeological endeavours is very limited. This is the case of the Basque Country [2].

Under these requirements, the IBeA group developed, in close collaboration with the Archaeological Museum of Bizkaia, an important research project (CTP10-P12) aimed at characterizing metallic artefacts recovered from Basque archaeological settlements. The work carried out in this PhD thesis falls within this framework.

### *3.1.1 Archaeological site of Ereñozar (Ereño, Spain)*

*Figure 3.2: a) Panoramic view from the Ereñozar mountain; b) archaeological excavation of Ereñozar necropolis.*

Thanks to the archaeological endeavours carried out in recent years on the top of Ereñozar mountain (430 mts above sea level, Urdaibai estuary, Basque Country, Figure 3.1), it was possible to identify the presence of wall remains belonging to several middle age buildings. Among them, considerable importance had the discovery of a necropolis, dating from the beginning of the 13$^{th}$ century. Indeed, in the flat area surrounding the current hermitage of San Miguel approximately 70 burials (Figure 3.2) were discovered [3]. The work of archaeologists allowed the recovery of numerous metallic artefacts that, after cataloguing, were entrusted to the Archaeology Museum of Bizkaia (Bilbao, Spain). As shown in Figures 3.3 and 3.4 the artefacts collection includes 7 buckles and two spurs.


*Figure 3.3: Images of some of the most interesting artefacts recovered from the archaeological excavation of the Ereñozar necropolis.*

As explained by archaeologists and conservators in charge of the excavation and preservation, the artefacts stood out for an excellent state of preservation, especially if compared with other archaeometallurgical objects (of the same historical epoch) recovered in the same geographical region [4].

Among the buckles, *H3043* (Figure 3.3g), which still retains the frame, the bar and the pin, can be considered as the best preserved one. As can be observed in Figure 3.3a and c, *H1001* and *H3003* artefacts have the same oval structure of the previous one, but both lack of the pin. *H3021* (Figure 3.3d) and *H3024* (Figure 3.3e) buckles are the most incomplete ones because they do not preserve either pin or bar, but only a fragment in which the pin notch can be observed. *H3042* (Figure 3.3f) is a complete buckle with the remains of textile on the metal surface. The last buckle (*H1002*, Figure 3.3b) stands out from all the previous ones because of a more elaborate structure and the presence of a decorative gilded layer.

The collection is completed by two iron-based spurs. On the one hand, the *E1037* spur (Figure 3.3h) is formed by two curved branch endings in a circular body on which a sharp point is developed. This artefact shows a worrier conservation problem with respect to the buckles caused by the continuous rust layer covering the surface.

On the other side, the second spur (*E294*) can be considered the most important object recovered from the archaeological site. It mainly differs from the artefact *E1037* by the presence of a gilded layer on its surface. As showed in Figure 3.4, the object was found fragmented and covered by a thick corrosion layer.


*Figure 3.4: Image of the two fragments of the gilded spur (E294) recovered during archaeological endeavours.*

The reason of the remarkable conservation state of most of these objects can be found in the pedological and geological characteristics of the Ereñozar mountain. On the one hand, the basic pH value of the soil (analyzed in previous works) favoured metal passivation, leading to the development of a protective rust patina [2]. On the other side, the geological profile of Ereñozar mountain (which is mainly composed of porous limestone) contributes considerably towards limiting the humidity level of the soils.

However, as mentioned in section 1.4.2, archaeological artefacts buried near the coastline often show the presence of reactive corrosion phases directly related to the influence of marine chlorides. This case of study is a clear example since Ereñozar mountain stands just few kilometres away from the coastline of the Gulf of Biscay. Thus, the archaeological site faces marine aerosols and chloride-containing precipitations [2].

Under this assumption, the artefacts shown in Figure 3.3 were subjected to conservation treatment soon after their recovery with the purpose of removing the $Cl^-$ ions infiltrated during the burial phase.

After desalinization and corrosion inhibition treatments, all artefacts have been constantly kept in an environment controlled room, ensuring constant levels of temperature (20 ± 2 °C) and humidity (65 ± 2% relative humidity). Furthermore, all artefacts have been stored in hermetic boxes equipped with desiccant silica gel beads that ensure humidity levels below 10% relative humidity and minimize post-excavation corrosion phenomena.

With regards to the gilded spur displayed in Figure 3.4, it must be underlined the lack of bibliography focused on evaluating the side effect entailed by the application of alkaline treatment (the most used technique for the desalination of iron-based artefacts) on archaeological object of similar metallic composition and conservation state (Figure 3.5).

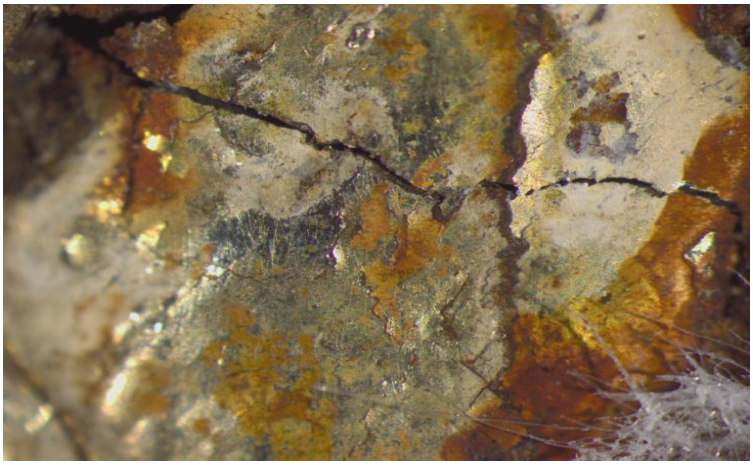

*Figure 3.5: Detail of the gilded spur affected by degradation processes. In the image, cracks and swellings can be observed.*

For this reason, the artefact was subjected to a specific analytical study prior to performing desalination baths. Concretely, laboratory analyses and experiments were performed on a number of corrosion fragments removed by conservators during the cleaning procedure. The purpose was to collect valuable data for choosing the optimal conservation treatment.

## 3.2 Mural paintings

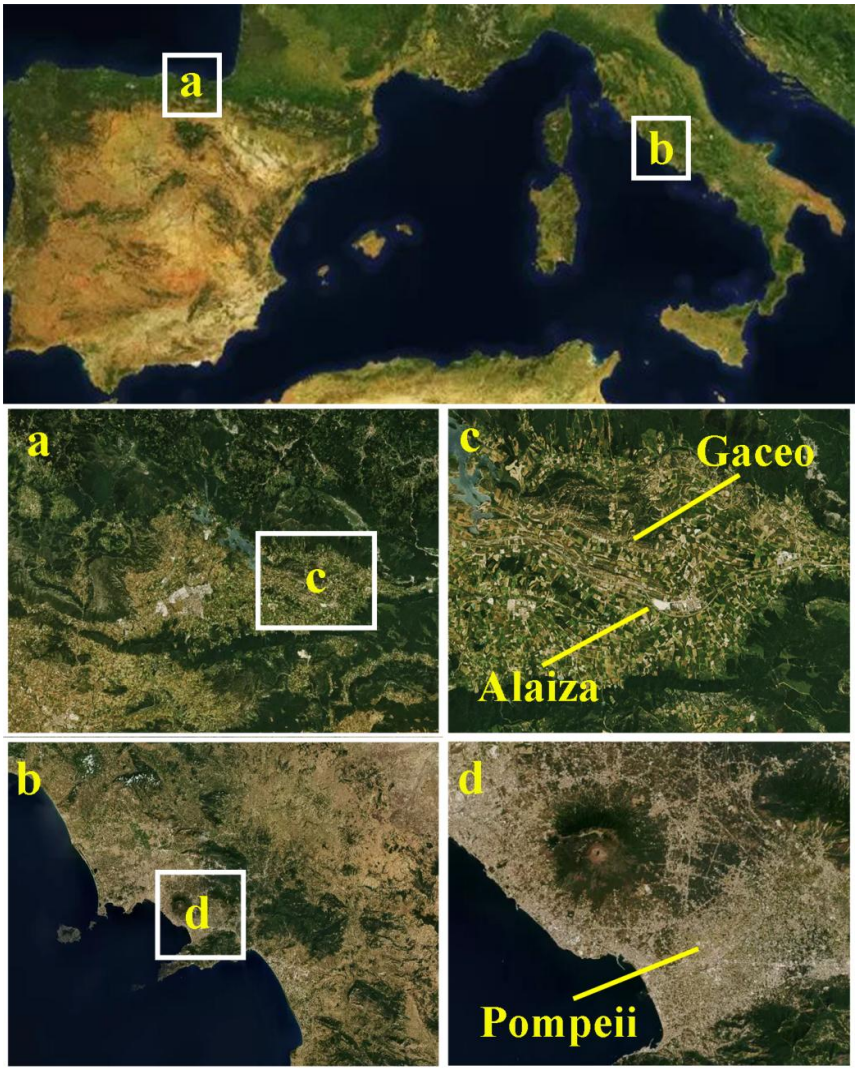


*Figure 3.6: Localization of the analyzed mural paintings. c) church of San Martín de Tours (Gaceo, Spain) and church of the Assumption (Alaiza, Spain); d) Ariadne's House (Archaeological site of Pompeii, Italy).*

In addition to the study of metallic archaeological artefacts, the working plan carried out in this PhD thesis also included the study of several mural paintings (Figure 3.6).

In a first phase of this PhD work, analytical studies were devoted to the characterization of the mural ensembles preserved in the church of the Assumption (Alaiza) and the church of San Martín the Tours (Gaceo), which represent some of the most outstanding examples of Middle Age paintings that can be found in the Basque Country.

The adopted experimental procedure aimed at: a) characterizing the original materials and their degradation products, b) diagnosing the state of conservation by means of chemometric tools and c) suggesting chemical reactions between the original materials and the environmental stressors leading to the onset of degradation pathways.

Thanks to the experience acquired during the characterization of the above mentioned artworks, the methodology developed was used in the APUV 2014 expedition [5], which continued with the study of some of the most magnificent examples of *frescoes* preserved in the archaeological site of Pompeii (Italy).

The Roman settlement was buried underneath the volcanic debris erupted by Mount Vesuvius in 79 AD. Massive ashfall deposits and pyroclastic surges sealed the remains of Pompeii, favouring their optimal preservation during centuries. However, since the archaeological excavations started in 1748, the ruins of the ancient Pompeii have been constantly undermined by the destructive effects of many degradation processes.

Within this context, the methodological approach developed in the study of the Basque mural paintings was used to assess the effects of environmental and biological factors on the degradation of a mural from the Ariadne's House, one of the most important residences of the archaeological site.

### *3.2.1 Church of San Martín de Tours (Gaceo, Spain)*

*Figure 3.7: Church of San Martín de Tours (Gaceo, Spain), external view.*

Since the Middle Age, northern Spain presents a series of trails that were traced by pilgrims going to the city of Santiago de Compostela (Galicia, Spain). During the 14$^{th}$ century, most villages located in the vicinity of these routes suffered a renewal of their religious buildings in order to give accommodation to the growing number of believers. Many of these churches were also enriched with artistic works (such as altarpieces and mural paintings) which, in addition to a decorative role, held an educational function [6]. Within this context, the Romanic church of San Martín de Tours (Figure 3.7) is probably the one conserving the most interesting paintings found in the Basque Country [7].

The murals were found hidden behind a Baroque altarpiece in 1967. Basing on the archaic character of the painting together with the study of some stylistic and iconographic details, the date of execution can be dated back to the middle of the 14$^{th}$ century. Mural paintings, created by an unknown author, involve the entire area of the apse and the presbytery and consist of five different scenes: the representation of the Holy Trinity, Judgment and the reward of the blessed, the Calvary, the Descent into hell and Episodes of the life of Christ (see Figure 3.8).


*Figure 3.8: Some of the most important mural paintings conserved in the church of San Martín de Tours: a) Holy Trinity, b) the Calvary; c) the Descent into hell; d) Episodes of the life of Christ.*

As far as we know, the whole ensemble was subjected to conservation treatments several times (the last one was performed between 2004 and 2007). Unfortunately, any documentation regarding earlier restorations has been found. However, the analytical studies presented by Artelab s.r.l. [8] in 2007 proved that the murals were subjected to an extensive repainting which overlapped the original paint layer. Furthermore, as can be observed in Figure 3.9, the painting cross sections prepared by Artelab s.r.l. evidenced the presence of a greyish translucent layer covering the paint layer.

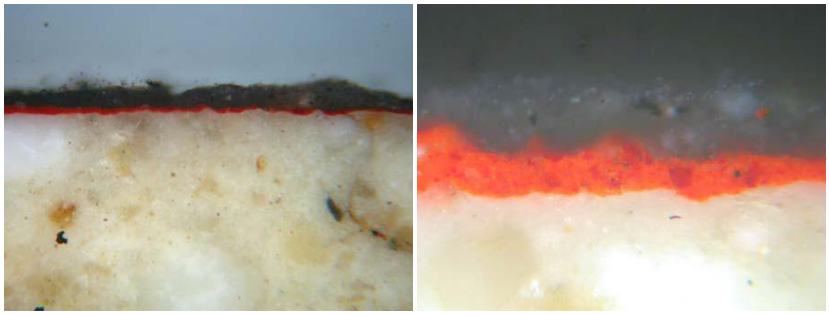

*Figure 3.9: Cross section prepared by Artelab s.r.l., showing a greyish layer of Paraloid B72 overlapping the original paint layer.*

The molecular characterization, achieved by FTIR spectroscopy, identified the layer as a conservation treatment (Paraloid B-72) applied in earlier restorations for consolidation and protective purposes.

As explained in the introduction, several pathologies can rise from the application of protective synthetic and organic layers on wall paintings, such as soluble salt crystallization, swelling and loss of material.

With the purpose of collecting more information regarding original, restoration and decay compounds, several campaigns of analysis (based on the use of portable and non destructive techniques) were carried out.

Furthermore, in order to deepen the knowledge about the materials composing the artwork, several micro metric wall painting fragments were collected using a scalpel. Sampled material was then analyzed by laboratory techniques, which provided complementary data to those collected by portable systems.

### *3.2.2 Church of the Assumption (Alaiza, Spain)*

*Figure 3.10: Church of the Assumption (Alaiza, Spain), external view.*

The discovery of wall paintings from the church of Alaiza (Figure 3.10) was an example of redemption from the ancient disinterest towards medieval art, which in this case brought the concealment of the murals under an anonymous layer of plaster. Since the moment of their discovery (1982) these paintings attracted great attention from the society. In fact, even if medieval mural art in the region of the Pyrenees could be generally related to a common artistic line, the paintings of

Alaiza (dated back in the 14th century) differ by the use of an unique style: two-dimensional figures, represented by the use of a very restricted range of colours, decorating the entire presbyterial area of the church. In the most important area of the mural, it is possible to observe several anthropomorphic figures, animals and plants, made exclusively with a red paint that contrasts with the white colour of the background [7]. This feature, instead of impoverishing the value of the mural, enriched it by a greater expressive power.

The main theme of the representation is based on a battle scene in which medieval warriors try to assault a castle (see Figure 3.11). This image, at the centre of the mural painting, is surrounded by secondary depictions of churches, votive offerings and processions. The interpretation of these images, divided between the sacred and the profane, is still far from being exactly defined.

*Figure 3.11: Main scene of the mural cycle, located in the half dome of the apse.*

With regard to the conservation state of the mural paintings, the bibliographic research allowed establishing that at the time of its discovery, the whole ensemble showed serious degradation problems due to the semi abandonment state of the structure. The restoration done in 1983 (which involved the complete reform of the roof) helped to mitigate the humidity problems arising from the infiltration of rainwater. However, the latest architectural intervention, carried out in 2004, leaded to the onset of new degradation problems. Indeed, as showed in Figure 3.12, the church was submitted to a critical structural reform which involved the removal of the sacristy adjacent to the secondary vault of the church. Thus, the south-oriented wall of the church was suddenly exposed to the direct contact with rainwater.

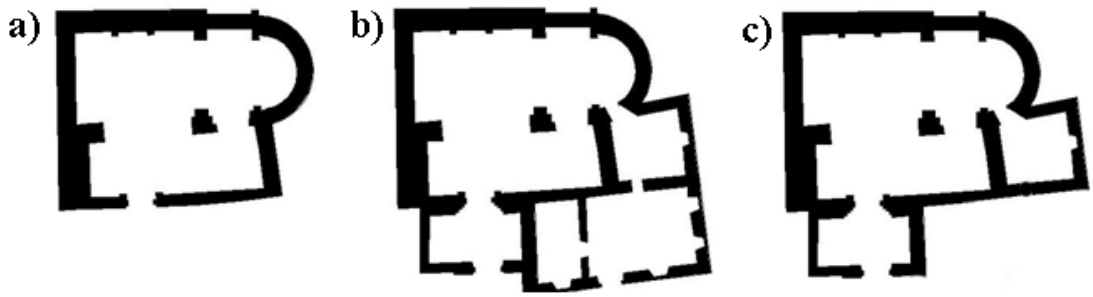


*Figure 3.12: Ground plans of the church, highlighting the original aspect (a), and the structural reforms carried out in the 18$^{th}$ century (b) and in 2004 (c).*

Nowadays, humidity rising from the soil and chemical weathering are producing critical damages to the mural paintings. As can be observed in Figure 3.13 the main effect of water infiltration is the crystallization of extensive efflorescence and crypto efflorescence.

*Figure 3.13: Extensive efflorescence salts observed in the secondary vault of the church.*

In this case of study, the information obtained in-situ through the use of portable analytical techniques was complemented by laboratory analyses of selected painting fragments. Moreover, water samples were collected from the surroundings of the church and analyzed by several techniques in an attempt to clarify the role of the environmental context on the onset of efflorescence salts crystallization.

### *3.2.3 Ariadne's House (Archaeological site of Pompeii, Italy)*


*Figure 3.14: 3D reconstruction of the Ariadne's House (source: Superintendency of Pompeii's website [9]).*

As previously explained, the removal of the volcanic material that sealed the archaeological site of Pompeii during centuries resulted in the activation of several deterioration processes [10]. Indeed, since the 19$^{th}$ century, the conservation of Pompeian *frescoes* has been constantly undermined by the destructive effects of many degradation phenomena, such as thermal and humidity fluctuations, direct exposure to sun-light, irreversible acid-base reactions between acid atmospheric pollution and the walls, leaching processes triggered by rainwater and capillary rise of soluble salts from the soil [11].

Taking into account the peculiar degradation problems of the archaeological site, the IBeA research group has been studying, since 2014, the conservation needs of the mural paintings located in the Ariadne's House. The patrician residence, located in the Regio VII, cuts straight through the insula IV with entrances on both Via degli Augustali and Via della Fortuna. Also known as the house of the Coloured Capitals, it was one of the largest residential buildings of the ancient city, covering over 1700 m$^2$. The structure was built at the beginning of the 2$^{nd}$ century BC and, as evidenced by the work carried out by C. Ribera et al. [12], it was subjected over years to several architectural and decorative reforms. At the time of the Vesuvius eruption (A.D. 79), the building (Figure 3.14) consisted of a large Tuscan atrium

and two peristyles surrounded by more than 40 rooms on the ground floor. Most of the rooms were decorated with *frescoes* of the 3rd and 4th style, painted in the decades proceeding to the volcanic eruption.

Although several rooftops were installed to protect the most important *frescoes*, most of the rooms are still directly exposed to atmospheric agents, among them, the west facing wall of room 56, which was analyzed in this work. It is opened to the north peristyle and corresponds to the exedra of the house. At that time, exedras were used to receive important visitors and, according to the Roman tradition, they had to be decorated with elaborated *frescoes*. In this case, however, the action of degradation processes resulted in the total loss of the paint layer and currently the inner preparation layer is exposed to the open air (Figure 3.15b).

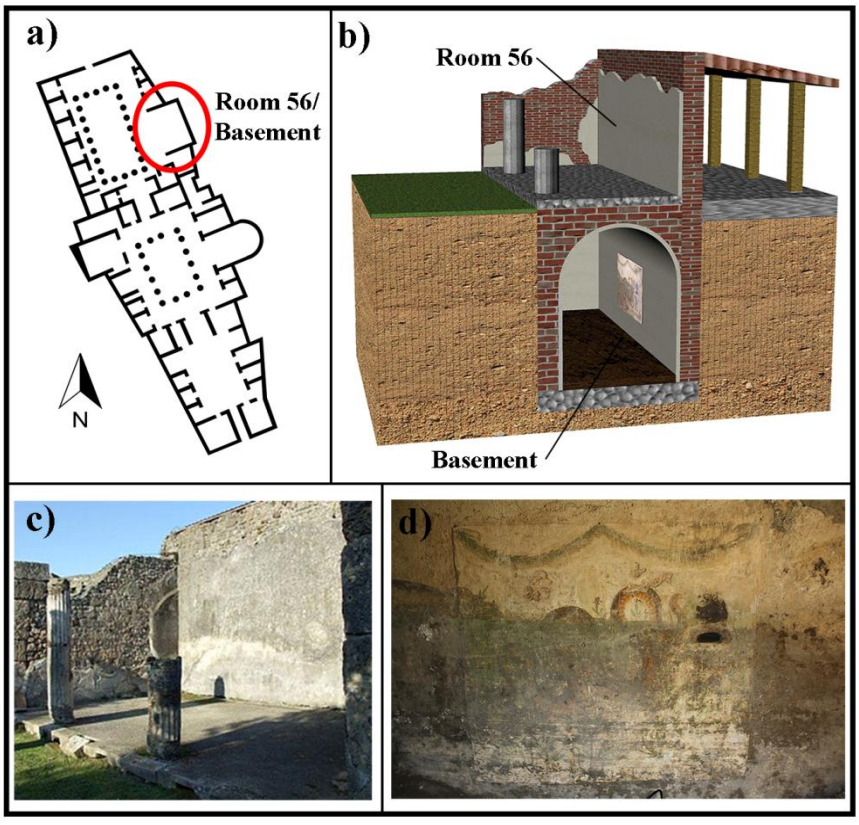


*Figure 3.15: a) Plan of the Ariadne's House located in the archaeological site of Pompeii; (b) 3D reconstruction and real pictures of both(c) room 56 and (d) basement.*

The second surface analyzed in this work was the west faced wall of the basement located just below the room 56 (Figure 3.15c). In this wall, the polychromatic decorations are still conserved and represent a snake and floral motifs on a white

background (Figure 3.15d). In this case, the artwork showed deep degradation issues related to: a) deposition of white crusts, b) crystallization of efflorescence salts and c) colonization of biodeteriogens. Among them, the biocolonization represents the most peculiar degradation process. In fact, the upper part of the *fresco*, recovered in 1988, was barely colonized by microorganisms while the lower part, excavated in 2005, was almost completely covered by different biological patinas.

During the visual assessment, a few detached fragments of mortar were also identified along the biocolonized surface. Thus, thanks to the permits issued by the *Superintendency of Pompeii,* painting and burial material samples were collected and analyzed through laboratory instruments with the aim of identifying clues to explain the reasons behind the heterogeneous distribution of biocolonization.

Moreover, with the purpose of characterizing the biological strains producing deterioration, sterile swabs were gently rubber over the mural painting and used to inoculate potato dextrose agar (PDA) medium in pre-poured Petri dishes. After confirming the growth of biological strains on the medium surface, the Petri dishes were sent to the BAT laboratory (CIAL institute, Madrid, [13]) for their treatment and characterization.

## 3.3 References

**[1]** E. May, M. Jones (2006) Conservation Science: Heritage Materials. *Royal Society of Chemistry*, *London (UK),* pp 376.

**[2]** L. García-Boullosa, J. Aramendia, M. Veneranda, S. Fdez-Ortiz de Vallejuelo, M. Neira, K. Castro, J.M. Madariaga, I. García-Camino (2015) Estudio y conservación de objetos metálicos procedentes de una necrópolis medieval costera (Castillo de Ereñozar, Bizkaia). *II Congreso de Conservación y Restauración del Patrimonio Metálico (MetalEspaña 2015), 1-3 October 201*5, Segovia (Spain).

**[3]** M.N. Zubieta (2008) Monte Ereñozar. *Arkeoikuska Investigación arqueológica*, 260-262.

**[4]** A.M. Salcedo (2004) Arqueología e Historia del Período Romano en Bizkaia (1972-2002). *Kobie*, 6, 353-370.

**[5]** APUV project website: http://apuv-ibea.com/es/ (May 28th 2017).

**[6]** M. Irazola, M. Olivares, K. Castro, M. Maguregui, I. Martínez-Arkarazo, J.M. Madariaga (2012) In situ Raman spectroscopy analysis combined with Raman and SEM-EDS imaging to assess the conservation state of 16th century wall paintings. *Journal of Raman Spectroscopy*, 43, 1676-1684.

**[7]** J.E. López de Sabando (1990) Gaceo y Alaiza, pinturas murales goticas. *Diputacion Foral de Alava*, *Victoria-Gasteiz (Spain)*, pp 48.

**[8]** Artelab s.r.l website: http://www.artelabsrl.it/ (May 28th 2017).

**[9]** Superintendency of Pompeii website: http://www.pompeiisites.org/ (May 28th 2017).

**[10]** M. Maguregui, K. Castro, H. Morillas, J. Trebolazabala, U. Knuutinen, R. Wiesinger, M. Schreiner, J.M. Madariaga (2014) Multianalytical Approach to explain the darkening process of hematite pigment in paintings from ancient Pompeii after accelerated weathering experiments, *Analytical Methods*, 6, 372-378.

**[11]** M. Maguregui, U. Knuutinen, K. Castro, J.M. Madariaga (2010) Raman spectroscopy as a tool to diagnose the impact and conservation state of Pompeian second and fourth style wall paintings exposed to diverse environments (House of Marcus Lucretius). *Journal of Raman Spectroscopy*, 41, 1400-1409.

**[12]** A. Ribera Lacomba, R. Albiach, C. Ballester, M. Bustamante, I. Caruana, I. Escrivà, E. Huguet, M. Olcina, V. Salavert, J.M. Vioque (2008) Pompeya: Excavaciones estratigráficas en la casa de Ariadna o dei Capitelli Colorati (Regio VII, 4,51 y 31). Campaña de 2007. *Informes y trabajos, Excavaciones en el exterior* 2007, 51-57.

**[13]** Bioanalytical Techniques Unit (BAT) website: http://www.cial.uam-csic.es/pagperso/bat/ (May 28th 2017).

# CHAPTER 4:
# EXPERIMENTAL TECHNIQUES

## 4.1 General purpose instruments and tools

Several laboratory instruments employed in this PhD thesis required specific sample treatments. For this purpose, the following tools were used:

**a) Loading analytical balance**

To know the exact weight of the samples under study it is of paramount importance to carry out reproducible quantitative (Ion Chromatography, Inductively Coupled Plasma-Mass Spectroscopy) and semi-quantitative (X-Ray Diffractometry, Fourier Transform Infrared Spectroscopy) analyses. Under this requirement, powder samples were weighed using an AS 200 analytical balance (Mettler Toledo, USA) with a precision of ± 0.0001g (see Figure 4.1a).

**b) Stereoscopic microscope**

The analytical study of iron corrosions and mural paintings samples was often assisted by their visual assessment at microscopic scale. Thanks to the support of Dr. X. Murelaga Bereicua from the Department of Stratigraphy and Paleontology

(UPV/EHU), high quality images of the fragments under analysis were acquired by means of the SMZ-U microscope (Nikon, Japan) coupled to the Nikon Digital Sight DS-L1 camera (Figure 4.1b).

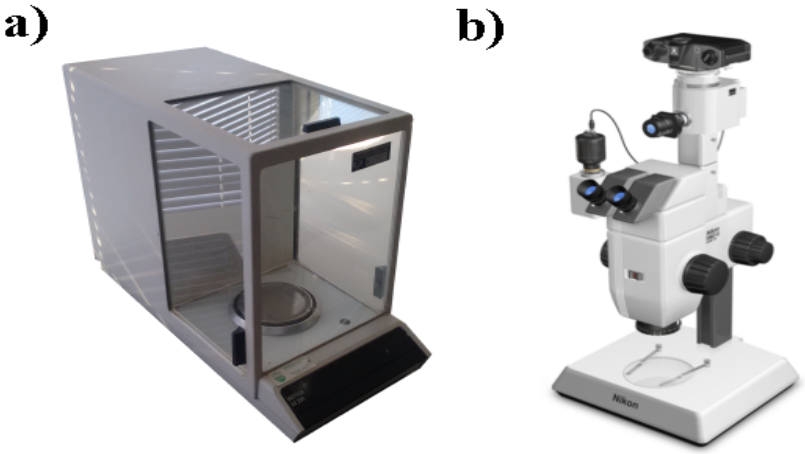


*Figure 4.1: a) AS 200 analytical balance; b) SMZ-U microscope.*

**c) Agate mortar**

In order to ensure reliable results from some of the analytical techniques described below, the particle size of some collected samples needed to be reduced and homogenized. To achieve this purpose, the grinding procedure was carried out manually by means of an agate mortar.

**d) Metallographic polisher**

With the aim of collect elemental (SEM-EDS) and molecular (Raman spectroscopy) chemical images, some of the corrosion and mural painting fragments were prepared following the methodology described by E.J. Roca et al. (2005) [1].

Taking into account the fragility of the materials under study, the fragments were first embedded into acrylic resin. Once the resin polymerization process was completed, embedded samples were treated with the Forcipol®1 metallographic polisher (Metkon, Turkey) shown in Figure 4.2. In the first step the fragments were ground with finer and finer sandpapers (P320-2000). Afterwards, the roughed samples were polished with a diamond suspension on a napless cloth to produce a scratch-free mirror finish.

*Figure 4.2: Forcipol®1 metallographic polisher.*

**e) Ultrasonic bath**

In order to carry out Ion IC and ICP-MS analyses, soil (from the archaeological site of Ereñozar), volcanic material (archaeological site of Pompeii) and mortar samples (Alaiza's church) were treated following the methodology described by N. Prieto-Taboada et al. (2012) [2].

Briefly, after grinding, powder samples were dispersed in ultrapure water and subjected to an ultrasonic bath with a frequency of 40 kHz (1000 W). As showed in Figure 4.3a, the used ultrasonic system was the Ultrasons-H bath (P-Selecta, Spain). The water extracts were then filtered prior to analytical determination.

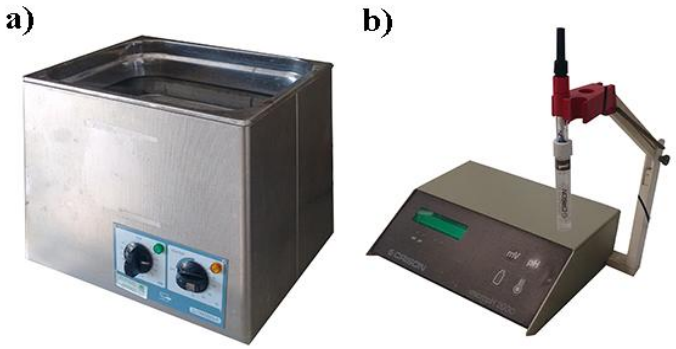


*Figure 4.3: a) Ultrasons-H ultrasonic bath; b) Crison micropH 2000 VoltMeter.*

**f) pHMeter/potentiometer**

In several cases, the used experimental approach also involved the study of several physic-chemical parameters of water samples. The analyses were performed by means of a Crison micropH 2000 potentiometer (Crison Instruments S.A., Spain) system (Figure 4.3b) coupled to different ion selective

electrodes. With regards to pH measurements, the 52-02 Crison electrode was first calibrated using pH 7.00 and 4.01 buffer solutions (Crison instruments). For the analysis of Redox potential, the 52–61 Crison electrode was calibrated by means of a Hamilton Redox buffer (475 ± 5 mV). Finally, 96-62 and 96-63 Crison electrodes were used for the quantification of nitrates and ammonium respectively. In these cases, ion quantification was carried out my means of external calibration curves, using 1000 $mg.L^{-1}$ standard solutions. For these potentiometric evaluations, an Ag/AgCl Crison reference electrode was always used.

**g) Heating oven**

As will be explained in detail in chapter 8, some of the experiments performed in the framework of this PhD thesis needed to be carried out at specific thermal condition. For this purpose, a Heraeus heating oven from the Function Line series (Thermo Scientific, USA) was used. The instrument (see Figure 4.4a) has a capacity of 110 litres and an accuracy of ± 0.5 °C on the 30-250 ºC range.

**h) Digital hydraulic press**

In order to carry out FTIR analyses in transmittance mode, KBr-based pellets were prepared. For this purpose, a CrushIR hydraulic press (Pike technologies, USA) was used. The press, specifically designed for making high quality KBr pellets, ensures excellent reproducibility thanks to the combination of digital pressure reading and adjustable pressure setting (maximum value: 13.6 $tons/cm^2$). As can be seen in Figure 4.4b, the instrument is equipped with a PIKE Evacuable Pellet Press having a pellet holder with a diameter of 13 mm.

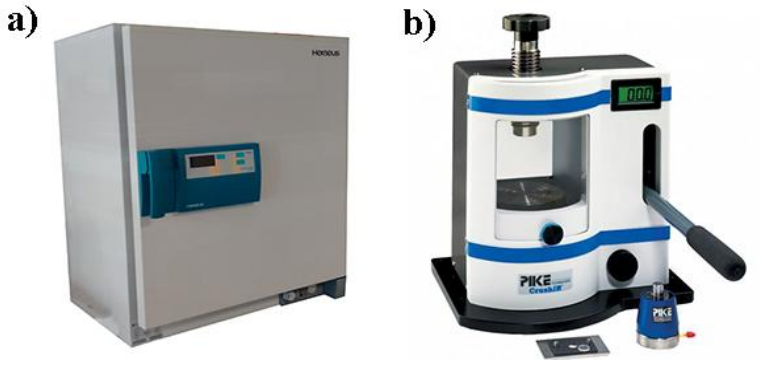


*Figure 4.4: a) Heraeus Function Line heating oven; b) CrushIR hydraulic press.*

## 4.2 Hand-held and portable analytical techniques for in-situ analyses

### *4.2.1 Energy Dispersive - X-Ray Fluorescence (ED-XRF)*

**XMET5100 ED-XRF spectrometer (Oxford Instruments, UK)**

*Figure 4.5: XMET5100 hand-held ED-XRF spectrometer.*

The hand-held XMET5100 ED-XRF spectrometer (Oxford Instruments, UK, Figure 4.5) makes use of an X-Ray tube excitation source composed of a rhodium anode (maximum voltage of 45 keV). The analyzer has a silicon drift detector that provides an energy resolution of 150 eV (calculated for the Mn Kα line at -20 °C) and a spectral resolution of 20 eV. Data acquisition is carried out thanks to a personal digital assistant (PDA) integrated into the instrument, which also provides semi-quantitative information of the detected elements.

In the case of archaeological artefacts, semi-quantitative analyses were made with a 50 s measurement time and with an analytical method specifically designed for metal alloys. In the case of mural paintings, in contrast, the SOIL FP method was used.

With regards to mural paintings characterization, in-situ ED-XRF data were collected by putting in contact the head of the system with the paint surface. On the other side, analyses of archaeological artefacts were carried out mounting the instrument on a bench top stand, which ensured the contact between the instrument and the artefacts without applying any pressure on them.

### *4.2.2 Laser-Induced Breakdown Spectroscopy (LIBS)*

**EasyLIBS IVEA system (model Easy 2C, IVEA, France)**


*Figure 4.6: EasyLIBS portable LIBS system.*

The used portable LIBS system (Figure 4.6) incorporates a pulsed Nd:YAG laser (1064 nm) that emits at the fundamental wavelength of 1064 nm. The energy pulse is about 25 mJ (on the sample) with a repetition rate of 1 Hz and duration of 4-5 ns for each laser pulse. The spot of analysis is around 193 μm of diameter and each pulse generates a crater of around 250 μm, depending on the sample.

The plasma-light produced by the laser pulse is collected with a spherical lens (Ocean Optics, USA) and sent to the detector device through optical fibres. The detector is composed of two spectrometers corresponding to the Ultraviolet (UV) (196-419 nm) and near Infrared (NIR) (580-1000 nm) spectral ranges (Czerny-Turner Ocean Optics HR 2000+, USA).

All analyses were carried out by setting a double pulse mode, a delay time of 50 μs to the laser pulse and a gate width of 5 ms.

The AnaLIBS 6.3 software (IVEA, France) was used for spectra acquisition, control and visualization, while the elemental identification was carried out by comparison with the NIST database [3].

### *4.2.3 Raman Spectroscopy*

**a) InnoRam$^{TM}$-785S Raman spectrometer (B&WTEK Inc., USA)**

*Figure 4.7: Portable InnoRam$^{TM}$-785S spectrometer (785nm).*

The InnoRam$^{TM}$-785S Raman spectrometer (Figure 4.7) is equipped with a 785 nm red laser (maximum power of 300 mW) and a CCD detector. This instrument works in a range between 175 and 3200 $cm^{-1}$ with a mean spectral resolution of 4.5 $cm^{-1}$.

In the case of mural painting characterization, most of the analyses were performed by means of the hand-held microprobe (150 μm of spot size). However, several points of interest were analyzed by coupling the Raman spectrometer to a XYZ motorized tripod system (MicroBeam, Barcelona, Spain). Thanks to long-distance objectives (4x, 20x and 50x), the tripod offers the possibility of performing microscopic analyses by avoiding the contact with the walls. On the other side, most of the archaeological artefacts were studied by coupling the instrument to the video microscope (20x and 50x objectives) showed in Figure 4.7.

Raman spectra were acquired by BWSpec™ 3.26 (B&WTEK Inc., USA) software, and processed by Nicolet Omnic 7.2 software (Madison, USA). Spectra interpretation was finally based on the comparison of the recorded spectra with those of several spectra libraries [4,5].

**b) BWS5445-532S Raman spectrometer (B&WTEK Inc., USA)**

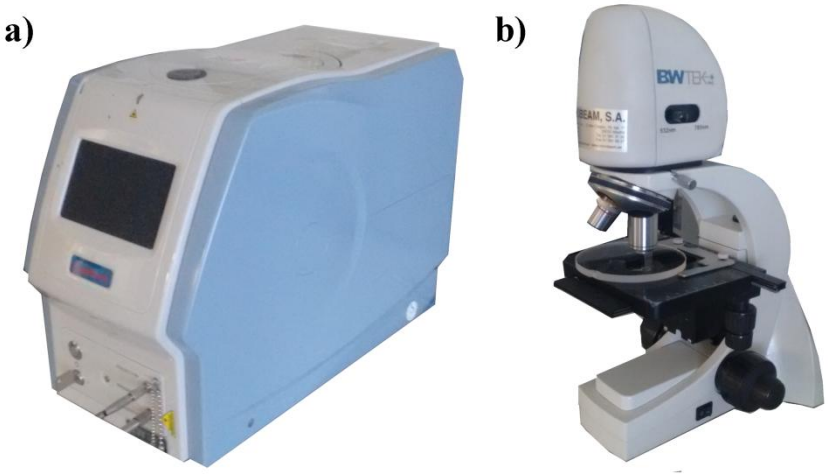


*Figure 4.8: BWS5445-532S Raman spectrometer.*

The BWS5445-532S portable Raman system (Figure 4.8a) is equipped with a 532 nm green laser (maximum power of 45 mW) and a CCD detector. The system works in a range between 62 and 3750 $cm^{-1}$ and with a mean spectral resolution of 4.2 $cm^{-1}$.

On the one hand, mural paintings were analyzed by putting in contact the hand-held probe with the wall surface. In the case of archaeological samples in contrast, the analyses were carried out by coupling the system to a BAC151B video-microscope (BWTECK, USA, Figure 4.8b). The benefits provided by the use of this tool are manifold. For example, the integrated camera and objectives (20x and 50x) allows to better focus on the sample, improving the Raman signal. Furthermore, its unique dual laser wavelength port provides flexibility because it allows collecting two molecular spectra from the same spot of analysis by sequentially using the green and the red lasers. Considering the different power of the excitation sources, specific measurement conditions were adopted for each Raman system.

Raman spectra were acquired with the BWSpec™ 4 (B&WTEK Inc., USA) software and their interpretation was carried out by comparison of the recorded spectra with those from RRUFF database [6].

### *4.2.4 Fourier Transform Infrared Spectroscopy (FTIR)*

**a) Transportable Alpha FTIR spectrometer (Bruker Optics Inc, Germany)**

*Figure 4.9: Transportable Alpha FTIR spectrometer.*

With the aim of assessing the possible use of portable FTIR systems to semi-quantify iron corrosion mixtures, an Alpha spectrometer (Bruker Optics Inc., Germany, Figure 4.9) was used.

The instrument implements a Ge on KBr beamsplitter and is equipped with an ATR (Bruker, Germany) accessory. The system implements a Diamond ATR plate and a Michelson interferometer that works with a maximum resolution of 4 $cm^{-1}$ in a spectral window ranging from 4000 to 400 $cm^{-1}$.

To collect ATR spectra, the diamond needs to be in contact with the sample in powder form. For this reason, a small portion of material (around 0.05 g) was collected from each sample and grinded by means of the agate mortar previously described. Then, the grinded material was placed in the microsample holder in its pure form, clamped against the ATR crystal and finally analyzed.

Molecular data was recorded by setting 64 scans to improve the signal-noise ratio. Spectra acquisition was carried out thanks to the Opus 7.2 software (Bruker Optics, Germany).

**b) Hand-held 4100 EXOSCAN FTIR spectrometer (Agilent, USA)**


*Figure 4.10: Hand-held 4100 EXOSCAN FTIR spectrometer.*

To determine the molecular composition of mural paintings in a non invasive way, an EXOSCAN FTIR spectrometer (A2 technology, currently Agilent, USA) working in DRIFT mode was used (see Figure 4.10). The system is equipped with a ZnSe beamsplitter and a deuterated triglycine sulphate detector (DTGS) coupled to a temperature stabilizer. The Michelson interferometer has a maximum resolution of 4 $cm^{-1}$ in a spectral window ranging from 4000 to 650 $cm^{-1}$.

It is important to highlight that to carry out DRIFT analyses the head of the hand-held system has to be in contact with the surface. Taking into account both, the fragility and the value of the analyzed mural paintings, a home-made thin protective device made of foam was placed between the DRIFT head and the wall in order to avoid physical damages.

For each measurement, 64 scans were acquired to improve the signal-noise ratio. Molecular data were collected in a PDA using the MicroLab Mobile Software (Agilent, USA). The interpretation of the spectra was performed by comparison of the acquired spectra with those of standard compounds contained in a home-made database [7].

## 4.3 Bench top analytical techniques for non destructive laboratory analyses

### *4.3.1 Scanning Electron Microscopy (SEM) Energy Dispersive X-Ray Spectrometer (EDS)*

**EVO40 Scanning Electron Microscope (Carl Zeiss STS, Germany)**

*Figure 4.11: EVO40 Scanning Electron Microscope.*

Elemental images of selected samples were performed using an EVO40 scanning electron microscope (Carl Zeiss STS, Germany, Figure 4.11) coupled to an X-Max Energy-Dispersive X-Ray Spectrometer (Oxford Instruments, UK), SEM-EDS.

Previous to SEM-EDS analyses, the selected samples were fixed in specific aluminium sample holders (pin) with carbon type. Furthermore, with the aim of improving the quality of SEM images collected from organic samples, a thin gold film (<20 μm) was applied on their surface using a Emitech K550X sputter coater vacuum chamber (Quorum Technologies, UK).

EDS analyses were carried out using a working distance of 8–10 mm, an I Probe of 180 pA, a 35º take-off angle, an acceleration potential of 30 kV, an integration time of 50 s and a number of scans between 6 and 10. The INCA Microanalysis Suite 4.3 (Oxford Instruments, UK) software was used to collect and manage the data.

### *4.3.2 Raman Spectroscopy*

**a) inVia Confocal Raman spectrometer (Renishaw, UK)**


*Figure 4.12: inVIa confocal Raman microscope.*

The inVia Confocal Raman microscope (Figure 4.12) is equipped with a 514 nm (maximum power of 50 mW) and a 785 nm (maximum power of 350 mW) excitation laser, a DMLM Leica microscope (Bradford, UK) and a CCD detector. The spectrometer works in a spectral range between 65 and 3800 $cm^{-1}$ with a mean spectral resolution of 1.2 $cm^{-1}$.

On the one side, StreamLine technology was employed to generate high definition molecular images of specific samples. Briefly, the motorized stage of the microscope coupled to the Raman spectrometer moves the sample beneath the lens so that the line of laser-light is rastered across the area under analysis. Afterwards, from the collected spectra, chemical images are generated by taking into account the position of key Raman bands.

In specific cases, the Raman spectrometer and the scanning electron microscopy previously described were combined by means of a structural and chemical analyzer (SCA, Renishaw, UK). The SCA interface, described by Gómez-Nubla and co-workers (2013) [8], allowed performing the molecular analysis of samples by taking advantage of the SEM magnification feature.

In both cases, the Renishaw Wire 3.2 (Renishaw, UK) software was used for data collection and analysis.

**b) Renishaw RA100 spectrometer (Renishaw, UK)**

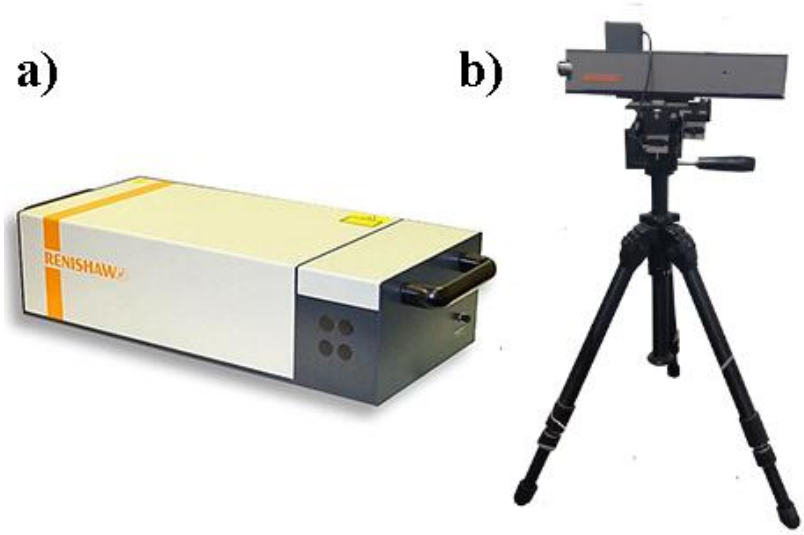


*Figure 4.13: a) Renishaw RA100 spectrometer; b) microprobe tripod.*

The RA100 Raman system (Renishaw, UK, Figure 4.13a) is equipped with a 785 nm red laser (maximum power of 150 mW) and a CCD detector. The system works in a spectral range from 200 to 3200 $cm^{-1}$ and with a mean spectral resolution of 2 $cm^{-1}$.

The spectrometer is coupled to a X-Y motorized tripod (Figure 4.13b), which mounts a microprobe implementing a video-camera (which allows focusing the laser beam on the sample) and long range objectives (4x, 10x, 20x and 50x).

Spectra acquisition was performed with the WIRE$^{TM}$ 2.0 software (Renishaw, UK), and data interpretation was carried out by comparison with the reference spectra included in the Raman databases previously mentioned [4,5].

### *4.3.3 Fourier Transform Infrared Spectroscopy (FTIR)*

**Jasco 6300 FTIR spectrophotometer (Jasco, Japan)**

*Figure 4.14: Jasco 6300 FTIR spectrophotometer.*

The Jasco 6300 FTIR spectrophotometer (Figure 4.14) is composed of a Ge on KBr beamsplitter, a Michelson interferometer and a DLaTGS detector with Peltier temperature control. The system is equipped with three interchangeable accessories that enable to carry out transmittance, diffuse reflection (DRIFT, Jasco DR PR0410M) and ATR (diamond crystal with a ZnSe focusing lens, PIKE Miracle™) analyses respectively. To collect ATR spectra, a small portion of homogenized sample (around 0.05 g) is placed in the microsample holder, firmly clamped against the ATR crystal and analyzed in its pure form. On the other side, KBr-matrix pellets need to be made to carry out transmittance analyses. To prepare the pellets, 0.5 mg of sample is mixed with 170 mg of dry KBr (>99% FTIR grade, Sigma-Aldrich), milled in an agate mortar and pressed under 10 tons/cm$^2$ for 8 minutes. For DRIFT analyses, the microsample holder is filled with a powder mixture composed of 10% (w/w) of sample and 90% (w/w) of KBr. This dilution ratio ensured a less specular component on the surface of the sample increasing the contribution of the diffuse reflectance component.

All analyses were carried out in the middle infrared region (from 4000 to 400 cm$^{-1}$) recording 64 scans at 4 cm$^{-1}$ spectral resolution. Spectra treatment was performed using Omnic software version 7.2 (Thermo Nicolet, USA).

### *4.3.4 X-Ray Diffraction (XRD)*

**PRO PANalytical Xpert X-Ray Diffractometer (PANalytical, Netherlands)**

*Figure 4.15: PRO PANalytical Xpert X-Ray Diffractometer.*

The used X-Ray Diffractometer (see Figure 4.15) is equipped with a copper tube, a vertical goniometer (Bragg-Brentano geometry), a programmable divergence slit, a secondary graphite monochromator and a Pixcel detector. The condition of all measurements were set at 40 KV, 40 mA and a scan ranging between 5 and 70º 2theta.

Considering that the peaks' shape of the XRD diffractogram depends on the crystallinity of the phases (the narrowness of the peaks increases with increasing short and long range ordering), semi-quantitative values were obtained by treating areas values. To obtain semi-quantitative data from the collected diffractograms, two different softwares were used. Both, Xpert HighScore and EVA software (PANanalytical, Netherlands), apply the Reference Intensity Ratio (RIR) method to predict the phase abundances. Considering that the intensity of a diffraction peak profile is a convolution of many factors, the RIR method measures and reduces to a constant all factors except concentration to determine phases concentration (by comparison to a reference pattern). Diffractograms interpretation was performed using WinPLOTR software, by comparison with the PDF-2 standards database [9].

## 4.4 Bench top analytical techniques for destructive laboratory analyses

### *4.4.1 Ion Chromatography (IC)*

**ICS 2500 Ion Chromatograph (Dionex Corporation, USA)**

*Figure 4.16: ICS 2500 Ion Chromatograph.*

Qualitative and quantitative analyses of water soluble salts, extracted from burial and ground samples, were performed by following the method developed by N. Prieto-Taboada et al. [2]. For this purpose, a Dionex ICS 2500 ion chromatograph equipped with an ED50 conductivity detector and an AS 40 auto sampler (Figure 4.16) was used. Ion quantification was carried out by means of external calibration curves, using 1000 $mg.L^{-1}$ standard solutions (Fluka Sigma Aldrich) of selected cations ($Na^+$, $K^+$, $Mg^{2+}$, $Li^+$, $Mn^{2+}$, $Ca^{2+}$, $Sr^{2+}$, $NH_4^+$ and $Ba^{2+}$) and anions ($F^-$, $Cl^-$, $NO_3^-$, $SO_4^{2-}$, $NO_2^-$ and $PO_4^{3-}$). The analysis of cations was conducted by means of a IonPac CS12A (4 × 250 mm) column, a IonPac CG12A (4× 50 mm) pre-column, a 20 mM $CH_4SO_3$ mobile phase, a 75 mA suppression current and a 1ml/min flow. The separation of anions was carried out using an IonPac AS23 (4× 250 mm) column, an IonPac AG23 (4 × 50 mm) pre-column, 4.5 mM $Na_2CO_3$/0.8 mM $NaHCO_3$ mobile phase, 25 mA suppression current and 1 ml/min flow. Finally, data processing was performed using 6.60-SPIA CHROMALEON software (Dionex Corporation, USA).

### *4.4.2 Inductively Coupled Plasma- Mass Spectroscopy (ICP-MS)*

**NexION 300 ICP-MS (PerkinElmer, USA)**

*Figure 4.17: NexION 300 ICP-MS.*

In order to assess the possible side effects (lixiviation of metals) of alkaline baths on standard mixtures and archaeological rust samples, a NexION 300 Inductively coupled Plasma- Mass Spectromety system was employed (see Figure 4.17).

Before analyses, alkaline bath samples were subjected to a dilution process using Milli-Q water. Then, taking into account that the solutions analyzed by ICP-MS must contain an acid concentration around 1% of nitric acid ($HNO_3$) to avoid damages to the equipment, a standard solution of $HNO_3$ (Tracepur grade, supplied by Merk, Germany) was employed to reach the optimal acidity value.

Depending on the sample under analysis, the quantification of $^{56}Fe$, $^{107}Ag$, $^{109}Ag$, $^{197}Au$ and $^{202}Hg$ isotopes was performed under the following experimental conditions: nebulizer flow of 0.9–1.0 L/min$^{-1}$, plasma flow of 18 L/min$^{-1}$ and radio frequency power of 1400 W. Argon with a purity of 99.995% was provided by Praxiar (Spain). Analyses were carried out inside a clean room (class 100) and quantitative data were obtained by means of external calibration curves, using 1000 mg.L$^{-1}$ standard solutions (Specpure, Plasma standard solution, Germany). Data acquisition and interpretation was carried out using the NexION 1.5 software (Perkin Elmer).

### *4.4.3 Capillary Electrophoresis (CE)*

**Agilent 7100 Capillary Electrophoresis system (Agilent Technologies, USA)**

*Figure 4.18: Agilent 7100 Capillary Electrophoresis system.*

With regards to the analytical study described in chapter 6, quantitative analyses of $Cl^-$ ions extracted from archaeological rust samples were performed using an Agilent Capillary Electrophoresis system (Agilent CE, Agilent Technologies, USA, Figure 4.18).

Agilent G1600-60211 fused silica capillaries coated with polyimide were used: 50 µm internal diameter×375 µm external diameter and a 40 cm effective length. The calibration was performed by injecting 10 standards at 400 mbar from a 500 $\mu g.L^{-1}$ mixed anion standard solution in water. Data acquisition was performed by HP Chemstation software (Agilent CE, Agilent Technologies, USA).

## 4.5 Isolation and characterization of biodeteriogens genomic DNA sequences via PCR amplification

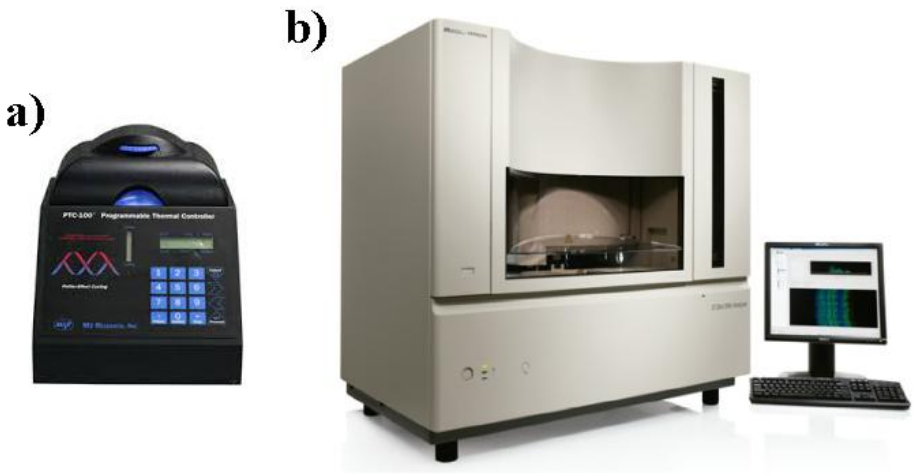


*Figure 4.19: a) PTC-100 thermal cycler; b) ABI Prism 3730 analyzer.*

To genomically characterize the main bioderiogens that jeopardize the conservation of the Pompeian mural painting described in section 3.2.3, the biological strains, collected in-situ by means of sterile swabs and PDA petri dishes, were sent to the BAT laboratory (CIAL institute, Madrid) for their treatment and characterization.

The collected samples were cultured during 7 days at room temperature (25 ºC). Then, metagenomic DNA was isolated in a biological safety cabinet (BIO II Advance, Telstar, Spain) using the soil DNA isolation commercial kit. In order to amplify the region of internal transcribed spacer (ITS), polymerase chain reaction (PCR) and secondary PCR procedures were performed as described by J.L. Leake et al. [10]. To verify the success of the extraction, the metagenomic DNA was checked by using 0.8% w/v agarose gel electrophoresis. A Inc PTC-100 (MJ Research, USA, Figure 4.19a) thermal cycler was used to amplify segments of DNA via the PCR. For the characterization of the fungi species, the 18S ribosomal RNA gene region was amplified and DNA sequencing was performed by means of the ABI Prism 3730 DNA analyzer (Thermo Fisher Scientific, USA, Figure 4.19b). Output file containing ITS sequences with partial 16s ribosomal RNA genes sequence were then analyzed by using the Bioedit software. Finally, ITS sequences identification was carried out by comparison with the National Center for Biotechnology Information (NCBI) database [11].

## 4.6 References

**[1]** E.J. Roca, A. Ruiz-Conde, P.J. Sánchez-soto (2005) Preparación de secciones estratigráficas: aspectos prácticos del análisis de estratos en obras del Patrimonio Cultural (pigmentos y soportes). *Boletín de la sociedad Española de Ceramica y Vidrio*, 44, 382-386.

**[2]** N. Prieto-Taboada, O. Gómez-Laserna, I. Martínez-Arkarazo, M.A. Olazabal, J.M. Madariaga (2012) Optimization of two methods based on ultrasound energy as alternative to European standards for soluble salts extraction from building materials. *Untrasonics Sonochemistry*, 19, 1260-1265.

**[3]** NIST database of atomic spectral data. Available at: http://physics.nist.gov/PhysRefData/ASD (May 21th 2017).

**[4]** M. Pérez-Alonso, K. Castro, J.M. Madariaga (2006) Vibrational spectroscopic techniques for the analysis of artefacts with historical, artistic and archaeological value. *Current Analytical Chemistry,* 2, 89-100.

**[5]** K. Castro, M. Pérez-Alonso, M.D. Rodríguez-Laso, L.A. Fernández, J.M. Madariaga (2005) On-line FT-Raman and dispersive Raman spectra database of artists' materials (e-VISART database). *Analytical and Bioanalytical Chemistry*, 382, 248-258.

**[6]** B. Lafuente, R.T. Downs, H. Yang, N. Stone (2015) The power of databases: the RRUFF project. In: *Highlights in Mineralogical Crystallography, T Armbruster and R M Danisi, eds. Berlin, Germany, W. De Gruyter*, pp 1-30.

**[7]** I. Arrizabalaga, O. Gómez-Laserna, J.A. Carrero, J. Bustamante, A. Rodríguez, G. Arana, J.M. Madariaga (2015) Diffuse reflectance FTIR database for the interpretation of the spectra obtained with a handheld device on built heritage materials. *Analytical Methods*, 7, 1061-1070.

**[8]** L. Gómez-Nubla, J. Aramendia, S. Fdez-Ortiz de Vallejuelo, K. Castro, J.M. Madariaga, (2013) From Portable to SCA Raman devices to characterize harmful compounds contained in used black slag produced in Electric Arc Furnace of steel industry. *Journal of Raman Spectroscopy*, 44, 1163-1171.

**[9]** PDF-2 Database, Available at: http://www.icdd.com/ (May 21th 2017).

**[10]** J.L. Leake, S.E. Dowd, R.D. Wolcott, A.M. Zischkau, Y. Sun (2009) Identification of yeast in chronic wounds using new pathogen - detection technologies. *Journal of Wound Care,* 18, 103–108.

**[11]** D.L. Wheeler, T. Barrett, D.A. Benson, S.H. Bryant, K. Canese, V. Chetvernin, D.M. Church, M. DiCuccio, R. Edgar, S. Federhen, L.Y. Geer, Y. Kapustin, O. Khovayko, D. Landsman, D.J. Lipman, T.L. Madden, D.R. Maglott, J. Ostell, V.

Miller, K.D. Pruitt, G.D. Schuler, E. Sequeira, S.T. Sherry, K. Sirotkin, A. Souvorov, G. Starchenko, R.L. Tatusov, T.A. Tatusova, L. Wagner, E. Yaschenko (2007) Database resources of the National Center for Biotechnology Information. *Nucleic Acids Research,* 35, D5-D12.

# CHAPTER 5:

# IN-SITU OVERALL CHEMICAL ASSESSMENT OF METALLIC ARTEFACTS RECOVERED FROM THE ARCHAEOLOGICAL SITE OF EREÑOZAR

As summarized in section 3.1, part of the research work developed during this PhD thesis was directed towards the multianalytical study of metallic artefacts recovered from the archaeological site of Ereñozar. In this chapter, the Ereñozar collection, composed of 7 buckles and 2 spurs, was characterized (directly in the Archaeological Museum of Bizkaia) by means of portable and non destructive techniques with the purpose of carrying out an overall assessment of their chemical composition and degradation problems.

The in-situ study of archaeological findings is an increasingly used practice in the field of *Conservation Science*. Indeed, analytical studies carried out so far prove that portable systems are able to provide results qualitatively comparable to those of laboratory equipments, avoiding any problem related to the transportation of the objects and to the changes of environmental conditions [1,2].

With regard to elemental analyses, portable Energy Dispersive X-Ray Fluorescence (ED-XRF) systems have been successfully employed in several works to analyze the alloys used to forge ancient metallic objects [3,4]. In fact, taking advantage of their sensitive detectors, ED-XRF systems are able to provide qualitative and semi-quantitative elemental data reaching the mg/kg of concentration level depending on the element and the characteristics of the sample.

Concerning the study of degradation processes, Raman spectroscopy has become a reference for the in-situ characterization of archaeological artefacts thanks to its ability to perform analyses without sampling and its sensitivity to many compounds usually found in this field [5].

In this context, it is important to emphasize that the position of the Raman signals (Raman shift), for each vibration mode of the molecular bonds of the different chemical compounds, is independent from the wavelength of the excitation laser, since it depends only on the difference between its vibrational states. However, it is possible that the use of different lasers on a sample can generate Raman signals with different intensities. Sometimes, this difference is so pronounced that some compounds do not provide any spectrum if they are not irradiated with the appropriate laser. In general, several analytical works have proved that Raman spectrometers equipped with green lasers are particularly suitable for the study of green and blue compounds (such as organic compounds, pigments, corrosions, etc) [6,7]. On the other hand, the use of red lasers is suggested for the chemical assessment of red and yellow compounds [8,9]. This concept underlines that it is possible to maximize the molecular information provided by Raman spectroscopy through the complementary use of different laser excitation sources [10].

In addition to the molecular and elemental characterization of archaeological artefacts, it is important to underline that many research works made also use of ion chromatographic studies of soil liquid extracts and rainwater samples (collected from the archaeological site) with the aim of identifying the factors leading to the onset of the detected degradation products [11-13].

## 5.1 Soil characterization

According to the described background, in the first part of this work chromatographic analyses of water extracts from burial soil samples were performed with the aim of studying the characteristics of the environment in which the Ereñozar artefacts were buried for more than eight centuries. Concretely, several soil samples were collected at a depth between 40 and 50 cm from the ground level. After grinding, soluble salts were extracted (using Milli-Q water) following the method of N. Prieto-Taboada and co-workers (2012) [14]. Afterwards, the quantification of soluble salts was carried out by means of the Dionex ICS 2500 Ion Chromatograph described in section 4.4.1.

In addition, fresh rainwater collected in the emplacement was also analyzed and its salts concentration was determined to know the salt input to the soils in Ereñozar. Three replicates of each sample were analysed in order to determine the repeatability of the quantitative method of analysis.

As shown in Table 5.1, the chromatographic results of the aqueous extracts from the soil samples treated with Milli-Q water highlighted a considerable concentration of $Cl^-$ (31.8 ± 1.1 mg/kg soil) and $Na^+$ (33.6 ± 1.2 mg/kg soil). The origin of this salt can be traced back to the rain composition. Chromatographic analysis of rainwater samples collected in the archaeological site showed the presence of $Cl^-$ and $Na^+$ with a concentration of 6.1 ± 0.4 and 3.5 ± 0.1 mg/L respectively. Considering that Ereñozar is located just few kilometres away from the coast line and that no geographical obstacles stand between them, it can be deduced that the high concentration of sodium chloride in the rain is directly due to the influence of marine aerosol. In fact, the molar ratio between $Cl^-$ and $Na^+$ in the rainwater of the area is approximately 1:1.

The chromatographic analysis of anions extracted by using Milli-Q water also revealed the presence of additional analytes. Among the anions, a large amount of $NO_3^-$ was quantified (36.1 ± 1.1 mg/kg). Considering that artefacts were found at depths varying between 40 and 70 cm from the ground line, it can be deduced that the high concentration of nitrates is associated with biological activity [15].

Among the extracted anions, $SO_4^{2-}$ was also identified. The sulphate content of soil samples ranked between the Limit of Detection (LoD) and Limit of Quantification (LoQ) of the implemented analytical procedure. Although the data indicates a low concentration of sulphates in the soil, their presence is not

negligible. In fact, as will be demonstrated in section 5.3, this anion may have played an active role in the corrosion mechanisms affecting some of the copper-based archaeological artefacts.

The concentration of bicarbonate had to be determined by the electroneutrality balance because the used chromatographic conditions ($Na_2CO_3/NaHCO_3$ as mobile phase) did not allow the determination of such anion. The presence of soluble bicarbonate would explain the pH increase from 6.92 (Milli-Q water) to 8.37 (after extraction).

Among the cations, sodium was accompanied by the presence of $Ca^{2+}$ and $K^{+}$, elements typically present in soils.

However, in nature, the lixiviation process of anions and cations is not done by Milli-Q water but rainwater. For this reason, another soluble salt extraction was carried out using rainwater collected from the archaeological site (see Table 5.1). The results revealed a net reduction of the quantity of extracted salts after subtracting the background (salt content in rainwater). The decrease is especially important in the case of sodium (49%), chloride (53%) and potassium (59%), which demonstrates that the rainwater is rich in these ions and the responsible of their presence to some extent in the soil, after their accumulation in the soil matrix.

In the case of calcium and bicarbonate, the reduction is not so high and it is very similar for both ions, around 35% for $Ca^{2+}$ and 36% for $HCO_3^{-}$, which reveals the strong dependence of calcium and carbonate systems. This effect can be explained by the chemical reactions taken place in the system.

We know that pure water extracts calcium and bicarbonate from the soil. But the rainwater can also dissolve ions that play an important role. The initial pH value of rainwater in the area is 6.02. This means carbonic acid and bicarbonate are soluble ions in the initial rainwater. But after the extraction, the carbonic acid from the rainwater has reacted (neutralization) with the insoluble carbonate of the soil (mainly calcium carbonate), giving as a result the double of bicarbonate concentration and the respective calcium from the neutralised calcium carbonate. Moreover, the pH experimentally measured increased up to 8.09. Thus, after the neutralization process, there is an increase of dissolved calcium as well as dissolved bicarbonate. If the saturation condition is fulfilled for calcium carbonate, this insoluble salt will reprecipitate, decreasing the concentration of soluble calcium and bicarbonate, without changing the pH value. This is what we

are experimentally observing after finishing the extraction of the soils with rainwater.

*Table 5.1: Concentration (mg/kg) obtained in the chromatographic analyses of soluble salts.*

| mg/kg | $Ca^{2+}$ | $Na^{+}$ | $K^{+}$ | $Cl^{-}$ | $NO_3^{-}$ | $SO_4^{2-}$ | $HCO_3^{-}$ |
|---|---|---|---|---|---|---|---|
| **Rainwater (mg/L)** | 2.1±0.1 | 3.5±0.1 | 0.5±0.1 | 6.1±0.4 | 1.2±0.2 | < LoD | 0.8±0.1 |
| **MilliQ soil extraction** | 293.4±7.2 | 33.6±1.2 | 10.5±0.2 | 31.8±1.1 | 36.1±1.1 | < LoQ | 909±50 |
| **Rainwater soil extraction** | 189.9±6.2 | 17.2±0.5 | 4.3±0.1 | 15.1±1.2 | 29.6±0.8 | < LoQ | 576±32 |

## 5.2 Study of the elemental composition of the artefacts

After characterizing the soluble salts content of burial soil samples, the hand-held ED-XRF system was used for the in-situ characterization of archaeological artefacts. Taking into account the fragility of the properties, analyses were carried out mounting the instrument on a bench top stand. As showed below, the preliminary results obtained from elemental studies allowed classifying the objects in two distinct groups.

### *5.2.1 Copper based-artefacts (buckles)*

All buckles considered in this study are composed of a copper-based matrix. However, remarkable differences in the semi-quantitative value of the detected major and minor elements suggested the use of different kind of alloys (see Table 5.2). For instance, the composition of *H1001, H3003, H3024* and *H3043* samples proves that these buckles were all manufactured with a quaternary bronze. In this alloy, also called “modified gunmetal” or “red brass” [16], the usual composition, based on tin and copper, is enhanced by significant percentages of lead (in this case, between 4.8 ± 1.2% and 7.6 ± 0.4%) and zinc (between 1.1 ± 0.1% and 5.3 ± 0.4%). Among these four buckles, *H3043* is the only one preserving the pin. The elemental analyses of this part showed a significant decrease in the amount of tin (from 30.5 ± 1.5% to 20.1 ± 0.2%) and an increase in the concentration of lead (from 5.4 ± 0.2% to 7.6 ± 0.4%) and zinc (from 1.3 ± 0.1% to 5.0 ± 0.1%) with respect to the main body. The *H3021* buckle also presents high concentrations of Cu (55.5 ± 1.0%) and Sn (20.3 ± 2.1%), but it can be distinguished from the previous ones due to the lack of Zn and the presence of Fe (1.2 ± 0.1%). The composition of the *H3042* buckle stands out because of the elemental composition: Pb is the main element of the alloy, also composed of tin (23.3 ±

0.6%), copper (18.5 ± 0.5%) and iron (6.0 ± 0.5%). The spectra obtained from the study of the *H3042* pin differs significantly from those of the frame. This part is almost entirely composed of copper (85.0 ± 4.1%), whereas Pb, Fe, Zn and Sn are present in concentrations below 5%.

The last buckle (*H1002*) differs from all the others as its frame is composed of a Cu-Fe alloy (98.9 ± 0.5% and 1.1 ± 0.4% respectively). Furthermore, the analyses carried out on the decoration remains of this artefact allowed the detection of gold. The absence of additional metals suggested that the gilding was carried out by means of gold foils, a method profusely employed in ancient times [17,18]. According to E. Darque-Ceretti et al. [19], this decoration technique is based on a two step process in which gold foils and leafs are first produced by rolling or hammering gold-based ingots and then mechanically fastened to the object.

### *5.2.2 Iron-based artefacts (spurs)*

In contrast to the alloys employed to forge the buckles described above, the metallic spurs recovered from archaeological endeavours are mainly composed of iron.

On the one hand, the ED-XRF analyses collected from the *E1037* spur highlighted the presence of two areas differing for their elemental compositions. Indeed, iron was the only metallic element detected in the artefact main body (see Table 5.2), whereas the study of the terminals at the end of the spur allowed to identify an alloy composed of iron (94.6 ± 0.2%), lead (3.8 ± 0.5%) and tin (1.6 ± 0.2%). Considering the high mechanical stress to which these terminals were subjected during their use, it can be deduced that lead and tin were added to increase the mechanical qualities of the alloy [20,21]. Before the restoration process, the main body of the specimen was covered by a thicker corrosion layer compared to that of the terminal, proving that tin and lead also played a key role on the inhibition of degradation processes [22].

On the other hand, iron was the only element detected on the core of the gilded spur (*E294*), whereas the terminals were mainly composed of copper. With regards to the decoration layer, elemental analyses displayed the characteristic peaks of gold, silver and mercury elements.

In this case, the presence of Hg suggested the use of mercury gilding as decoration technique. Also called fire gilding, this method is based on the use of

an Au-Hg alloy that, once applied over the item surface, is heated until the evaporation of the mercury. As showed in the literature [18], this method presupposed a higher technological level compared to the more usual techniques based on the use of gold foils.

The elemental composition of the spur is very interesting considering the lack of examples of fire gilding applied on iron matrix items. Furthermore, compared to other documented cases [23,24], this artefact can be considered extremely rare since its decoration stands out for the presence of high percentages of Ag. Indeed, the presence of silver is unusual in fire gilding since this method permits to reduce the production cost without resorting to the mix of gold with other metals such as Ag.

*Table 5.2: Elemental composition of the Ereñozar artefacts obtained by ED-XRF.*

| Sample | Alloy composition (%w/w) | Trace elements |
|---|---|---|
| **H1001 frame** | **Cu** (59.5±1.5), **Sn** (22.3±1.2), **Pb** (6.7±0.6), **Zn** (5.3±0.4); | **S**, **Cl**, **K**, **Ca** |
| **H3003 frame** | **Cu** (69.9±2.5), **Sn** (20.3±0.2), **Pb** (5.2±0.2), **Zn** (1.2±0.1); | **S**, **Cl**, **K**, **Ca** |
| **H3024 frame** | **Cu** (62.1±3.1), **Sn** (29.5±0.4), **Pb** (4.8±1.2), **Zn** (1.4±0.2); | **S**, **Cl**, **K**, **Ca** |
| **H3043 frame** | **Cu** (60.0±2.0), **Sn** (30.5±1.5), **Pb** (5.4±0.2), **Zn** (1.3±0.1); | **S**, **Cl**, **K**, **Ca** |
| **H3043 pin** | **Cu** (60.1±0.5), **Sn** (20.1±0.2), **Pb** (7.6±0.4), **Zn** (5.0±0.1); | **S**, **Cl**, **K**, **Ca** |
| **H3021 frame** | **Cu** (55.5±1.0), **Sn** (20.3±2.1), **Pb** (5.2±0.2), **Fe** (1.2±0.1); | **S**, **Cl**, **K**, **Ca** |
| **H3042 frame** | **Pb** (48,2±1.1), **Sn** (23.3±0.6), **Cu** (18.5±0.5), **Fe** (6.0±0.5); | **S**, **Cl**, **K**, **Ca** |
| **H3042 pin** | **Cu** (85.0±4.1%), **Pb** (4.8±0.5), **Fe** (4.0±0.9), **Zn** (2.3±0.2),**Sn** (2.2±1.2); | **S**, **Cl**, **K**, **Ca** |
| **H1002 frame** | **Cu** (98.9±0.5%), **Fe** (1.1±0.4); | **S**, **Cl**, **K**, **Ca** |
| **H1002 decoration** | **Cu** (93.5±0.5), **Fe** (1.0±0.3), **Au** (4.9±0.3); | **S**, **Cl**, **K**, **Ca** |
| **E1037 body** | **Fe** (100) | **S**, **Cl**, **K**, **Ca** |
| **E1037 terminals** | **Fe** (94.6±0.2), **Pb** (3.8±0.5), **Sn** (1.6±0.2); | **S**, **Cl**, **K**, **Ca** |
| **E294 body** | **Fe** (100) | **S**, **Cl**, **K**, **Ca** |
| **E294 terminals** | **Cu** (95.6±2.6), **Fe** (2.1±0.2 ), **Pb** (2.0±0.5),); | **S**, **Cl**, **K**, **Ca** |
| **E294 decoration** | **Fe** (55.1±2.3), **Au** (28.1±0.9), **Ag** (16.0±0.7); | **S, Cl, K, Ca** |

As can be observed in Table 5.2, all studied artefacts showed small percentages of S, Cl, K and Ca (below 0.1%). The presence of these elements can be attributed to the transfer from the soil in which the findings were buried for centuries.

## 5.3 Study of the degradation compounds

After completing the assessment of their elemental composition, molecular analyses were performed to identify the corrosion products of the artefacts.

The main degradation forms were analyzed thanks to the two portable Raman systems described in section 4.2.3, which were used in a complementary way by coupling them with the BAC151B video microscope (BWTECK, USA). This procedure, systematically applied to all selected points of interest, also helped to highlight the different suitability of the excitation sources for the detection of several degradation products. As in the case of elemental analyses, molecular data are shown according to the characteristic of the artefacts' alloys.

### *5.3.1 Copper-based artefacts (buckles)*

As can be observed in Figures 5.1, 5.2, and 5.3, the Raman system equipped with a 532 nm excitation laser proved to be particularly suitable for the characterization of copper-based corrosions, enabling the identification of three degradation phases (cuprite, malachite and brochantite). On the other side, malachite was the only corrosion product detected by means of the 785 nm excitation source.

Cuprite is a copper oxide ($Cu_2O$) recognizable by its reddish-brown colour. By using the 532 nm laser, most of the vibrational modes of this compound were detected (Figure 5.1b, Raman peaks at 145, 413 and 622 $cm^{-1}$) [23].

The formation process of cuprite depends on the environment in which the object is conserved. On the one hand, if it is directly exposed to the atmosphere, copper and its alloys form a thin corrosion layer on the metal surface through the following oxidation reaction (reaction 5.1) [24].

$$2Cu + ½O_2 \rightarrow Cu_2O \qquad \text{(Reac. 5.1)}$$

On the other hand, if the artefact is located in environments with high level of humidity, cuprite formation can be favoured by the presence of chlorides. In this case, the formation process can be divided into two steps. In the first one, the elemental copper reacts with the $Cl^-$ ions dissolved in the soil leading to the formation of cuprous chloride (CuCl, reaction 5.2). This reaction requires oxidant condition, thus it cannot be produced in anoxic environments like burials at depth higher than 0.5 meters. Then, the cuprous chloride reacts with water and turns

into cuprite (reaction 5.3) [25-27]. The $H^+$ formed as side specie reacts with the carbonate from the soil producing bicarbonate ions. Considering that the artefacts from Ereñozar were buried for centuries and that their elemental analysis showed the presence of chlorine, the formation of this compound could be explained with reactions 5.2 and 5.3.

$$Cu + Cl^- \rightarrow CuCl + e^- \qquad \text{(Reac. 5.2)}$$

$$2CuCl + H_2O \rightarrow Cu_2O\ (s) + 2H^+ + 2Cl^- \qquad \text{(Reac. 5.3)}$$

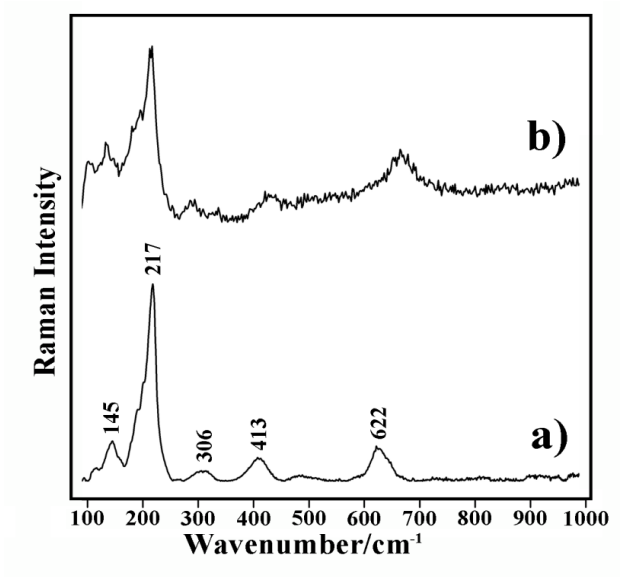


*Figure 5.1: Comparison between a) standard (from RRUFF database, 532 nm excitation laser) and b) cuprite Raman spectra (532 nm excitation laser).*

The presence of cuprite is very important in the degradation process of archaeological findings because, as it will be explained later, provides the basis for the formation of more complex products.

During analyses, the corrosion phase detected most frequently was malachite ($Cu_2CO_3(OH)_2$). The comparison between the processed standard spectra from IBeA database (our own database, Figure 5.2a) with those obtained from portable systems highlights the different sensitivity of the two excitation sources. By using the 532 nm laser source, the main peaks at 155, 180, 222, 270, 353, 433, 536, 1058, 1099, 1366 and 1493 $cm^{-1}$ were detected (Figure 5.2b) [23]. However, through the analysis of the same spots by the 785 nm laser, only the peaks at 149, 155, 180, 222, 433, 1058, 1099 $cm^{-1}$ were observed (Figure 5.2c). By comparing the spectra collected with the two portable systems, a remarkable difference in the

ratio between the peaks intensities can be noted, specifically, the vibrational mode at 1493 $cm^{-1}$, which is very intense in the spectra obtained by using the 532 nm excitation laser, but completely disappears in the spectrum pursued by the 785 nm laser. This phenomenon could be due to a Raman resonance effect. In fact, it is well known that in particular conditions, the intensity of Raman peaks can be increased when the excitation laser has an energy close to that required to activate an electronic transition of the sample. In this case, the 532 nm laser is in electronic resonance conditions with that specific malachite vibrational mode, resulting in an enhancement of its Raman signal [28].

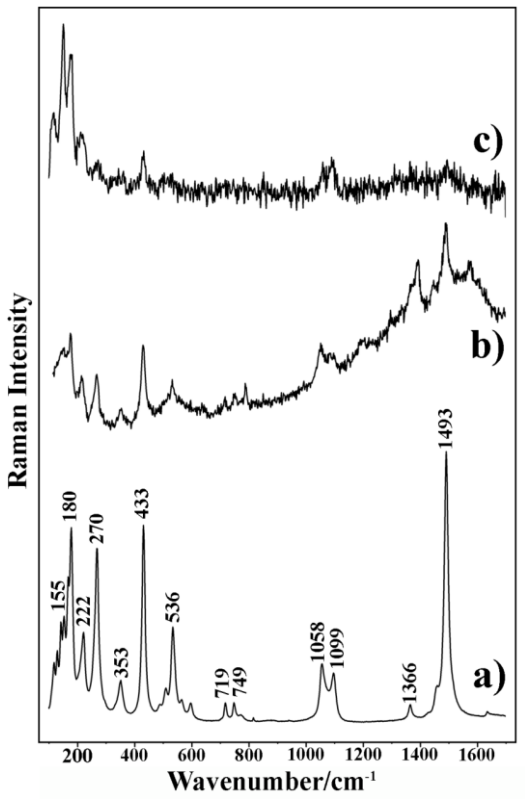


*Figure 5.2: Comparison between a) malachite standard spectrum (from IBeA database, 532 nm excitation laser) with those obtained by b) BWS5445-532S and c) InnoRam™-785S portable Raman systems.*

There are studies [29,30] explaining that this compound can be frequently found in artefacts preserved buried in carbonate rich environments (like Ereñozar), while it is more difficult to find in objects directly exposed to the atmosphere. For this reason copper carbonate can be often detected in artefacts coming from archaeological endeavours, as is the case of the analyzed samples in the present chapter. The formation of malachite [25,31] in buried objects could be due to a

further reaction of cuprite, which reacts with $O_2$, $H_2O$ and $CO_2$ turning into malachite (reaction 5.4):

$$Cu_2O + 1/2O_2 + HCO_3^- + H_2O \rightarrow Cu_2CO_3(OH)_2 + OH^- \quad \text{(Reac. 5.4)}$$

This reaction can only take place in burials with less than 0.5 meters because down this value the atmospheric $O_2$ is absent.

The third phase detected during the analyses of the copper-based artefacts was brochantite. In this case, the characteristic peaks at 137, 155, 195, 241, 318, 387, 422, 448, 481, 595, 698, 621 and 972 $cm^{-1}$ (Figure 5.3b) [23] were detected thanks to the 532 nm laser source. When exposed to environments with high relative humidity in presence of sulphate-based compounds, cuprite can be transformed into brochantite according to the reaction 5.5 [24].

$$2Cu_2O + SO_4^{2-} + 4H_2O + O_2 \rightarrow Cu_4(OH)_6SO_4 + 2OH^- \quad \text{(Reac. 5.5)}$$

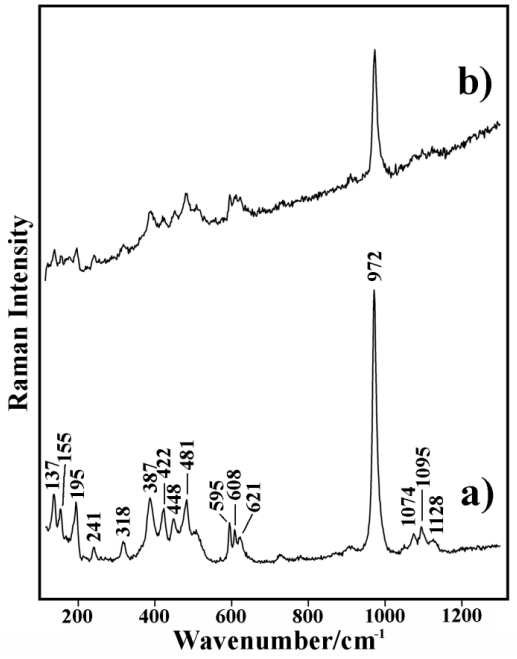


*Figure 5.3: Comparison between a) brochantite standard spectrum (from RRUFF database, 532 nm excitation laser) and b) BWS5445-532S brochantite Raman spectrum from sample H3021.*

As summarized in Table 5.3, the molecular composition of rust layers differs depending on the objects. For example, in the case of *H3021* sample, malachite, brochantite and cuprite were detected, constituting a very small corrosion crust in the rupture surface of the frame. In the case of *H3042* buckle only brochantite

was found, but compared to the previous case, it formed an uniform and extended rust layer that covered almost the whole surface. Finally, the *H3043* buckle showed small corrosion spots composed entirely of malachite.

*Table 5.3: Summary of the corrosion products detected in all artefacts.*

| Detected corrosion phases | Archaeological artefacts | | | | | | | | |
|---|---|---|---|---|---|---|---|---|---|
| | H1001 | H1002 | H3003 | H3021 | H3024 | H3042 | H3043 | E1037 | E294 |
| Malachite | | | | ✔ | | | ✔ | | |
| Brochantite | | | | ✔ | | ✔ | | | |
| Cuprite | | | | ✔ | | | | | |
| Magnetite | | | | | | | | ✔ | ✔ |
| Akaganeite | | | | | | | | ✔ | ✔ |
| Lepidocrocite | | | | | | | | ✔ | ✔ |
| Goethite | | | | | | | | ✔ | ✔ |

As shown in Table 5.3, no corrosion products were detected from the four remaining artefacts. The different conservation state cannot be related to their metallic composition since both uncorroded and degraded objects are composed of similar alloys. Furthermore, it must be considered that, after excavation, all objects were subjected to the same conservation protocol. For this reason it can be assumed that the different conservation state of the artefacts might have been induced by a different exposure to both soluble salts and oxygen during the burial phase. The different exposure may be related to the burial depth: *H3021* and *H3042* buckles, found at a depth between 40 and 50 cm from ground level, probably came in contact with a higher concentration of soluble salts and oxygen with respect to the other objects, found deeper (around 70 cm).

### *5.3.2 Iron-based artefacts (spurs)*

As previously explained (see chapter 3), both spurs were covered by thick corrosion systems. For this reason, the analysis of the outer rust layers was coupled to the molecular characterization of the areas affected by the detachment of corrosion fragments. In this way, the molecular composition of inner and outer parts of the corrosion systems was identified and compared.

As displayed in Table 5.3, the molecular results obtained by Raman analyses revealed, in both artefacts, a corrosion system composed of magnetite, goethite,

lepidocrocite and akaganeite.

Magnetite (Figure 5.4b, main Raman peak at 658 $cm^{-1}$) [32], correspond to an iron oxide ($Fe_3O_4$), whose formation is favoured by partial anoxic environments. This iron phase was detected in the inner part of the spurs corrosion systems, which means in the area less exposed to the external environment. Due to its high compactness and stability, this compound normally represents a protective layer to the findings cores.

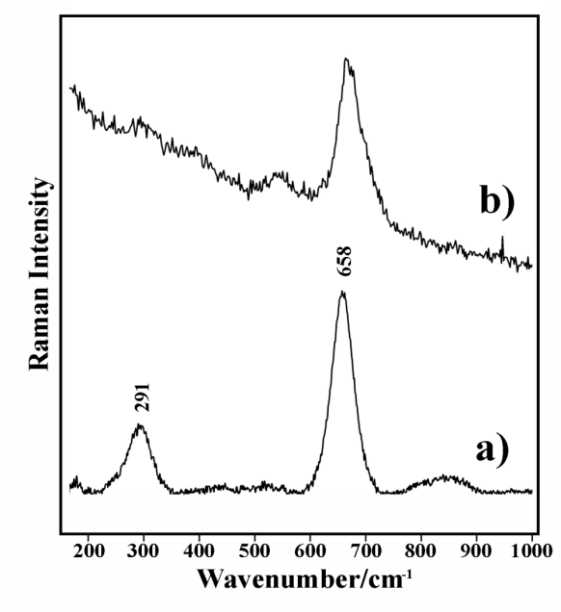


*Figure 5.4: Comparison between a) magnetite standard spectrum (from RRUFF database, 780 nm excitation laser) and b) magnetite Raman spectrum (785 nm excitation laser) from sample E1037.*

The formation of this compound seems to occur at the initial stage of the burial process that is when the object is covered by a thin layer (a few cm) of sediment. In these conditions, water and oxygen lead to the oxidation of the ferrous matrix and the subsequent formation of magnetite according to the reactions 5.6 and 5.7.

$$Fe^0 + 1/2O_2 + H_2O \rightarrow Fe^{2+} + 2OH^- \quad \text{(Reac. 5.6)}$$

$$3Fe^{2+} + 1/2O_2 + 6OH^- \rightarrow Fe_3O_4\,(s) + 3H_2O \quad \text{(Reac. 5.7)}$$

On the outer surface of both spurs three corrosion phases were identified. Through the assignment of their characteristic peaks, the InnoRam$^{TM}$-785S Raman system allowed the identification of goethite (Figure 5.5b, Raman peaks at 163,

202, 244, 299, 388, 481 and 553 $cm^{-1}$) [30], lepidocrocite (Figure 5.6b, Raman peaks at 217, 251, 309, 347, 378 588, 651 and 1302 $cm^{-1}$) [26] and akaganeite (Figure 5.7b, main signals at 140, 311, 395, 541 and 722 $cm^{-1}$) [26] iron corrosion phases.

The same compounds were also identified by using the BWS5445-532S portable system. In this case, however, the different excitation source emphasizes variations in the peaks intensity ratio. In the case of goethite, the secondary peak at 244 $cm^{-1}$ greatly increases its intensity (Figure 5.5c) in comparison with the spectra collected using the 785 nm excitation source. With regards to lepidocrocite's vibrational spectra, the green laser also allows the enhancement of its characteristic peak at 1302 $cm^{-1}$ (Figure 5.6c).

Considering that the intensity of Raman scattering is inversely proportional to the fourth power of the laser wavelength, an overall increase of spectra intensity was expected due to the use of the 532 nm excitation source. However, the strong increase of specific Raman bands is generally due to the resonance Raman effect.

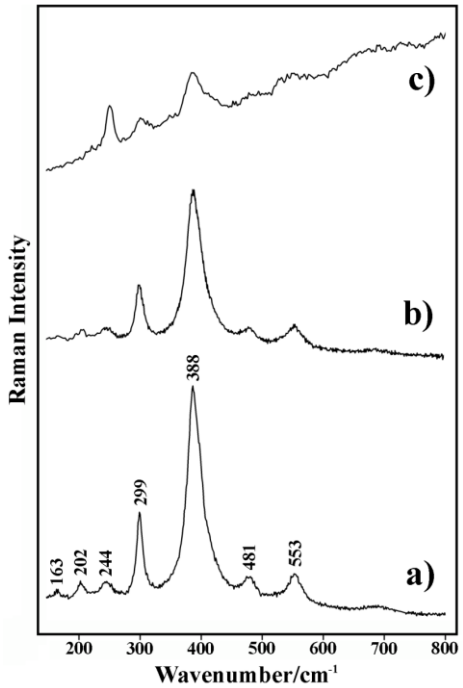


*Figure 5.5: Comparison between a) goethite standard spectrum (from IBeA database, 785 nm excitation laser) with those obtained by b) InnoRam™-785S and c) BWS5445-532S portable Raman systems.*

These phases affect the conservation of iron objects in a very different way. On the one hand, goethite is a highly stable compound that creates compact

corrosion layers. On the other hand, lepidocrocite and akaganeite are reactive phases facilitating cracks and loss of material.

It is well known that these iron corrosion products can be generated either from the reaction of metallic iron (due to the presence of water and oxygen) or from the transformation of iron oxides (due to a change of environmental parameters) according to reactions 5.8 and 5.9 respectively.

$$2Fe^0 + 3/2O_2 + H_2O \leftrightarrow 2FeO(OH)\ (s) \qquad \text{(Reac. 5.8)}$$

$$2Fe_3O_4\ (s) + 1/2O_2 + 3H_2O \rightarrow 6FeO(OH)\ (s) \qquad \text{(Reac. 5.9)}$$

Several publications differentiates these compounds exclusively for their crystal structure (α-FeO(OH) for goethite, β-FeO(OH) for akaganeite and γ-FeO(OH) for lepidocrocite) [33,34]. However, from the molecular point of view, akaganeite stands out because of the additional presence of chloride. Indeed, the akaganeite crystal structure has been deeply studied in recent years, and its chemical formula can now be written as $FeO_{0.883}(OH)_{1.167}Cl_{0.167}$ [35]. On the wake of these studies, it can be therefore deduced that $Cl^-$ ions infiltration has a paramount importance in the process of akaganeite formation.

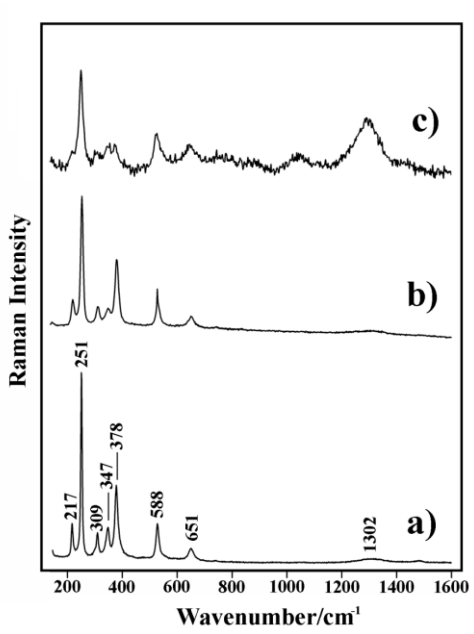


*Figure 5.6: Comparison between a) lepidocrocite standard spectrum (from IBeA database, 785 nm excitation laser) with those obtained by b) InnoRam™-785S and c) BWS5445-532S portable Raman systems.*

As demonstrated in several works, the theoretical chloride content in the tunnel structure of akaganeite is in the range between 6 and 8 % w/w [35]. Consequently, the $Cl^-$ ions that cannot be included within the tunnel structure of akaganeite tend to be weakly bonded on its outer surface.

During the post excavation step, surface and structural $Cl^-$ ions have a different behaviour. On the one side, $Cl^-$ ions incorporated in the tunnel structure are strongly bounded and, therefore are hardly removed by conventional desalination treatments. On the contrary, surface-bonded chlorides become unstable due to change of environmental conditions and can easily migrate along the corrosion layer by leaching and redeposition processes [36].

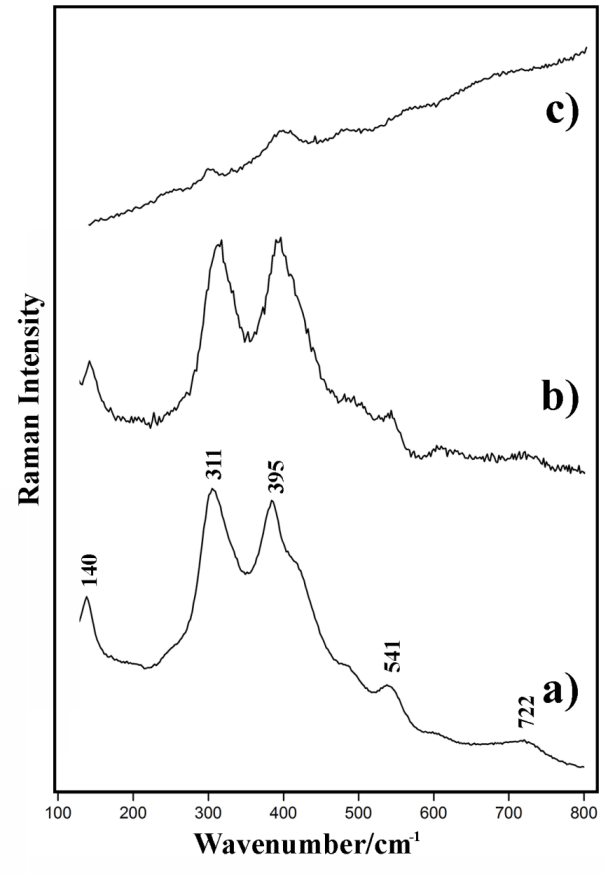


*Figure 5.7: Comparison between a) akaganeite standard spectrum (from IBeA database, 785 nm excitation laser) with those obtained by b) InnoRam$^{TM}$-785S and c) BWS5445-532S portable Raman systems.*

Ions' migration followed by hydrolysis and oxidation phenomena results in the development of new akaganeite. The consequent increase of porosity and volume due to the porous structure of this oxyhydroxide, causes fractures and

detachments that expose the inner layers to the environment [37,38]. This cyclical phenomenon, if not properly controlled, can quickly lead to the total destruction of the objects [39,40].

This corrosion mechanism helps to understand that, by preserving the artefacts under controlled environmental conditions (constant temperature and low levels of humidity), it is possible to minimize the reactivation of degradation phenomena in the post-excavation phase.

## 5.4 Conclusions

The research work summarized in this chapter highlights that, through the use of portable analytical techniques, conservation scientists can provide information of paramount importance to conservators avoiding any side-effect related to the preservation of the artefacts.

Indeed, thanks to in-situ ED-XRF analyses, the elemental composition of the objects and their decoration layers were revealed. Thanks to the obtained data, it was also deduced that the remarkable preservation state of the Ereñozar buckles is probably attributable to the presence of tin and lead in the alloys that plays a key role on the inhibition of degradation phenomena.

Thanks to the combined use of portable Raman systems equipped with different excitation lasers, it was possible to optimize the identification of the main corrosion products. The interpretation of molecular data, combined with the chromatographic analysis of burial soil samples, allowed the modelling of the chemical reactions that led to the formation of the identified degradation products. In this sense, the degradation mechanisms proposed in this chapter suggest that most of the detected corrosion phases were directly related to the infiltration of chlorides proceeding from marine aerosols.

In spite of the fact that in-situ analyses enabled the overall assessment of Ereñozar artefacts, the *E294* spur deserved a deepen laboratory study for two main reasons. First of all, molecular analyses pointed out the presence of reactive phases in its corrosion system. Thus, the characterization of the stratigraphic distribution of the iron phases was needed for the purpose of helping conservators to assess the stability of the artefact corrosion system. Furthermore, as will be deeply explained in the following chapter, laboratory experiments needed to be carried out with the purpose of evaluating the possible side effects

triggered by the application of alkaline treatments on gilded iron-based objects in order to help in the desalination treatment of these objects for their better preservation.

Under these requirements, the second step of the collaboration with the Archaeological Museum of Bizkaia was focused on deepen the understanding of the spur by carrying out laboratory analyses on a number of corrosion samples detached from the object during cleaning procedures.

## 5.5 References

**[1]** J.M. Madariaga, M. Maguregui, S. Fdez-Ortiz De Vallejuelo, U. Knuutinen, K. Castro, I. Martínez-Arkarazo, A. Giakoumaki, A. Pitarch (2014) In situ analysis with portable Raman and ED-XRF spectrometers for the diagnosis of the formation of efflorescence on walls and wall paintings of the Insula IX 3 (Pompeii, Italy). *Journal of Raman Spectroscopy*, 45, 1059-1067.

**[2]** O. Gómez-Laserna, M.A. Olazabal, H. Morillas, N. Prieto-Taboada, I. Martínez-Arkarazo, G. Arana, J.M. Madariaga (2013) In-situ spectroscopic assessment of the conservation state of building materials from a Palace house affected by infiltration water. *Journal of Raman Spectroscopy,* 44, 1277-1284.

**[3]** M. Martinón-Torres, B. Valcárcel Rojas, J.S. Samper, M.F. Guerra, (2012) Metallic encounters in Cuba: The technology, exchange and meaning of metals before and after Columbus. *Journal of Anthropological Archaeology*, 31, 439-454.

**[4]** S. Shalev, S.S. Shilstein, Y. Yekutieli (2006) XRF study of archaeological and metallurgical material from an ancient copper-smelting site near Ein-Yahav, Israel. *Talanta*, 70, 909-913.

**[5]** J.M. Madariaga (2010) Raman spectroscopy in art and archaeology. *Journal of Raman Spectroscopy*, 41, 1389-1393.

**[6]** R. García Moreno, D. Strivay, B. Gilbert (2008) Maya blue–green pigments found in Calakmul, Mexico: a study by Raman and UV-visible spectroscopy. *Journal of Raman Spectroscopy*, 39, 1050-1056.

**[7]** P. Ropret, T. Kosec (2012) Raman investigation of artificial patinas on recent bronze – Part I: climatic chamber exposure. *Journal of Raman Spectroscopy*, 43, 1578-1586.

**[8]** D. Neff, S. Reguer, L. Bellot-Gurlet, Ph. Dillmann, R. Bertholon (2004) Structural characterization of corrosion products on archaeological iron: an integrated analytical approach to establish corrosion forms. *Journal of Raman Spectroscopy,* 35, 739-745.

**[9]** A. Rousaki, C. Bellelli, M.C. Calatayud, V. Aldazabal, G. Custo, L. Moens, P. Vandenabeele, C. Vázquez (2015) Micro-Raman analysis of pigments from hunter–gatherer archaeological sites of North Patagonia (Argentina). *Journal of Raman Spectroscopy,* 46, 1016-1024.

**[10]** F. Ospitali, D.C. Smith, M. Lorblanchet (2007) Preliminary investigations by Raman microscopy of prehistoric pigments in the wall-painted cave at Roucadour, Quercy, France. *Journal of Raman Spectroscopy*, 37, 1063-1071.

**[11]** W. Gerwin, R. Baumhauer (2000) Effect of soil parameters on the corrosion of archaeological metal finds. *Geoderma*, 96, 63-80.

**[12]** V. Fell, J. Williams (2004) Monitoring of archaeological and experimental iron at Fiskerton, England. *National Museum of Australia Canberra ACT* 4–8 October 2004.

**[13]** K. Tronner, A.G. Nord, G.C. Borg (1995) Corrosion of archaeological bronze artefacts in acidic soil. *Water, Air, and Soil Pollution*, 85, 2725-2730.

**[14]** N. Prieto-Taboada, O. Gómez-Laserna, I. Martínez-Arkarazo, M.A. Olazabal, J.M. Madariaga (2012) Optimization of two methods based on ultrasound energy as alternative to European standards for soluble salts extraction from building materials. *Ultrasonic Sonochemistry,* 19, 1260-1265.

**[15]** J.M. Sánchez Pérez, I. Antiguedad, I. Arrate, C. García-Linares, I. Morell (2003) The influence of nitrate leaching through unsaturated soil on groundwater pollution in an agricultural area of the Basque country: a case study. *Science of the Total Environment*, 317, 173-187.

**[16]** M. Weichert, G. Eggert, A.M. Jones, H.A. Ankersmit (2004) Trees, bunches, cauliflowers - A closer look at sulphurus corrosion on copper alloys and minerals ('Black Spots'). *National Museum of Australia Canberra* ACT 4–8 October 2004.

**[17]** T. Trojek, M. Hlozek (2012) X-Ray fluorescence analysis of archaeological finds and art objects: Recognizing gold and gilding. *Applied Radiation Isotopes*, 70, 1420-1423.

**[18]** I. Ortega-Feliu, A.I. Moreno-Súarez, B. Gómez-Tubió, F.J. Ager, M.A. Respaldiza, S. García-Dils, O. Rodríguez-Gutiérrez (2010) A comparative study of PIXE and XRF corrected by Gamma-Ray Transmission for the non-destructive characterization of a gilded roman railing. *Nuclear Instruments and Methods in Physics Research Section B*, 268, 1920-1923.

**[19]** E. Darque-Ceretti, E. Felder, M. Aucouturier (2011) Foil and leaf gilding on cultural artifacts; forming and adhesion. *Revista Materia*, 16, 540-559.

**[20]** E. Cano, D. Lafuente, D.M. Bastidas (2010) Use of EIS for the evaluation of the protective properties of coatings for metallic cultural heritage: a review. *Journal of Solid State Electrochemistry,* 14, 381-391.

**[21]** M. Mödlinger, P. Piccardo (2013) Corrosion on prehistoric Cu–Sn-alloys: the influence of artificial environment and storage. *Applied Physics A*, 113, 1069-1080.

**[22]** S. Chen, L. Xie, F. Xue (2013) X-ray photoelectron spectroscopy investigation of commercial passivated tinplate surface layer. *Applied Surface Science*, 276, 454-457.

**[23]** Ph. Colomban, A. Tournié, M. Maucuer, Ph. Meynard (2012) On-site Raman and XRF analysis of Japanese/Chinese bronze/brass patina – the search for specific Raman signatures. *Journal of Raman Spectroscopy*, 43, 799-808.

**[24]** F. Clarelli, B. De Filippo, R. Natalini (2014) A Mathematical model of copper corrosion. *Applied Mathematical Modeling*, 28, 4804-4816.

**[25]** Y. Li, Z. Bao, J. Jiang, G. Chen, C. Pan (2012) Specific corrosion product on interior surface of a bronze wine vessel with loop-handle and its growth mechanism, Shang Dynasty, China. *Material Characterization*, 68, 88-93.

**[26]** D.A. Scott (1990) Bronze Disease: A Review of Some Chemical Problems and the Role of Relative Humidity. *Journal of the American Institute for Conservation* 29, 193-206.

**[27]** R.M. Organ (1963) Aspects of Bronze Patina and its Treatment. *Studies in Conservation,* 8, 1-9.

**[28]** Ph. Colomban, S. Cherifi, G. Despert (2008) Raman identification of corrosion products on automotive galvanized steel sheets. *Journal of Raman Spectroscopy*, 39, 881-996.

**[29]** D.A. Scott (2002) Copper and Bronze in ART: Corrosion, Colorants and Conservation, *Getty Trust Publications*, *Los Angeles (USA),* pp 532.

**[30]** M. Saheb, M. Descostes, D. Neff, H. Matthiesen, A. Michelin, Ph. Dillmann (2010) Raman identification of corrosion products on automotive galvanized steel sheets. *Applied Geochemistry,* 25, 1937-1948.

**[31]** L. Robbiola, J.M. Blengino, C. Fiaud (1998) Morphology and mechanisms of formation of natural patinas on archaeological Cu–Sn alloys. *Corrosion Science*, 40, 2083-2111.

**[32]** J. Aramendia, L. Gómez-Nubla, L. Bellot-Gourlet, K. Castro, C. Paris, Ph. Colomban, J.M. Madariaga (2014) Protective ability index measurement through Raman quantification imaging to diagnose the conservation state of weathering steel structures. *Journal of Raman Spectroscopy*, 45, 1076-1084.

**[33]** C. Remazeilles, P. Refait (2007) On the formation of β-FeOOH (akaganeite) in chloride-containing environments. *Corrosion Science*, 49, 844-857.

**[34]** E.A. Deliyanni, D.N. Bakoyannakis, A.I. Zouboulis, K.A. Matis, L. Nalbandian (2001) Akaganeite-type β-FeO(OH) nanocrystal: preparation and characterization. *Microporous and Mesoporous Materials*, 42, 49-57.

**[35]** K. Stahl, K. Nielsen, J. Jiang, B. Lebech, J.C. Hanson, P. Norby, J.V. Lanschot, (2003) On the akaganéite crystal structure, phase transformations and possible role in post-excavational corrosion of iron artifacts. *Corrosion Science*, 45, 2563-2575.

**[36]** L. Selwyn (2004) Overview of archaeological iron: the corrosion problem, key factor affecting treatment, and gaps in current knowledge. *National Museum of Australia Canberra* ACT 4–8 October 2004.

**[37]** K.E. García, C.A. Barrero, A.L. Morales, J.M. Greneche (2009) Magnetic structure of synthetic akaganèite: A review of Mossbauer data. *Revista Facultad de Ingeniería Universidad de Antioquia*, 49, 185-191.

**[38]** S. Reguer, F. Mirambet, E. Dooryhee, J.L. Hodeau, Ph. Dillmann, P. Lagarde (2009) Structural evidence for the desalination of akaganeite in the preservation of iron archaeological objects, using synchrotron X-ray powder diffraction and absorption spectroscopy. *Corrosion Science*, 51, 2795-2802.

**[39]** B. Schmutzler, N. Ebinger-Rist (2008) The conservation of iron objects in archaeological preservation – Application and further development of alkaline sulphite method for conservation of large quantities of iron finds. *Materials and Corrosion*, 59, 248-253.

**[40]** M. Rimmer, Q. Wang (2010) Assessing the effects of alkaline desalination treatments for archaeological iron using scanning electron microscopy. *The British Museum Technical Research Bulletin,* 4, 79-86.

# CHAPTER 6:

# MULTIANALYTICAL LABORATORY APPROACH TO DEEPEN THE STUDY OF THE EREÑOZAR GILDED SPUR (*E294*)

Even though portable and non destructive techniques provide essential data regarding their chemical composition, the in-situ study of archaeological objects is often flanked by the complementary characterization of samples by means of laboratory systems.

For example, several research works have demonstrated that crucial information regarding the conservation state of the object under study can be obtained from the interpretation of both molecular and elemental maps of cross sectioned samples.

With regards to elemental mapping, the SEM-EDS system has been extensively used for *Cultural Heritage* research purposes [1,2]. Its magnification feature and its ability to identify most of the elements help to thoroughly understand the composition of the alloys as well as to understand the presence of layers or heterogeneities.

Regarding molecular mapping, most of the modern studies are based on the use of Raman spectroscopy [3]. Among all methods developed for this technique, the "point by point" analysis can be considered as the most common one. It works by focusing the laser on a sample spot. Then, each point of the selected region is sequentially analyzed thanks to a motorized stage that moves the sample under the laser beam. After analyzing one by one all the points of the region, a dedicated software studies the distribution of each detected compound along the point grid in order to create molecular distribution images.

In spite of the good results, the point by point mapping method often requires long times to perform the analysis of the selected region. In recent years, the acquisition of molecular maps has been facilitated by the development of Raman imaging methods [4]. This method offers several advantages compared to the point by point one, such as the considerable reduction of time and the possibility to use higher laser powers without damaging the sample.

In addition to molecular mapping and imaging, one of the last frontiers in the field of Raman spectroscopy consists in the development of specific interfaces that allows to carry out the molecular analysis of samples inside the vacuum chamber of SEM systems [5,6]. Thanks to the optical system connecting both instruments, it is therefore possible to take advantage of the magnification feature of the SEM to collect the molecular vibration spectra of compounds that cannot be detected through the use of conventional molecular techniques.

In the light of this background, a few corrosion samples were collected before the cleaning of the *E294* gilded spur in the Archaeological Museum of Bizkaia. The fragments were then pre-treated and analyzed by laboratory techniques with the aim of deepen the understanding of the artefact's decoration layer and of its corrosion system.

## 6.1 Decoration and corrosion system evaluation

### *6.1.1 Cross section analyses*

In order to better understand the elemental and molecular composition of the artefact, *M03, M04* and *M05* samples were cross sectioned, and elemental and molecular chemical images were collected by means of the EVO40 Scanning Electron Microscope and inVia Renishaw confocal microRaman spectrometer described in chapter 4.

*M03* fragment was first analyzed to better understand the gilded layer composition. As can be observed in Figure 6.1, several elemental maps proved the presence of two decoration layers. The inner one, composed of pure silver, was overlapped by a gold-based coat applied by fire gilding [7,8]. As described in Middle Age manuscripts, the accessories belonging both to, squires and knights, contained a rigorous symbolism: the squires could wear only silver-plated decorations since gilded items were for the exclusive use of the knights [9]. According to this information, it can be assumed that the spur was decorated in two phases. At first, the squire applied a silvered decoration, and then, the spur was coated by a gilded layer after his promotion to knight.

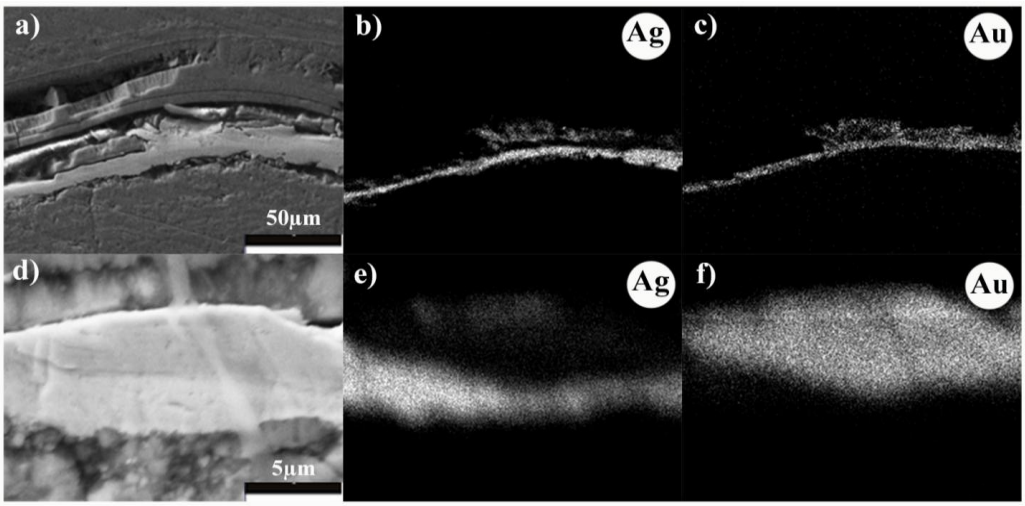


*Figure 6.1: SEM-EDS images of M03 cross section sample focusing on the decoration layers (a) and (d); (b) and (e) images show the silver layer overlapped by a gold coating (c) and (f) applied by fire gilding technique.*

Regarding the stratigraphic distribution of iron corrosions, the elemental image (Figure 6.2) obtained from the *M03* SEM-EDS map showed the presence of two thick layers (red colour identifies the Fe element) separated by the decoration coating (blue colour identifies the Au element). In the same image, the violet colour assigned to the Cl element demonstrates that $Cl^-$ ions reached the inner corrosion layers by penetrating through cracks and porous.

The elemental characterization of the sample helped to select the most interesting areas for Raman molecular imaging. Although, in comparison with the in-situ data no new degradation compounds were detected, molecular images provided new important information regarding their stratigraphic distribution. In fact, as can be seen in Figure 6.2, the outer corrosion crust on *M03* sample was

predominantly composed of goethite (blue image), while magnetite (red image) was the main compound of the inner layer.

This stratigraphic distribution is quite common in Fe-based archaeological findings. In fact, iron oxides tend to be located in the inner corrosion layers. On the contrary, the corrosion surface, being more exposed to the external environment, tends to be mainly composed of iron oxyhydroxides [10].

As showed in Figure 6.2, Raman imaging also helped demonstrating that $Cl^-$ affected areas were characterized by the presence of reactive phases such as akaganeite (yellow image) and lepidocrocite (light blue image).

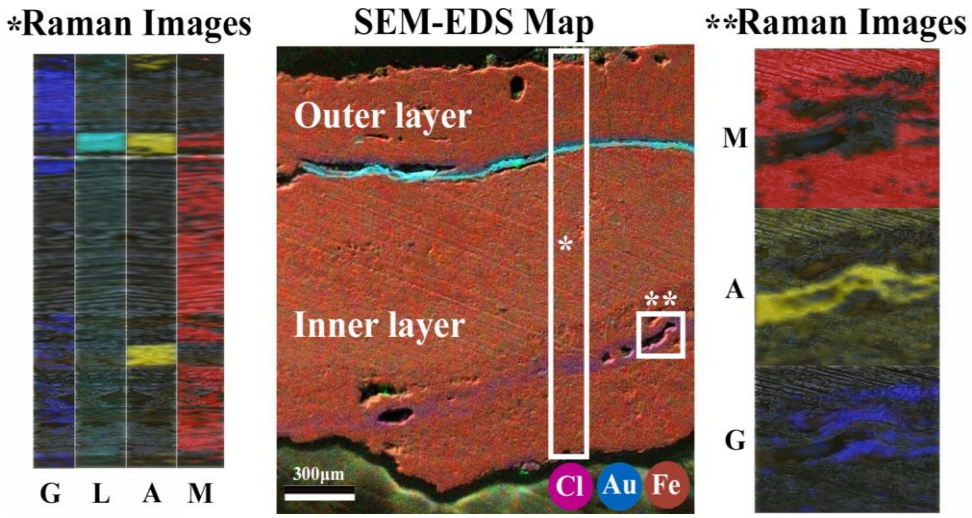


*Figure 6.2: SEM-EDS image of M03 sample proving the presence of chloride infiltration problems. The stratigraphic distribution of goethite (G), lepidocrocite (L), akaganeite (A) and magnetite (M) in the selected areas was carried out by means of the Raman imaging system.*

The analytical procedure applied to the study of sample *M03* was repeated on other samples at our disposal. Both elemental and molecular data obtained from all corrosion fragments showed a similar composition to sample *M03*. In fact, all cross-sections showed an inner part almost entirely composed of magnetite and covered by external iron oxyhydroxide layers. Furthermore, the correspondence between Cl-affected areas and the development of reactive iron oxyhydroxide phases (akaganeite and lepidocrocite) was also confirmed.

### *6.1.2 Surface analyses*

With regard to the analyses of fragments' surfaces, SEM-EDS maps of sample *M01* allowed to study in depth the conservation state of the two decoration layers. Indeed, the elemental image obtained by the use of INCA software (Figure 6.3c) [11] proved that, in contrast to the remarkable conservation state of the fire gilded layer, the silver-based decoration was strongly degraded. A possible reason of this degradation was found in the spatial distribution of Cl that perfectly overlapped to the Ag distribution, suggesting the presence of chlorinated corrosion phases.

Considering that silver degradation compounds are not easily detectable by means of Raman spectrometers, definitive evidence was provided by coupling SEM-EDS and Raman systems through the SCA interface. In this sense, the spectra collected from several spots of the silver surface displayed the characteristic peaks of silver chloride (97, 143sh and 233 $cm^{-1}$, Figure 6.3b) [12], a degradation compound easy to find in Ag-containing artefacts coming from archaeological sites near the coast line.

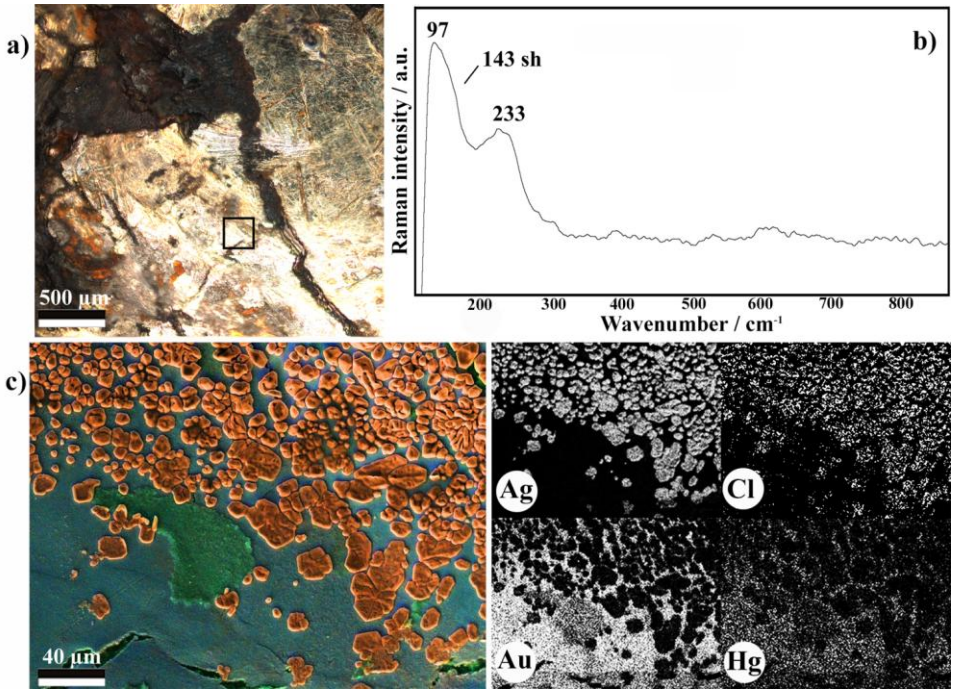


*Figure 6.3: a) Optical image of M01 sample; B) Raman spectrum of silver degradation product detected on the gilded layer surface through the use of the coupled SEM-Raman system; c) SEM-EDS analysis of M01 sample (blue and orange colours indentify the Au- and Ag-based layers respectively).*

During the analysis of the *M02* sample, both optical and SEM-EDS images acquired from the outer surface of this fragment (which was in contact with the soil during burial) showed the presence of white filamentous incrustations. The elemental maps (Figure 6.4a) proved that these filaments were mainly composed of calcium. Raman analyses performed inside the SEM chamber favoured identifying the molecular composition of these incrustations (Figure 6.4b) as calcium carbonate ($CaCO_3$, main Raman peak at 1085 $cm^{-1}$). The particular structure of such degradation suggested a calcification process promoted by biological activity. In fact, manifold varieties of organisms able to mineralize $CO_2$ to carbonates (such as $CaCO_3$) are usually present in soils [13].

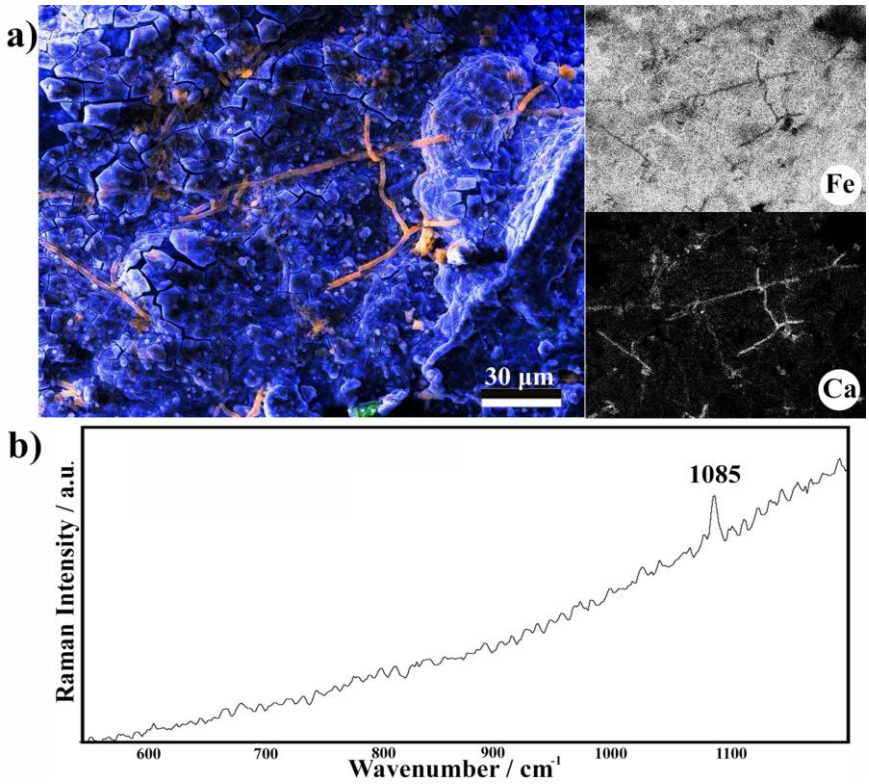


*Figure 6.4: a) SEM-EDS image and element maps of M02 sample, showing the Ca-based filamentous incrustations covering the iron corrosion surface; b) molecular analyses carried out by means of the coupled SEM-Raman system proved the presence of calcium carbonate.*

## 6.2 Treatments assessment

The laboratory analyses described above, combined with the in-situ studies summarized in the previous chapter, proved that the *E294* spur had critical degradation problems related to soluble salts infiltration.

Considering their active role on the onset of degradation products, conservators must act promptly to remove soluble salts soon after the recovery of artefacts from archaeological endeavours.

The desalination of iron-based artefact is generally carried out by means of alkaline baths. Even though their efficiency have been widely corroborated [12], the bibliography highlights a lack of research works focused on the evaluation of the possible side effects that basic solutions can trigger to gold and/or silver-based decoration layers.

Considering this background and recognizing the need of restorers, the last part of this work was focused on the study of advantages and disadvantages that alkaline baths could entail during the treatment of the *E294* gilded spur.

To make this, the effects of the most used desalination treatment (0.5 molar NaOH bath) were compared with those provided by a neutral pH bath (Milli-Q water). The experiment was carried out by treating *M01* and *M03* samples with Milli-Q and NaOH baths respectively. Both NaOH treatment and Milli-Q reference were applied at a constant temperature of 25 °C during 60 days. During and after treatment, the desalination efficiency was evaluated by quantifying the chlorides extracted from the samples. The analyses were performed by means of the Capillary Electrophoresis system described in chapter 4. On the other hand, the quantification of possible lixiviated Fe, Ag, Au and Hg elements in both solutions was carried out by ICP-MS.

Considering the gilded area preserved on it, *M01* sample was selected for the application of the NaOH treatment (pH≈13.3). The results were then compared with those obtained by treating the *M03* sample with a Milli-Q bath (pH≈6.8).

The main data obtained from both experiments are summarized in Figure 6.5. Starting from the study of the treatments dechlorination effect, the overall amount of chloride extracted from both samples (Figure 6.5a) described a similar curve that reflects the experimental results carried out by E. Guiminot et al. [13]. Most of chlorides were extracted in the first weeks. Then, a progressive decrease of the quantity of extracted chlorides was observed.

The most relevant conclusions obtained by comparison of treatments arise from ICP-MS data. The quantification of the metals dissolved by NaOH solution during the treatment of sample *M01* showed that the dissolution of Ag, Au and Hg was

below the quantification limit of the instrument. Considering that the sensitivity of the ICP-MS reaches the µg/kg, it can be therefore affirmed that this treatment did not involve any solubilisation of gilding metals.

Finally, considering that chloride extraction may cause the transformation of $Cl^-$ containing phases into more stable compounds, the EVO 40 SEM-EDS system and the inVia Renishaw Raman spectrometer were used to characterize the samples before, during and after the application of desalination baths.

As shown in Figure 6.5b and c, SEM-EDS and Raman analyses excluded any change in the elemental and molecular composition of sample *M01*, excluding the $Cl^-$ concentration decrease.

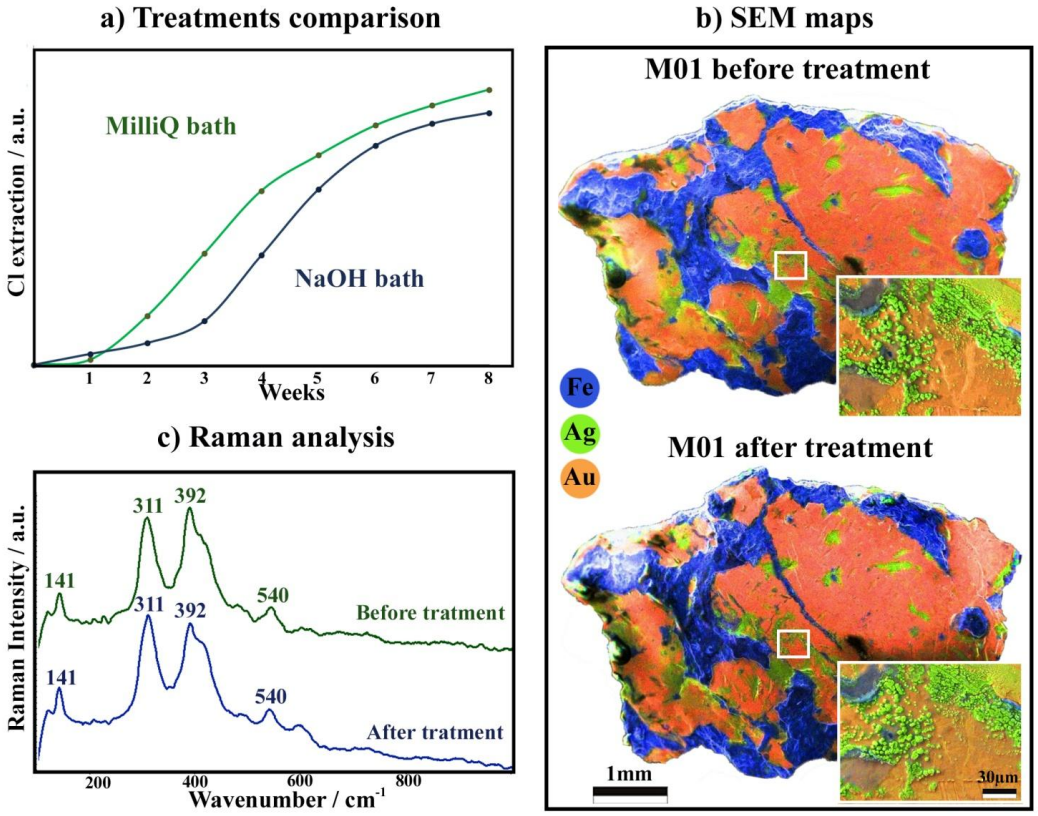


*Figure 6.5: a)NaOH chloride extraction on spur samples and its comparison to the Milli-Q bath reference; b) SEM-EDS maps of M01 fragment before and after NaOH treatment excluded any damage of the gilded layer; c) Raman spectra, showing that no transformation of akaganeite occurred after the NaOH-based treatment.*

To sum up, desalination experiments proved that the use of basic treatments (NaOH) caused no side effects to iron artefacts decorated by fire gilding. At the

same time, the comparison with the Milli-Q reference bath confirmed that the use of alkaline baths also helped to inhibit the leaching of the iron matrix. Moreover, the monitoring carried out before, during and after sample treatments showed that the NaOH solution did not cause the transformation of akaganeite into a more stable compound. However, thanks to the removal of uncomplexed chlorides from the artefact core, the chance of reactivation of this degradation process dramatically decreased.

Supported by the experimental results herein summarized, conservators finally performed the desalination of the spur by using a 0.5 molar NaOH bath. As shown in Figure 6.6 the artefact is nowadays preserved in perfect conditions and represents one of the most important objects exhibited in the Archaeological Museum of Bizkaia.


*Figure 6.6: Middle Age gilded spur proceeding from the Ereñozar necropolis before (a) and after (b) restoration. The conservation treatments applied by restorers included desalination, consolidation and removal of the outer corrosion layers.*

## 6.3 Conclusions

The analytical work outlined in this chapter represents a practical example of the benefits provided by the use of laboratory *Conservation Science* tools for the characterization and the conservation of *Cultural Heritage* materials.

Indeed, thanks to the elemental mapping of sample cross sections, the presence of a double decorative layer was identified, which provided new information regarding the history and the evolution of the artefact.

Furthermore, the molecular images obtained from *M03, M04* and *M05* samples cross sections allowed to evidence the stratigraphic distribution of the iron corrosion phases. On the one hand, molecular images collected by means of Raman spectroscopy allowed to distinguish the stratigraphic distribution of goethite, magnetite, lepidocrocite and akaganeite.

Considering that lepidocrocite and (above all) akaganeite are reactive phases, semi-quantitative data are needed for the purpose of evaluating the overall stability of the corrosion system. Even though semi-quantitative values can be obtained by Raman spectra treatment, this technique is poorly suitable for the study of materials featuring high auto-fluorescence emissions. To overcome this problem, a novel semi-quantification method was developed (see chapter 7).

Regarding the results summarized in section 6.2, desalination experiments carried out on corrosion fragments proved that NaOH baths did not compromise the integrity of the two decoration layers, ensuring its suitability for the treatment of iron artefact decorated by fire gilding. These results helped to partially fill the lack of literature in this field. However, it is clear that more research was needed for better understand the effects entailed by the application of desalination treatments. Under this requirement, the laboratory experiments described in chapter 8 were designed and carried out with the specific aim of deepening the knowledge and optimizing the extractive capability of NaOH-based desalination baths.

## 6.4 References

**[1]** G.M. Ingo, T. De Caro, C. Riccucci, S. Khosroff (2006) Uncommon corrosion phenomena of archaeological bronze alloys. *Applied Physics A*, 83, 581–588.

**[2]** E. Figueiredo, P. Valério, M.F. Araújo, R.J.C. Silva, A.M.M. Soares (2011) Inclusions and metal composition of ancient copper-based artefacts: a diachronic view by micro-EDXRF and SEM-EDS. *X-Ray Spectrometry*, 40, 325–332.

**[3]** S. Sasic, Y. Ozaki (2010) Raman, infrared, and near-infrared chemical imaging. *John Wiley & Sons, Inc., Hoboken (USA),* pp 325.

**[4]** A. Wang, R.L. Lootev, L.B. Jolliff, Z. Ling (2015) Raman imaging of extraterrestrial materials. *Planetary and Space Science*, 112, 23–34.

**[5]** L. Gómez-Nubla, J. Aramendia, S. Fdez-Ortiz de Vallejuelo, K. Castro, J.M. Madariaga (2013) From portable to SCA Raman devices to characterize harmful compounds contained in used black slag produced in electric arc furnace of steel industry. *Journal of Raman Spectroscopy*, 44, 1163–1171.

**[6]** I. Guerra, C. Cardell (2015) Optimizing use of the structural chemical analyser (variable pressure FESEM-EDX raman spectroscopy) on micro-size complex historical paintings characterization. *Journal of Microscopy*, 260, 47-61.

**[7]** F.M. Guerra, T. Calligaro (2003) Gold cultural heritage objects: a review of studies of provenance and manufacturing technologies. *Measurement Science and Technology*, 14, 1527–1537.

**[8]** S. Lang, U. van Lilienfeld (2011) Budapest concordantiae caritatis, facsimile edition. *Schöck ArtPrint Kft, Budapest (Hungary),* pp 524.

**[9]** D. Talbot, J. Talbot (1997) Corrosion science and technology. *CRC press, Boca Ratón (USA),* pp 432.

**[10]** INCA Energy Operator Manual, available at: https://investigacion.us.es/docs/web/files/manual_instrucciones_eds_inca.pdf (May 07th 2017).

**[11]** I. Martina, R. Wiesinger, D. Hembrih-Simburger, M. Schreiner (2012) Micro-Raman characterisation of silver corrosion products: instrumental set up and reference database. *E-Preservation Science*, 9, 1–8.

**[12]** N.A. Kamennaya, C.M. Ajo-Franklin, T. Northen, C. Jansson (2012) Cyanobacteria as biocatalysts for carbonate mineralization. *Minerals,* 2, 338–364.

**[13]** E. Guilminot, D. Neff, C. Remazeilles, S. Reguer, F. Kergourlay, C. Pele, Ph. Dillmann, P. Refait, F. Mielcarek, N. Huet, J. Rebiere (2012) Influence of crucial parameters on the dechlorination treatments of ferrous objects from seawater. *Studies in Conservation*, 57, 227–236.

# CHAPTER 7:

# DEVELOPMENT OF A NOVEL METHOD TO EVALUATE THE STABILITY OF CORROSION SYSTEMS IN ARCHAEOLOGICAL ARTEFACTS

The multianalytical study summarized in chapter 5 underlined that most of the metallic object recovered from the archaeological site of Ereñozar presented degradation pathways related to chlorides infiltration. In addition, laboratory analyses performed on corrosion fragments sampled from the gilded spur (*E294*), proved that chlorides are particularly dangerous for iron-based artefacts, since induce the formation of reactive corrosion phases [1], such as akaganeite (see chapter 6).

As previously mentioned, the presence of akaganeite can seriously threaten the conservation of archaeological iron samples in the post excavation step due to its porous crystalline structure that promotes cracks, swellings and loss of material. Considering that many conservation problems are induced by the presence of reactive compounds, it is clear that the work of restorers might be strongly

benefited by the quantitative or semi-quantitative study of the phases composing the corrosion system.

For example, the quantitative analysis of rust layers that, one after the other, are removed by restorers during the conservation work helps to identify the in-depth distribution of reactive degradation products and to characterize the reactivity of the whole corrosion system [2]. Such approaches are also carried out in the context of atmospheric corrosion where the quantification of iron phases has been used to describe the stability of the corrosion layers [3,4].

The quantitative analysis of iron corrosions can also find reliable applications in the steps following the conservation works. In the short term, it can be used to control whether conservation treatments are capable of stabilizing the reactive corrosion phases. In the long term, it can also be used to identify the new corrosion processes triggered by the interaction between the restored object and the storage/exhibition environmental conditions.

In this context, it is important to emphasize that the analysis of *Cultural Heritage* should be carried out in the least intrusive way. Raman technique, for example, has been extensively used in this field to semi-quantify iron corrosion phases with good results, as explained in chapter 6.

Considering that the intensity of Raman signals are proportional to the concentration of the compounds, the most employed quantification method is the one based on the use of external calibration curves [5,6]. In order to get out of establishing calibration curves for each analyzed compound and their mixtures, an approach using the spectral decomposition in a linear combination of reference spectra was proposed for studying atmospheric corrosion of Middle Age irons [4]. Further than using point analyses, the corrosion heterogeneities were taken into account using the automated treatment of Raman maps over the corrosion system. This approach was also applied for the diagnostic of self-weathering steel atmospheric corrosion of contemporary works of art [7].

However, it must be pointed out that Raman spectroscopy is poorly suitable for the study of materials featuring high auto-fluorescence emissions. In these cases, the use of FTIR spectroscopy is more indicated, since it avoids any problem related to the auto-fluorescence of the sample. Moreover, working with powdered samples, FTIR systems also ensure a better accuracy and repetitiveness of the

results over the sample heterogeneities by taking into account a sampling of the whole corrosion system [8].

Even though FTIR systems have been successfully applied for the semi-quantification of several kind of liquid [9,10] and solid [11,12] samples, only one work describes the use of this spectroscopic technique for the quantification of iron phases. This work, presented by H. Namduri et al. (2008) [13], was focused on the study of corrosion products (composed of a mixture of magnetite, maghemite and hematite) formed in the secondary cycle of pressurized water reactors.

Considering the state-of-the-art, this chapter presents an innovative approach to semi-quantify archaeological artefacts corrosions by means of FTIR spectroscopy.

## 7.1 Methodology

### Samples preparation

The experimental work was based on the analysis of both, standard mixtures and archaeological rust samples.

On the one hand, 10 standard mixtures were prepared by mixing iron oxide and oxyhydroxide standards at different proportions. Pure magnetite, lepidocrocite and goethite iron phases were kindly provided by D. Neff from the LAPA research group (NIMBE UMR3685 CEA/CNRS, France). Pure akaganeite, in contrast, was synthesized using the method described by S. Reguer et al. (2009) [14]. Considering that FTIR spectroscopy needs a small particle size (1-2 μm) to avoid any distortion phenomena, an agate mortar was used for the grinding and the homogenization of all samples. The relative weight of each iron phase in the mixtures was monitored by using the AE200 analytical balance described in chapter 4.

On the other hand, real archaeological rust samples were collected (with the collaboration of the conservators of the Archaeological Museum of Bizkaia) from the outer corrosion layers of Middle Age iron nails affected by $Cl^-$ infiltration.

### Semi-quantification of corrosion phases

As previously explained, the semi-quantification method is based on the decomposition of FTIR spectra.

First, the Jasco 6300 system was used in transmittance, DRIFT and ATR modes with the aim of checking which configuration provided the most reliable results.

In addition, the transportable Alpha FTIR spectrometer (see chapter 4) was also used with the purpose of: a) verifying if semi-quantification studies could be performed also in the case of in-situ analyses and b) testing the reproducibility of the method by using different FTIR systems.

In order to perform the semi-quantification of FTIR spectra, the PALME software (Program d'AnaLyse vibrationnelle de spectres de MElanges à partir de spectres purs) developed by the LADIR Laboratory (nowadays MONARIS, University Pierre et Marie Curie, France) was used. This program was specifically designed to treat spectra obtained by vibrational spectroscopy techniques. PALME software automatically performs the semi-quantification of compounds mixtures by the linear combination of spectra of pure reference standards [15,16]. The process consists of two steps. In the first one, the software uses a sum of Gaussian and/or Lorentzian band profiles and a least-square fitting to produce for each reference compound (in this work akaganeite, lepidocrocite, goethite and magnetite) a calculated spectrum that perfectly fits the recorded experimental one.

In a second step, a linear combination of the calculated standard spectra is used for the fitting of a spectrum similar to the sample spectrum by means of the least-squares criterion and the Levenberg-Marquardt algorithm. After the user validation of the fitting, the PALME software provides a .txt file including the contribution of each standard (expressed as a weighting coefficient) to the decomposition of the sample spectrum.

## Stability evaluation of corrosion systems

After completing the semi-quantification of the iron phases, the percentage values of each compound were used to determine the sample corrosion stability. In this regard, the stability calculation was inspired by the protection ability index (PAI index), proposed for the first time by M. Yamashita et al. (1994) [17] and subsequently adjusted by Ph. Dillmann et al. (2004) [1] for the analysis of rust layers covering ancient iron objects exposed to atmospheric corrosion.

The adjusted index (*PAI index) considers the presence of akaganeite-lepidocrocite as reactive phases and goethite-magnetite as protective ones (equation 7.1).

In this light, the stability of archaeological corrosion samples was calculated as follows:

$$\text{Corrosion stability} = \frac{\text{mass fraction } (\alpha FeO(OH)) + (Fe_3O_4)}{\text{mass fraction } (\gamma FeO(OH)) + (\beta FeO(OH))} \quad \text{(Eq. 7.1)}$$

In the case of standards' mixtures, the reliability of the stability calculation was determined by comparison with the results obtained using the real weighted proportions of each compound. In the case of archaeological samples, the reliability evaluation was performed using as a reference the value calculated by the XRD system described in chapter 4.

## 7.2 Characterization of pure standards

The semi-quantification performed by the PALME software is based on the decomposition of the vibrational spectrum of a sample by comparison with pure reference spectra. Thus, FTIR spectra of pure akaganeite, lepidocrocite, goethite and magnetite were collected under the same experimental conditions in order to obtain absorbances (relative intensities between bands) related to each sample specificities, spectrometer characteristics and measurement mode (transmittance, DRIFT, ATR). For example, Figure 7.1 reports the FTIR spectra of pure iron phases collected by using the Jasco 6300 laboratory system in transmittance mode.

As showed in Figure 7.1, the magnetite vibrational spectrum was characterized by the presence of strong signals at 588 and 3437 $cm^{-1}$ (Figure 7.1a). Goethite spectrum showed three strong peaks at 615, 798 and 905 $cm^{-1}$ respectively, together with two broad bands at 3136 and 3431 $cm^{-1}$ (Figure 7.1b). Lepidocrocite spectrum stood out by the presence of a main peak at 1023 $cm^{-1}$, followed by several secondary signals at 485, 615, 759, 1152, 3014 and 3414 $cm^{-1}$ (Figure 7.1c). Finally, akaganeite standard provided an intense double peak at 648 and 693 $cm^{-1}$, together with two weak signals at 844 and 1623 $cm^{-1}$ and a broad band at 3385 $cm^{-1}$ (Figure 7.1d).

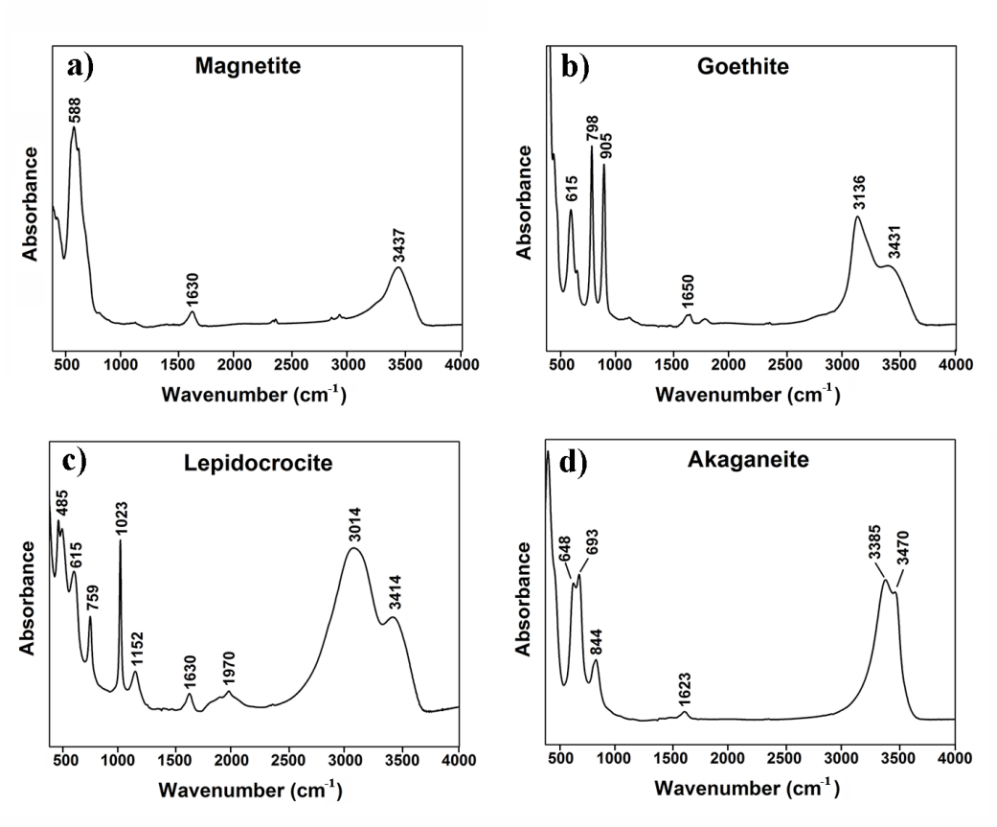


*Figure 7.1: FTIR raw spectra of iron oxide standards carried out using the Jasco 6300 system in transmittance mode.*

To illustrate the signal differences produced by each acquisition mode, the comparison of akaganeite spectra recorded using the Jasco 6300 in ATR, DRIFT and transmittance modes are displayed in Figure 7.2.

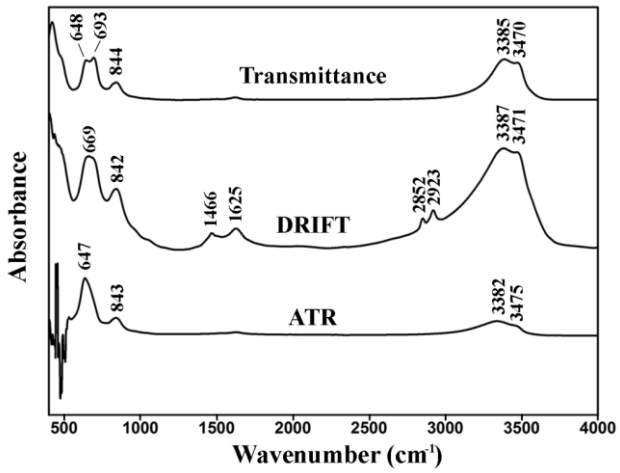


*Figure 7.2: Comparison among akaganeite spectra obtained using the Jasco 6300 system in ATR, DRIFT and transmittance modes.*

As evidenced in Figure 7.2, transmittance and DRIFT modes were more sensitive to the O-H bonds vibrations with respect to the ATR mode [18,19], promoting the enhancement of the hydroxide signals on the spectrum of pure akaganeite (3385 and 3470 $cm^{-1}$). Furthermore, it must be pointed out that, using the DRIFT method, the infrared radiation penetrates the sample/KBr mixture, producing a high number of refractions and absorption processes, which result in an enhancement of the intensity in the interfaces contribution and combination bands [20]. This statement was confirmed by experimental data owing to the presence of several secondary peaks in a wavelength range between 1400 and 3000 $cm^{-1}$ (Figure 7.2). Furthermore, both position and shape of DRIFT and ATR peaks are more or less shifted/modified because of the complexity of the interaction (superimposition of absorption and reflection), which explains the differences, especially below 1000 $cm^{-1}$ [21,22].

After completing laboratory analyses, the characteristic spectra of pure standards were also collected by means of the portable FTIR Alpha system. This instrument offered better performance to low wavelengths (below 525 $cm^{-1}$) with respect to the Jasco 6300 due to the different sensitivity of the coupled beamsplitter and ATR cell.

## 7.3. Semi-quantification of pure standards mixtures

### Semi-quantification using raw spectra

Once confirmed that both FTIR systems were able to differentiate the iron oxides and oxyhydroxides typically developed in the corrosion system of archaeological artefacts, the next step of this work was focused on the molecular analysis of the reference mixtures described in section 7.1. After analyzing all mixtures with laboratory (transmittance, diamond/ZnSe-ATR and DRIFT modes) and transportable (diamond-ATR mode) spectrometers, the raw spectra were semi-quantified by means of the PALME software in order to determine the contribution of each iron phase in the mixtures.

As can be clearly observed in Table 7.1, the semi-quantification reliability of the laboratory system varied widely depending on the measurement configuration used.

*Table 7.1: Comparison between the real weighted and experimental concentration values of standard mixtures obtained with raw spectra. Experimental values were obtained by semi-quantifying raw FTIR spectra acquired in different modes and devices using PALME software.*

| Sample | Real composition | | Predicted composition | | | | | | | |
|---|---|---|---|---|---|---|---|---|---|---|
| | | | Laboratory Jasco 6300 ATR | | Laboratory Jasco 6300 DRIFT | | Laboratory Jasco 6300 Transmittance | | Portable Alpha ATR | |
| | Iron compound | % weighted | % exper. | Diff. | % exper. | Diff. | % exper. | Diff. | % exper. | Diff. |
| **Sample 1** | **Akaganeite** | **83.3** | **78.0** | -5.3 | **63.3** | -20.0 | **77.8** | -5.5 | **69.3** | -14.0 |
| | **Goethite** | **16.7** | **22.0** | 5.3 | **36.7** | 20.0 | **22.2** | 5.5 | **30.7** | 14.0 |
| **Sample 2** | **Akaganeite** | **50.0** | **49.3** | -0.7 | **61.2** | 11.2 | **43.0** | -7.0 | **37.8** | -12.2 |
| | **Goethite** | **50.0** | **50.7** | 0.7 | **38.8** | -11.2 | **57.0** | 7.0 | **61.2** | 12.2 |
| **Sample 3** | **Akaganeite** | **26.1** | **26.3** | 0.2 | **39.0** | 12.9 | **18.3** | -7.8 | **21.4** | -4.7 |
| | **Goethite** | **73.9** | **73.7** | -0.2 | **61.0** | -12.9 | **81.7** | 7.8 | **78.6** | 4.7 |
| **Sample 4** | **Magnetite** | **77.3** | **65.0** | -12.3 | **83.5** | 6.2 | **75.6** | -1.7 | **65.8** | -11.5 |
| | **Lepidocrocite** | **22.7** | **35.0** | 12.3 | **16.5** | -6.2 | **24.4** | 1.7 | **34.2** | 11.5 |
| **Sample 5** | **Magnetite** | **27.3** | **32.5** | 5.2 | **38.8** | 11.5 | **24.2** | -3.1 | **5.2** | -22.1 |
| | **Lepidocrocite** | **72.7** | **67.5** | -5.2 | **61.1** | -11.5 | **75.8** | 3.1 | **94.8** | 22.1 |
| **Sample 6** | **Magnetite** | **47.1** | **52.0** | 4.9 | **55.5** | 8.4 | **48.6** | 1.5 | **47.0** | -0.1 |
| | **Lepidocrocite** | **52.9** | **48.0** | -4.9 | **44.5** | -8.4 | **51.4** | -1.5 | **53.0** | 0.1 |
| **Sample 7** | **Goethite** | **17.8** | **20.6** | 2.8 | **16.6** | -1.2 | **17.1** | -0.7 | **31.2** | -13.4 |
| | **Lepidocrocite** | **46.6** | **53.8** | 7.2 | **51.7** | 5.1 | **44.5** | -2.1 | **56.6** | 10.0 |
| | **Magnetite** | **35.6** | **25.6** | -10.0 | **31.7** | -3.9 | **38.4** | 2.8 | **12.2** | -23.4 |
| **Sample 8** | **Goethite** | **23.2** | **28.8** | 5.6 | **21.7** | -1.5 | **27.2** | 4.0 | **36.7** | 13.5 |
| | **Magnetite** | **49.5** | **36.2** | -13.3 | **69.9** | 20.4 | **57.7** | 8.2 | **38.9** | -10.6 |
| | **Akaganeite** | **27.3** | **35.0** | 7.7 | **8.4** | -18.9 | **15.1** | -12.2 | **24.4** | -2.9 |
| **Sample 9** | **Magnetite** | **31.5** | **37.9** | 6.4 | **50.2** | 18.7 | **36.5** | 5.0 | **-6.7** | -38.2 |
| | **Akaganeite** | **39.3** | **36.0** | -3.3 | **27.3** | -12.0 | **35.3** | -4.0 | **67.5** | 28.2 |
| | **Lepidocrocite** | **29.2** | **27.9** | -1.3 | **22.5** | -6.7 | **28.2** | -1.0 | **39.2** | 10.0 |
| **Sample 10** | **Magnetite** | **16.9** | **36.0** | 19.1 | **48.6** | 31.7 | **29.0** | 12.1 | **-1.4** | -18.3 |
| | **Akaganeite** | **41.6** | **28.8** | -12.8 | **22.1** | -19.5 | **28.9** | -12.7 | **33.5** | -8.1 |
| | **Goethite** | **12.3** | **11.5** | -0.8 | **17.8** | 5.5 | **15.5** | 3.2 | **21.1** | 8.8 |
| | **Lepidocrocite** | **29.2** | **23.6** | -5.6 | **11.4** | -17.8 | **26.6** | -2.6 | **46.9** | 17.7 |

For example, analyses carried out in transmittance mode ensured concentration absolute errors below 12.7%. On the other hand, the values obtained by using the DRIFT and ATR configurations, provided amount differences from 0.2 to 19.1% and from 1.2 to 31.7% respectively. Finally, the concentration values obtained

through the use of the portable system in ATR mode showed less reliable results in comparison with the previous cases (errors ranging from 0.1 to 38.2%).

The semi-quantification of raw spectra brought to misleading considerations. For example, sample 10 was mainly constituted by akaganeite but, independently of the FTIR system and the configuration used, the PALME software assigned the role of main phase to magnetite. As magnetite has the less structured spectrum (Figure 7.1) on the whole spectral range, it was deduced that the calculation made use of this spectrum just in order to improve the fit quality without taking into account a specific spectral range/band.

**Spectra treatment**

In order to improve the reliability of the proposed method, the FTIR spectra obtained from both portable and laboratory systems were treated using the Opus 7.2 software (Bruker Optics, Germany).

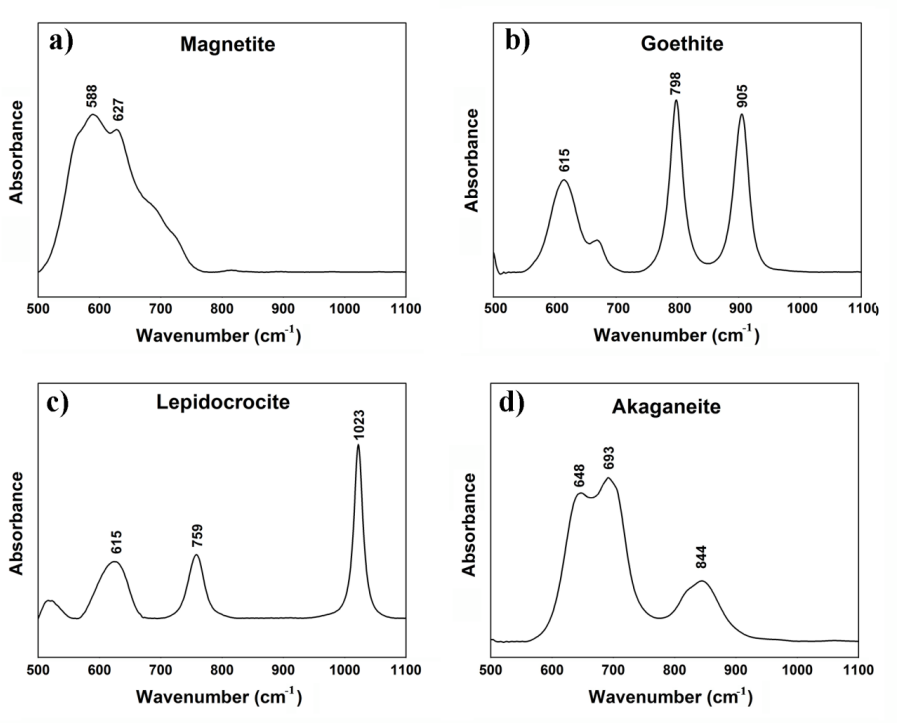


*Figure 7.3: FTIR spectra of iron oxide standards obtained by using the Jasco 6300 system in transmittance mode, spectral range between 500 and 1100 cm$^{-1}$ and baseline corrected.*

As displayed in Figure 7.3, the range of wavelengths between 500 and 1100 cm$^{-1}$ was selected as the spectral fingerprint region, since it includes all the main

characteristic bands of the analyzed iron-based phases and focus on bands specific to each compound. In addition, both pure phases and mixture of standards were subjected to baseline correction. Hereafter, these spectra will be called “treated spectra”.

### Semi-quantification using treated spectra

Once treated, all spectra were re-processed by means of the PALME software. The new semi-quantification results are summarized in Table 7.2.

*Table 7.2: Comparison between weighted and experimental concentration values of standard mixtures obtained with treated spectra. Experimental values were obtained by semi-quantifying treated FTIR spectra using PALME software.*

| Sample | Real composition | | Predicted composition | | | | | | | |
|---|---|---|---|---|---|---|---|---|---|---|
| | | | Laboratory Jasco 6300 ATR | | Laboratory Jasco 6300 DRIFT | | Laboratory Jasco 6300 Transmittance | | Portable Alpha ATR | |
| | Iron compound | % weighted | % exper. | Diff. | % exper. | Diff. | % exper. | Diff. | % exper. | Diff. |
| Sample 1 | Akaganeite | 83.3 | 78.5 | -4.8 | 81.2 | -2.1 | 78.7 | -4.6 | 73.6 | -9.6 |
| | Goethite | 16.7 | 21.5 | 4.8 | 18.8 | 2.1 | 21.3 | 4.6 | 26.4 | 9.6 |
| Sample 2 | Akaganeite | 50.0 | 49.7 | -0.3 | 56.9 | 6.9 | 46.8 | -3.2 | 44.9 | -5.1 |
| | Goethite | 50.0 | 50.3 | 0.3 | 43.1 | -6.9 | 53.2 | 3.2 | 55.1 | 5.1 |
| Sample 3 | Akaganeite | 26.1 | 26.5 | 0.4 | 33.6 | 7.5 | 26.0 | -0.1 | 27.9 | 1.8 |
| | Goethite | 73.9 | 73.5 | -0.4 | 66.4 | -7.5 | 74.0 | 0.1 | 72.1 | -1.8 |
| Sample 4 | Magnetite | 77.3 | 70.0 | -7.3 | 80.9 | 3.6 | 83.6 | 6.3 | 66.4 | -10.9 |
| | Lepidocrocite | 22.7 | 30.0 | 7.3 | 19.1 | -3.6 | 16.4 | -6.3 | 33.6 | 10.9 |
| Sample 5 | Magnetite | 27.3 | 39.4 | 12.1 | 41.0 | 13.7 | 30.6 | 3.3 | 28.3 | 1.0 |
| | Lepidocrocite | 72.7 | 60.6 | -12.1 | 59.0 | -13.7 | 69.4 | -3.3 | 71.7 | -1.0 |
| Sample 6 | Magnetite | 47.1 | 79.9 | 32.8 | 33.8 | -13.3 | 31.0 | -16.1 | 44.6 | -2.5 |
| | Lepidocrocite | 52.9 | 20.1 | -32.8 | 66.2 | 13.3 | 69.0 | 16.1 | 55.4 | 2.5 |
| Sample 7 | Goethite | 17.8 | 19.5 | 1.7 | 23.3 | 5.5 | 19.9 | 2.1 | 21.3 | 3.5 |
| | Lepidocrocite | 46.6 | 41.8 | -4.8 | 40.6 | -6.0 | 46.5 | -0.1 | 49.5 | 2.9 |
| | Magnetite | 35.6 | 38.7 | 3.1 | 36.1 | 0.5 | 33.6 | -2.0 | 29.2 | -6.4 |
| Sample 8 | Goethite | 23.2 | 28.5 | 5.3 | 26.8 | 3.6 | 28.3 | 5.1 | 37.0 | 13.8 |
| | Magnetite | 49.5 | 50.1 | 0.6 | 38.7 | -10.8 | 46.3 | -3.2 | 38.1 | -11.4 |
| | Akaganeite | 27.3 | 21.4 | -5.9 | 34.5 | 7.2 | 25.4 | -1.9 | 24.9 | -2.4 |
| Sample 9 | Magnetite | 31.5 | 41.5 | 10.0 | 43.2 | 11.7 | 32.4 | 0.9 | 30.8 | -0.7 |
| | Akaganeite | 39.3 | 37.8 | -1.5 | 48.4 | 9.1 | 39.1 | -0.2 | 40.3 | 1.0 |
| | Lepidocrocite | 29.2 | 20.7 | -8.5 | 8.4 | -20.8 | 28.5 | -0.7 | 28.9 | -0.3 |
| Sample 10 | Magnetite | 16.9 | 43.0 | 26.1 | 12.1 | -4.8 | 20.2 | 3.3 | 29.3 | 12.4 |
| | Akaganeite | 41.6 | 35.9 | -5.7 | 46.8 | 5.2 | 34.5 | -7.1 | 36.8 | -4.8 |
| | Goethite | 12.3 | 10.8 | -1.5 | 13.9 | 1.6 | 13.8 | 1.5 | 17.4 | 5.1 |
| | Lepidocrocite | 29.2 | 10.3 | -18.9 | 27.2 | -2.0 | 31.4 | 2.2 | 16.5 | -12.7 |

The new semi-quantification values proved that the use of treated spectra helped to remarkably increase the reliability of the proposed method. The comparison between weighted and experimental values obtained by using the Jasco 6300 spectrometer in transmittance mode showed the most reliable results, providing absolute error between 0.1 and 7.1%. The values obtained by using the DRIFT and ATR configuration in contrast, displayed absolute errors ranging from 0.5 to 20.8% and from 0.3 to 32.8% respectively. Finally, the semi-quantification values obtained by using the transportable Alpha spectrophotometer provided concentration absolute errors ranging from 0.3 to 13.8%. The accuracy of the semi-quantification method was assessed by means of the paired t-test. By comparing the experimental data to the weighted concentration values it was proved that the two groups were not statistically different from each other.

After completing the semi-quantification of all treated spectra, a trend line (with the value of all iron corrosion phases) was constructed for each FTIR mode. The linear correlation between both weighed and experimental concentrations allowed to more clearly determine the reliability of the FTIR-PALME method.

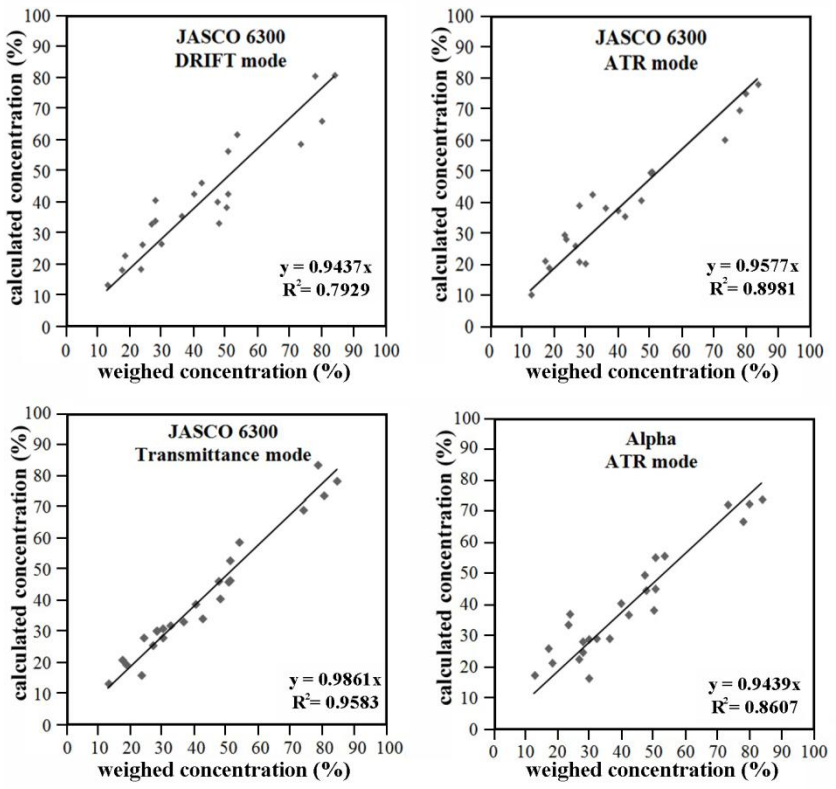


*Figure 7.4: Trend lines, constructed after excluding outliers, between weighed and calculated concentration values (using treated spectra).*

By analyzing the obtained trend lines (Figure 7.4), several important issues can be deduced. First of all, the comparison between FTIR configurations showed that, as expected the most reliable results were ensured by the use of the transmittance mode (y=0.9861x, $R^2$=0.9583), because with this procedure band position and shape are almost not distorted by combination of absorption and reflection phenomena, especially important for solids exhibiting electronic conductivity (for instance magnetite). Besides, the comparison between the ATR trend lines proved that the reliability of the portable FTIR (y=0.9439x, $R^2$=0.8607), after data treating is comparable to that obtained from laboratory system (y=0.9577x $R^2$=0.8981). Further than spectroscopic reasons, the higher spread of the ATR measurements can be related to the significant reduction of the amount of sample measured in ATR mode, which could enhance the detection of the samples heterogeneities (because of resulting in a mixing of powders), therefore, introducing dispersion in the results.

**Stability evaluation of pure standard mixtures**

The content values of pure standards mixtures were used to determine the stability of the reference samples. Considering the results summarized in Figure 7.4, the ratio between stable and reactive phases was calculated by using laboratory and portable FTIR systems in transmittance and ATR modes respectively. The experimental stability values obtained from mixture of pure corrosion standards are summarized in Table 7.3.

*Table 7.3: Comparison between expected and calculated stability values of standard mixtures (from treated FTIR spectra).*

| Stability value | Sample 1 | Sample 2 | Sample 3 | Sample 4 | Sample 5 | Sample 6 | Sample 7 | Sample 8 | Sample 9 | Sample 10 |
|---|---|---|---|---|---|---|---|---|---|---|
| **Expected** | 0.20 | 1.00 | 2.83 | 3.41 | 0.38 | 0.89 | 1.15 | 2.66 | 0.46 | 0.41 |
| **Jasco 6300 (transmittance)-PALME** | 0.27 | 1.14 | 2.85 | 5.10 | 0.44 | 0.45 | 1.15 | 2.94 | 0.48 | 0.52 |
| **Alpha (ATR)-PALME** | 0.36 | 1.23 | 2.58 | 1.98 | 0.39 | 0.81 | 1.02 | 3.02 | 0.44 | 0.88 |

Trend lines were constructed with the purpose of comparing the stability values obtained with FTIR-PALME data with those obtained with expected concentrations values (Figure 7.5).

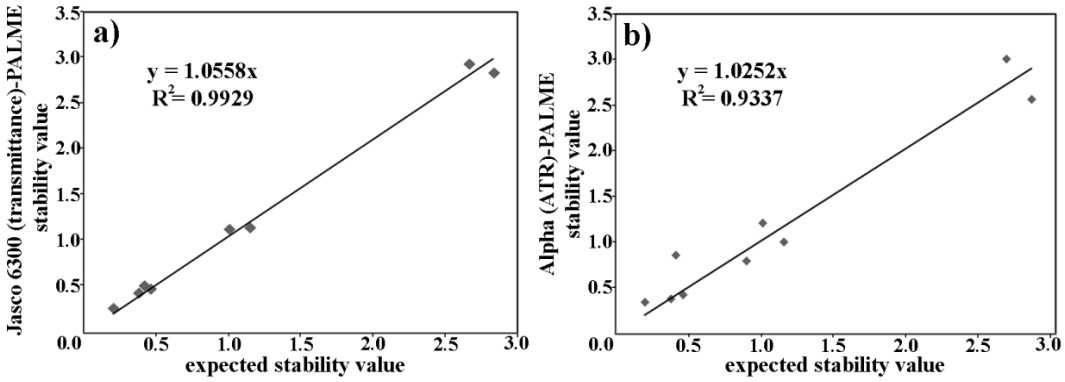


*Figure 7.5: Trend lines constructed in order to compare the stability values obtained from the deconvolution of both Jasco 6300 (a) and Alpha (b) spectra with those obtained with expected concentrations.*

The trend line values, obtained after excluding outliers, were y=1.0558x $R^2$=0.9929 for the laboratory FTIR system used in transmittance mode (Figure 7.5a) and y=1.0252x $R^2$=0.9337 for the portable FTIR system used in ATR mode (Figure 7.5b). Thus, the results clearly demonstrated that real and experimental data fitted well to the linear model.

To assess the accuracy of the stability calculation, the paired t-test was also applied. The results statistically proved that regardless of the analytical configuration used, there were no significant differences between the stability values obtained from real and experimental data.

## 7.4 Application to archaeological samples

### Spectra treatment

After completing the study of standard mixtures as well as the optimization of the proposed semi-quantification method, the analytical work was focused on the study of archaeological rust samples. Raw spectra were collected by using the Jasco 6300 and the Alpha systems in transmittance and ATR mode respectively. Then, all spectra were treated as previously described.

### Semi-quantification using treated spectra

The concentration values obtained with the proposed semi-quantification method were compared with those provided by X-Ray diffractograms. The experimental concentrations of each iron phase detected by XRD were calculated using both

*Xpert HighScore* and *EVA* software. The results, summarized in Table 7.4, clearly demonstrated that the proposed FTIR-PALME method ensured similar semi-quantification results to those obtained by XRD.

It is important to emphasize that, as proved by several works [23,24], the XRD technique has been often used for semi-quantification purposes despite the low reliability of its results (about 10–20 % relative percent error [1]). For this reason, the proposed method can be considered as a viable alternative to those based on the use of XRD analyses to perform the semi-quantification of archaeological iron corrosion systems.

*Table 7.4: Comparison between FTIR and XRD semi-quantification results of archaeological rust samples.*

| **Arq. Sample 1** | Akaganeite | Lepidocrocite | Goethite | Magnetite |
|---|---|---|---|---|
| XRD-*Eva* | 4.0% | 2.0% | 47.0% | 47.0% |
| XRD-*HighScore* | 7.0% | 2.0% | 41.0% | 50.0% |
| Jasco 6300 (trasmittance)-PALME | 4.9% | 3.3% | 42.7% | 49.1% |
| Alpha (ATR)-PALME | 5.9% | 2.1% | 47.2% | 55.2% |
| **Arq. Sample 2** | Akaganeite | Lepidocrocite | Goethite | Magnetite |
| XRD-*Eva* | 24.0% | 2.0% | 55.0% | 19.0% |
| XRD-*HighScore* | 39.0% | 3.0% | 41.0% | 17.0% |
| Jasco 6300 (trasmittance)-PALME | 37.2% | 6.2% | 41.1% | 15.5% |
| Alpha (ATR)-PALME | 35.2% | 5.3% | 46.3% | 13.2% |
| **Arq. Sample 3** | Akaganeite | Lepidocrocite | Goethite | Magnetite |
| XRD-*Eva* | 38.0% | 0.0% | 28.0% | 34.0% |
| XRD-*HighScore* | 53.0% | 0.0% | 18.0% | 29.0% |
| Jasco 6300 (trasmittance)-PALME | 54.8% | 0.0% | 24.1% | 21.1% |
| Alpha (ATR)-PALME | 48.0% | 0.0% | 23.9% | 29.1% |
| **Arq. Sample 4** | Akaganeite | Lepidocrocite | Goethite | Magnetite |
| XRD-*Eva* | 10.0% | 7.0% | 57.0% | 26.0% |
| XRD-*HighScore* | 12.0% | 6.0% | 50.0% | 32.0% |
| Jasco 6300 (trasmittance)-PALME | 8.0% | 11.9% | 54.9% | 25.2% |
| Alpha (ATR)-PALME | 15.,3% | 8.3% | 49.2% | 27.2% |
| **Arq. Sample 5** | Akaganeite | Lepidocrocite | Goethite | Magnetite |
| XRD-*Eva* | 24.0% | 4.0% | 64.% | 8.0% |
| XRD-*HighScore* | 35.0% | 3.0% | 52.0% | 10.0% |
| Jasco 6300 (trasmittance)-PALME | 32.3% | 7.0% | 57.2% | 3.5% |
| Alpha (ATR)-PALME | 25,2% | 5.5% | 52.3% | 17.0% |

**Stability evaluation of archaeological samples**

Considering the excellent results obtained by calculating the stability of pure standards mixtures, the FTIR-PALME method was also applied for the study of real archaeological samples. In order to evaluate the reliability of Jasco 6300 and Alpha results, FTIR-PALME stability values were compared with those calculated from the semi-quantification of X-Ray diffractograms.

As can be observed in Figure 7.6, the stability values provided by the decomposition of Jasco 6300 (transmittance mode) and Alpha (ATR mode) FTIR spectra fitted to those obtained with XRD data. In this sense, the reliability of the semi-quantification method proposed in this chapter was further demonstrated, except for the *Arq. Sample 1.* However, it must be underlined that this sample is characterized by the lower akaganeite and lepidocrocite amounts (and also a higher dispersion of their quantification), on which small variations would induce high stability value variations. When small amounts of reactive or stable compounds are present, that is, small numerator or denominator in the stability index calculation, some slight variations in the quantification will introduce high variations of the calculated index.

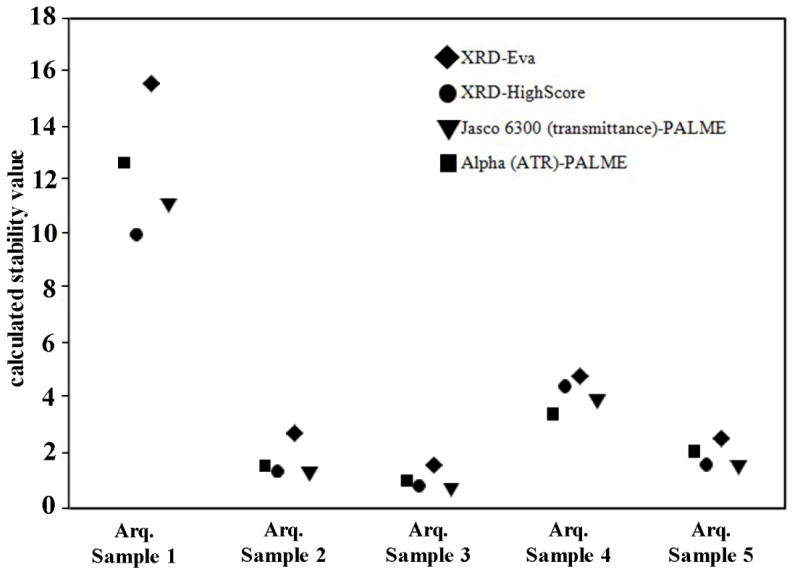


*Figure 7.6: Comparison between the stability values of archaeological samples provided by the use of both XRD and FTIR analytical techniques.*

## 7.5 Conclusions

The analytical results summarized in this chapter present a new analytical method based on the use of FTIR spectroscopy to evaluate the stability of archaeological artefacts corrosion systems.

In the first step, the semi-quantification of standard mixtures spectra collected by means of laboratory system (Jasco 6300) indicated that the most reliable results were provided by the decomposition of transmittance spectra (powder dispersed in a KBr pellet). This experimental work also demonstrated that, by performing spectra treatments (fingerprint region selection and baseline correction), the method accuracy (especially for DRIFT or ATR modes) can be significantly improved.

Afterwards, the results obtained by means of laboratory systems (Transmittance, DRIFT and ATR) were compared to those of the portable Alpha IR spectrometer in ATR mode. As proved by the trend lines showed in Figure 7.4, the results obtained by semi-quantifying treated Alpha spectra were good enough as to enable the application of the proposed protocol also to in-situ analyses.

PALME concentration values obtained by the decomposition of both portable (in ATR mode) and laboratory (in Transmittance mode) spectra were used to calculate the stability index of both standard mixtures and archaeological iron corrosion samples. Concretely, the experimental stability values obtained with PALME were in line with those calculated with XRD data. For this reason, it was proved that FTIR-PALME method represents a viable alternative to those based on X-Ray diffractograms for the iron phases semi-quantification and stability evaluation.

## 7.6 References

**[1]** Ph. Dillman, F. Mazaudier, S. Hoerlé (2004) Advances in understanding atmospheric corrosion of iron. Rust characterization of ancient ferrous artefacts exposed to indoor atmospheric corrosion. *Corrosion Science*, 46, 1401-1429.

**[2]** D. Neff, S. Reguer, L. Bellot-Gurlet, Ph. Dillmann, R. Bertholon (2004) Structural characterization of corrosion products on archaeological iron: an integrated analytical approach to establish corrosion forms. *Journal of Raman Spectroscopy*, 35, 739-745.

**[3]** M. Yamashita, T. Misawa (1998) Recent progress in the study of protective rust-layer formation on weathering steel. *NACE Corrosion Conference, 22-27 March, San Diego (USA),* Nº 357.

**[4]** J. Monnier, L. Bellot-Gurlet, D. Baron, D. Neff, I. Guillot, Ph. Dillmann (2011) A methodology for Raman structural quantification imaging and its application to iron indoor atmospheric corrosion products. *Journal of Raman Spectroscopy*, 42, 773-781.

**[5]** J.H. Giles, D.A. Gilmore, M.B. Denton (1999) Quantitative analysis using Raman spectroscopy without spectral standardization. *Journal of Raman Spectroscopy,* 30, 767-771.

**[6]** F. Dubois, C. Mendibide, T. Pagnier, F. Perrard, C. Duret (2008) Raman mapping of corrosion products formed onto spring steels during salt spray experiments. A correlation between the scale composition and the corrosion resistance. *Corrosion Science*, 50, 3401-3409.

**[7]** J. Aramendia, L. Gómez-Nubla, L. Bellot-Gurlet, K. Castro, C. Paris, Ph. Colomban, J.M. Madariaga (2014) Protective ability index measurement through Raman quantification imaging to diagnose the conservation state of weathering steel structures. *Journal of Raman Spectroscopy,* 45, 1076–1084.

**[8]** I. Arrizabalaga, O. Gómez-Laserna, J.A. Carrero, A. Rodríguez, G. Arana, J.M. Madariaga (2015) Diffuse reflectance FTIR database for the interpretation of the spectra obtained with a handheld device on built heritage materials. *Analytical Methods,* 7, 1061-1070.

**[9]** I.F. Duarte, A. Barros, I. Delgadillo, C. Almeida, A.M. Gil (2002) Application of FTIR Spectroscopy for the Quantification of Sugars in Mango Juice as a Function of Ripening. *Journal of Agricultural and Food Chemistry*, 50, 3104–3111.

**[10]** O. Anjos, M.G. Campos, P.C. Ruiz, P. Antunes (2015) Application of FTIR-ATR spectroscopy to the quantification of sugar in honey. *Food Chemistry,* 169, 218-223.

**[11]** M.A. Legodi, D. De Waal, J.H. Potgieter (2001) Quantitative determination of $CaCO_3$ in cement blends by FT-IR. *Applied Spectroscopy*, 55, 361–365.

**[12]** F.B. Reig, J.V.G. Adelantado, M.C.M.M. Moreno (2002) FTIR quantitative analysis of calcium carbonate (calcite) and silica (quartz) mixtures using the constant ratio method. Application to geological samples. *Talanta,* 58, 811–821.

**[13]** H. Namduri, S. Nasrazadani (2008) Quantitative analysis of iron oxides using Fourier transform infrared spectrophotometry. *Corrosion Science*, 50, 2493–2497.

**[14]** S. Reguer, F. Mirambet, E. Dooryhee, J.L. Hodeau, Ph. Dillmann, P. Lagarde (2009) Structural evidence for the desalination of akaganeite in the preservation of iron archaeological objects, using synchrotron X-Ray powder diffraction and absorption spectroscopy. *Corrosion Science,* 51, 2795-2802.

**[15]** F. Salpin, F. Trivier, S. Lecomte, C. Coupry (2006) A new quantitative method: non-destructive study by Raman spectroscopy of dyes fixed on wool fibres. *Journal of Raman Spectroscopy*, 37, 1403-1410.

**[16]** C. Daher, V. Pimenta, L. Bellot-Gurlet (2014) Towards a non-invasive quantitative analysis of the organic components in museum objects varnishes by vibrational spectroscopies: methodological approach. *Talanta*, 129, 336-345.

**[17]** M. Yamashita, H. Miyuki, Y. Matsuda, H. Nagano, T. Misawa (1994) The long term growth of the protective rust layer formed on weathering steel by atmospheric corrosion during a quarter of a century. *Corrosion Science*, 36, 283-299.

**[18]** I. Arrizabalaga, O. Gómez-Laserna, J. Aramendia, G. Arana, J.M. Madariaga (2014) Determination of the pigments present in a wallpaper of the middle

nineteenth century: The combination of mid-diffuse reflectance and far infrared spectroscopies. S*pectrochimica Acta Part A.* 124, 308-314.

**[19]** I. Arrizabalaga, O. Gómez-Laserna, J. Aramendia, G. Arana, J.M. Madariaga (2014) Applicability of a Diffuse Reflectance Infrared Fourier Transform handheld spectrometer to perform in situ analyses on Cultural Heritage materials. *Spectrochimica Acta Part A*, 129, 259-267.

**[20]** C. Miliani, F. Rosi, B.G. Brunetti, A. Sgamelloti (2010) In situ noninvasive study of artworks: The MOLAB multitechnique approach. *Accounts of Chemical Research*, 43, 728–738.

**[21]** Ph. Colomban (1992) Hydrogen bonding in hydrogen-substituted lithium aluminosilicates. *Journal of Molecular Structure*, 270, 407-416.

**[22]** T.H. Anderson, F.W. Weaver, N.L. Owen (1991) Anomalies in diffuse reflectance infrared spectra of wood and wood polymers. *Journal of Molecular Structure,* 249, 257-275.

**[23]** R. Tisserand, M. Rebetez, M. Grivet, S. Bouffard, A. Benyagoup, F. Levesque, J. Carpena (2004) Comparative amorphization quantification of two apatitic materials irradiated with heavy ions using XRD and RSB results. *Nuclear Instruments and Methods in Physics Research Section A,* 215, 129-136.

**[24]** P. Blanc, O. Legendre, E.C. Gaucher (2007) Estimate of clay minerals amounts from XRD pattern modeling: The Arquant model. *Physics and Chemistry of the Earth*, 32, 135-144.

# CHAPTER 8:

# APPLICATION OF EXPERIMENTAL DESIGN TO OPTIMIZE NaOH-BASED DECHLORINATION TREATMENTS

As previously explained, one of the main problems related to the conservation of iron-based artefacts recovered near the coast line is the formation of corrosion products containing chloride. Among them, the most dangerous one is akaganeite ($FeO_{0.883}(OH)_{1.167}Cl_{0.167}$), an unstable iron phase that accelerates the deterioration process through the formation of highly porous corrosions [1].

Considering that akaganeite is usually generated when iron artefacts rich in chloride come in contact with the atmosphere, conservators must act soon after the recovery of the finding from archaeological endeavours by applying dechlorination treatments.

As described in section 1.4.3, several novel methods have been recently developed for this purpose, such as the immersion in alkaline subcritical fluids [2,3]. In spite of the recognized effectiveness of this method, its use is not very widespread because of its high operational cost. For this reason, the immersion in alkaline baths is still the most used strategy to desalinate archaeological irons.

Used for decades, alkaline baths favour the dissolution of some soluble ions (including $Cl^-$), while inhibit iron leaching [4].

In recent years, the effectiveness of sodium hydroxide baths has been further demonstrated by the analytical work of conservation scientists. For example, the results presented by F. Kergourlay et al. in 2005 [6] showed the benefits provided by the use of this treatment on the conservation of several iron-based ingots that were immersed in seawater during 2000 years. Well-known for being highly effective, NaOH-based solutions are frequently modified by conservators with the purpose of improving their features [5].

For examples, it is believed that sodium sulphite ($Na_2SO_3$) increases the desalination capability of NaOH solutions. For this reason, numerous conservation treatments are nowadays carried out by employing an aqueous mixture of NaOH and $Na_2SO_3$ [7,8]. Besides, L.S. Selwyn et al. introduced in 2005 a new desalination bath based on the synergic use of NaOH and ethylenediamine [9].

In addition to the use of additives, further analytical studies clearly prove that the efficacy of NaOH solutions can be strongly enhanced by increasing their temperature above 50 ºC [10]. In the same way, other studies stated that deoxygenation of alkaline baths helps to limit iron lixiviation during treatment [11].

Even though literature shows many scientific articles focused on evaluating the effects of these desalination methods on archaeometallurgical remains, just a few of them aimed at assessing the real influence entailed by the above mentioned variables on the yield of NaOH-based baths.

Due to this lack of studies, conservators are often forced to choose the method that seems most effective without the scientific support of analytical data.

Recognizing the need of conservators, the experimental work summarized in this chapter consisted in the development of experimental designs that, taking into consideration the variables previously described, have the purpose of optimizing the extractive capability of NaOH desalination treatments.

## 8.1 Akaganeite synthesis

As in the case of the scientific articles referenced above, most of the desalination studies are generally tested on real archaeological objects and rust samples. However, the use of this kind of material is not recommended to carry out experimental designs since the presence of heterogeneities and impurities could lead to unreliable results.

For this reason, the first part of this work consisted in synthesizing pure akaganeite in the laboratory. The use of pure akaganeite provides two advantages. In addition of avoiding variance due to heterogeneity of the sample, it also allows to verify whether the tested treatment could transform akaganeite into more stable phases.

Akaganeite synthesis was performed by following the method proposed by S. Reguer et al. (2009) [12], which consists in heating (at a constant temperature of 70 °C) an aqueous solution of $FeCl_3$ (0.1 M) in a sealed baker during 48 hours.

Afterwards, the precipitated powder was subjected to a thorough washing process (with Milli-Q water) with the purpose of removing free $Cl^-$ ions.

The molecular characterization of the final product was carried out by means of the Analytical Xpert PRO XRD system. From the diffractogram shown in Figure 8.1, two important data were obtained. First of all, the position of all detected peaks coincides with those of the reference pattern, proving the synthesis of pure akaganeite. Moreover, taking into consideration the narrowness of the collected signals, the high crystallinity of the iron-phase was also verified.

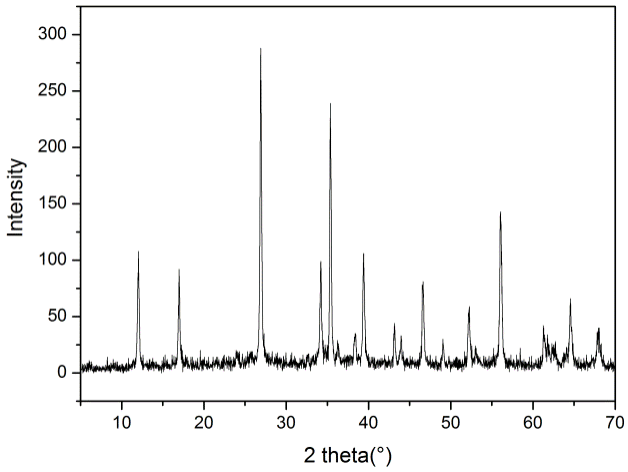


*Figure 8.1: XRD diffractogram collected from synthesized akaganeite.*

## 8.2 Screening experimental design

The synthesized akaganeite was first used to carry out a screening experimental design [13], which had the purpose of: a) identifying the variables having the highest influence in both, $Cl^-$ extraction and Fe leaching inhibition and b) monitoring the possible positive/negative interactions between variables.

Concretely, a full factorial design composed of 5 variables, 2 levels (low and high) and without centre points was proposed. On the basis of the background previously described, NaOH (A), $Na_2SO_3$ (B), ethylenediamine (C), temperature (D) and deoxygenation (E), were the selected variables. The defined low (-1) and high (+1) levels listed in Table 8.1, where chosen according to bibliographic data.

*Table 8.1: Variable and levels used in the full factorial screening design.*

| Variables | | Codified levels | |
|---|---|---|---|
| | | -1 | 1 |
| **A** | NaOH (M) | 0 | 0.5 |
| **B** | $Na_2SO_3$ (M) | 0 | 0.05 |
| **C** | Ethylenediamine (% v/v) | 0 | 5 |
| **D** | Temperature (ºC) | 25 | 70 |
| **E** | Deoxygenation | no | yes |

The experiments composing the $2^5$ factorial design (see Table 8.2) were carried out by treating 0.25 g of pure akaganeite with 50 ml of alkaline solution during 48 hours. The ratio between sample weight and solution volume of 1/200 was established in order to avoid saturation phenomena. With regard to variables C and D, deoxygenation and temperature control were performed through the Ultrasons-H ultrasonic bath and the Heraeus Function Line heating oven respectively (see chapter 4).

The 32 experiments were carried out simultaneously (during the process, the vessels containing the mixture of akaganeite and NaOH solutions were sealed). After 48 hours of treatment, solid and liquid phases were separated by centrifugation. After filtering, washing and dilution process (ratio of 1:10), the $Cl^-$ content of each solution was quantified by ICS 2500 Ion Chromatograph. Besides, the concentration of dissolved iron ($^{56}Fe$ isotope) was analyzed by means of the NexION 300 ICP-MS.

The results reported in Table 8.2 were used to carry out the analysis of effects, which was performed by The Unscambler software (CAMO ASA, Norway).

*Table 8.2: Design matrix and results of the $2^5$ full factorial screening design.*

| Experiments | Codified variables | | | | | Variable responses | |
|---|---|---|---|---|---|---|---|
| | A | B | C | D | E | Cl (mg/L) | Fe (μg/L) |
| **T01** | -1 | -1 | -1 | -1 | 1 | 6037 | 119.1 |
| **T02** | 1 | -1 | -1 | -1 | 1 | 18090 | 13.5 |
| **T03** | -1 | 1 | -1 | -1 | 1 | 17956 | 27.4 |
| **T04** | 1 | 1 | -1 | -1 | 1 | 18338 | 13.9 |
| **T05** | -1 | -1 | 1 | -1 | 1 | 20251 | 2.4 |
| **T06** | 1 | -1 | 1 | -1 | 1 | 19065 | 13.6 |
| **T07** | -1 | 1 | 1 | -1 | 1 | 20752 | 11.7 |
| **T08** | 1 | 1 | 1 | -1 | 1 | 19251 | 18.5 |
| **T09** | -1 | -1 | -1 | 1 | 1 | 7105 | 151.6 |
| **T10** | 1 | -1 | -1 | 1 | 1 | 31573 | 5.9 |
| **T11** | -1 | 1 | -1 | 1 | 1 | 22418 | 26.1 |
| **T12** | 1 | 1 | -1 | 1 | 1 | 32063 | 14.7 |
| **T13** | -1 | -1 | 1 | 1 | 1 | 21237 | 4.1 |
| **T14** | 1 | -1 | 1 | 1 | 1 | 33265 | 7.5 |
| **T15** | -1 | 1 | 1 | 1 | 1 | 23145 | 21.0 |
| **T16** | 1 | 1 | 1 | 1 | 1 | 33435 | 7.9 |
| **T17** | -1 | -1 | -1 | -1 | -1 | 6021 | 254.2 |
| **T18** | 1 | -1 | -1 | -1 | -1 | 35081 | 8.9 |
| **T19** | -1 | 1 | -1 | -1 | -1 | 17554 | 23.8 |
| **T20** | 1 | 1 | -1 | -1 | -1 | 18033 | 21.4 |
| **T21** | -1 | -1 | 1 | -1 | -1 | 20820 | 12.5 |
| **T22** | 1 | -1 | 1 | -1 | -1 | 18998 | 24.4 |
| **T23** | -1 | 1 | 1 | -1 | -1 | 20757 | 18.4 |
| **T24** | 1 | 1 | 1 | -1 | -1 | 18972 | 42.7 |
| **T25** | -1 | -1 | -1 | 1 | -1 | 6826 | 161.8 |
| **T26** | 1 | -1 | -1 | 1 | -1 | 31981 | 14.3 |
| **T27** | -1 | 1 | -1 | 1 | -1 | 22665 | 33.9 |
| **T28** | 1 | 1 | -1 | 1 | -1 | 32626 | 9.5 |
| **T29** | -1 | -1 | 1 | 1 | -1 | 22124 | 14.7 |
| **T30** | 1 | -1 | 1 | 1 | -1 | 34065 | 11.8 |
| **T31** | -1 | 1 | 1 | 1 | -1 | 23310 | 16.1 |
| **T32** | 1 | 1 | 1 | 1 | -1 | 32889 | 18.6 |

In this sense, Table 8.3 describes how the variables and their two-way interactions influence both $Cl^-$ extraction and Fe lixiviation responses (the standard cutoff α=0.05 was set).

*Table 8.3: Codified effects overview. Plus (+) and minus (-) signs describe positives and negatives effects respectively. The significance level of each effect is expressed as a single (weak effect, p-value from 0.05 to 0.01), double (medium effect, p-value from 0.01 to 0.005) or triple (strong effect, p-value ≤ 0.005) sign. Finally, no-significant effects (p-value ≥ 0.05 ) are represented as "ns".*

| Variables | Cl (mg/L) | Fe (µg/L) |
|---|---|---|
| **NaOH (A)** | +++ | -- |
| **$Na_2SO_3$ (B)** | + | -- |
| **Ethylenediamine (C )** | + | -- |
| **Temperature (D)** | +++ | ns |
| **Deoxygenation (E)** | ns | ns |
| **AB** | -- | ++ |
| **AC** | -- | ++ |
| **AD** | ++ | ns |
| **AE** | ns | ns |
| **BC** | ns | ++ |
| **BD** | ns | ns |
| **BE** | ns | ns |
| **CD** | ns | ns |
| **CE** | ns | ns |
| **DE** | ns | ns |

Starting from $Cl^-$ extraction data, important inferences were deduced from p-value determination. Indeed, statistical results of single variables effects proved that NaOH and temperature have significant positive main effect on the yield of $Cl^-$ extraction (p-value of 0.0001 and 0.0005 respectively). Ethylenediamine also has a positive influence on this variable response (p-value=0.0135) while $Na_2SO_3$ and deoxygenation show low (p-value=0.0475) and no significant (p-value=0.3065) influence, respectively.

Regarding the synergic effects of variables, analysis of variance proved that the two-way interaction of NaOH with $Na_2SO_3$ (A-B p-value=0.0475) and ethylenediamine (A-C p-value=0.0135) have a negative influence on $Cl^-$ extraction.

On the contrary, NaOH and temperature show a positive synergic effect (A-D p-value=0.0036).

Analysis of variance provided the β-coefficients of main effects and 2-way and 3-way interactions of the selected variables. The determined β-values were therefore employed to write the regression equation of $Cl^-$ response:

R [$Cl^-$] = 2208 + 464.8A + 130.1B + 181.2C + 358.6D – 240.8AB - 237.6AC + 249.6AD (mg/L)

The obtained model presents a square correlation coefficient ($R^2$) of 0.976, which indicates that the 97.6% of the extraction variability is explained by the model.

Switching to the interpretation of Fe lixiviation results, the single variables NaOH (p-value=0.0022), $Na_2SO_3$ (p-value=0.0083) and ethylenediamine (p-value=0.0022) negatively affect the concentration of Fe in the solutions, which suggests their active role in the inhibition of lixiviation process. On the contrary, the synergic effect of A-B (p-value=0.0037), A-C (p-value=0.0012) and C-D (p-value=0.0028) variables increase iron lixiviation. Table 8.3 shows the null influence of temperature and deoxigenation on the iron leaching.

As showed below, the β-coefficients determined by ANOVA were employed to write the regression equation of Fe response:

R [Fe] = 35.18 – 20.37A – 15.46B -20.44C +19.01AB + 23.87AC +20.09BC (µg/L)

The square correlation coefficient ($R^2$=0.984) corroborated from a statistical point of view the validity of the obtained model.

## 8.3 Optimization experimental design

Afterwards, a second experimental design was carried out with the purpose of optimizing the $Cl^-$ extraction feature of the alkaline desalination bath.

According to the results obtained from the screening design, NaOH and temperature parameters were selected for their remarkable positive effect on the $Cl^-$ variable response.

Regarding to $Na_2SO_3$ (B) and ethylenediamine (C) variables, the $Cl^-$ regression equation displayed above clearly shows that their single variable influence have a weak positive effect on chloride extraction ($\beta_b$ = +130.1 and $\beta_c$ = +181.2). However, their synergic effect with NaOH (A) ($\beta_{AB}$ = -240.8 and $\beta_{AC}$ = -237.6) produces a

considerable negative effect. From those results, it was deduced that B and C variables has a positive influence only when their concentration in the solution is low (below 0.0025M of $Na_2SO_3$ and 2.5 % v/v of ethilendiamine). As the use of inappropriate concentrations of the two compounds may trigger remarkable side effects on the extractive capacity of bath solutions, it was decided to exclude them from the optimization design.

Similarly, deoxygenation was also excluded, since analysis of variance proved that has no significance effect on either of the two responses under study.

In addition to NaOH and temperature, the variable of time was now included in the optimization experimental design. This parameter was not considered in the screening study since several research works already proved its determinant influence in the process of desalination [14].

The three selected parameters were used to develop a central composite design (CCD). As explained by F. Torrades et al. (2011) [15], this methodology analyses each variable at 5 different levels. The low, centre and high levels of each variable are designated as −1, 0 and + 1, respectively, while -1.68 and +1.68 codified levels have the purpose of predicting the response functions outside the cubic domain. According to this, Table 8.4 shows the levels of the factors studied in the CCD.

*Table 8.4: Factors and levels used in the central composite optimization design.*

| **Factors** | | **Codified levels** | | | | |
|---|---|---|---|---|---|---|
| | | -1.68 | -1 | 0 | +1 | +1.68 |
| **A** | **NaOH (M)** | 0.01 | 0.2 | 0.5 | 0.8 | 1 |
| **B** | **Temperature (ºC)** | 26 | 40 | 60 | 80 | 94 |
| **C** | **Time (h)** | 6 | 30 | 65 | 100 | 124 |

As shown in Table 8.5, 6 centre point experiments were performed with the purpose of evaluating the repetitiveness of desalination baths. Considering that each operation was carried out in triplicates, the centre composite design matrix was finally composed of 48 experiments.

As in the case of the screening design, the optimization work was carried out by treating 0.25 g of pure akaganeite with 50 ml of alkaline solution. After treatment, solid and liquid phases were separated by centrifugation, washed and diluted

(ratio of 1:10). The amount of extracted $Cl^-$ and lixiviated Fe by each solution was then quantified by IC and ICP-MS systems respectively (see Table 8.5).

Surprisingly, several treated samples showed a chromatic variation. Taking into account that this phenomenon is linked to the formation of new iron-phases [16], the PALME-FTIR method presented in chapter 7 was employed with the purpose of carrying out a molecular semi-quantification of all solid samples. In order to ensure reliable results, treated samples were analyzed through the Jasco 6300 FTIR spectrometer working in transmittance mode (see chapter 4).

As it can be clearly deduced from the results shown in Table 8.5, most of akaganeite samples were partially transformed into goethite after treatment. Since the chemical formula akaganeite differs from that of goethite for the only presence of chloride, it was proved that several alkaline baths were able to remove chlorides from the crystalline structure of the original compound, triggering its transformation.

In addition, FTIR-PALME results verified that experiments carried out at high temperatures involve a partial transformation of treated samples into hematite. This phenomenon is consistent with numerous analytical studies proving that the transformation of oxyhydroxides into hematite can be thermally induced [17,18].

Considering that the transformation of akaganeite into more stable phases is of paramount importance for the purpose of ensuring the optimal preservation of archaeological artefacts, the CCD was also used to identify the optimal conditions to obtain the highest concentration of hematite and goethite.

*Table 8.5: Design matrix and results of the central composite optimization design.*

| Experiments | Codified factors | | | Factor responses | | | | |
|---|---|---|---|---|---|---|---|---|
| | A | B | C | Cl (mg/L) | Fe (μg/L) | Hematite % (w/w) | Goethite % (w/w) | Akaganeite % (w/w) |
| **T01** | -1.68 | 0 | 0 | 40953 | 149.7 | 0 | 3 | 97 |
| **T02** | -1.68 | 0 | 0 | 39892 | 92.0 | 0 | 2.9 | 96.1 |
| **T03** | -1.68 | 0 | 0 | 39545 | 140.1 | 0 | 2.7 | 97.3 |
| **T04** | 1.68 | 0 | 0 | 39544 | 9.5 | 0 | 98.5 | 1.5 |
| **T05** | 1.68 | 0 | 0 | 63756 | 6.2 | 0 | 99.4 | 0.6 |
| **T06** | 1.68 | 0 | 0 | 65474 | 5.0 | 0 | 98.7 | 1.3 |
| **T07** | 0 | -1.68 | 0 | 38709 | 63.0 | 0 | 3.3 | 96.7 |
| **T08** | 0 | -1.68 | 0 | 38966 | 103.0 | 0 | 3.6 | 96.4 |
| **T09** | 0 | -1.68 | 0 | 39615 | 59.1 | 0 | 2.9 | 97.1 |
| **T10** | 0 | 1.68 | 0 | 46537 | 41.8 | 3.2 | 96.8 | 0 |
| **T11** | 0 | 1.68 | 0 | 51511 | 75.4 | 3,1 | 96.9 | 0 |
| **T12** | 0 | 1.68 | 0 | 59335 | 75.3 | 2,5 | 97.5 | 0 |
| **T13** | 0 | 0 | -1.68 | 49472 | 38.0 | 0 | 34.3 | 65.7 |
| **T14** | 0 | 0 | -1.68 | 50070 | 25.9 | 0 | 34.3 | 65.7 |
| **T15** | 0 | 0 | -1.68 | 51993 | 33.0 | 0 | 34.2 | 65.8 |
| **T16** | 0 | 0 | 1.68 | 61783 | 9.7 | 0 | 100 | 0 |
| **T17** | 0 | 0 | 1.68 | 63693 | 5.7 | 0 | 100 | 0 |
| **T18** | 0 | 0 | 1.68 | 62442 | 6.3 | 0 | 98.9 | 1.1 |
| **T19** | -1 | -1 | -1 | 40425 | 92.0 | 0 | 12.2 | 87.8 |
| **T20** | -1 | -1 | -1 | 40047 | 58.2 | 0 | 5.2 | 94.8 |
| **T21** | -1 | -1 | -1 | 39257 | 88.9 | 0 | 12.9 | 87.1 |
| **T22** | 1 | -1 | -1 | 45667 | 15.3 | 0 | 40.5 | 59.5 |
| **T23** | 1 | -1 | -1 | 45624 | 12.8 | 0 | 36.5 | 63.5 |
| **T24** | 1 | -1 | -1 | 46289 | 12.7 | 0 | 39.3 | 60.7 |
| **T25** | -1 | 1 | -1 | 40832 | 116.4 | 0.7 | 1.3 | 97.8 |
| **T26** | -1 | 1 | -1 | 42249 | 106.9 | 0.6 | 0.5 | 98.9 |
| **T27** | -1 | 1 | -1 | 42240 | 101.3 | 0.6 | 0.6 | 98.8 |
| **T28** | 1 | 1 | -1 | 45860 | 60.6 | 26 | 34.6 | 39.4 |
| **T29** | 1 | 1 | -1 | 44403 | 68.0 | 25.3 | 33.8 | 40.9 |
| **T30** | 1 | 1 | -1 | 47244 | 57.0 | 57.3 | 40.6 | 2.1 |
| **T31** | -1 | -1 | 1 | 39475 | 130.4 | 0 | 3.5 | 96.5 |
| **T32** | -1 | -1 | 1 | 39885 | 121.7 | 0 | 2.6 | 97.4 |
| **T33** | -1 | -1 | 1 | 39231 | 63.7 | 0 | 4 | 96 |
| **T34** | 1 | -1 | 1 | 53389 | 23.1 | 0 | 77.7 | 22.3 |
| **T35** | 1 | -1 | 1 | 54803 | 21.1 | 0 | 77.5 | 22.5 |
| **T36** | 1 | -1 | 1 | 53075 | 26.9 | 0 | 76.5 | 23.5 |
| **T37** | -1 | 1 | 1 | 41434 | 160.3 | 0.6 | 0 | 99.4 |
| **T38** | -1 | 1 | 1 | 41230 | 88.0 | 0.9 | 0.5 | 98.6 |
| **T39** | -1 | 1 | 1 | 41988 | 122.5 | 0.5 | 0.8 | 98.7 |
| **T40** | 1 | 1 | 1 | 63599 | 79.9 | 1.2 | 97.9 | 0.9 |
| **T41** | 1 | 1 | 1 | 63716 | 76.7 | 1.1 | 97.3 | 1.6 |
| **T42** | 1 | 1 | 1 | 65429 | 80.5 | 0.5 | 99.5 | 0 |
| **T43** | 0 | 0 | 0 | 67834 | 13.0 | 0 | 97.4 | 2.6 |
| **T44** | 0 | 0 | 0 | 63963 | 14.5 | 0 | 99.4 | 0.6 |
| **T45** | 0 | 0 | 0 | 64068 | 15.2. | 0 | 98.3 | 1.7 |
| **T46** | 0 | 0 | 0 | 65745 | 5.0 | 0 | 97.7 | 2.3 |
| **T47** | 0 | 0 | 0 | 67324 | 19.3 | 0 | 98.7 | 1.3 |
| **T48** | 0 | 0 | 0 | 63801 | 6.5 | 0 | 98 | 2 |

The Unscambler software was employed for data interpretation. Analysis of variance (ANOVA) was first performed with the aim of corroborating, from a statistical point of view, the validity of the obtained results.

The square correlation coefficients of $Cl^-$ ($R^2$=0.967), Fe ($R^2$=0.837), goethite ($R^2$=0.994) and akaganeite ($R^2$=0.967) responses indicate that most of the variance was explained by the model. In the case of hematite, the R-square value was 0.720.

Afterwards, the response surface was employed to identify the settings of the input factors ensuring the most advantageous responses [13]. Considering the non-linear relationship between input factors and responses, plot results were calculated by using a full quadratic model that considers all interactions and square effects [19]. The obtained response surfaces are displayed in Figure 8.2.

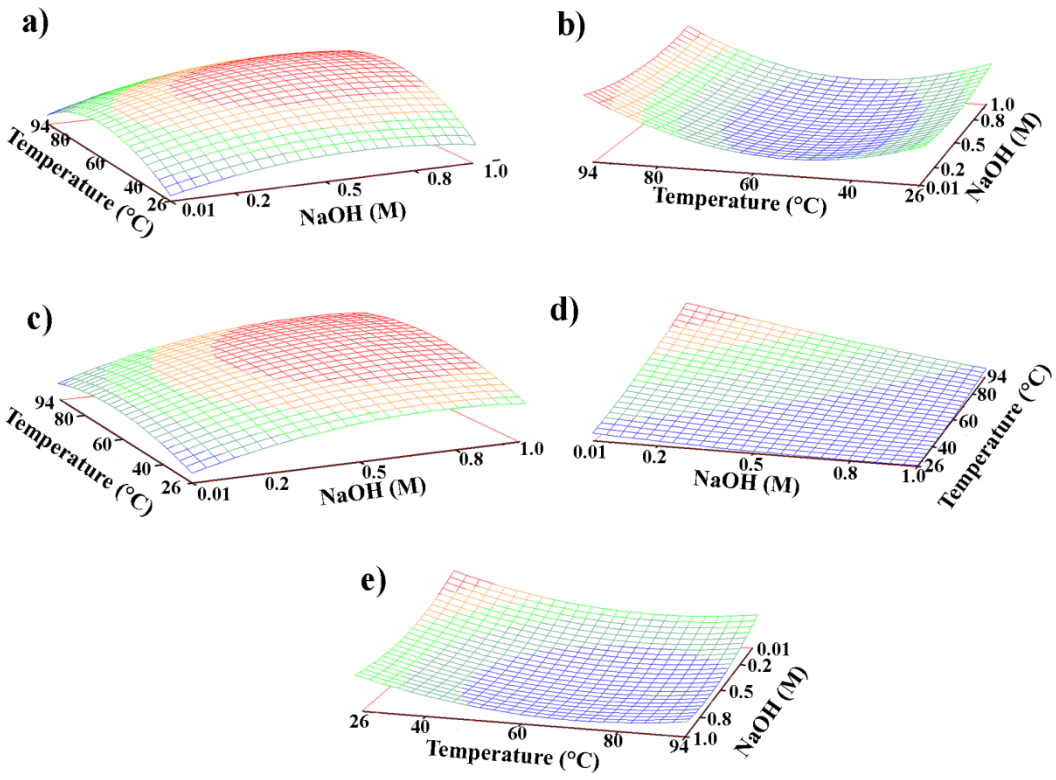


*Figure 8.2: Response surfaces for a) maximum $Cl^-$ extraction (t = 85.0 h); b) minimum Fe lixiviation (t = 89.6 h); c) maximum goethite content (t = 99.4 h); d) maximum hematite content (t = 124.0 h); e) minimum akaganeite content (t = 99.4 h).*

Thanks to response surfaces the optimal temperature, NaOH molarity and time values were determined for each considered response (see Table 8.6).

*Table 8.6: Optimal variables conditions obtained by using the surface response.*

| Variables | Cl max | Fe min | Goethite max | Hematite max | Akaganeite min |
|---|---|---|---|---|---|
| **Time (h)** | 85.0 | 89.6 | 99.4 | 124.0 | 99.4 |
| **NaOH (M)** | 0.71 | 0.42 | 0.79 | 0.01 | 0.67 |
| **Temperature (ºC)** | 65.7 | 57.2 | 68.5 | 94.0 | 74.1 |

The results summarized in the Table 8.6 emphasize that the optimal condition of NaOH molarity and temperature enhancing $Cl^-$ extraction are very similar to those enabling the transformation of akaganeite into goethite. Thus, to perform desalination treatment by using a 0.7 molar solution of NaOH at the temperature between 65 and 75 ºC is strongly suggested.

Furthermore, the collected data are concordant with past studies, indicating that the variable of time has a strong influence on the desalination efficacy. Based on the obtained results, it was deduced that the optimal time to maximize the extraction of chlorides and the transformation (into goethite) of powdered akaganeite samples is in the range between 85 and 100 hours.

On the other side, the response surface displayed in Figure 8.2d clearly proves that the minimum NaOH molarity and maximum temperature values are required for the purpose of enhancing the transformation of akaganeite into hematite. However, such treatment is not suggested for the conservation of archaeometallurgical artefacts since low molarity values do not guarantee iron passivation. Indeed, the response surface showed on Figure 8.2b clearly proves that the highest lixiviation of Fe occurs when desalination baths are performed using a 0.01 molar solution of NaOH at the temperature of 94 ºC.

## 8.4 Conclusions

The analytical research summarized in this chapter represents a clear example of the benefits provided by the work of conservation scientists for the preservation of *Cultural Heritage* materials. Indeed, thanks to the experimental work carried out in the laboratory, it was possible to partially fill the lack of knowledge regarding the influence of several parameters on the yield of NaOH-based desalination treatments.

For example, the results obtained through the screening design proved that, even though several conservation works are carried out by mixing NaOH with ethylenediamine or $Na_2SO_3$, their synergic effect has a negative influence on the

Cl-extraction feature of the bath if their concentration in the solution is too high. On the contrary, it was proved that the efficiency of alkaline baths can be enhanced by increasing the temperature of the treatment.

Once the main variables were identified, an optimization design was performed with the aim of determining the optimal values of temperature, NaOH molarity and time. The response surfaces displayed in Figure 8.2 clearly show that, by applying a 0.7 molar NaOH solution at a temperature between 65 and 75 ºC, it was possible to optimize chlorides solubilisation and to trigger the transformation of powdered akaganeite into a more stable iron-phase (goethite) with treatments of around 96 hours (4 days).

Taking into account that archaeometallurgical artefacts are often treated at room temperature by means of NaOH solutions with a molarity between 0.1 and 0.5, the data hereby presented will help conservators to increase the yield of desalination treatments.

With regards to the variable of time, it must be considered that the obtained optimal conditions are referred to the treatment of powdered synthetic samples. However, in the case of real archaeological artefacts a great amount of variables, such as size and shape of the finding, porosity of the corrosion system, presence of cracks and fractures, influence the time needed to perform an effective desalination. In fact, as explained by L.M.E. Näsänen et al. (2004) [2], an average of 150 days is generally required for NaOH treatments performed at room temperature. Nevertheless, the results obtained in this chapter could simplified the work of conservators by reducing the time required for artefacts desalination.

Under this requirement, further laboratory experiments will be performed (by using naturally aged iron-nails) with the objective of optimizing the penetration feature of NaOH solutions. This aspect will be deepened in the integrated conclusion chapter.

## 8.5 References

**[1]** K.E. García, C.A. Barrero, A.L. Morales, J.M. Greneche (2009) Magnetic structure of synthetic akaganèite: A review of Mossbauer data. *Revista Facultad de Ingeniería, Universidad de Antioquia*, 49, 185-191.

**[2]** L.M.E. Näsänen, N.G. González-Pereyra, S.A. Cretté, P. De Viviés (2013) The applicability of subcritical fluids to the conservation of actively corroding iron artifacts of cultural significance. *The Journal of Supercritical Fluids*, 79, 289-298.

**[3]** M. Bayle, P. De Viviés, J.B. Memet, E. Foy, Ph. Dillmann, D. Neff (2016) Corrosion product transformations in alkaline baths under pressure and high temperature: The sub-critical stabilisation of marine iron artefacts stored under atmospheric conditions. *Materials and Corrosion*, 67, 190-199.

**[4]** C. Degrigny, L. Spiteri (2004) Electrochemical monitoring of marine iron artefacts during their storage/stabilisation in alkaline solutions. *Proceedings of Metal 2004 National Museum of Australia Canberra ACT, Camberra (Australia).*

**[5]** F. Kergourlay, E. Guilminot, D. Neff, C. Remazeilles, S. Reguer, P. Refait, F. Mirambet, E. Foy, Ph. Dillmann (2010) Influence of corrosion products nature on dechlorination treatment: case of wrought iron archaeological ingots stored 2 years in air before NaOH treatment. *Corrosion Engineering, Science and Technology*, 45, 407-413.

**[6]** F. Kergourlay, C. Remazeilles, D. Neff, E. Foy, E. Conforto, E. Guilminot, S. Reguer, Ph. Dillmann, F. Nicot, F. Mielcarek, J. Rebière, Ph. Refait (2011) Mechanisms of the dechlorination of iron archaeological artefacts extracted from seawater. *Corrosion Science*, 53, 2474-2483.

**[7]** A. Doménech-Carbó, M. Lastras, F. Rodríguez, E. Cano, J. Piquero-Cilla, L. Osete-Cortina (2014) Monitoring stabilizing procedures of archaeological iron using electrochemical impedance spectroscopy. *Journal of Solid State Electrochemistry*, 18, 399-409.

**[8]** E. Guilminot, D. Neff, C. Remazeilles, S. Reguer, F. Kergourlay, C. Pele, Ph. Dillmann, P. Refait, F. Nicot, F. Mielcarek, N. Huet, J. Rebière (2012) Influence of crucial parameters on the dechlorination treatments of ferrous objects from seawater. *Studies in Conservation*, 57, 227-236.

**[9]** L.S. Selwyn, V. Argyropoulos (2005) Removal of chloride and iron ions from archaeological wrought iron with sodium hydroxide and ethylendiamine solutions. *Studies in Conservation*, 50, 81-100.

**[10]** N.A. North, C. Pearson (1975) Alkaline sulphite reduction treatment of marine iron. *ICOM Committee for Conservation, 4th Triennial Meeting Venice, International* Council of Museums, pp 1-14.

**[11]** K. Stahl, K. Nielsen, J. Jiang, B. Lebech, J.C. Hansond, P. Norby, J. van Lanschote (2003) On the akaganeite crystal structure, phase transformations and possible role in post-excavational corrosion of iron artifacts. *Corrosion Science,* 45, 2563-2575.

**[12]** S. Reguer, F. Mirambet, E. Dooryhee, J.L. Hodeau, Ph. Dillmann, P. Lagarde (2009) Structural evidence for the desalination of akaganeite in the preservation of iron archaeological objects, using synchrotron X-ray powder diffraction and absorption spectroscopy. *Corrosion Science*, 51, 2795-2802.

**[13]** M. Preu, D. Guyot, M. Petz (1998) Development of a gas chromatography–mass spectrometry method for the analysis of aminoglycoside antibiotics using experimental design for the optimisation of the derivatisation reactions. *Journal of Chromatography A*, 818, 95-108.

**[14]** Ph. Dillmann, D. Watkinson, E. Angelini, A. Adriaens (2013) Corrosion and conservation of cultural heritage metallic artefacts. *Elsevier, Amsterdam (Netherlands),* pp 640.

**[15]** F. Torrades, S. Saiz, J.A. García-Hortal (2011) Using central composite experimental design to optimize the degradation of black liquor by Fenton reagent. *Desalination,* 268, 97-102.

**[16]** R.A. Antunes, I. Costa, D.L. Araújo de Faira (2013) Characterization of corrosion products formed on steels in the first months of atmospheric exposure. *Materials Research*, 6, 403-408.

**[17]** R.M. Cornell, R. Giovanoli (1990) Transformation of Akaganeite into Goethite and Hematite in Alkaline Media. *Clays and Clay Minerals*, 28, 469-476.

**[18]** B. Lu, H. Guo, P. Li, H. Liu, Y. Wei, D. Hou (2011) Comparison study on transformation of iron oxyhydroxides: Based on theoretical and experimental data. *Journal of Solid State Chemistry*, 184, 2139-2144.

**[19]** M.Y. Noordin, V.C. Venkatesh, S. Sharif, S. Elting, A. Abdullah (2004) Application of response surface methodology in describing the performance of coated carbide tools when turning AISI 1045 steel. *Journal of Materials Processing Technology*, 145, 46-58.

# CHAPTER 9:

# DISCOVERING PAST CONSERVATION MATERIALS AND THEIR INFLUENCE ON MURAL DEGRADATION

## Mural paintings from Gaceo

As explained previously, part of this PhD thesis was focused on the study of three different set of mural paintings. This chapter describes the results obtained from the multianalytical characterization of the paintings conserved in the church of San Martín the Tours (Gaceo, Spain).

As summarized in section 3.2.1, these murals were subjected to several conservation treatments that involved the execution of an extensive repainting.

For this reason, the first purpose of the analytical research was to carry out an overall chemical assessment of the paintings, aimed at determining: a) the materials employed for the elaboration of the original artwork and b) the number and nature of the over paintings from the successive interventions and conservation works carried out in the past.

## 9.1 In-situ analyses

As in the case of archaeological artefacts, portable and hand-held Raman spectroscopy systems have demonstrated a high versatility and adaptability in the study of painting materials [1–4]. However, it must be underlined that the study of the chemical composition of pigments and mortars is usually very complex, and their characterization is a challenging task. That is the reason why, in many research works, Raman analyses have been often complemented by the use of other portable analytical systems, such as FTIR and ED-XRF (see section 4.2) [5-7].

**Characterization of mortars**

The in-situ analysis of mortars and preparation layers was carried out in those areas where the loss of the paint layer exposed the underlying support to the open air. According to the results obtained by means of Raman and FTIR techniques, two different types of mortars were identified. As shown in Figure 9.1, a mortar made of calcite ($CaCO_3$, Raman bands at 157, 281, 710 and 1085 $cm^{-1}$) and gypsum ($CaSO_4 \cdot 2H_2O$, Raman bands at 414, 492, 620, 670, 1008 and 1135 $cm^{-1}$) was identified. This mortar presented the common composition found in other mural paintings in the Basque Country [8-10].

However, it was surprising to find lead white $2(PbCO_3) \cdot Pb(OH)_2$ (Raman bands at 106 and 1054 $cm^{-1}$, Figure 9.1) together with calcite and gypsum. The presence of lead white is, in principle, unusual because it is supposed to be unsuitable for mural paintings [11]. Nevertheless, there are evidences of its abundant use in this artwork. In fact, a detailed in-situ screening analysis was done by portable ED-XRF to check if lead was present in the whole surface of the artwork. According to this analysis, the distribution of lead white was not homogeneous all over the mural painting because there was a lack of lead in some areas whereas it was present in other ones. This fact, as will be discussed later, suggested the presence of two types of mortars.

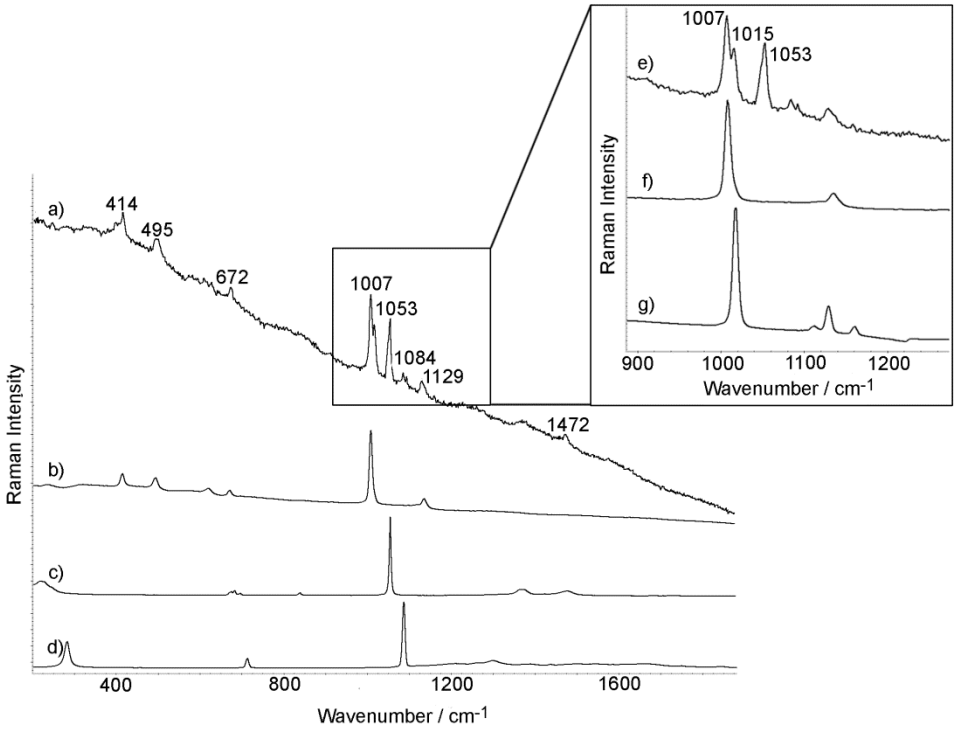


*Figure 9.1: a) Raman spectrum of the mortar; b) gypsum standard; c) lead white standard; d) calcite standard; e) detailed area of the spectrum; f) gypsum standard; g) anhydrite standard.*

Additionally, in the Raman spectra obtained from the mortars, traces of black carbon (Raman bands at 1290 and 1580 $cm^{-1}$) were detected. Its presence may be explained due to the natural presence of carbon in the stone from which calcite was extracted [12]. In the regions of Álava and Navarra there are numerous mural paintings composed of a grey mortar. The presence of quartz ($SiO_2$, characteristic Raman band at 464 $cm^{-1}$) was also detected in most of the Raman spectra, suggesting the presence of an aggregate predominantly composed of siliceous sand.

**Characterization of the original pigment layer**

Concerning the characterization of pigments, in-situ analyses led to the identification of several compounds belonging to different epochs.

With regard to the analyses of red areas, a great variety of pigments was found. Red lead ($Pb_3O_4$, Raman bands at 120, 148, 223, 312, 390 and 550 $cm^{-1}$) appeared to be prevalent, and its presence was confirmed by both molecular and elemental analyses. Known since antiquity, it could belong to the original painting, though its

characteristics make it generally unsuitable for *fresco* paintings [13]. Vermilion (HgS, Raman bands at 251, 283 and 342 $cm^{-1}$) was also identified in many analyzed points of the artwork. In several cases, Raman spectra showed the presence of both pigments. In addition, all the characteristic Raman bands of hematite ($Fe_2O_3$, Raman bands at 226, 246, 293, 410, 498 and 612 $cm^{-1}$) were clearly observed in several molecular spectra.

Raman analyses carried out in yellow areas showed the presence of goethite (α-FeO(OH), Raman bands at 206, 245, 300, 392 and 551 $cm^{-1}$), while the original blue pigment could be identified as azurite ($2CuCO_3{\cdot}Cu(OH)_2$, Raman bands at 247, 279, 329, 399, 763, 837, 932, 1095, 1418, 1577 and 1622 $cm^{-1}$). Known since ancient times, azurite has been used for mural paintings during centuries [14].

According to the obtained results, black carbon was used for the elaboration of black shades, recognizable due to its two broad Raman bands located around 1300 and 1600 $cm^{-1}$.

**Determination of past restoration works**

In-situ analyses also enabled the identification of the pigments used during the most recent restoration works ($20^{th}$-$21^{st}$ century). For example, the synthetic pigment arylamide yellow ($C_{17}N_3O_3H_8$, Raman bands at 383, 459, 509, 595, 623, 785, 824, 959, 999, 1137, 1191, 1252, 1313, 1335, 1385, 1450, 1470, 1534, 1569, 1607 and 1668 $cm^{-1}$, Figure 9.2a) was found in some yellow areas, as well as phthalocyanine green, ($C_{32}H_3Cl_{13}CuN_8$, Raman bands at 688, 740, 744, 815, 977, 1079, 1208, 1278, 1334 and 1534 $cm^{-1}$, Figure 9.2b) and phthalocyanine blue ($C_{32}H_{16}N_8Cu$, Raman bands at 236, 257, 483, 594, 680, 747, 779, 832, 953, 1007, 1108, 1143, 1193, 1307, 1340, 1450 and 1527 $cm^{-1}$) in some greenish and bluish areas, respectively.

In the same way, a modern synthetic red pigment was found in some spectra. The obtained results showed a Raman spectrum (Figure 9.2c) with very intense bands at 243, 344, 427, 526, 570, 614, 679, 725, 743, 812, 968, 1060, 1107, 1159, 1227, 1278, 1355, 1388, 1457, 1480, 1551 and 1577 $cm^{-1}$ that, according to literature [15], fit with those of the naphtol red pigment ($C_{24}H_{16}Cl_3N_3O_2$, also known as arylamide red ).

Besides, mixtures of chrome yellow ($PbCrO_4$, Raman bands at 369, 376 and 840 $cm^{-1}$, first synthesized at the beginning of the $19^{th}$ century) and chrome orange

($PbCrO_4$·PbO, main Raman band at 824 $cm^{-1}$) were found in several yellowish areas. On the basis of the relative intensities of their main Raman bands, both pigments were present in different proportions. Chrome yellow/orange were also found mixed together with Prussian blue (Figure 9.2d). This mixture could be the one known as chrome green, a 19th century synthetic mixture that sometimes presented the addition of barium white as extender [11]. However, the presence of barium white was not detected. Prussian blue ($Fe_4[Fe(CN)_6]_3$, Raman bands at 274, 364, 533, 590, 948, 1014, 2092 and 2153 $cm^{-1}$) was also found alone in several blue areas. Thus, it is possible to state that, during the 19th century, some repainting or restoration works were probably carried out. This issue is discussed below.

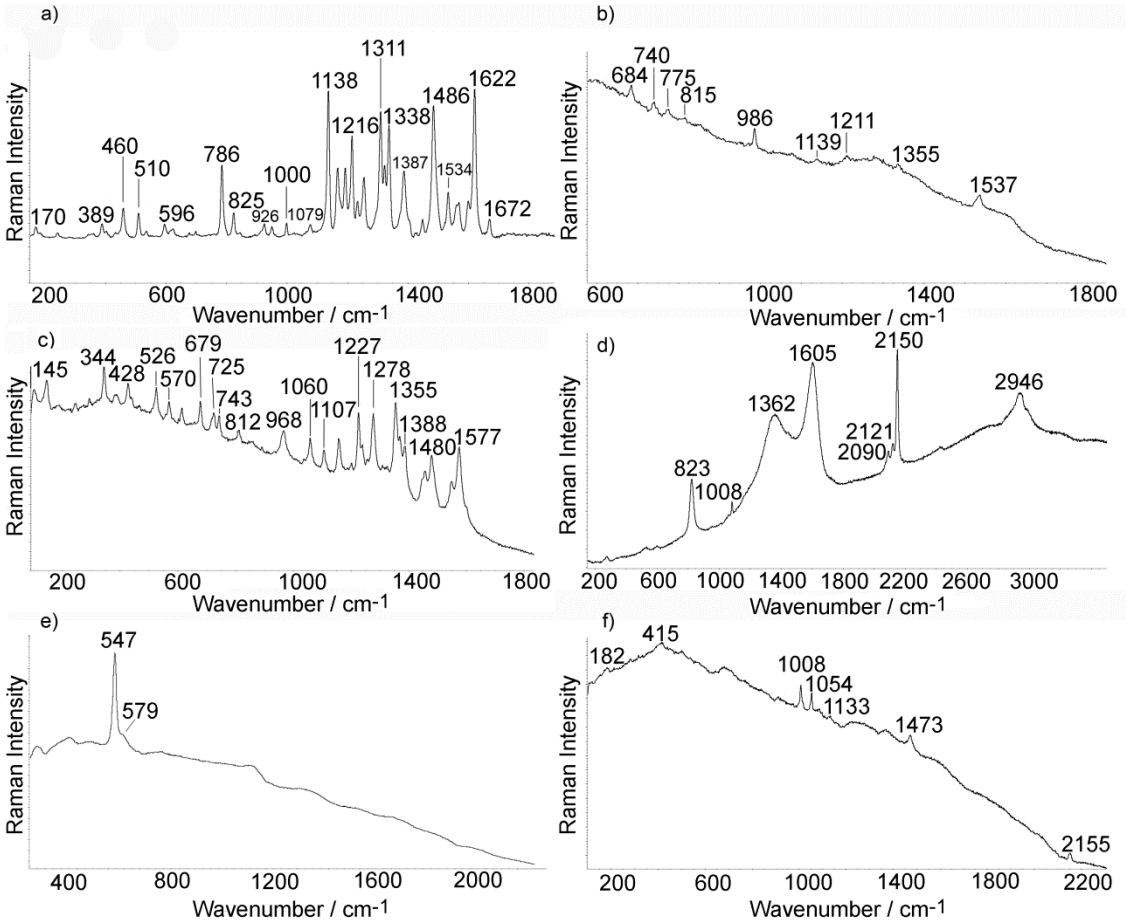


*Figure 9.2: Raman spectra of a) arylamide yellow; b) phthalocyanine green; c) naphtol red; d) a mixture of chrome orange, carbon and Prussian blue; e) ultramarine blue; f) a mixture of gypsum, lead white, weddellite and Prussian blue.*

Ultramarine blue ($Na_{8-10}Al_6Si_6O_{24}S_{2-4}$, Raman bands at 547 and 579 $cm^{-1}$, Figure 9.2e) was found in different scenes of the mural painting. This pigment, extremely expensive in early medieval times, became of common use since the mid-19$^{th}$ century onwards with its synthetic elaboration. Thus, another intervention between the 19$^{th}$ century and the beginning of the 20$^{th}$ century could be possible. This would be reinforced with the presence of rutile ($TiO_2$, Raman bands at 143, 396, 516 and 639 $cm^{-1}$) in the areas where ultramarine blue was detected. Rutile was synthesized only since the beginning of the 20$^{th}$ century. Thus, this restoration work had to be done in the 20$^{th}$ century.

Finally, looking at the mural painting surface, the presence of a thin greyish film was noticed. According to the in-situ DRIFT punctual analyses, it was possible to identify the presence of an acrylic resin, with its characteristic IR bands at 2983, 1736, 1448, 1239, 1148 and 1028 $cm^{-1}$ (Figure 9.3).

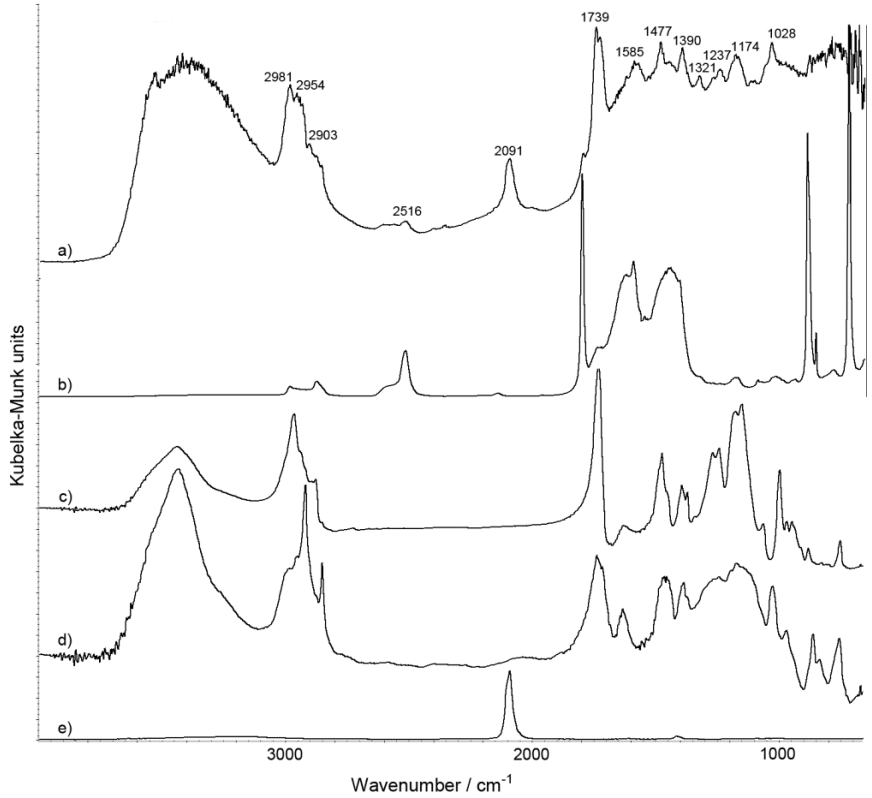


*Figure 9.3: a) DRIFT spectrum of the superficial layer, blue area;b) standard spectrum of calcium carbonate; c) standard spectrum of acrylic resin; d) standard spectrum of silicate; e) standard spectrum of Prussian blue.*

This result is consistent with the analytical study carried out by Artlab s.r.l. in 2007 which, as explained in section 3.2.1, detected the presence of a Paraloid layer in several areas of Gaceo murals. This thermoplastic resin, commonly used in the second half of the 20$^{th}$ century, was applied in the course of a modern restoration in order to reinforce and protect the painting surface from potential external weathering agents. Its waterproofing function, which may be an advantage in some cases, may block the normal transpiration of the wall and promote the dehydration of the mortar [8], as it will be discussed later.

## 9.2 Laboratory analyses

Even though the non invasive approach often provides enough information about the nature and state of preservation of the artwork [8], there are cases in which the obtained data are not conclusive or they have to be supported by analyses in the laboratory [8]. The mural paintings from the church of San Martín de Tours belong to this category. Indeed, in spite of the fact that the above mentioned analyses allowed to identify several compounds attributable to modern restorations, the collected data did not allow to distinguish the stratigraphic distribution of those materials.

For this reason, the analysis of cross sectioned samples became mandatory for the purpose of distinguishing original and restoration materials. In this sense, the image and chemical map analyses have become one of the most important tools for the study of *Cultural Heritage* materials. Actually, amongst the techniques used for molecular image analyses, Raman spectroscopy is the most popular tool to deeper assess original and decay materials on painting micro-samples [17,18]. In several case of study, Raman imaging has been also combined with information obtained using complementary analytical techniques [19-21]. Among them, SEM-EDS is often used in the field of *Conservation Science*, since it can yield information about the surface morphology and the elemental composition of the artwork over micron or even sub-micron areas [22,23].

Based on this background, the second step of this work was focused on deepening the knowledge about the multilayered structure of the paintings through the use of laboratory systems.

In this sense, extraction of the samples was carried out based on the results obtained after in-situ analyses, so that the most interesting areas were only

selected. Considering that the detection of Prussian blue suggested the presence of an additional undocumented repainting, two mural fragments (*blue01* and *blue02*) were collected from blue areas. After being cross sectioned, molecular and elemental chemical images of the two samples were collected by means of the InVia Raman and the EVO40 Scanning Electron Microscope respectively (see chapter 4).

As explained below, the stratigraphic study of these cross sections was extremely significant, confirming the presence of a great number of past interventions.

Regarding the substrate of sample *blue01*, the distribution of three compounds was elucidated (Figure 9.4): a mixture of lead white and gypsum as preparation layer and calcite as mortar.

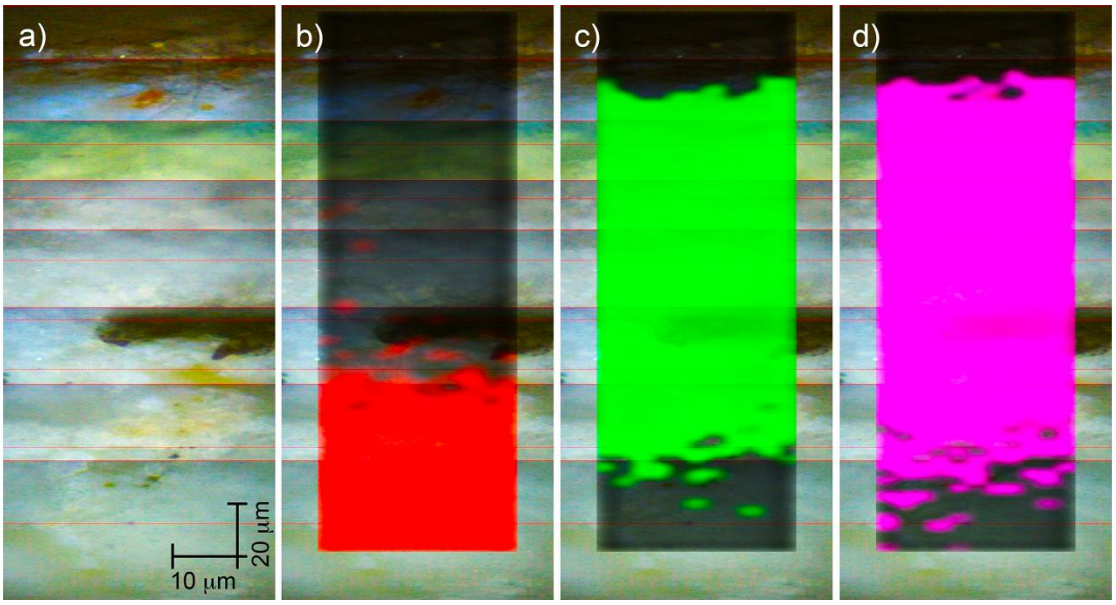


*Figure 9.4: Raman imaging analysis of sample blue01: a) the selected area for the mapping; b) distribution of calcite; c) distribution of gypsum; d) distribution of lead white.*

Looking more closely to the pigmented layers in the cross sections of sample *blue01*, it was possible to see that there were at least three paint layers. As shown in Figure 9.5, SEM-EDS analyses detected the presence of high concentrations of Ti, Si, Na and Al that suggested the presence of rutile mixed with ultramarine blue. The synthetic nature of this last pigment was corroborated through the SEM-EDS images by the lack of typical impurities (such as Mg and Fe) of natural ultramarine blue [24].

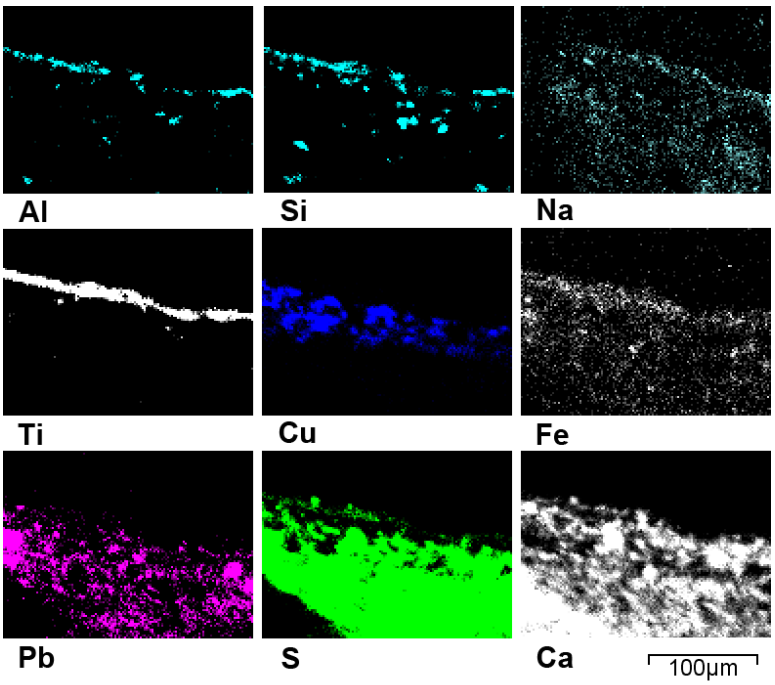


*Figure 9.5: SEM-EDS mapping based on the chemical composition of layers of sample blue01.*

Thanks to Raman imaging analyses (Figure 9.6) the assumptions made on the basis of SEM-EDS maps were confirmed. In addition to that, through molecular analyses the presence of phthalocyanine blue was also detected. The key element for this synthetic pigment (Cu) could not be distinguished by SEM-EDS due to its presence in the original pigment (azurite).

Taking into consideration all the results, it was assumed that this layer belonged to a restoration process made after 1930. Located under this blue layer described above, there was another bluish paint layer thicker than the previous one. Observed under the microscope, the layer was more heterogeneous and coarse.

According to the SEM-EDS data, this layer was characterized by the presence of copper with a rather heterogeneous distribution. Raman imaging analyses of this area yielded perfectly overlapping peaks with those of the azurite. Based on this information and according to the literature [25], it can be therefore affirmed that azurite was one of the pigments employed for the elaboration of the original painting.

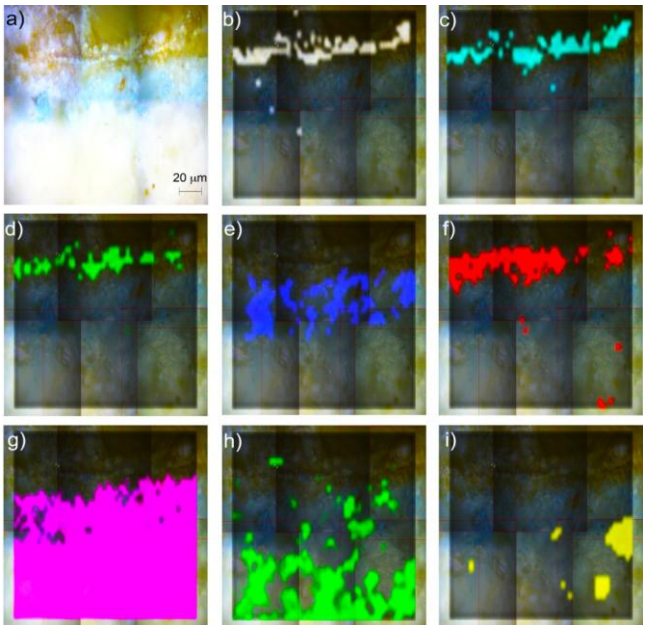


*Figure 9.6: Raman imaging analysis of the sample blue01: a) the picture of the selected area; b) rutile; c) ultramarine blue; d) phthalocyanine blue; e) azurite; f) carbon black; g) lead white; h) gypsum; i) bassanite.*

Although it could not be identified by Raman imaging analyses due to fluorescence problems, point analyses on sample *blue01* enabled the detection of a Prussian blue layer between the original blue layer and the nowadays visible one.

Its presence was confirmed thanks to the elemental distribution given by SEM-EDS analyses. In fact, as can be observed in Figure 9.7, traces of Fe were observed between the two layers, reinforcing the idea of a restoration work or repainting with Prussian blue during the 19$^{th}$ century, as suspected when in-situ analyses were performed.

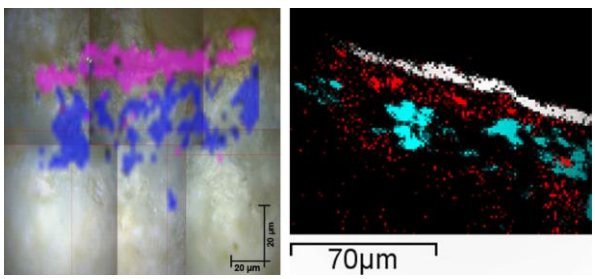


*Figure 9.7: Chemical mapping of the cross section of sample blue01: a) Raman mapping, azurite illustrated in blue colour and rutile in magenta; b) SEM-EDS mapping, cupper illustrated in cyan, iron illustrated in red and titanium illustrated in white.*

Focusing on sample *blue02*, as previously described on the basis of in-situ analyses, the substrate was composed of a mixture of calcite and gypsum, without any preparation layer (Figure 9.8 and 9.9) and without lead white. Besides, it presented coarse grains of quartz mixed with calcite and gypsum.

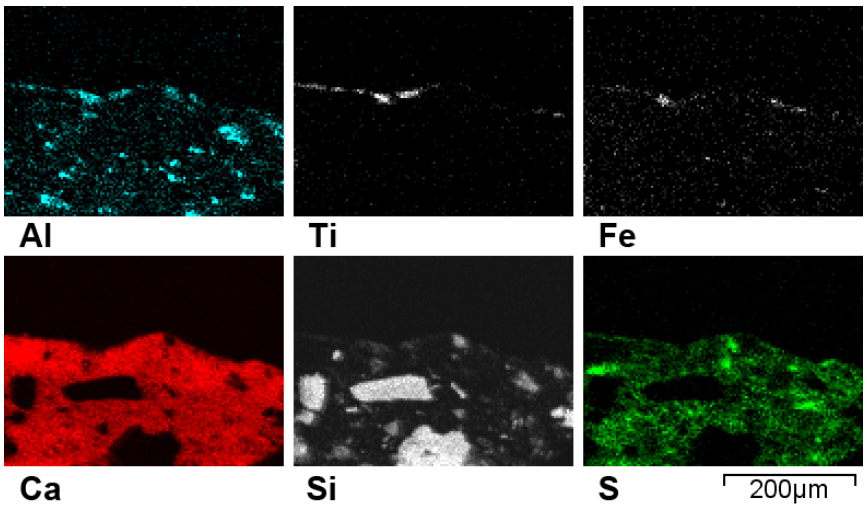


*Figure 9.8: SEM-EDS chemical maps of sample blue02.*

Furthermore, dealing with the pigment layers of sample *blue02*, two paint layers were clearly distinguished. SEM-EDS analyses (Figure 9.8) detected the presence of Ti, Si and Al as in the case of sample *blue01*. Raman imaging analyses (Figure 9.9) also revealed the previously mentioned rutile, ultramarine blue and phthalocyanine blue. In contrast, in sample *blue02*, there was no layer of azurite, and the layer of Prussian blue could be clearly determined together with carbon black.

The results obtained from sample *blue02* reinforced the idea of a restoration work or a repainting during the 19$^{th}$ century. That is, in the 19$^{th}$ century some areas originally painted with azurite were already degraded or lost, and consequently repainted with Prussian blue. Then, in the 20$^{th}$ century, the paintings were repainted again, but in this case with ultramarine blue and phthalocyanine blue.

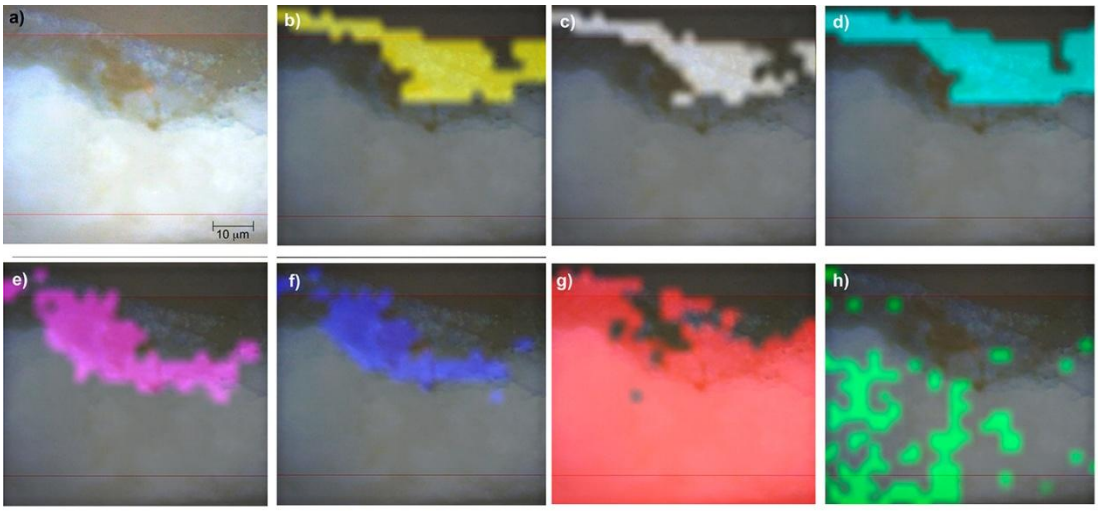


*Figure 9.9: Raman imaging analysis of the sample blue02: a) the picture of the selected area; b) phthalocyanine blue; c) rutile; d) ultramarine blue; e) carbon black; f) Prussian blue; g) calcite; h) gypsum.*

## 9.3 Degradations forms

As explained in chapter 3, the artwork showed a remarkable state of conservation. However, in addition to the characterization of original and restoration materials, the above mentioned in-situ and laboratory systems also enabled the detection of two different kinds of degradation compounds.

As shown in Figure 9.1, Raman in-situ analyses of the gypsum from the plaster showed the presence of a secondary peak at 1015 $cm^{-1}$, which is the characteristic signal of bassanite ($CaSO_4 \cdot 1/2H_2O$) promoted as a consequence of gypsum degradation. The different intensities of the bands found in many examined areas suggested that the mortar degradation phenomenon was heterogeneous. This compound was also detected during Raman imaging analyses, which was very useful to understand the degree of this degradation process.

It is considered that the presence of bassanite could be due to the fact that gypsum used in the mortar was heat treated to make it more easily manipulated, thus, forming bassanite. However, being a metastable phase, it could not be possible to find bassanite after the period of mortar hardening. Hence, the bassanite found in the mortar has to be related to some kind of dehydration process, which may be triggered by physical and/or biological factors. This deduction is concordant with the fact that bassanite appears mainly in those areas where cohesion has been lost.

Among the physical factors it must be underlined that, in previous works [8], the use of acrylic resin for wall painting consolidation has been related to the dehydration of gypsum. Indeed it is well known that synthetic and organic coatings change the hydrophilicity/hydrophobicity and capillary rise profiles and reduce the pore size distribution, water transpiration capability, etc. This seems to be the case of Gaceo.

In this context, the salt solutions occurring in the mortar pores also play a special role, decreasing the temperature required to the gypsum dehydration process due to the pressure exerted by the soluble ions when crystallizing [26]. In this case of study, several Raman bands belonging to soluble salts were identified, such as 1049 $cm^{-1}$ (nitrocalcite, $Ca(NO_3)_2{\cdot}4H_2O$) and 1068 $cm^{-1}$ (natron, $Na_2CO_3{\cdot}10H_2O$).

Although the presence of humidity could contradict the crystallization of bassanite, for its formation, first, gypsum is partially solubilised and then re-precipitated as dehydrated gypsum [26].

Nevertheless, the presence of microorganisms has been also pointed out to be relevant in this degradation process [26]. Biological attack of wall paintings was also detected primarily in the blue and green-coloured areas, since weddellite ($CaC_2O_4{\cdot}2H_2O$, characteristic Raman bands at 910 and 1473 $cm^{-1}$, Figure 9.2f) was often found in these areas by the in-situ Raman analyses carried out. Calcium oxalate may occur due to different weathering sources. According to some authors, the origin of this compound may be a consequence of the biochemical activity of bacteria, algae, fungi or lichens [27,28], whereas other authors state that the oxalate could be related to chemical decomposition of organic materials like the binding media [29].

Assuming the biological source of oxalates, if the acrylic resin was set in the mural painting some years ago, the absence of transpiration could make possible the absence of water for the biological growth. In such situation, the microorganisms take the water from hydrated minerals, like gypsum, synthesizing the hydrated $Ca_2CO_4{\cdot}H_2O$ and leaving less hydrated compounds of gypsum, such as bassanite ($Ca_2SO_4{\cdot}1/2H_2O$) [10].

## 9.4 Conclusions

This analytical study, based on the combination of in-situ spectroscopies with laboratory analyses proved to be extremely useful for the characterization of original and restoration materials constituting the mural painting.

The study of the collected micro-samples by means of Raman and SEM-EDS imaging analyses helped to better understand not only important aspects concerning the composition of the work but also the stratigraphic succession of the painted layers and the execution technique used by the artist.

Indeed, by taking into account both, the literature and the scientific results, it was elucidated that the *secco* technique was used, since azurite and lead-based pigments are not suitable for *frescoes* [30].

Thanks to the analyses carried out, several modern pigments were also identified. On the one side, the presence of naphtol red, arylamide yellow, ultramarine blue, rutile, phtalocyanine green and phtalocyanine blue was related to the documented conservation works achieved in the $20^{th}$-$21^{st}$ century.

On the other side, molecular and chemical images also revealed the presence of a non recorded restoration work carried out during the $19^{th}$ century. The presence of Prussian blue together with the absence of azurite (the original pigment) and the change in the mortar composition disclosed this issue. This assumption was further proved by the presence of chrome yellow and chrome orange mixed with Prussian blue.

Regarding the degradation products, Raman analyses of the paint surface also proved the presence of weddellite. The most probable origin of this compound is the biological activity of microorganisms present in the support and inside the painted surface.

However, more worrying is the presence of bassanite as the consequence of degradation of gypsum. In open systems, dehydration of gypsum is associated with a volume decrease of up to 39% [31-33]. Furthermore, shrinkage in the gypsum layer and the pore pressure effects of water released from the crystal structure of gypsum cause a stress within the mortar, which may result on significant deformation and fracturing [34]. Linked to this issue, it is important to mention the use of acrylic resins (Paraloid). Some authors claim that the changes

of surface properties (hydrophilicity/hydrophobicity, capillary rise profiles, pore size distribution or water transpiration capability amongst others) observed in the presence of acrylic copolymer coatings and the ageing effect explain why the use of these materials should be avoided when not strictly necessary [35].

As explained in the chapter 1, several researchers are nowadays experimenting with the use of micellar solutions for the removal of undesirable synthetic polymer layers [37-39]. Considering the promising results obtained so far, the use of these novel conservation products should be taken into account for further restoration treatments.

## 9.5 References

**[1]** A. Hernanz, J.M. Gavira-Vallejo, J.F. Ruiz-López, S. Martín, Á. Maroto-Valiente, R. de Balbín-Behrmann, M. Menéndez, J.J. Alcolea-González (2012) Spectroscopy of Palaeolithic rock paintings from the Tito Bustillo and El Buxu Caves, Asturias, Spain. *Journal of Raman Spectroscopy*, 43, 1644-1650.

**[2]** S. Lahlil, M. Lebon, L. Beck, H. Rousselière, C. Vignaud, I. Reiche, M. Menu, M.P. Paillet, F. Plassard (2012) The first *in situ* micro-Raman spectroscopic analysis of prehistoric cave art of Rouffignac St-Cernin, France. *Journal of Raman Spectroscopy*, 43, 1637-1643.

**[3]** M. Olivares, K. Castro, M.S. Corchón, D. Gárate, X. Murelaga, A. Sarmiento, N. Etxebarria (2013) Non-invasive portable instrumentation to study Palaeolithic rock paintings: the case of La Peña Cave in San Roman de Candamo (Asturias, Spain). *Journal of Archaeological Science*, 40, 1354-1360.

**[4]** M. Maguregui, U. Knuutinen, I. Martínez-Arkarazo, A. Giakoumaki, K. Castro, J.M. Madariaga (2012) Field Raman analysis to diagnose the conservation state of excavated walls and wall paintings in the archaeological site of Pompeii (Italy). *Journal of Raman Spectroscopy*, 43, 1747-1753.

**[5]** L. Apollonia, D. Vaudan, V. Chatel, M. Aceto, P. Mirti (2009) Combined use of FORS, XRF and Raman spectroscopy in the study of mural paintings in the Aosta Valley (Italy). *Analytical and Bioanalytical Chemistry,* 395, 2005-2013.

**[6]** N. Proietti, V. Di Tullio, F. Presciutti, G. Gentile, B.G. Brunetti, D. Capitani (2016) A multi-analytical study of ancient Nubian detached mural paintings. *Microchemical Journal*, 124, 719-725.

**[7]** S.R. Amanto, D. Bersani, P.P. Lottici, P. Pogliani, C. Pelosi (2017) A Multi-Analytical Approach to the Study of the Mural Paintings in the Presbitery of Santa Maria Antiqua Al Foro Romano in Rome. *Archaeometry,* DOI:10.1111/arcm.12296.

**[8]** M. Irazola, M. Olivares, K. Castro, M. Maguregui, I. Martínez-Arkarazo, J.M. Madariaga (2012) *In situ* Raman spectroscopy analysis combined with Raman and SEM-EDS imaging to assess the conservation state of 16th century wall paintings. *Journal of Raman Spectroscopy,* 43, 1676-1684.

**[9]** J.A. Barrio (1993) La pintura mural religiosa en Bizkaia, *Diputación de Bizkaia*, *Bilbao (Spain)*, pp 27.

**[10]** M. Pérez-Alonso, K. Castro, J.M. Madariaga (2006) Investigation of degradation mechanisms by portable Raman spectroscopy and thermodynamic speciation: The wall painting of Santa María de Lemoniz (Basque Country, North of Spain). *Analytica Chimica Acta,* 571, 121-128.

**[11]** R.J. Gettens, G.L. Stout (1966) Painting Materials, *Courier Dover Publications*, *Mineola (USA)*, pp 368.

**[12]** M. Olivares, A. Tarriño, X. Murelaga, J.I. Baceta, K. Castro, N. Etxebarria (2009) Non-destructive spectrometry methods to study the distribution of archaeological and geological chert samples. S*pectrochimica Acta Part A,* 73, 492-497.

**[13]** E. Kotulanová, P. Bezdicka, D. Hradil, J. Hradilová, S. Svarcová, T. Grygar (2009) Degradation of lead-based pigments by salt solutions. *Journal of Cultural Heritage,* 10, 367-378.

**[14]** N. Eastaugh, V. Walsh, T. Chaplin, R. Siddall (2008) Pigment Compendium: A Dictionary and Optical Microscopy of Historical Pigments. *Butterworth-Heinemann, Oxford (UK)*, pp 958.

**[15]** P. Vandenabeele, L. Moens, H.G.M. Edwards, R. Dams (2000) Raman spectroscopic database of azo pigments and application to modern art studies. *Journal of Raman Spectroscopy*, 31, 509-517.

**[16]** M. Maguregui, U. Knuutinen, K. Castro, J.M. Madariaga (2010) Raman spectroscopy as a tool to diagnose the impact and conservation state of Pompeian second and fourth style wall paintings exposed to diverse environments (House of Marcus Lucretius). *Journal of Raman Spectroscopy*, 41, 1400-1409.

**[17]** P. Ropret, C. Miliani, S.A. Centeno, Č. Tavzes, F. Rosi (2010) Advances in Raman mapping of works of art. *Journal of Raman Spectroscopy*, 41, 1462-1467.

**[18]** E.B. Halac, M. Reinoso, M. Luda, F. Marte (2012) Raman mapping analysis of pigments from *Proas Iluminadas* by Quinquela Martín. *Journal of Cultural Heritage*, 13, 469-473.

**[19]** S. Aze, J.M. Vallet, A. Baronnet, O. Grauby (2006) The fading of red lead pigment in wall paintings: tracking the physico-chemical transformations by means of complementary micro-analysis techniques. *European Journal of Mineralogy*, 18, 835-843.

**[20]** A. Deneckere, B. Vekemans, L. Van de Voorde, P. De Paepe, L. Vincze, L. Moens, P. Vandenabeele (2012) Feasibility study of the application of micro-Raman imaging as complement to micro-XRF imaging. *Applied Physics A*, 106, 363-376.

**[21]** C. Conti, C. Colombo, M. Matteini, M. Realini, G. Zerbi (2010) Micro-Raman mapping on polished cross sections: a tool to define the penetration depth of conservation treatment on cultural heritage. *Journal of Raman Spectroscopy*, 41, 1254-1260.

**[22]** Q.G. Zeng, G.X. Zhang, C.W. Leung, J. Zuo (2010) Studies of wall painting fragments from Kaiping Diaolou by SEM/EDX, micro Raman and FT-IR spectroscopy. *Microchemical Journal*, 96, 330-336.

**[23]** L. de Ferri, D. Bersani, Ph. Colomban, P.P. Lottici, G. Simon, G. Vezzalini (2012) Raman study of model glass with medieval compositions: artificial weathering and comparison with ancient samples. *Journal of Raman Spectroscopy*, 43, 1817-1823.

**[24]** D. Angelici, A. Borghi, F. Chiarelli, R. Cossio, G. Gariani, A. Lo Giudice, A. Re, G. Pratesi, G. Vaggelli (2015) μ-XRF Analysis of Trace Elements in Lapis Lazuli-Forming Minerals for a Provenance Study. *Microscopy and Microanalysis*, 21, 526-533.

**[25]** R.J. Gettens, E. West (1997) Artists' Pigments: A Handbook of Their History and Characteristics, *Oxford University Press*, *Oxford (UK)*, pp 300.

**[26]** Y. Mastai (2012) Advances in Crystallization Processes, *InTech, Rijeka (Croatia),* pp 668.

**[27]** A.A. Gorbushina, J. Heyrman, T. Dornieden, M. Gonzalez-Delvalle, W.E. Krumbein, L. Laiz, K. Petersen, C. Saiz-Jiménez, J. Swings (2004) Bacterial and fungal diversity and biodeterioration problems in mural painting environments of St. Martins church (Greene–Kreiensen, Germany). *International Biodeterioration and Biodegradation*, 53, 13-24.

**[28]** M.F. Macedo, A.Z. Miller, A. Dionisio, C. Saiz-Jiménez (2009) Biodiversity of cyanobacteria and green algae on monuments in the Mediterranean Basin: an overview. *Microbiology*, 155, 3476-3490.

**[29]** M. Franzini, C. Gratziu, E. Wicks (1984) Patine ad ossalato di calico sui monumenti marmorei. *Societá Italiana Mineralogia et Petrografia*, 39, 39-46.

**[30]** G. Cavallo, R.C. Vergani, L. Gianola, A. Meregalli (2012) Archaeological, stylistic and scientific research on 11th–13th century ad painted fragments from the S*an Giovanni Battista* church in Cevio (Switzerland). *Archaeometry,* 54, 294-310.

**[31]** S. Azam (2007) Study on the geological and engineering aspects of anhydrite/gypsum transition in the Arabian Gulf coastal deposits. *Bulletin of Engineering Geology and the Environment*, 66, 177-185.

**[32]** I. Yılmaz (2001) Gypsum/anhydrite: some engineering problems. *Bulletin of Engineering Geology and the Environmen*t, 59, 227-230.

**[33]** W. Wittke (1990) Rock Mechanics, Theory and Applications with Case Histories, *Springer Verlag, Heidelberg (Germany),* pp 1076.

**[34]** S. Ko, D.L. Olgaard, U. Briegel (1995) The transition from weakening to strengthening in dehydrating gypsum: Evolution of excess pore pressures. *Geophysical Research Letters*, 22, 1009-1012.

**[35]** E. Carretti, L. Dei (2004) Physicochemical characterization of acrylic polymeric resins coating porous materials of artistic interest. *Progress in Organic Coating*, 49, 282-289.

**[36]** M. Baglioni, D. Rengstl, D. Berti, M. Bonini, R. Giorgi, P. Baglioni (2010) Removal of acrylic coatings from works of art by means of nanofluids: understanding the mechanism at the nanoscale. *Nanoscale*, 2, 1723-1732.

**[37]** M. Baglioni, R. Giorgi, D. Berti, P. Baglioni (2012) Smart cleaning of cultural heritage: a new challenge for soft nanoscience. *Nanoscale*, 4, 42-53.

**[38]** E. Carretti, L. Dei, P. Baglioni (2003) Solubilization of Acrylic and Vinyl Polymers in Nanocontainer Solutions. Application of Microemulsions and Micelles to Cultural Heritage Conservation. *Langmuir*, 19, 7867-7872.

CHAPTER 10:

# THE INFLUENCE OF AGRICULTURAL ACTIVITIES ON THE ONSET OF DEGRADATION PROCESSES

## Mural paintings from Alaiza

Standing just a few kilometres away from Gaceo, the church of the Assumption (Alaiza, Spain) preserves one of the most peculiar Middle Age murals that can be found in the Basque Country.

As summarized in section 3.2, those paintings are clearly distinguishable from most of the artworks of the same epoch from both, iconographic and (above all) stylistic point of view. Indeed, the mural paintings that cover the entire presbyterial area of the church were carried out by exclusively using red pigments on a white background.

As in the case of San Martín de Tours (Gaceo), the paintings present in the church of Alaiza were subjected to conservation treatments. On the one side, it is known that an extensive restoration work was achieved in 1983, the year of its discovery. However, in the case of the secondary nave, the presence of a third painted layer

(overlapping the conservation materials applied in 1983) suggested the presence of a further undocumented restoration.
Recognizing the importance of deepening the understanding of the materials that compose the artwork, the first campaign of analysis was carried out with the purpose of identifying the nature of the original compounds and to distinguish them from those used in recent conservation treatments.

## 10.1 Chemical assessment of original and restoration materials

Considering the excellent results obtained thanks to the analytical procedure described in the previous chapter, original and conservation products were identified by means of the portable InnoRam$^{TM}$-785S Raman spectrometer. The molecular data were then supported by elemental analyses performed through the hand-held ED-XRF system. As shown below, the complementary data enabled the overall chemical assessment of the paintings.

**Original mortars and pigments**

The in-situ study of the substrate was achieved by analyzing the areas where the degradation caused the fall of the paint layer. These analyses showed the presence of two plasters. The superficial layer, consisting entirely of calcite ($CaCO_3$, Raman peaks at 281, 713 and 1085 $cm^{-1}$), overlaps a thicker layer composed of calcite and sand ($SiO_2$, Raman features at 464, 804 and 1162 $cm^{-1}$).

This composition agrees with the classical preparation of Middle Age mural paintings [1]. Indeed, a layer of plaster was applied on the wall surface in order to homogenize it while a second layer smoothed the surface facilitating the decoration with the paintings. In this pictorial cycle the last layer of plaster constituted not only the medium but also the white background for the red figures and motifs.

The in-situ analysis of the colour palette used for the painting reflected the austere style of this work. Excluding the white colour of the background described above, the painting was composed of only two pigments. Red figures, which constitute almost the entire cycle, were made of minium (Figure 10.1a), $Pb_3O_4$, identified thanks to the intense Raman peaks at 224, 314, 391 and 550 $cm^{-1}$. The presence of this compound was further confirmed by the elemental analyses with ED-XRF showing high intensity Pb-L lines. On the red areas, several spectra

showed the presence of additional weak signals attributable to carbon black, whose function was to darken the tone of the composition.

Some details of the composition, as the band with gothic lettering adorning the top edge of the presbyterial walls, were painted with carbon black (amorphous carbon, with two broad Raman bands at 1310 and 1595 $cm^{-1}$) (see Figure 10.1b).

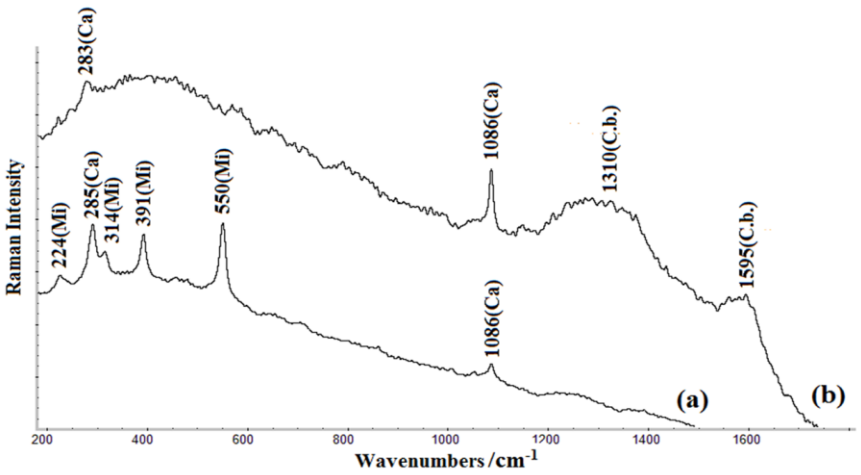


*Figure 10.1: The two spectra, collected in the original areas, showed the original pigments. a) red areas were made of minium (Mi); b) grey decorations were made of carbon black (C.b.). In both spectra, the main peaks of calcite (Ca, coming from the mortar) can be observed.*

**1983's restoration works**

According to the documents found in the archives from Diputación Foral de Álava, a modern restoration project dating back to 1983 was done [2]. This project indicated the reconstruction of the substrate and the paint layer where the degradation compromised the readability of the mural painting. These interventions were clearly distinguished during the visual analysis: red figures showed darker shades of colour overlapping the original paintings. Nevertheless, a scientific study was done to confirm the visual analysis.

The in-situ study of these retouches led to the identification of hematite, $Fe_2O_3$, recognizable thanks to the Raman peaks at 225, 294, 410 and 608 $cm^{-1}$ as well as to the intensity of Fe peaks detected by ED-XRF. In an attempt to imitate the hue of the original colour, the conservators mitigated the intense red colour of hematite by the addition of titanium white ($TiO_2$, in the rutile form, with Raman

bands at 444 and 606 $cm^{-1}$ and Ti detected by elemental analyses). Figure 10.2 shows the characteristic peaks of both pigments collected in the same spectrum.

Due to the lack of photographic documentation it was not possible to establish the conservation conditions of the mural paintings at the time of their discovery. However, the presence of hematite and titanium white was detected in most of the analyzed areas. This information allows to state that the current aspect of the pictorial cycle differs from the past insofar as the result of an extensive and deep restoration.

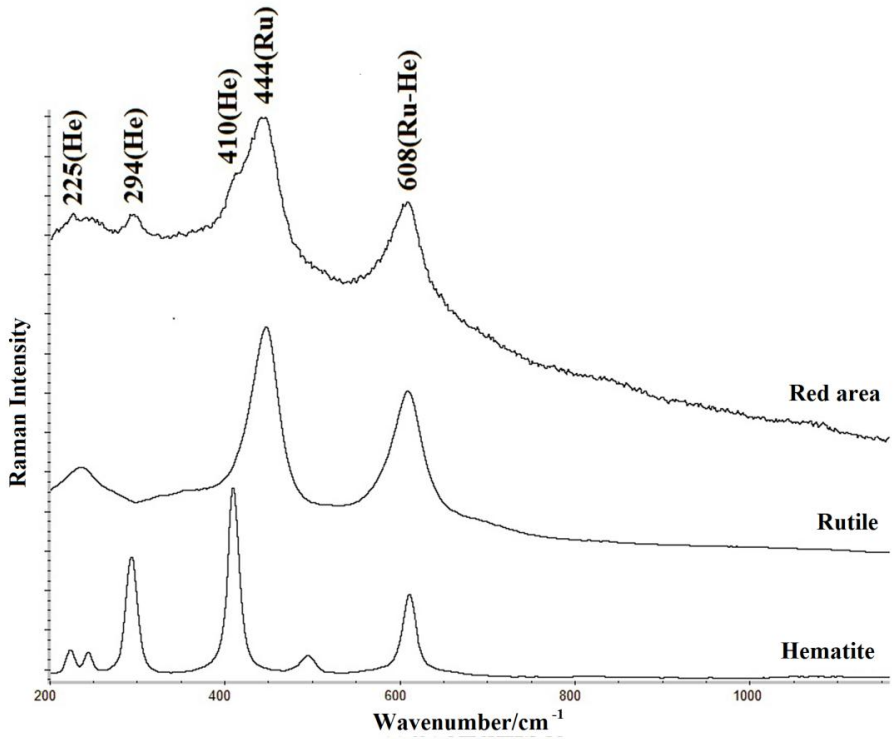


*Figure 10.2: Raman spectrum from the red repainted areas, showing the use of a mixture of rutile (Ru) and hematite (He).*

In several cases the restoration of the paint layer was accompanied by the reconstruction of the substrate. This task was performed mainly in the lower parts of the walls using a mixture of gypsum ($CaSO_4 \cdot 2H_2O$, identified in-situ by its main Raman peak at 1008 $cm^{-1}$ and its two characteristic doublets at 493, 414 $cm^{-1}$ and 670, 619 $cm^{-1}$, apart from other secondary signals at 1135 and 217 $cm^{-1}$) and calcite ($CaCO_3$, with its Raman bands at 156, 281, 712 and 1086 $cm^{-1}$), but also in other areas. According to the large areas reconstructed with this mixture, the lower parts of the walls were severely affected and degraded in the past.

**Restoration works after 1983's**

The secondary nave of the church presents decorations whose colours and styles differ completely from the originals. The loss of material in different areas of the wall allowed establishing that such paintings, as well as their support, were applied over those of the restoration from 1983. This fact proved the presence of materials belonging to an undocumented intervention subsequent to that date.

The plaster was done with a mixture of calcite and quartz. This support was also covered by a white layer of barium sulphate ($BaSO_4$, main Raman peak at 988 $cm^{-1}$) forming the base of the overlying blue and yellow decorations.

Pigments characterization of blue areas led to the identification of artificial ultramarine blue (Figure 10.3a, main Raman peak at 545 $cm^{-1}$). On the other side, yellow areas were painted by using a mixture of chrome orange ($PbCrO_4 \cdot PbO$, Raman peaks at 323, 343, 380, 826 and 847 $cm^{-1}$) and vanadinite, ($Pb_5(VO_4)_3Cl$, Raman peaks at 322, 792 and 825 $cm^{-1}$) (see Figure 10.3b).

The molecular characterization of vanadinite was difficult to achieve since the position of its main Raman bands coincides with those of chrome orange pigment. However, the presence of a shoulder peak around 790 $cm^{-1}$ in the collected spectra suggested that yellow areas were probably done by the use of both pigments.

The interpretation of molecular data was supported by elemental analyses. For example, as shown in Figure 10.4, in-situ ED-XRF analyses of yellow areas detected the presence of several peaks that fit with the characteristic lines of (among others) Cr, Pb, Ba and V elements.

The presence of Cr and Pb was easily explained by the use of chrome orange, as Raman analyses showed, whereas Ba would be due to $BaSO_4$ from the substrate. On the other side, the presence of vanadium (which was only detected in yellow areas) and chromium confirmed the use of vanadinite and chrome orange pigments.

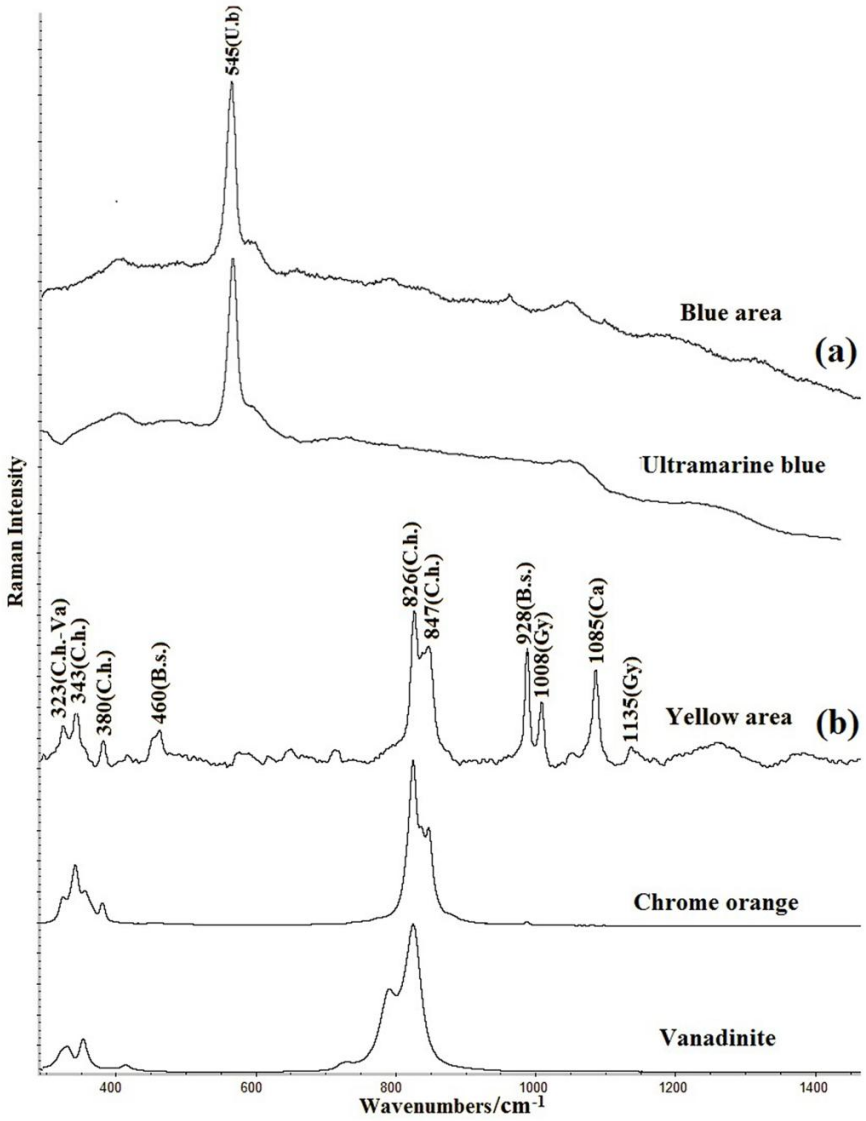


*Figure 10.3: a) The spectrum shows artificial ultramarine blue pigment in the blue areas; b) the spectrum suggest the use of vanadinite (Va) and chrome orange (C.h.) in the yellow areas. Barium sulfate (B.s) is due to the white background, while calcite (Ca) and gypsum (Gy) are from the plaster.*

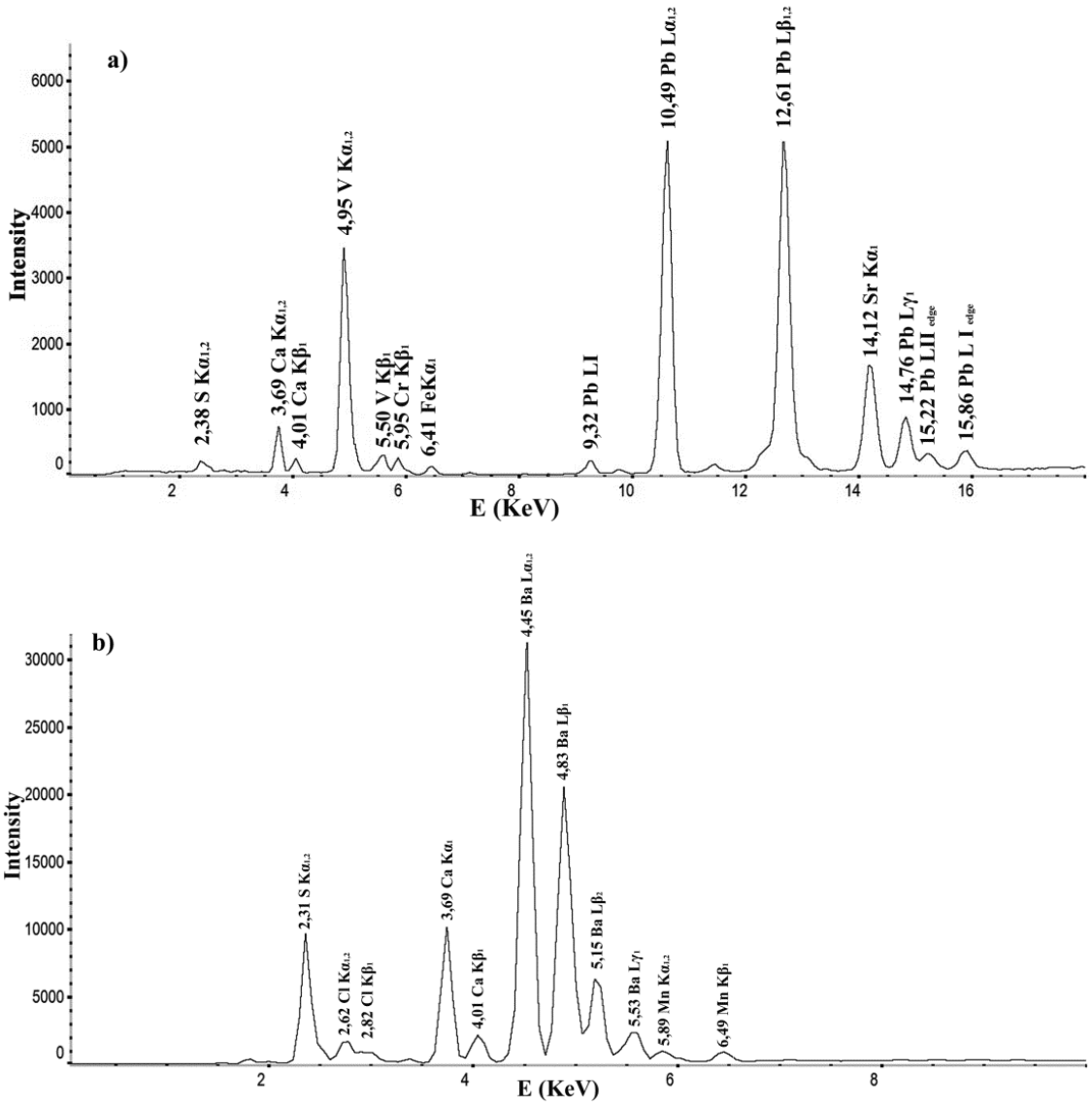


*Figure 10.4: ED-XRF spectra of: a) yellow pigment layer with the characteristic peaks of Pb, Cr and V among others; b) substrate layer of $BaSO_4$.*

## 10.2 Characterization of degradations forms

In comparison with the previous case of study, the paintings from the church of Alaiza were clearly undermined by the presence of extensive degradation processes.

In fact, during the campaign of analysis, Raman and ED-XRF portable systems allowed the detection of several problems, mostly linked to soluble salts crystallization.

Focusing on the upper part of the walls, the portable Raman spectrometer allowed to identify compounds such as ammonium sulphate ($(NH_4)_2SO_4$, main Raman band at 973 $cm^{-1}$) and sodium nitrate (nitratine, $NaNO_3$, with Raman bands at 722 and 1065 $cm^{-1}$) but only in a few of the more than 250 spectra collected in this area during the study. This fact, apparently, suggests a low degradation degree of these high areas due to the scarce presence of soluble compounds. However, the presence of ammonium salts in the upper part of the wall was symptomatic.

The good conservation of the high part of the paintings contrasts with the strong deterioration phenomena detected in the lower parts of the walls. Up to a height of 2 meters from the floor, the mural showed intense and extensive degradations, such as salt efflorescence, collapse of the paint layer and mortar disaggregation, which are compromising the integrity of large areas of the painting.

Moreover, in the lower parts of the walls only gypsum was found as the constituent of the plaster, without any traces of calcite. In fact, calcite had disappeared from this part of the wall, as it will be explained below.

### Salt efflorescence composition

In order to deepen the knowledge about the degradation forms threatening the integrity of the lower part of the murals, a few mortar microsamples were collected. As shown in Figure 10.5, the selected area of sampling (located in the south wall of the secondary nave) was characterized by the presence of several efflorescence showing different size and appearance.

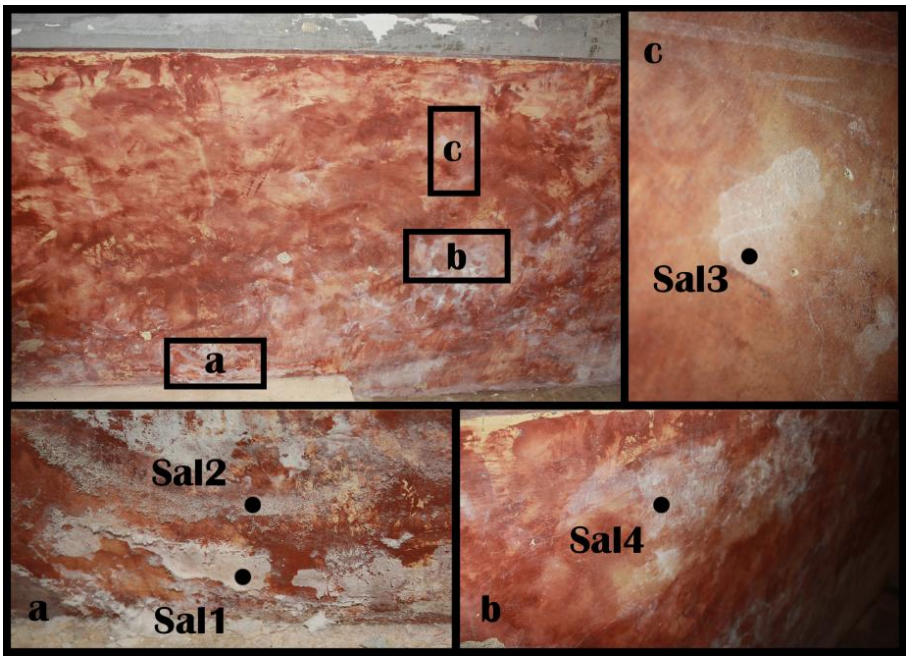


*Figure 10.5: Details from the basal part of the wall, showing the points selected for the salt efflorescence sampling.*

The collected fragments were analyzed in the laboratory by means of the RA100 Raman spectrometer described in section 4.3.2.

According to molecular results, *Sal1* sample (which, as shown in Figure 10.5a, corresponded to a white efflorescence with a high crystallization, partially detached from the paint surface) was composed of anhydrous sodium sulphate (thenardite, $Na_2SO_4$, with Raman bands at 451, 621, 639 and 992 $cm^{-1}$), sodium nitrate (nitratine, $NaNO_3$, Raman Bands at 772 and 1065 $cm^{-1}$) and potassium nitrate (niter, $KNO_3$, Raman bands at 714 and 1050 $cm^{-1}$).

Sample *Sal2* (Figure 10.5a) was obtained in the same area of *Sal1*, but differed from the previous one because of its dusty appearance. In this case, Raman spectroscopy confirmed the presence of the same compounds mentioned before (Figure 10.6) but with a different ratio between the intensities of their main peaks. As proved by several works, there is a direct proportionality between the intensity of the main peaks of salts with their concentration [4]. This fact suggests that semi-quantification values can be obtained from the treatment of Raman spectra.

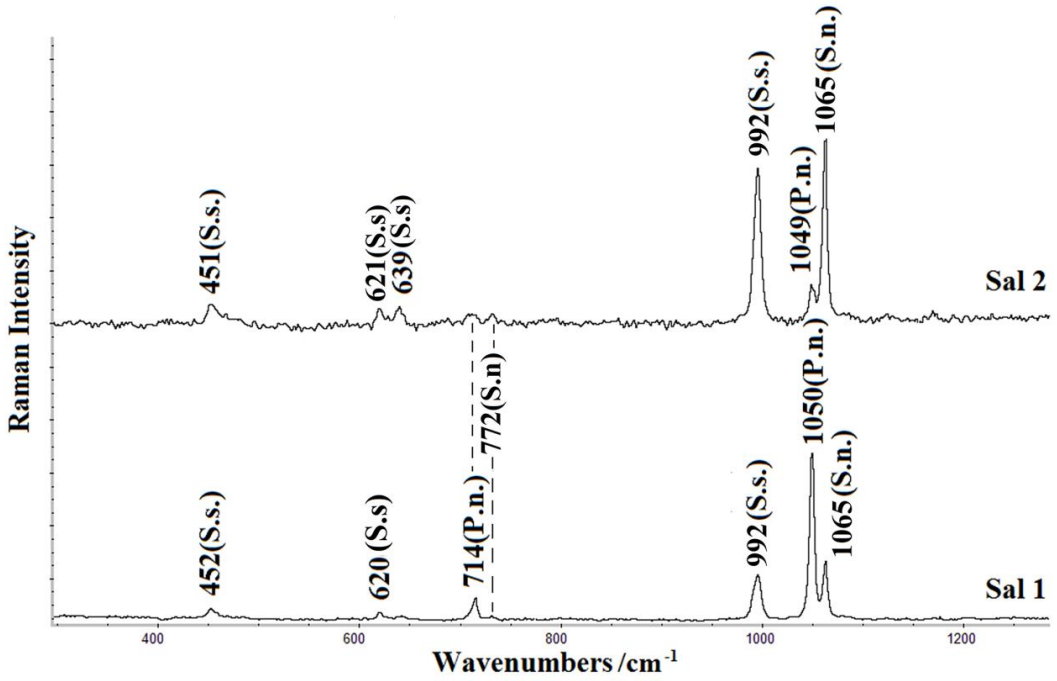


*Figure 10.6: Comparison of the Raman spectra obtained from Sal1 and Sal2 samples. The first efflorescence shows an intense peak due to the potassium nitrate (P.n.), while the major signals of Sal2 are due to the presence of sodium sulphate (S.s.) and sodium nitrate (S.n.).*

From the analytical point of view, the quantification process in solid state is rather difficult and almost always discouraged because a good quantification method requires homogeneity, a fact very difficult to reach when doing microanalyses. However, recent studies demonstrate that the semi-quantification of soluble salts composing efflorescence can be achieved by using the external calibration curve or multivariate linear regression methods [4,5].

Thus, calibration curves for $Na_2SO_4$, $KNO_3$ and $NaNO_3$ were prepared with the purpose of semi-quantifying the contribution of each salt in the two samples. To do so, pellets composed of the three salts in different proportions between 0 and 750 mg/g of each salt were prepared after grinded them carefully during several minutes. Both, the height of the main Raman band of each compound and the area of those bands were monitored: 1065 $cm^{-1}$ for $NaNO_3$, 1050 $cm^{-1}$ for $KNO_3$ and 992 $cm^{-1}$ for $Na_2SO_4$.

The curves obtained by taking into account the areas of the peaks were the following ones:

$y = 520.9x - 13529$ $R^2 = 0.961$ for $NaNO_3$;

$y = 397.0x - 7108$ $R^2 = 0.996$ for $KNO_3$;

$y = 209.6x + 9911$ $R^2 = 0.924$ for $Na_2SO_4$;

In order to ensure the repeatability of the results, samples *Sal1* and *Sal2* were grinded and employed to carry out pellets. Each pellet was analyzed in several spots (7) and the collected data were used to calculate both average concentration and standard deviation. In this way, it was obtained that in *Sal1* there was 235 ± 69 mg/g of $Na_2SO_4$, 150 ± 42 mg/g of $NaNO_3$ and 720 ± 54 mg/g of $KNO_3$, whereas in *Sal2* there was 570 ± 3 mg/g of $Na_2SO_4$, 270 ± 43 mg/g of $NaNO_3$ and 215 mg/g ± 36 of $KNO_3$.

Therefore, the semi-quantitative data proved that *Sal1* was predominantly composed of potassium nitrate while *Sal2* showed a higher concentration of sodium nitrate and sodium sulphate.

Sample *Sal3* (Figure 10.5c) belonged to an encrustation strongly anchored to the paint layer. This fact was probably due to the presence of sodium carbonate (natron, $Na_2CO_3 \cdot 10H_2O$, main Raman band at 1069 $cm^{-1}$), detected together with sodium sulphate (thenardite) and lausenite ($Fe_2(SO_4)_3 \cdot 5H_2O$, main Raman band at 1024 $cm^{-1}$).

Finally, sample *Sal4* (Figure 10.5b) was also distinguished by a strong cohesion attributable to the presence of gypsum. Calcium sulphate was the prevailing element of this efflorescence, which was also composed of potassium nitrate (niter, main Raman band at 1050 $cm^{-1}$).

These results are consistent with other studies, which demonstrated the influence of the salt composition in the appearance of efflorescence [6]. The presence of lausenite also reflects the intense degradation that is happening on the walls, which promotes the reaction between efflorescence salts and pigments.

## Efflorescence salts distribution

The restoration works failed in the protection of mural painting from further degradation probably due to the problems caused by water infiltration from the

soil. Thus, with the aim to trace dynamics and causes of these degradations, further micro-samples were taken to carry out deeply analyses in the laboratory.

Concretely, four mortar samples were taken at different heights (10, 50, 100 and 150 cm) from an area characterized by the presence of efflorescence salts and an intensive degradation of the plaster (see Figure 10.7).

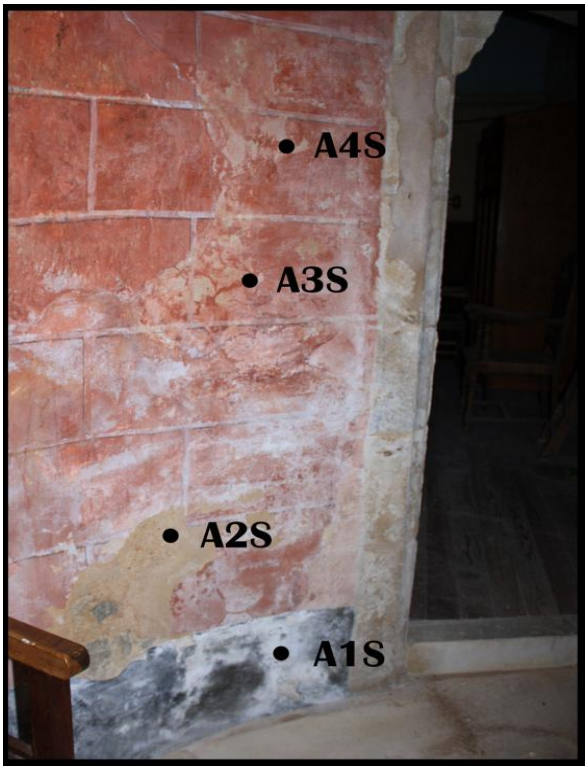


*Figure 10.7: Area characterized by efflorescence salts and degradation of the plaster. Four mortar samples were selected to be analyzed by Ion Chromatography after performing the soluble salt tests.*

The purpose was to identify their salt content and to relate it with the spatial (vertical) distribution. Taking advantage of the presence of some gaps in the paint layer it was possible to collect mortar samples (0.15 to 0.20 g) without causing further damage to the mural painting. Then, the quantification of soluble salts was conducted by the ICS 2500 Ion Chromatograph described in section 4.4.1.

According to the Table 10.1, chromatographic results showed the presence of sodium, potassium, calcium, magnesium, strontium, chloride, sulphate and nitrate ions with variable concentration depending on the sample. Due to the nature of the mobile phase used, it was not possible to analyze the concentration of the dissolved bicarbonate. It was then theoretically determined through the

completion of the mass balance and electroneutrality in the liquid extracts after performing the soluble salt tests [7].

*Σ (valence * cation conc.) - Σ (valence * anion conc.) = Bicarbonate concentration*

This value, added to the chromatographic data, helped to better understand the salt distribution as well as the mechanism of degradation.

*A1S* and *A2S* samples (10 and 50 cm, respectively) showed a high concentration of the sulphate anion and at the same time the almost total absence of dissolved bicarbonate. This fact demonstrated that the degradation in the lower part of the wall was so high as to cause the dissolution of the cementing matrix of plaster (calcite) through acid attack (see below). This deduction was confirmed by Raman analyses made on the samples, which always showed the presence of the gypsum mean peak (1008 $cm^{-1}$) instead of calcite (1085 $cm^{-1}$). These results explain the disaggregation process showed in the areas where *A1S* and *A2S* were sampled.

In *A3S* and *A4S* samples, a high concentration of chloride and nitrate anions and sodium and magnesium cations was detected. As shown in Table 10.2 chemometrics analyses demonstrates the high correlation between these analytes, suggesting the presence of several salts such as sodium chloride (r = 0.971), magnesium chloride (r = 0.883), sodium nitrate (r = 0.963), magnesium nitrate (r = 0.867), calcium sulphate (r = 1.000) and strontium sulphate (r = 0.973).

Finally, these analyses proved the spatial separation of salts. Calcium sulphate and strontium were concentrated in the basal part of the wall. In contrast, the compounds based on chloride and nitrate crystallized at higher heights. This spatial separation was mainly due to the different ascending ability of each ion [8,9]: Sulphates have less mobility than nitrates and chlorides and for this reason are concentrated in the lower part of the walls. This behaviour explains also why the concentration of nitrates and chlorides is so high on the top.

*Table 10.1: Concentration (mg/kg) obtained in the chromatographic analysis of soluble salts. *The $HCO_3^-$ value was theoretically determined.*

| mg/kg | $Na^+$ | $K^+$ | $Mg^{2+}$ | $Ca^{2+}$ | $Sr^{2+}$ | $Cl^-$ | $NO_3^-$ | $SO_4^{2-}$ | $HCO_3^-$* |
|---|---|---|---|---|---|---|---|---|---|
| ***A1S*** | 131 ± 18 | 443 ± 21 | <LOD | 52645 ± 1642 | 1813 ± 90 | <LOD | <LOD | 137686 ± 5795 | <LOD |
| ***A2S*** | 165 ± 11 | 240 ± 12 | <LOD | 66029 ± 1890 | 2015 ± 96 | <LOD | <LOD | 185148 ± 5738 | <LOD |
| ***A3S*** | 1425 ± 45 | 734 ± 26 | 2687 ± 61 | 15912 ± 1502 | <LOD | 2472 ± 43 | 10015 ± 163 | 18452 ± 1087 | 29317 ± 3021 |
| ***A4S*** | 1280 ± 179 | 1283 ± 12 | 3403 ± 80 | 25943 ± 2174 | <LOD | 1523 ± 20 | 5839 ± 80 | 46835 ± 2056 | 48713 ± 3317 |

*Table 10.2: Relying in the value of critical r (0.7) positive correlations between the detected ions are marked.*

| | $Na^+$ | $K^+$ | $Mg^{2+}$ | $Ca^{2+}$ | $Sr^{2+}$ | $Cl^-$ | $NO_3^-$ | $SO_4^{2-}$ | $HCO_3^-$ |
|---|---|---|---|---|---|---|---|---|---|
| **$Na^+$** | 1.000 | | | | | | | | |
| **$K^+$** | 0.800 | 1.000 | | | | | | | |
| **$Mg^{2+}$** | 0.969 | 0.919 | 1.000 | | | | | | |
| **$Ca^{2+}$** | -0.962 | -0.768 | -0.914 | 1.000 | | | | | |
| **$Sr^+$** | -0.992 | -0.861 | -0.984 | 0.971 | 1.000 | | | | |
| **$Cl^-$** | 0.971 | 0.648 | 0.883 | -0.962 | -0.945 | 1.000 | | | |
| **$NO_3^-$** | 0.963 | 0.624 | 0.867 | -0.957 | -0.935 | 0.999 | 1.000 | | |
| **$SO_4^{2-}$** | -0.961 | -0.785 | -0.919 | 1.000 | 0.973 | -0.954 | -0.948 | 1.000 | |
| **$HCO_3^-$** | 0.912 | 0.966 | 0.985 | -0.843 | -0.941 | 0.788 | 0.768 | -0.853 | 1.000 |

## 10.3 Determining the influence of environmental context

The detected intense degradation processes proved the presence of a strong input of dissolved ions from the soils. The origin of the ions could be attributed to several causes. Among them, the extensive agricultural activities all around the Alaiza village could have a significant role in both formation of efflorescence and degradation of mortars from the lower part of the walls. Indeed, many studies prove that the water of agricultural soils recorded a large increase in the concentration of nitrate and sulphate due for example to the ammonium products ($NH_4NO_3$ or $KNH_4(NO_3)_2$ and $(NH_4)_2SO_4$) used for fertilization [10].

In order to confirm this hypothesis, further analyses were carried out. In a first step, information about the methods and the products used to fertilize the farmlands surrounding Alaiza was collected.

In this way, it was possible to identify that most of the farmers make use of two specific products. The first one, named "*NAC 27*", is a nitrogen-based fertilizer that contains a concentration of ammonium nitrate ($NH_4NO_3$) between 20 and 28%. Beside, the "*NPK 14-20-9*" fertilizer contains 14% of ammonium nitrate ($NH_4NO_3$), 20% of phosphorus pentoxide ($P_2O_5$) and 9% of potassium oxide ($K_2O$). The *NAC 27* product is generally applied in a single operation the month before seeding (February). On the contrary, the *NPK 14-20-9* fertilizer is periodically applied over the period that goes from germination to harvest.

With the objective of verifying whether the use of fertilizers leads to the increase of soluble salts concentration in the aquifer, water samples were periodically collected from an irrigation channel flowing just a few meters away from the church.

Water samples, collected every second week from January to April 2016, were then analyzed by means of the Crison micropH 2000 potentiometer (coupled to different ion selective electrodes) with the purpose of evaluating possible variations in the concentration of nitrate ($NO_3^-$) and ammonium ($NH_4^+$) ions.

The obtained data highlighted that ammonium did not show any significant variation during the period of monitoring. In fact, its concentration varied from 27 to 33 mg/L, which is in line with the average $NH_4^+$ concentration of the nearby Alegria river (25-40 mg/L). Moreover, clean rivers and water flows near Alaiza, present a background $NH_4^+$ concentration of 25-35 mg/L.

On the contrary, as shown in Figure 10.8, the collected samples highlighted a strong increase of nitrates content just after the fertilization of agricultural fields (end of February) with *NAC 27*, reaching a concentration value of 345 mg/L.

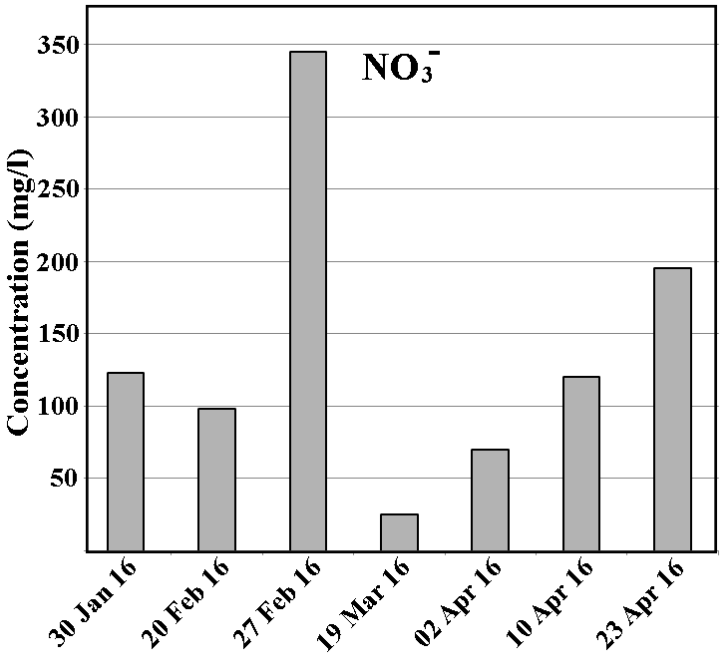


*Figure 10.8: Nitrate concentrations of water samples periodically collected from the irrigation channel near the Alaiza church.*

This data acquires even greater significance when compared to the average nitrate concentration value of the Alegria river (30-50 mg/L) [11], suggesting that the use of fertilization products in the agricultural fields located in the surroundings of Alaiza increases the soluble salt content of the aquifer.

At this point, it must be emphasized that the topography around Alaiza directs all the waters from the soils and the runoff to the lower part of the village where the church under study is located. Due to that drainage, the water coming from the farmlands is constantly channelled to this area. That is also the cause of the several floods suffered by the church in the past and recent years. The superficiality of the aquifer, proved by the presence of an irrigation channel just a few meters from the church, constantly wets the foundation of the church (see Figure 10.9). This fact can explain the nearly permanent presence of infiltration waters, with all of its dissolved ions, from the foundations of the church to its walls.

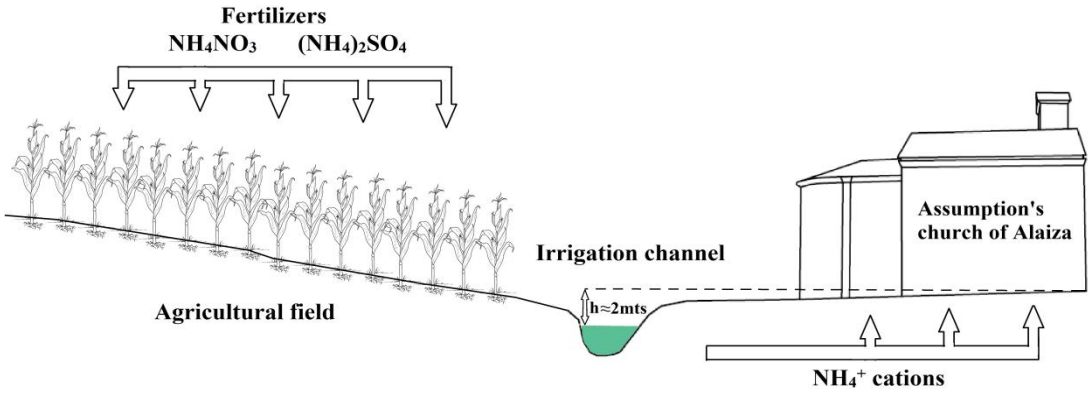


*Figure 10.9: As visually resumed in this image, the chemicals used to fertilize the agricultural fields surrounding the village of Alaiza represent the primary cause of the increase of the concentration of acidic ion $NH_4^+$ in the soil. These cations ascent the walls of the Assumption's Church thanks to the infiltration waters provoking the main deteriorations of the medieval paintings such as efflorescence salts and mortar disaggregation.*

In addition of leading to the onset of extensive efflorescences, the input of soluble salts from the soil also plays a key role in the process of mortar disaggregation. Indeed, the dissolved $NH_4^+$ cation, can be considered the responsible of the dissolution of calcite mortar by an acid/base reaction (reactions 10.1 and 10.2):

$$CaCO_3\,(s) + NH_4^+ \rightleftarrows Ca^{2+} + HCO_3^- + NH_3\,(g), \text{ if pH} \approx 8 \qquad \text{(Reac. 10.1)}$$

$$CaCO_3\,(s) + 2NH_4^+ \rightleftarrows Ca^{2+} + CO_2\,(g) + H_2O + 2NH_3\,(g), \text{ if pH} \approx 6 \qquad \text{(Reac. 10.2)}$$

According to the results of bicarbonate concentrations shown in Table 10.2, the first reaction is the predominant one in the high parts of the walls (samples *A3S* and *A4S*) while the second is the one acting in the lower parts (samples *A1S* and *A2S*). Moreover, as $CO_2$ and $NH_3$ are gases, and the walls have usually an excess of calcite, it is difficult to find $NH_4^+$ in the soluble salts present in the mortars. But as a consequence of the acid/base reactions, dissolved $Ca^{2+}$ was found, together with the previously mentioned $Na^+$, $K^+$, $Cl^-$, $NO_3^-$ and $SO_4^{2-}$, in the soluble salts present in the walls.

The detection of $NH_4^+$ salts by Raman spectroscopy in the upper part of the walls reflects the active role of this cation in the degradation of the lower parts, because $NH_4^+$ salts can only be present if the impact of this ion is constant over years and if the calcite on the lower parts has completely disappear, as demonstrated in the analyses.

## 10.4 Conclusions

In this chapter, the usefulness of portable analytical techniques in the study of *Cultural Heritage* has been further demonstrated. In fact, thanks to the use of portable Raman and ED-XRF spectrometers, it was possible to characterize the original materials composing the paintings and to distinguish them from those used in recent conservation treatments.

In comparison with the mural paintings from Gaceo, the walls of Alaiza's church showed much more extensive degradation processes. The main problems are located in the lower part of the walls, where a massive crystallization of efflorescence salts critically compromises the integrity of the murals.

Thanks to spectroscopic and chromatographic analyses carried out in the laboratory on mortar and water samples, it was possible to determine the soluble salts composing the efflorescences, their spatial distribution and above all, the cause leading to ions accumulation in the walls. Indeed, as showed in Figure 10.9, fertilization of agricultural fields, combined with the superficiality of the aquifer, explain the nearly permanent input of soluble salts from the soil. The constant supply of new ions increases their concentration in the walls, causing the crystallization of efflorescences and the dissolution of calcite. In some areas this process is so intense as to cause the complete disaggregation of the mortar.

Considering that the disaggregation of mortars leads the irrimediable lost of the painted layer, it is of paramount importance for restorers to find a reliable method to consolidate the painting substrate. To solve this problem, conservation scientists are developping novel conservation products aimed at consolidating wall paintings and other calcium carbonate-based materials.

As explained in the introduction section, one of most interesting advances in this field is the syntesis of calcium hydroxide nanoparticles that, once applied on the surface, penetrate into the mortar and consolidate it through a carbonation reaction [12,13]. Even though, in this case of study, the use of calcium hydroxide nanoparticles is suggested, this proposal cannot be considered definitive until the achievement of structural interventions. In fact, the crystallization of efflorescence salts can be only prevented by isolating the walls of the church from direct contact with the ground and with the ions contained therein.

## 10.5 References

**[1]** D.V. Thompson (1956) The Materials and Techniques of Medieval Painting. *Dover Pubblications, Mineola (USA)*, pp 1040.

**[2]** Diputación Foral de Álava (1984) Documento DAIC 16017 023000*, Archivo Historico diputación Foral de Álava, Vitoria-Gasteiz (Spain)*.

**[3]** V. Walsh, T. Chaplin (2008) Pigment Compendium: A Dictionary and Optical Microscopy of Historical Pigments. *Butterworth-Heinemann, Oxford (UK),* pp 960.

**[4]** A. Broggi, E. Petrucci, M.P. Bracciale. M.L. Santarelli (2012) FT-Raman spectroscopy for quantitative analysis of salt efflorescences. *Journal of Raman Spectroscopy,* 43, 1560-1566.

**[5]** I. Costantini, M. Veneranda, N. Prieto-Taboada, L. Bellot-Gurlet, K. Castro, J.M. Madariaga (2016) Comparison of semiquantification experimental methodologies usin micro-Raman spectroscopy: Palme software as an alternative tool for the study of salt efflorescence*. Journal of Raman Spectroscopy*, 47, 1415-1421.

**[6]** V. López-Acevedo, C. Viedma, V. González, A. La Iglesia (1997) Salt crystallization in porous construction materials. II. Mass transport and crystallization processes. *Journal of Crystal Growth,* 182, 103-110.

**[7]** N. Prieto-Taboada, M. Maguregui, I. Martínez-Arkarazo, M.A. Olazabal, G. Arana, J.M Madariaga (2011) Spectroscopic evaluation of the environmental impact on black crusted modern mortars in urban-industrial areas. *Analytical and Bioanalytical Chemistry*, 399, 2949-2959.

**[8]** C.M. Grossi, R.M Esbert (1994) Las sales solubles en el deterioro de rocas monumentales. Revision bibliográfica. *Materiales de Construcción,* 44, 15-30.

**[9]** M. Auxiliadora Vázquez, E. Galán, P. Ortiz, R. Ortiz (2013) Digital image analysis and EDX SEM as combined techniques to evaluate salt damp on walls. *Construction and Building Materials,* 45, 95-105.

**[10]** J.M.S. Pérez, I. Antigüedad , I. Arrate , C. García-Linares, I. Morell (2003) The influence of nitrate leaching through unsaturated soil on groundwater

pollution in an agricultural area of the Basque country: a case study. *Science of the Total Environment,* 317, 173-187.

**[11]** X. Sánchez-Vila, M.C. Cabrera, M. Valverde (2006) De la toma de datos a la realización de modelos de agua subterránea a la gestión integrada. *Instituto Geológico y Minero de España*, *Madrid (Spain),* pp 657.

**[13]** A. Daehne, C. Herm (2013) Calcium hydroxide nanosols for the consolidation of porous building materials – result from EU-STONECORE. *Heritage Science*, 1: 11.

**[14]** R. Giorgi, M. Ambrosi, N. Toccafondi, P. Baglioni (2010) Nanoparticles for Cultural Heritage Conservation: Calcium and Barium Hydroxide Nanoparticles for Wall Painting Consolidation. *Chemistry-A European Journal,* 16, 9374-9382.

CHAPTER 11:

# COMPARISON OF DEGRADATION PATHWAYS JEOPARDIZING TWO MURALS EXPOSED TO DIFFERENT ENVIRONMENTS

## Mural paintings from Pompeii

As previously mentioned, the city of Pompeii was completely destroyed during the eruption of the Mount Vesuvius occurred in A.D. 79. Ashes, pumices and debris that poured down caused the sudden burial of the city to a depth of several meters [2]. The volcanic debris sealed the remains of Pompeii, favouring their optimal preservation during centuries. Since archaeological excavations started in 1748 [3], more than two thirds of the city have been brought to light, offering to humanity a full and unique picture of the daily life of ancient Roman civilization.

As explained above, thanks to the characterization of materials and production techniques used in the past it is possible to know important aspects about ancient societies.

Therefore, due to the remarkable conservation state of its remains, the archaeological site of Pompeii can be considered as an unique open-air laboratory in which the work of conservation scientists allows to deepen the knowledge about Roman civilization.

In this context, the present chapter summarizes the results obtained from the characterization of two mural paintings conserved in the Ariadne's House, which are exposed to different environments. The east facing wall of room 56, located in the ground floor of the house, has no roof and is directly exposed to the external environment. On the contrary, the second mural, from a basement built just below room 56, has been constantly sheltered from sun-light and temperature fluctuation but expose to high relative humidity.

## 11.1 Characterization of original materials

The campaign of analysis, carried out in 2014, was first focused on the characterization and comparison of the original materials composing the two murals.

To achieve this objective, several portable instruments were used. For the molecular identification of chemical compounds, Raman spectroscopy played a key role. In fact, the chemical assessment of the paintings was performed using both, the InnoRam$^{TM}$-785S (equipped with a 785 nm laser) and the BWS5445-532S (equipped with a 532 nm laser) portable Raman spectrometers described in chapter 4. In addition, molecular data was complemented by the elemental characterization of mortars and pigments, which was carried out by means of the LIBS system (chapter 4).

**Mortars**

Starting from the analyses performed in the basement, analytical data proved the presence of two mortars. The superficial one, also representing the white background of the painting, was composed of pure calcium carbonate ($CaCO_3$, main Raman peaks at 155, 282, 713 and 1086 $cm^{-1}$). This fine mortar was only applied within the rectangular perimeter of the mural painting including the paint decoration. For this reason, analyses carried out outside the painted perimeter allowed to characterize the composition of the preparation raw mortar (*arriccio*). Molecular analyses enabled the detection of volcanic material aggregates, such as augite ($(Ca,Na)(Mg,Fe,Al,Ti)(Si,Al)_2O_6$, main Raman peaks at 136, 229, 325, 357, 391,

480, 532, 665, 860, 964, 1010, 1086, 1461, 1523 and 2436 $cm^{-1}$) and albite ($AlSi_3O_8$, main Raman peaks at 290, 480 and 507 $cm^{-1}$), in a binder composed of calcite and dolomite ($CaMg(CO_3)_2$, main Raman peaks at 174, 297 and 1094 $cm^{-1}$). As can be observed in Figure 11.1, numerous collected spectra also highlighted the presence of a small peak at 1048 $cm^{-1}$, suggesting the presence of potassium nitrate ($KNO_3$).

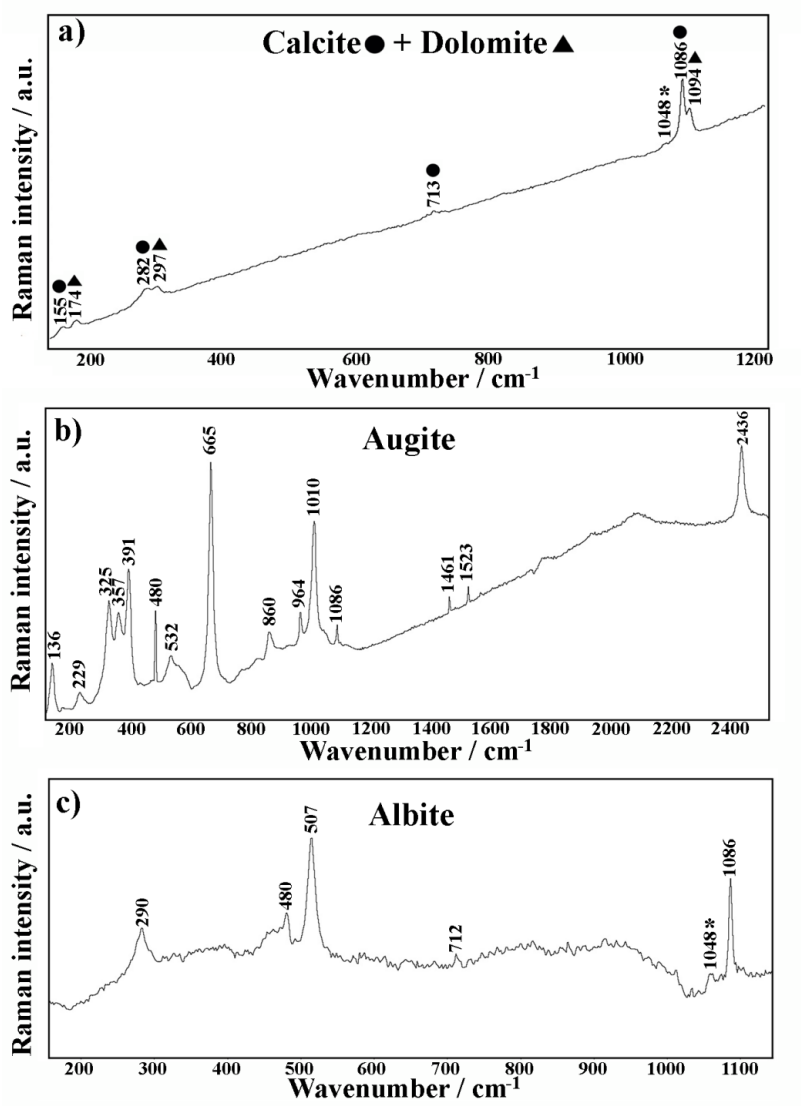


*Figure 11.1: Raman spectra collected from the arriccio layer of the basement, showing the presence of a) calcite and dolomite as binder material, b) augite and c) albite as volcanic material aggregates. The Raman peak labelled with an asterisk suggests the additional presence of potassium nitrate ($KNO_3$) soluble salt.*

As described by R. De Luca et al. in 2014, the use of volcanic materials as aggregate was a very common technique in ancient Pompeii to increase the strength, the hydraulicity and the durability of the mortars [4].

Besides, several Raman analyses were also carried out on the *arriccio* layer still conserved on the west facing wall of room 56. The compositional results from the study of both binder and aggregates agreed with the results obtained from the analysis of the second mortar of the basement, suggesting the same fabrication in both rooms.

Molecular analyses were supported by the elemental data provided by the portable LIBS system. Plasma emissions collected from the two mortars were comparable and agreed with the molecular information provided by Raman analyses. That is, all LIBS spectra remarked the presence of very intense signals of Ca coming from the calcium carbonate used as binder material. In addition, several elements such as Mg, Al, Si, K and Na were also detected. According to the molecular results previously described, their signal could come from the laser ablation of both, volcanic material aggregates and $KNO_3$ soluble salt.

**Pigments**

Taking into account that the wall of room 56 lost every trace of mural painting, the characterization of pigments was only focused on the *fresco* conserved inside the basement. To characterize the colour palette used by the artists, more than 50 areas were analyzed using both molecular and elemental portable techniques in a complementary way.

Starting from elemental analyses, all LIBS spectra collected from both red (Figure 11.2a) and yellow (Figure 11.2b) areas showed several Fe emission lines in the spectral range between 230 and 390 nm, suggesting that both colours were obtained using iron-based pigments. Analyzing the intensity of the Fe peaks and their ratio with the Ca signal from the mortar, it was systematically obtained that red areas gave more intense iron peaks than the yellow ones. This difference may be influenced by several factors, for instance the thickness of the paint layer as well as the chemical composition of the pigments.

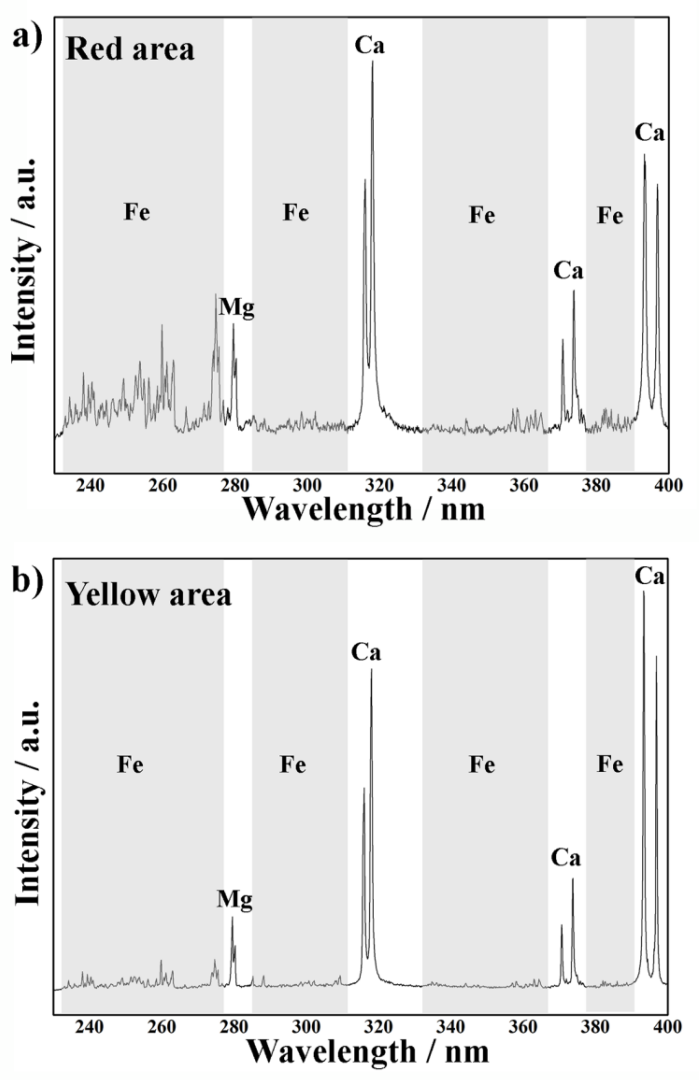


*Figure 11.2: LIBS spectra collected from red (a) and yellow (b) areas.*

The same areas of interest were then studied by means of the InnoRam$^{TM}$-785S Raman system. Hematite (α-$Fe_2O_3$, characteristic Raman peaks at 225, 244, 291, 409, 497 and 611 $cm^{-1}$, Figure 11.3a) and red ochre ($Fe_2O_3 \cdot nH_2O$, characteristic peaks at 224, 295 and 405 $cm^{-1}$, Figure 11.3b) were the most detected compounds in the red areas. Furthermore, it was proved that the darkest shades in red decorations were obtained by adding carbon black (Figure 11.3d, broad band at 1360 and 1590 $cm^{-1}$). On the other hand, the main iron phase identified in the yellow areas corresponded to goethite (α-FeO(OH), Raman peaks at 245, 298, 397, 553 and 683 $cm^{-1}$, Figure 11.3c).

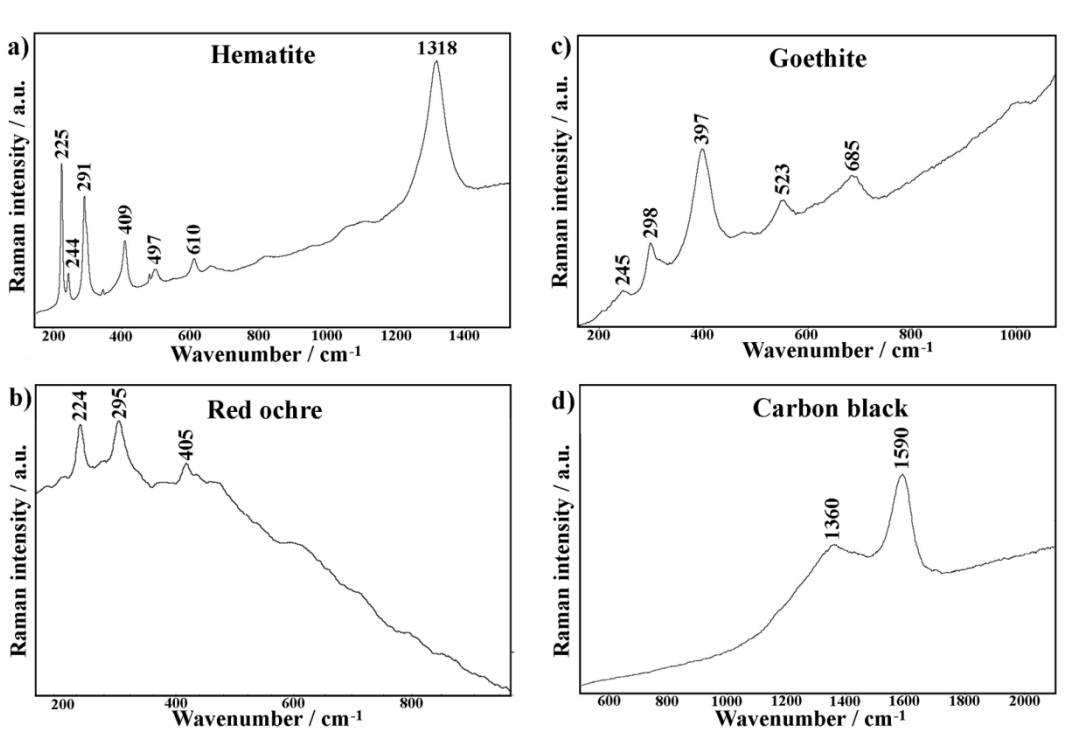


*Figure 11.3: Raman spectra of hematite, goethite and red ochre collected by means of the innoRam$^{TM}$-785S system, proving the use of Fe-based pigments in both red and yellow decoration. In several red areas, carbon black was also detected.*

The Raman characterization of green areas was carried out by means of the 532 nm excitation laser. By analyzing more than 10 points of interest, the use of a green earth with a high celadonite content ($KMgFeSi_4O_{10}(OH)_2$, main Raman peaks at 179, 271, 322, 395, 460, 552 and 701 $cm^{-1}$) was proved (Figure 11.4) [5].

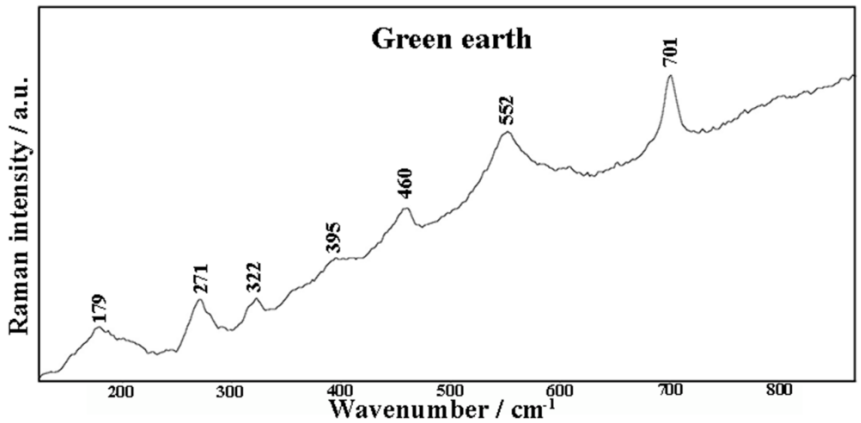


*Figure 11.4: Raman spectrum from the green areas collected by means of the BWS5445-532S system, showing the use of a green earth pigment (rich in celadonite).*

## 11.2 Characterization of degradation patterns

In recent years, the analytical studies carried out by most of the research groups are more and more directed towards the understanding of the degradation mechanisms jeopardizing the conservation of the archaeological site [6].

In fact, it is important to highlight that the volcanic material removal carried out for the resumption of Pompeian remains also resulted in the activation of several deterioration processes [7,8]. Indeed, in the last 270 years, the conservation of Pompeian *frescoes* has been constantly undermined by the destructive effects of many degradation phenomena, such as thermal and humidity fluctuations, direct exposure to sunlight, irreversible acid-base reactions between acid atmospheric compounds and wall materials, leaching processes triggered by rainwater and capillary rise of soluble salts from the soil [9,10].

In this context, the second purpose of the work presented in this chapter was to determine and compare the main degradation processes affecting the conservation state of the two murals.

Considering that the degradation patterns observed on the wall of room 56 were very different from those of the basement, their description has been divided into two specific sections.

### *11.2.1 Study of room 56*

The west facing wall of room 56 has been directly exposed to weathering and direct atmospheric pollution for almost two centuries. Considering both, climatic and environmental context, the main degradation pathways involving the complete loss of the painted layer can be described as follows:

**Leaching**

In the *fresco* technique, pigments are applied on a layer of calcium hydroxide ($Ca(OH)_2$) that reacts with the atmospheric $CO_2$ producing calcium carbonate ($CaCO_3$). The carbonation reaction fixes the pigments to the substrate, providing great stability to the painted layer. Nevertheless, ancient *frescoes* can be subjected to leaching process when contact with acid solutions. In the case of room 56, the leaching process is triggered by the direct exposure of the wall to rainwater.

As proved in previous works [11], the pH value of the rainwater falling in the Vesuvius region is strongly influenced by the dissolution of aerosol with maritime, continental and anthropogenic origins. The abundant atmospheric acid pollutants ($CO_2$, $NO_x$, $SO_x$) dissolved in the rainwater react irreversibly with the calcium carbonate ($CaCO_3$) of the binder first, and after, of the mortars, producing calcium hydrogen carbonate (reaction 11.1). This soluble compound can dissociate into $Ca^{2+}$ and $HCO_3^-$ ions and are easily removed from the wall surface by rain-wash (reaction 11.2).

$$CaCO_3\,(s) + CO_2\,(g) + H_2O \leftrightarrow Ca(HCO_3)_2\,(\text{soluble}) \qquad \text{(Reac. 11.1)}$$

$$Ca(HCO_3)_2 \leftrightarrow Ca^{2+} + 2HCO_3^- \qquad \text{(Reac. 11.2)}$$

The leaching process is extremely damaging for *frescoes* since, as in the presented case, can dissolve the carbonate-based mortars of exposed mural paintings [12].

**Thermal fluctuations**

The *arriccio* layer preserved on the west facing wall of the exedra had less compactness and stability compared to the mortar still conserved on the north facing wall of the same room. As the walls suffer the same leaching process described above, it was then proposed that the difference in their conservation state was connected to their orientation respect to the sun. In fact, the west facing wall analyzed in this chapter was much more exposed to direct sun-light irradiation than the north facing one. This fact means significant differences in terms of daily and seasonal thermal fluctuations.

As clearly demonstrated in other works [11], strong temperature fluctuations can afford a negative impact on the conservation state of wall paintings. In this sense, Figure 11.5 summarizes the temperature data collected by the weather station located inside the archaeological site of Pompeii (from December 2014 to September 2016).

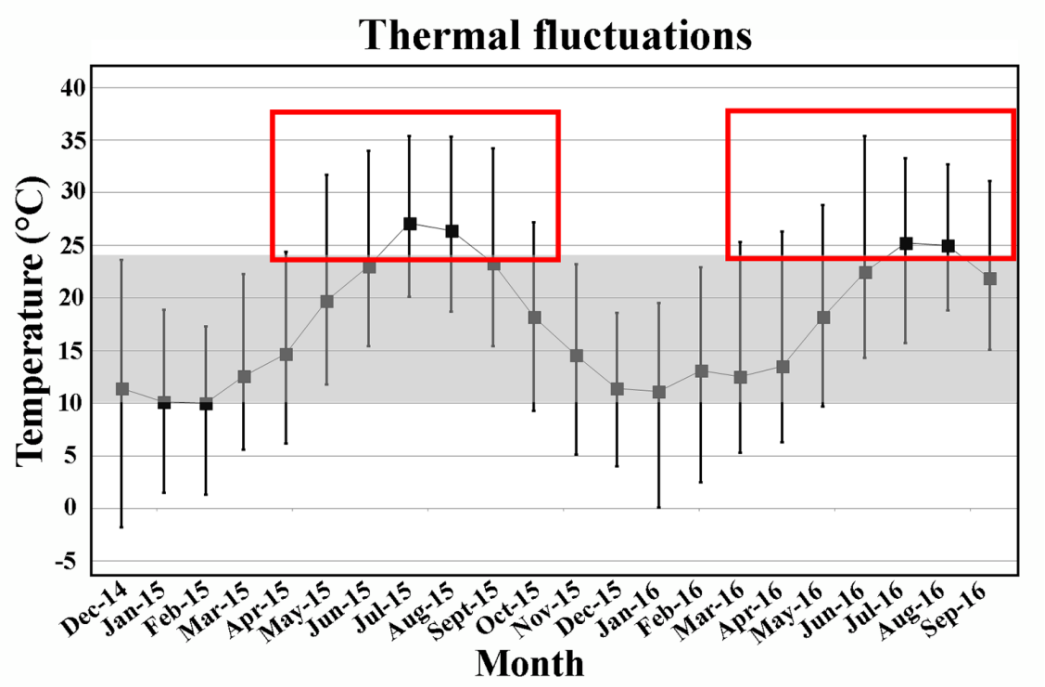


*Figure 11.5: Average thermal values monitored from December 2014 to September 2016 by the weather station located inside the archaeological site of Pompeii (Italy). Red squares enclose the most critical temperature values for the conservation of mural painting.*

As it can be observed in Figure 11.5, most of the values collected from December 2014 to September 2016 do not fit within the ideal range of temperature recommended by the UNI 10829 for the optimal conservation of mural paintings (T = 10-24 °C) [13]. This means that their conservation is mostly endangered by temperatures higher than 24 °C (as highlighted in Figure 11.5, it is occurring 6-7 months per year), which enhances the thermal expansion of *frescoes* materials. The diurnal and seasonal variations detected by the weather station, accentuated by the exposition of the wall to direct sun-light, involve important physical stresses to the original materials. These stresses are mainly due to the different behaviour of the materials present in the mortar due to thermal fluctuations. In fact, the coefficient of volumetric thermal expansion (α), analyzed in a range of temperature between 20 and 400 °C, is equal to 2.24 ($10^{-5}$ per °C) for albite, 2.19 ($10^{-5}$ per °C) for augite and 2.01 ($10^{-5}$ per °C) for calcite [14]. The cycles of expansion and contraction, affecting both binder and aggregates, led to the formation of microfractures in the mortar, resulting in a decrease of compactness and loss of material.

### *11.2.2 Study of the basement*

The west facing wall of the basement did not present the degradation phenomena caused by leaching and thermal fluctuations since, being under the ground level, it has been constantly sheltered from direct rainwater and sun-light exposure. However, as summarized in Figure 11.6, several other degradation evidences were identified.

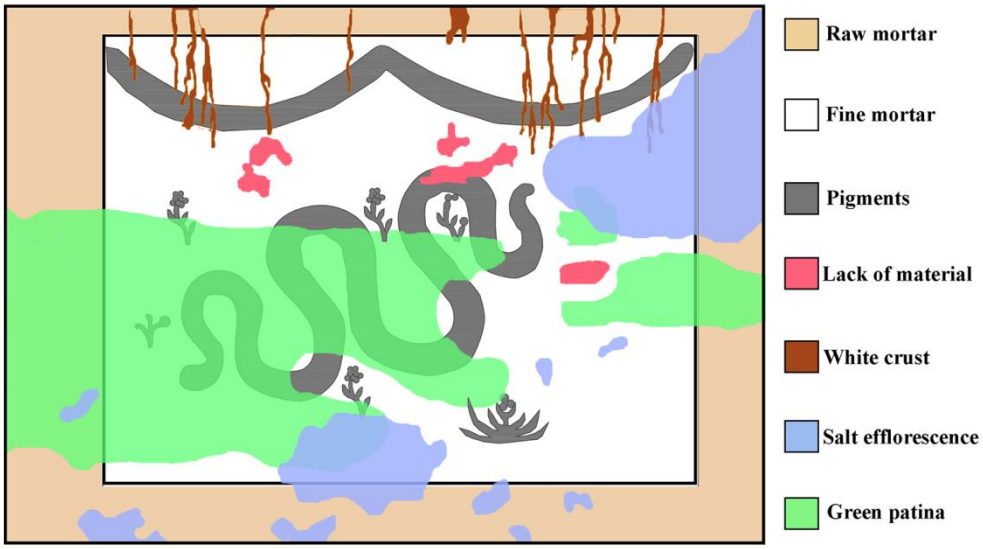


*Figure 11.6: Original and degradation materials detected on the basement's wall.*

**White crusts**

As represented in Figure 11.6, several white drips rising from the vault of the basement were partially covering the upper part of the mural painting. Those white crusts, analyzed by means of Raman spectroscopy, were identified as pure calcium carbonate.

Considering the environmental context, their formation was probably induced by a solubilization/recrystallization process of the binder used on the vault structure. In fact, as explained before, the rain that falls on Pompeii is able to dissolve carbonates by following the reactions 11.1 and 11.2. Considering that room 56 has no roof, the rainwater wets its floor and percolates through the structure of the underlying vault. During this process, the acid solution transforms the $CaCO_3$ into $Ca(HCO_3)_2$ and pours down the perimeter walls. Then, the solution suffers $H_2O$ evaporation and $CO_2$ release, causing the precipitation of white crusts made of calcium carbonate (reaction 11.3).

$$Ca(HCO_3)_2 \rightarrow CO_2\,(g) + H_2O + CaCO_3\,(s) \qquad \text{(Reac. 11.3)}$$

The solubilisation and recrystallization of carbonates is a very common process in both urban and natural environments. For instance, it is the principal cause of speleothems formation in caves and this phenomenon was also identified in more modern building materials used in constructions belonging to the *Immovable Heritage* [15].

**Efflorescence Salts**

As can be seen in Figure 11.6, several efflorescence salts were detected along the wall surface. Considering their shape, size and position, different groups were identified. The first one includes the numerous small soluble efflorescence salts located in the lower part of the wall (below 50 cm). The second one corresponds to the wide white efflorescence standing 120-200 cm high from the floor of the basement.

Starting from the first group, the molecular characterization carried out by Raman spectroscopy allowed the detection of sodium nitrate ($NaNO_3$, main peaks at 188, 722 and 1065 $cm^{-1}$) and calcium sulphate dihydrate ($CaSO_4 \cdot 2H_2O$, main peaks at 180, 414, 493 and 1008 $cm^{-1}$) (Figure 11.7).

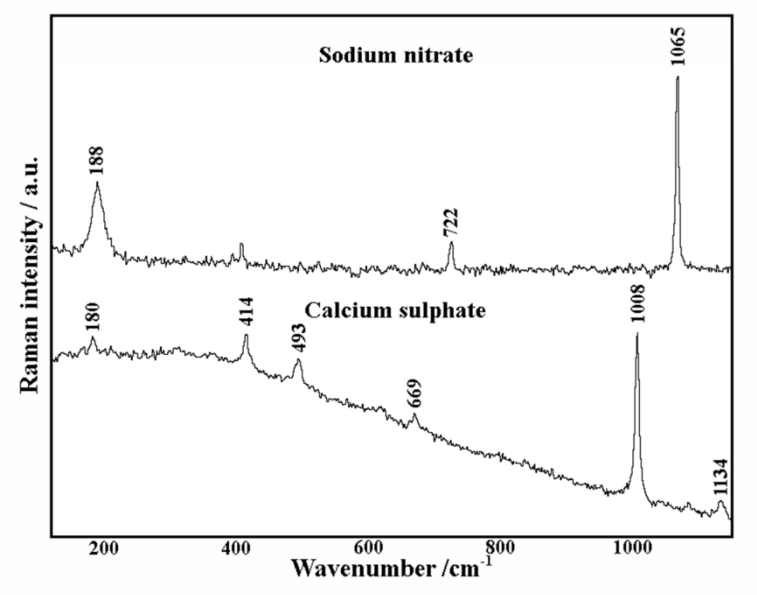


*Figure 11.7: Raman spectra from the efflorescence salts detected on the lower part of the wall, showing the presence of sodium nitrate and calcium sulphate compounds.*

In order to identify the possible origin of the soluble salts generating efflorescences, burial material was collected and analyzed by Ion Chromatography. The soluble salt extraction was carried out following an ultrasound-assisted extraction method [16] and the obtained results are showed in *Table 11.1*:

*Table 11.1: Concentration values (mg/kg) of soluble salts extracted from burial material samples.*

| Cations (mg/kg) | | | Anions (mg/kg) | | |
|---|---|---|---|---|---|
| $Na^+$ | $K^+$ | $Ca^{2+}$ | $Cl^-$ | $NO_3^-$ | $SO_4^{2-}$ |
| 556 ± 21 | 1169 ± 46 | 6675 ± 36 | 3041 ± 46 | 9717 ± 98 | 4095 ± 33 |

The high concentration of soluble ions is an important issue since, as in the case of work summarized in chapter 10, they can solubilise (when water is present) and ascent the walls by capillarity, favouring the formation of soluble efflorescence salts. However, the remains of burial material still present inside the basement, being sheltered from atmospheric precipitations, suffered a minimum solubilisation of the salts contained therein. The low solubilisation also limits the capillary rise, explaining why sulphates and nitrates-based degradation patterns were only detected at heights below 50 cm [17].

The efflorescence salts included in the second group, analyzed by means of Raman spectroscopy, were composed of calcium carbonate and calcium sulphate dihydrate. Considering the height, their development could not be explained by the capillary rise of soluble salts from the burial soil still conserved inside the basement. In this case the crystallization process could be triggered by the infiltration of soluble salts from the adjacent soil, located upwards of this room.

**Biological patinas**

The most extended degradation form observed in the basement, and mainly developed on the bottom part of the wall, corresponded to biological patinas.

It must be emphasized that, during the in-situ campaign in 2014, most of the mural paintings conserved in the Ariadne's House were analyzed. However, the artwork preserved inside the basement was the only one jeopardized by biodegradation processes. One of the main reasons lies in the particular environmental context of the basement. In fact, as proved by several works

[18,19], the factors that most contribute to the growth of fungi and algae colonies on murals are high levels of humidity and low exposition to sun-light and temperature fluctuations. The basement of the Ariadne's House, having a relatively stable environment in comparison to outdoors rooms, fully fits with the climate requirements necessary for the growth of heterophilic organisms. However, it must be pointed out that the colonization process was not uniform, but rather focused on the lower part of the wall.

## 11.3 Conclusions

This chapter aimed at the analysis and comparison of two walls (Ariadne's House, Archaeological site of Pompeii, Italy) with a completely different state of preservation.

The multianalytical approach applied for the study of both surfaces, enabled the characterization of original materials as well as the main degradation forms threatening their conservation.

By interpreting the experimental results it was possible to establish that most of the detected degradation processes were directly triggered by the environmental context of the walls.

With regards to the roofless wall of room 56, it was demonstrated that the paint layer has been completely degraded by leaching and thermal fluctuations phenomena (triggered by the direct exposition to sun-light and rainwater).

On the contrary, the second wall, being in a basement located just below the room 56, is protected from the degradation pathways jeopardizing the upper wall. Nevertheless, the mural is threatened by the percolation of rainwater from the ground floor, which has caused a dissolution and re-precipitation of calcium carbonate. Furthermore, Raman and IC analyses proved that the burial material remains inside the basement are the source of ions transported to the wall by rising capillarity that led to the crystallization of efflorescence salts on the painted surface. Finally, the presence of extended biological patinas was visually detected, whose development was certainly favoured by high humidity values and reduced temperature fluctuations of the basement environment.

In conclusion, by comparing the degradation pathways of the two walls, the fundamental role played by the environmental context on the conservation of the wall paintings was remarked.

However, the analyses carried out in the first campaign of analysis did not allow identifying the reasons behind the heterogeneous distribution of biological patinas over the surface of mural painting preserved inside the basement. For this reason, a further campaign was needed with the specific purpose of deepen this issue, as it will be shown in the next chapter.

## 11.4 References

**[1]** M. D'Aprile (2014) Planned conservation and cultural enhancement strategy: the Vesuvius's UNESCO archeological site management, in: *S. Della Torre (ed.) Sguardi ed esperienze sulla conservazione del patrimonio storico architettonico, Nardini,* 189-198.

**[2]** L. Giacomelli, A. Perrotta, R. Scandone, C. Scarpati (2003) The eruption of Vesuvius of 79 AD and its impact on human environment in Pompei. *Episodes*, 26, 234-237.

**[3]** M. Pagano (2005) I primi anni degli scavi di Ercolano, Pompei e Stabiae, Raccolta e studio di documenti e disegni inediti. *L'erma di Bretschneider,* pp 110.

**[4]** R. De Luca, D Miriello, A. Pecci, S. Domínguez Bella, D. Bernal Casasola, D. Cottica, G.M. Crisci (2014) Mortars and plasters from the "garum workshop" at Pompei (Italy): an archaeometric study. *VIII congresso nazionale di Archeometria. Schienze e beni culturali: stato dall'arte e prospettive.*

**[5]** F. Ospitali, D. Bersani, G. Di Lonardo, P.P. Lottici (2008) 'Green earths': Vibrational and elemental characterization of glauconites, celadonites and historical pigments. *Journal of Raman Spectroscopy*, 8, 1066-1073.

**[6]** M. Maguregui, U. Knuutinen, K. Castro, J.M. Madariaga (2010) Raman spectroscopy as a tool to diagnose the impact and conservation state of Pompeian Second and Fourth style wall paintings exposed to diverse environments (House of Marcus Lucretius). *Journal of Raman Spectroscopy*, 41, 1400-1409.

**[7]** M. Maguregui, K. Castro, H. Morillas, J. Trebolazabala, U. Knuutinen, R. Wiesinger, M. Schreiner, J. M. Madariaga (2014) Multianalytical Approach to explain the darkening process of hematite pigment in paintings from ancient Pompeii after accelerated weathering experiments. *Analytical Methods,* 6, 372-378.

**[8]** M. Maguregui, U. Knuutinen, I. Martínez-Arkarazo, K. Castro, J.M. Madariaga (2011) Thermodynamic and Spectroscopic Speciation to Explain the Blackening Process of Hematite Formed by Atmospheric $SO_2$ impact: The case of Marcus Lucretius House (Pompeii). *Analytical Chemistry*, 83, 3319-3326.

**[9]** P. Merello, P. Beltrán, F.J. García-Diego (2016) Quantitative non-invasive method for damage evaluation in frescoes: Ariadne's House (Pompeii, Italy). *Environmental Earth Science*, 75, 165-174.

**[10]** P. Merello, F.J. García-Diego, M. Zarzo (2012) Microclimate monitoring of Ariadne's house (Pompeii, Italy) for preventive conservation of fresco paintings. *Chemistry Central Journal*, 6, 145-160.

**[11]** P. Madonia, M. Liotta (2010) Chemical composition of precipitation at Mt. Vesuvius and Vulcano Island, Italy: volcanological and environmental implications. *Environmental Earth Science*, 61, 159-171.

**[12]** P.F.G. Banfill, E.M. Szadurski, A.M. Foster (2016) Deterioration of natural hydraulic lime mortars, II: Effects of chemically accelerated leaching on physical and mechanical properties of carbonated material. *Construction and Building Materials*, 111, 182-190.

**[14]** UNI 10829 (1999) Works of art of historical importance. Ambient Conditions for the Conservation, Measurement and Analysis [Beni di interesse storico e artistico – Condizioni ambientali di conservazione, misurazione ed analisi], available at: http://store.uni.com/magento-1.4.0.1/index.php/uni-10829-1999.html (May 28th 2017).

**[15]** E.C. Robertson (1988) Thermal properties of rocks. *U.S. Geological Survey*, pp 110.

**[16]** C. García-Florentino, M. Maguregui, H. Morillas, U. Balziskueta, A. Azkarate, G. Arana, J.M. Madariaga (2016) Portable and Raman imaging usefulness to detect decaying on mortars from Punta Begoña Galleries (Getxo, North of Spain). *Journal of Raman Spectroscopy,* 47, 1458-1466.

**[17]** N. Prieto-Taboada, O. Gómez-Laserna, I. Martínez-Arkarazo, M. A. Olazabal, J.M. Madariaga (2012) Optimization of two methods based on ultrasound energy as alternative to European standards for soluble salts extraction from building materials. *Ultrasonics Sonochemistry*, 19, 1260-1265.

**[18]** M.A Vázquez, E. Galán, P. Ortiz, R. Ortiz (2013) Digital image analysis and EDX SEM as combined techniques to evaluate salt damp on walls. *Construction and Building Materials,* 45, 95-105.

**[19]** M. Guglielminetti, C.D.G. Morghen, A. Radaelli, F. Bistoni, G. Carruba, G. Spera, G. Caretta (1994) Mycological and ultrastructural studies to evaluate biodeterioration of mural paintings. Detection of fungi and mites in Frescos of the monastery of St Damian in Assisi. *International Blodeterioration and Biodegradation*, 33, 269-283.

**[20]** O. Pepe, L. Sannino, S. Palomba, M. Anastasio, G. Blaiotta, F. Villani, G. Moschetti (2010) Heterotrophic microorganisms in deteriorated medieval wall paintings in southern Italian churches. *Microbiological Research*, 165, 21-32.

CHAPTER 12:

# LABORATORY ANALYSES TO DEEPEN THE UNDERSTANDING OF BIODETERIORATION PROCESS

## Mural painting from Pompeii

Considering the wide variety of microorganisms, as well as the countless variables that tend to favour or inhibit their growth, comprehensive studies are often needed to fully understand the biocolonization mechanisms of a mural surface.

In the case of the mural painting conserved in the basement of the Ariadne's House, it is clear that the growth of biological patinas over the walls was favoured by the characteristics of the environmental context, such as high levels of humidity and low exposition to sun-light and temperature fluctuations. However, this degradation process strongly attracts the interest of researchers owing to the peculiar spatial distribution of biological patinas, being mainly located in the lower area of the painting.

The bibliographic review carried out with the purpose of collecting more information about the recent history of this painting, excluded past restorative interventions. This fact is corroborated by the analytical studies summarized in

the previous chapter, which excluded the presence of modern pigments and conservation products.

However, the collected documentation helped to find out that the resumption of the painting was carried out in two different stages: the discovery of the upper part dates back to 1988, when the basement was partially excavated to consolidate its damaged barrel vault [1]. In contrast, the lower part was recovered several years later, thanks to the archaeological works started by A. Ribera et al. in 2005 [2].

In order to evaluate the possible connection between colonization phenomena and archaeological excavation works, a second campaign of analysis was performed.

## 12.1 Genomic analysis of biodeteriogens

The first step consisted in the genomic characterization of the biological patinas. To do it, sterile swabs were gently rubber over seven different biocolonized areas (*C1-C7*, Figure 1). Then, the collected biomasses were used to inoculate PDA media in pre-poured Petri dishes. After confirming the growth of biological strains on the medium surface, the Petri dishes were sent to the BAT laboratory (CIAL institute, Madrid) for their study as described in chapter 4.

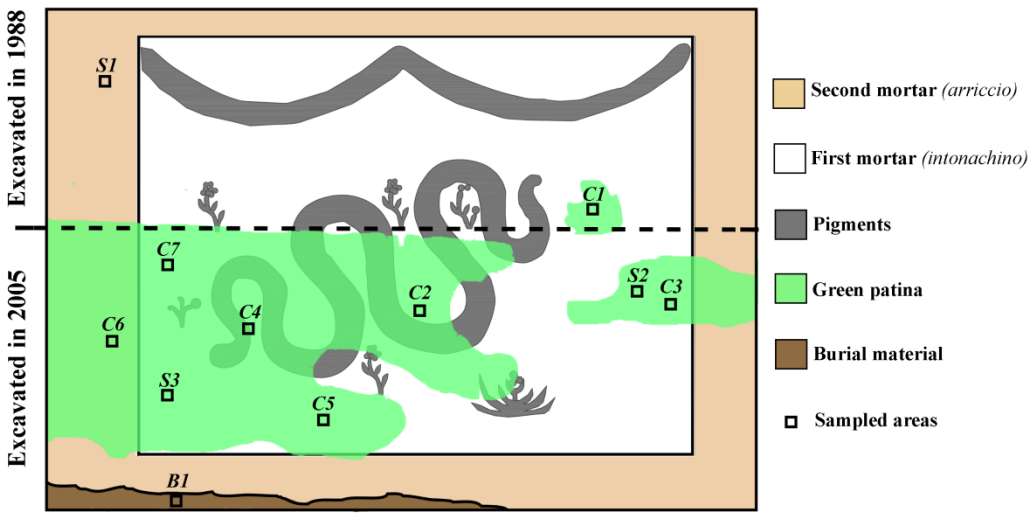


*Figure 12.1: Graphic map showing the heterogeneous spatial distribution of the biological colonies threatening the conservation of the mural painting. In the image, the areas selected for sampling are also highlighted.*

As shown in Figure 12.1 the colonization of biodeteriogens of the upper part of the painting (excavated in 1988) was limited to a blackish biofilm observable on the right part of the artwork.

In order to identify the strain morphology in a micro scale, sample *C1* was analyzed by means of the SEM system.

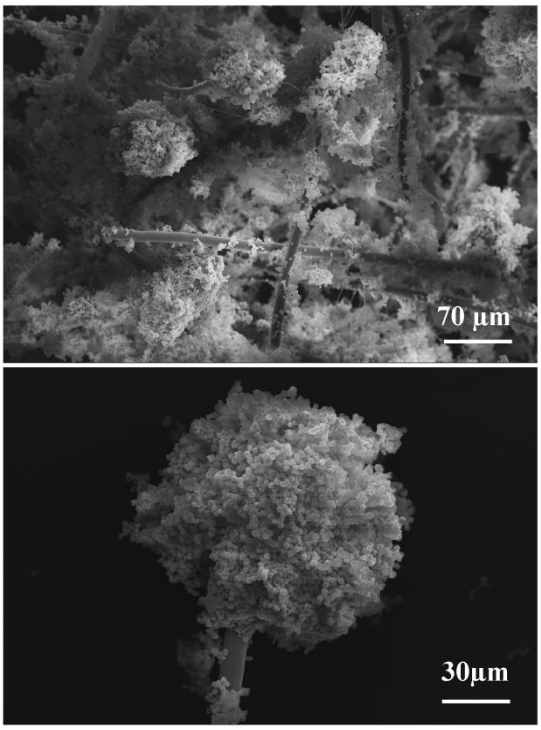


*Figure 12.2: SEM analyses carried out on sample C1. The images highlighted the typical filamentous structure of fungi strains, composed of conidiophores and spores.*

As can be observed in Figure 12.2, the images collected from the sampled biomass display the presence of *conidiophores*, a typical structure of filamentous fungus specialized in the asexual production of spores called *conidia* [3].

With regards to the genomic characterization of the fungus, thanks to DNA sequencing and PCR amplification, it was possible to set a 99% of affinity with the *Aspergillus niger* pattern. This deuteromicetes fungus is able to colonize a wide variety of substrates and its presence has been already detected in many other paintings and artworks [4,5].

The limited biocolonization of the upper part of the mural strongly contrasts with the presence of wide biological patinas covering almost entirely the surface excavated in 2005. Guided by the different shades of colour, six biopatina

samples were collected and analyzed in the laboratory. The results obtained from DNA extraction and sequencing of the isolated organisms, allowed to identify seven different fungal strains. By comparing the isolated 18S sequences to those included in the NCBI database, the presence of *Penicillium turbatum* (match of 100% with the reference pattern), *Penicillium italicum* (match of 100%), *Penicillium commune* (match of 99%); *Alternaria alternate* (mach of 100%), *Allophoma labilis* (match of 99%), *Aspergillus niger* (match of 99%) and *Fusarium equiseti* (match of 100%) fungi was confirmed (Figure 12.3).

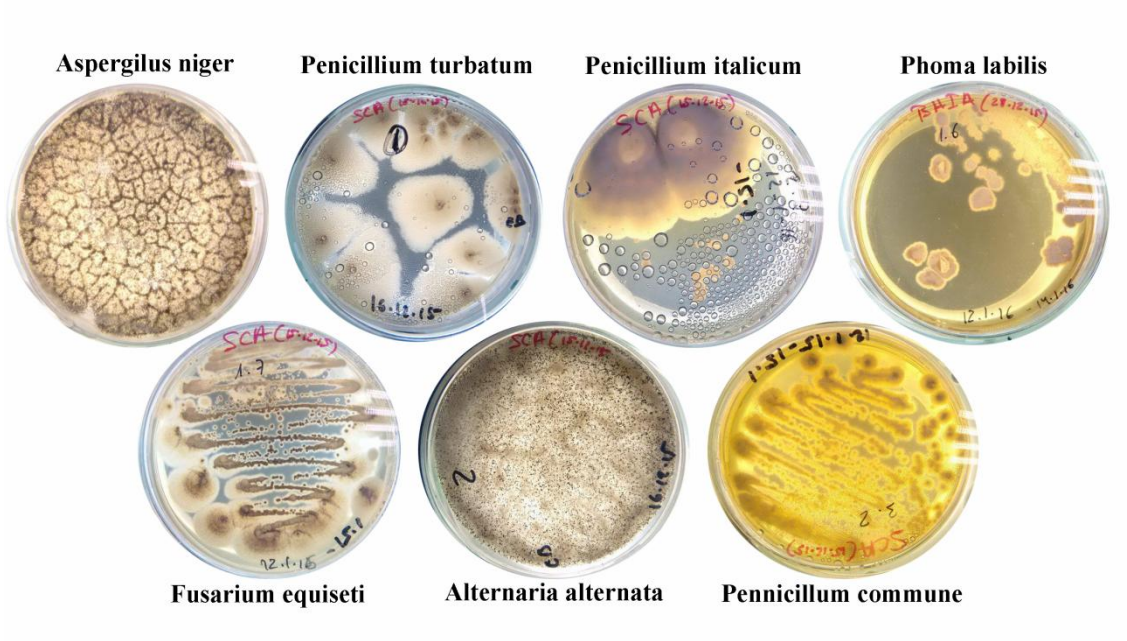


*Figure 12.3: Fungi strains isolated from the lower part of the painting and cultured in PDA Petri dishes. The images were collected after 1 week of incubation at room temperature (25 ºC).*

The presence of fungi is a relevant issue for the conservation of artworks since leads to the onset of aesthetic, chemical and physical degradation processes [6]. With regard to the preservation of the mural described in this chapter, the main conservation problem could be triggered by the hyphae. In fact, these filamentous outgrowths contribute to the physical weathering of the substrate, leading to the formation of cavities and cracks that debilitate the compactness of the paint layer. Furthermore, fungi colonies also result in the deposition of biomass, which enriches the substrate of nutrients and favour the further colonization by higher organisms [7].

## 12.2 Evaluation and comparison of painting materials

Taking into account that the two parts of the painting are conserved under the same environmental conditions, it can be therefore deduced that the different biological growth may be influenced by the characteristics of the colonized substrate.

Thus, XMET5100 (ED-XRF) and InnoRam$^{TM}$-785S (Raman) portable systems were used to identify and compare the original materials of the two sections of the painting. The aim was to understand whether the heterogeneous biological colonization was favoured by the presence of specific materials that were not detected during the first campaign of analysis (chapter 11).

On the one hand, no difference was detected on the molecular composition of the two areas. Indeed, according to Raman analyses, the composition of both mortar and pigments perfectly matched, confirming the results presented in the previous chapter.

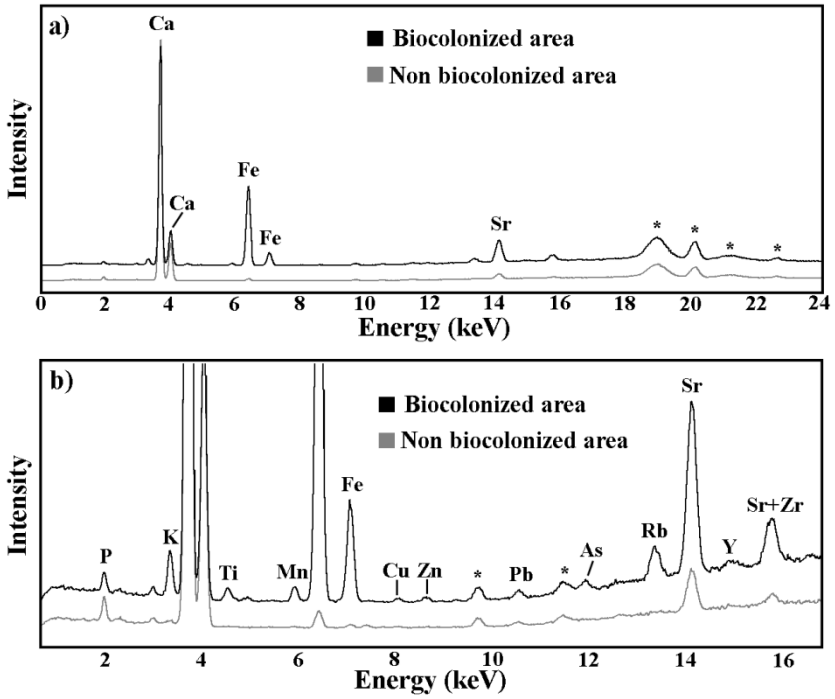


*Figure 12.4: a) ED-XRF spectra collected from biocolonized and non biocolonized areas; b) the same spectra were enlarged with the aim of highlighting the presence of secondary elements. Signal marked with an asterisk belongs to Compton and Rayleigh scatter.*

According to ED-XRF analyses, the main elements detected in the upper part of the mural fit with the composition of original mortar and pigments. However, the analyses carried out on the area of the mural retrieved in 2005 showed several additional elements such as P, K, Ti, Mn, Cu, Zn, Pb, As, Rb Sr, Y and Zr. As showed in Figure 12.4, most of those signals (except the ones assigned to P, K, Fe and Sr elements) were only observable in spectra collected from the biocolonized areas.

## 12.3 Laboratory characterization of samples

Aiming at identifying the possible link between the elemental results collected in-situ and the heterogeneous distribution of biodeteriogens, three samples were collected from the areas of the mortar described in Figure 12.1.

Sample *S1* was removed from the upper part of the wall, outside the perimeter including the paint decoration. In contrast, sample *S2* and *S3* were collected from the colonized surface of the painting section recovered during the archaeological excavations in 2005. Samples *S1* and *S2* were directly cold embedded in an acrylic resin and cross sections were prepared by following the methodology described by E. Jiménez et al. [8]. Elemental images were then carried out by means of the EVO 40 SEM-EDS system.

On the other side, sample *S3* was divided into two fragments: one was used to prepare a cross section, while the other was scratched with a sterile scalpel to collect the biodegradation crust observed on its surface. The collected material was then powdered using an agate mortar and analyzed by means of PRO PANalytical Xpert X-ray Diffractometer. The molecular results from *S3* were finally compared to those obtained from burial material (*B1,* Figure 12.1) collected from the basement.

**Optical analyses**

*S1*, *S2* and *S3* cross sections were observed first by means of the Nikon SMZ-U microscope, coupled to the Nikon Digital Sight DS-L1 camera.

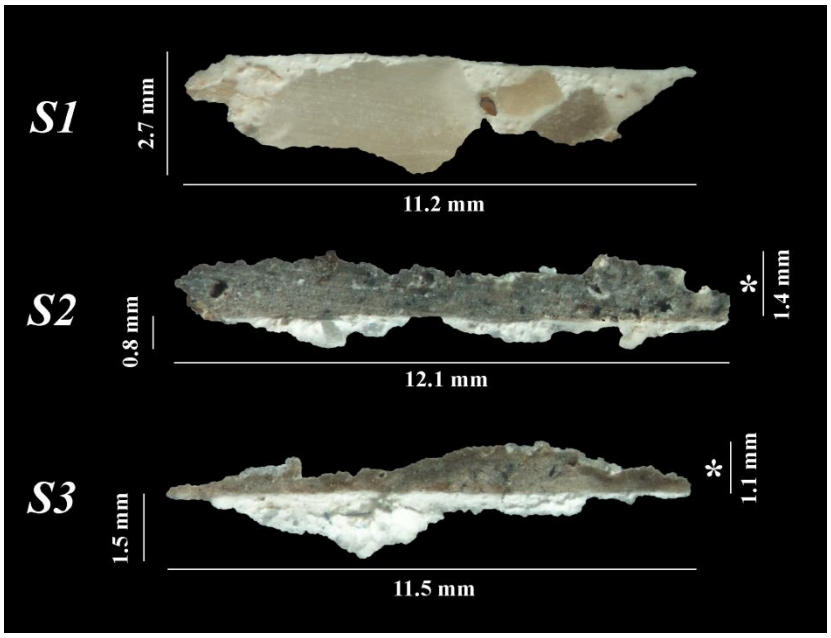


*Figure 12.5: Optical images collected from S1, S2 and S3 cross sections. The values labeled with an asterisk are referred to the thickness of the greyish layer deposited on the mortar surface.*

From the optical images shown in Figure 12.5 interesting information was obtained. For instance, the mortar layer of sample *S1* (which unlike *S2* and *S3* samples was removed from the raw mortar outside the painted perimeter) presented several whitish crystals. Previous works have been already centred on the characterization of raw mortars (*arriccio*) from the Ariadne's House, proving that those crystals corresponded to volcanic material included in the calcium carbonate-based binder [9]. This information is consistent with the analytical data collected during the first campaign of analysis (see section 11.1).

In contrast, the samples collected from the lower section of the painting (*S2* and *S3*) evidenced a greyish layer (up to 1.4 mm thick) interposed between the fine plaster (*intonachino*) and the biological patina. This material may have had different origins and could have played a key role in the biocolonization process. Therefore, its elemental and molecular composition was deeply studied by means of laboratory instruments.

**SEM-EDS analyses**

To characterize the elemental composition of the intermediate layer, *S2* and *S3* cross sections were analyzed by SEM-EDS. The results obtained from the study of

sample *S2* showed that the main elements composing the greyish layer were Ca, Si, Fe, Al, K and F.

The elemental distribution maps, included in Figure 12.6, showed that the layer was not uniform, but rather composed of numerous crystals of heterogeneous size and composition, inserted in a Ca-based matrix.

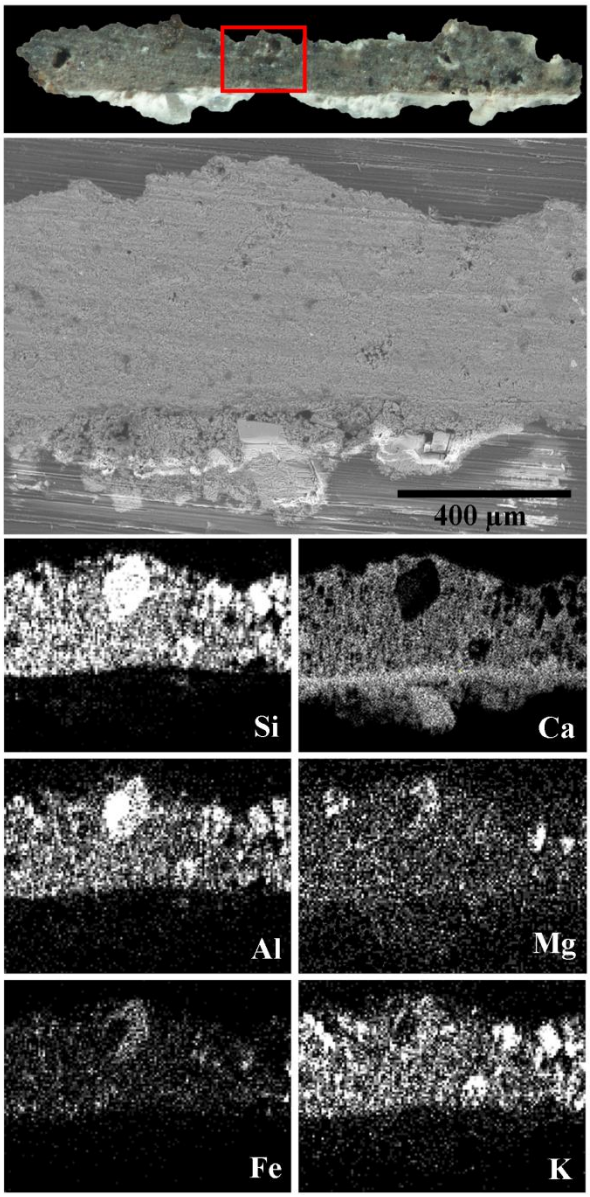


*Figure 12.6: Optical image and SEM-EDS mapping based on the chemical composition of S2 cross section. The elemental distribution of the detected elements showed the presence of several Si-based inclusions (rich in Al, Mg, Fe and K) embedded in a Ca-based binder.*

The spatial distribution of Si, Ca, Al, Mg, Fe and K, observed through the SEM-EDS analysis of the cross section of sample *S3,* confirmed the results obtained from the previous fragment, that is, the presence of silicate-based crystals differing in both, size and composition (Figure 12.7).

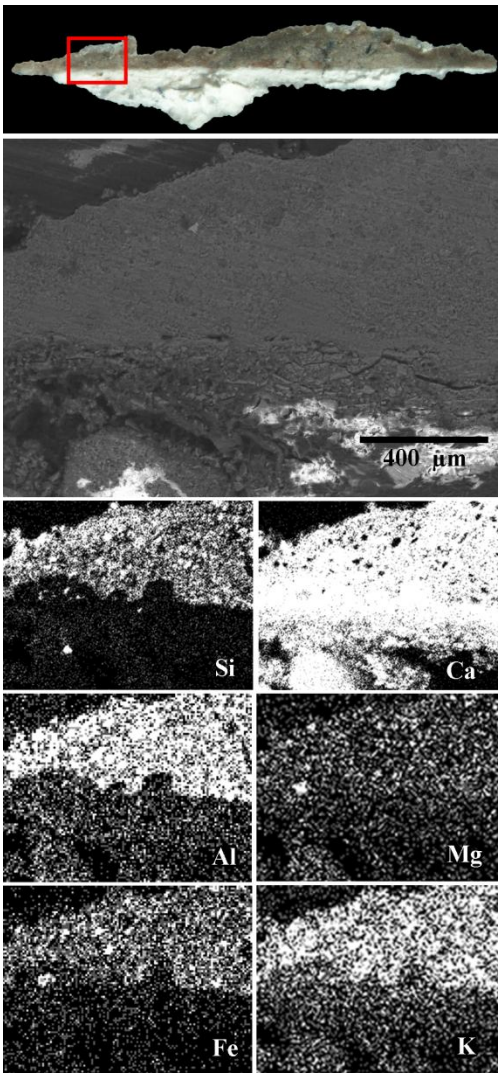


*Figure 12.7: Optical image and SEM-EDS mapping based on the chemical composition of S3 cross section.*

**XRD analyses**

To identify the molecular composition of the greyish layer, a small amount of material was sampled from fragment *S3* and analyzed by means of the XRD technique. The diffractogram was then compared to the one obtained from the analysis of the burial material sample (*B1*).

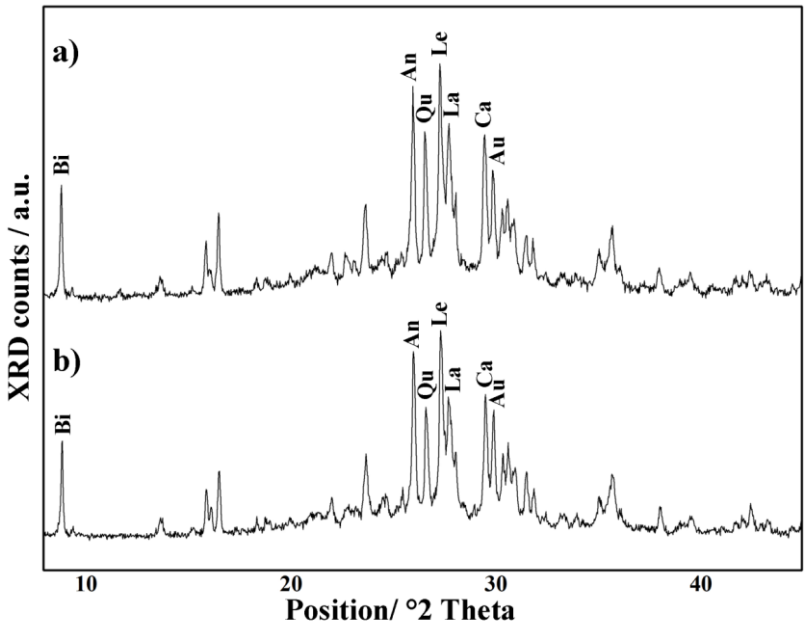


*Figure 12.8: XRD diffractograms collected from a) the layer covering the lower part of the painting and b) the burial material residues of the basement. The presence of leucite (Le), analcime (An), augite (Au), labradorite (La) and biotite (Bi) fits with the volcanic origin of the analyzed samples. Quartz (Qu) and calcite (Ca) were also detected.*

As showed in Figure 12.8, the XRD results perfectly fit together, turning out that both samples were a complex mixture of low symmetry crystalline phases such as calcite (Ca, $CaCO_3$), leucite (Le, $KAl(Si_2O_6)$), analcime (An, $NaAlSi_2O_6{\cdot}H_2O$), quartz (Qu, $SiO_2$), augite (Au, $(Ca,Na)(Mg,Fe,Al,Ti)(Si,Al)_2O_6$), labradorite (La, $(Ca,Na)(Si,Al)_4O_8$) and biotite (Bi, $K(Mg,Fe)_3AlSi_3O_{10}(OH)_2$). Furthermore, the results also highlighted the presence of amorphous vitreous material in the mixture (which does not generate peaks but significantly raise the background of the diffractograms).

The XRD results obtained from the greyish layer of fragment *S3* allowed interpreting the molecular composition of the silicate-based inclusions observed in Figures 12.6 and 12.7. For example, inclusions composed of Si, K and Al can be identified as leucite crystals. On the contrary, the areas in which the spatial distributions of Si, Al, Fe, Mg and K perfectly match can be interpreted as biotite crystals.

The semi-quantitative estimations expressed in Table 12.1 were carried out taking into account all the detected phases with the exception of the amorphous

vitreous material. In this sense, the obtained values were considered only as an estimation of the relative contents of the identified crystalline phases.

*Table 12.1: Semi-quantitative estimations of the crystalline phases detected by means of the XRD technique on greyish layer (S3) and burial material (B1) samples.*

| **Crystalline phases** | **Semi-quantitative results (% w/w)** | |
|---|---|---|
| | **Sample *S3*** | **Sample *B1*** |
| Calcite | 12.3 ± 1.2 | 9.3 ± 0.2 |
| Augite | 12.8 ± 0.3 | 14.2 ± 0.1 |
| Analcime | 12.0 ± 0.1 | 13.8 ± 1.4 |
| Leucite | 20.4 ± 2.2 | 22.0 ± 1.1 |
| Labrodorite | 29.8 ± 2.5 | 27.1 ± 2.1 |
| Biotite | 11.1 ± 0.5 | 11.2± 1.1 |
| Quartz | 2.0 ± 0.2 | 3.2 ± 0.5 |

Comparing qualitative and semi-quantitative results, important conclusions were deduced. For instance, the composition of the two samples perfectly fits together, proving that the presence of the greyish layer was due to the failure to remove the burial residues from the wall during the excavation in 2005. Moreover, most of the detected compounds belong to feldspar, pyroxene and mica families (characteristic of igneous rocks), highlighting the volcanic origin of the sampled materials [10].

Among all the identified phases, quartz must be considered as a secondary mineral phase since feldspars only form in a lack of silica, while $SiO_2$ implies an excess of silica once the silicates crystallize [11]. Calcite also represents a secondary compound and its presence in this greyish layer was probably due to the transformation of some of the original compounds by a carbonation process. Carbonation corresponds to the typical *pedogenic* process in soils developed in volcanic material and could be triggered by different mechanisms including a) in-situ dissolution and re-precipitation of carbonates by rainwater, b) infiltration of dissolved bicarbonate from the adjacent soil, and c) biogenic precipitation due to the action of microorganisms.

The identification of a widespread volcanic material layer between the organic patinas and the wall surface provides the final clue to explain the origin of the heterogeneous microorganism colonization phenomenon.

In the literature, numerous works describe volcanic materials as an ideal starting substrate for the development of extremely fertile soils [12]. As described by M. Nanzyo (2002), ashes, pumices and debris ejected from volcanoes are subjected to pedogenic processes soon after their deposition. Those physical and chemical reactions, combined with the accumulation of biomass, leads to the formation of volcanic ash soil, also called *andosols* [13]. To better understand the unique properties of *andosols*, many researchers in the last decades analyzed the mechanisms of vegetation regrowth on lands interested by volcanic eruptions. In this sense, most of them indicated a high rate of spread of macroorganisms during years following the eruption [14]. However, it is important to emphasize that the growth of macroorganisms is only the last stage of a more complex biological colonization process. In fact, the role of pioneers must be assigned to microorganisms which colonize volcanic material soon after their deposition, providing the necessary nutrients for the colonization of higher plants [14,15].

## 12.4 Conclusions

This chapter aimed to identify the causes of the heterogeneous biocolonization of a Pompeian mural painting excavated in two different steps. The results obtained from DNA extraction and sequencing proved that all biological patinas were composed of fungal strains, mainly belonging to the *Penicilluim* species.

The analytical studies performed in-situ excluded any link between the heterogeneous colonization and the original materials used by the artist. On the other hand, laboratory analyses of cross sections highlighted the presence of a thin greyish layer overlying the wall surface excavated in 2005. XRD analyses proved that the lower part of the painting was still covered by a thin volcanic material layer that, in contrast to the area recovered in 1988, was not completely removed during the archaeological excavation.

Taking into account that biological patinas mainly covered the section excavated in 2005, the role of volcanic material layer as a suitable support for colonization was pointed out.

This work also emphasized the presence of chemical and physical transformations of the intermediate layer. Carbonation process, joined to biomass deposition and the physical stress triggered by fungi hyphae, pointed out that the volcanic material is under pedogenic process. That fact represents a real danger for the preservation of the analyzed *fresco* since the transformation of volcanic ashes and debris into *andosols* could facilitate the colonization of higher plants.

In conclusion, the analytical work summarized in this chapter pointed out that the biological growth can be strongly favoured by the presence of burial residues on the mural surface. In this sense, it was also proved that volcanic material could play a key role on biocolonization and further biodegradation of the mural paintings recovered from the archaeological site of Pompeii.

Considering that manifold degradation problems can be triggered by the development of biological patina on *Cultural Heritage* materials, to plan a periodical conservation treatment to neutralize the colonization of Pompeian remains is of paramount importance.

In this sense, as it will be elucidated in the following chapter, several experiments were carried out to evaluate the possible exploitability of several essential oils (EOs) as a green alternative to conventional chemical products for preventing *Cultural Heritage* biocolonization.

## 12.5 References

**[1]** M. Bustamante, I. Escrivá, A. Fernández, E. Huguet, P. Iborra, D. Quixal, A. Ribera, J. Vioque (2010) Pompeya. Alrededor de la via “degli Augustali”: el macellum (VII, 9, 25) y la casa del “Forno a riverbero” (VII, 4, 29). Campaña de 2009, available at: Fold&r http://www.fastionline.org/docs/FOLDER-it-2010-210.pdf (May 28th 2017).

**[2]** A. Ribera, R. Albiach, C. Ballester, M. Bustamante, I. Caruana, I. Escrivá, E. Huguet, M. Olcina, V. Salavert, J.M. Vioque (2008) Pompeya: Excavaciones estratigráficas en la casa de Ariadna o dei Capitelli Colorati (Regio VII, 4,51 y 31). Campaña de 2007. *Informes y trabajos, Excavaciones en el exterior* 2007, 51-57.

**[3]** R.J. Pinto, A. Almeida, S.C. Fernandes, C.S. Freire, A.J. Silvestre, C.P. Neto, T. Trinidade (2013) Antifungal activity of transparent nanocomposite thin films of pullulan and silver against Aspergillus niger. *Colloid Surface B,* 103, 143-148.

**[4]** O. Ciferri (1996) Microbial Degradation of Paintings. *Applied and Environmental Microbiology*, 65, 879-885.

**[5]** F.M. Helmi, H.R.R. Elmitwall, M.A. Rizk, A.F. Hagrassy (2011) Antibiotic extraction as a recent biocontrol method for Aspergillus niger and Aspergillus flavus fungi in ancient Egyptian mural paintings. *Mediterranean Archaeology and Archaeometry,* 11, 1-7.

**[6]** K. Sterflinger, G. Piñar (2013) Microbial deterioration of cultural heritage and works of art – tilting at winfmills?. *Applied and Environmental Microbiology,* 97, 9637-9646.

**[7]** J.S. Singh, A.S. Raghubanshi, R.S. Singh, S.C. Srivastava (1989) Microbial biomass acts as a source of plant nutrients in dry tropical forest and savanna. *Nature,* 338, 499-500.

**[8]** E. Jiménez, A. Ruiz-Conde, P.J. Sánchez-Soto (2005) Preparación de secciones estratigráficas: aspectos prácticos del análisis de estratos en obras del Patrimonio Cultural (pigmentos y soportes). *Boletín de la Sociedad Española de Cerámica y Vidrio*, 44, 382-286.

**[9]** M.C. Pérez, F.J. García-Diego, P. Merello, P. D'Antoni, A. Fernández-Navajas, A. Ribera, L. Ferrazza, J. Pérez-Miralles, J.L. Baró, P. Merce, H. D'Antoni, J. Curiel-Esparza (2013) Ariadne's house (Pomeii, Italy) wall paintings: A multidisciplinary study of its present state focused on a future restoration and preventive conservation. *Materiales de Construcción*, 63, 449-467.

**[10]** H. Balcone-Boissard, B. Villemant, B. Boudon, A. Michel (2008) Non-volatile vs volatile behaviours of halogens during the AD 79 plinian eruption of Mt. Vesuvius, Italy. *Earth and Planetary Science Letters,* 269, 66-79.

**[11]** M.J. Le Blas, A.L. Streckeisen (1991) The IUGS systematic of igneous rocks. *Journal of the Geological Society*, 148, 825-833.

**[12]** T. Takahashi, S. Shoji (2002) Distribution and classification of volcanic ash soils. *Global Environmental Research,* 6, 83-97.

**[13]** M. Nanzyo (2002) Unique properties of Volcanic Ash Soils. *Environmental Research*, 6, 99-112.

**[14]** G.A. Smathers, D. Mueller-Dombois (1972) Technical report No. 10-Inveasion and recovery of vegetation after a volcanic eruption in Hawaii. *Department of Botany, University of Hawaii*, available at: https://scholarspace.manoa.hawaii.edu/bitstream/10125/25908/1/10.pdf (May 28$^{th}$ 2017).

**[15]** T.D. Brock (1973) Primary colonization of Surtsey, with special reference to the blue-green algae. *Oikos*, 24, 239-243.

CHAPTER 13:

# EVALUATING THE EXPLOITABILITY OF ESSENTIAL OILS CONSTITUENTS AS A NOVEL TREATMENT AGAINST MURAL PAINTINGS BIOCOLONIZATION

As explained previously, biological colonization represents one of the most dangerous degradation processes jeopardizing *Cultural Heritage* materials. In this context, fungi have been recognized as one of the main biodeteriogens of mural paintings and mortars [1,2].

Even though several fungal species are capable of colonizing walls paintings, most of the works published so far on this issue have detected the presence of *Aspergillus niger* strains [3-5]. One reason of the widespread of this biodeteriogen lies in its profuse germination of *conidia* spores (produced from filamentous structures called *conidiophore*) which, being distributed via the air, are able to colonize surfaces located at great distances. In addition, the great adaptability of *A. niger* makes him capable of tolerating and proliferating over a wide range of temperatures (between 6 and 47 ºC) and pH (from 1.4 to 9.8) values [6].

As proved in other works, *A. niger* is capable of triggering several chemical, physical and aesthetical deterioration processes on paintings and building materials [7-9].

In order to minimize the onset of irremediable damages to the colonized substrate, conservators need to periodically neutralize the biological patinas. Several chemicals have been used for this purpose, such as acids, pyridines, quaternary ammonium salts and organometallic compounds. However, some of these products have been banned over time due to their environmental and health hazards. To regulate this field, United States [10] and European Union [11] intervened by adopting specific regulations that indicate all active substances legally employable to protect humans, animals, materials or articles against microorganisms.

Considering that both, private companies and public institutions, are investigating in the development of new biocide products, the list of adoptable chemicals is constantly expanding. Among the products under evaluation to be included in the European Biocidal Products Regulation list (BPR, Regulation (EU) 528/2012) it must be underlined the presence of essential oils (EOs) extracted from aromatic plants, such as lavender (CAS number: 1245629-80-4) and eucalyptus (CAS: 91722-69-9) [11]. Their evaluation by competent committees is supported by several scientific works that have proved the effectiveness of those EOs against the growth of several kinds of fungi and bacteria [12-15].

Even though their use has been mainly tested for medical purposes [16-19], a few conservation scientists are nowadays assessing the possible exploitability of EOs in the field of *Cultural Heritag*e preservation [20-24].

Despite the promising results obtained so far, the use of EOs in this field is still limited by the presence of some disadvantages. For instance, the possible implications entailed by photo-oxidation processes on their antifungal activity have still to be clarified [25]. Similarly, further experimental works need to be carried out for the purpose of evaluating the possible interaction between EOs and the materials to be treated.

Under this requirement, the experimental work described in this chapter aimed at performing further progresses towards the possible exploitation of several essential oils constituents as novel conservation products against the fungal colonization of *Cultural Heritage* materials.

## 13.1 Antifungal activity of fresh EOs constituents

The first objective of the work summarized in this chapter was to analyze the biocide activity of several EOs constituents against a wild strain of *A. niger* collected from a mural painting conserved in the basement of the Ariadne's House (from the Archaeological site of Pompeii, see chapter 12).

For this reason, a comprehensive literature review was carried out with the aim of identifying the EOs capable of inhibiting the growth of the isolated fungal strain. In this sense, an important background was obtained from the work by V.C. Pawar and V.S. Thaker (2006) [26], in which the inhibitory effect of 75 different EOs was tested against hyphal growth and spore formation of *A. niger*. Thus, the main constituent of the most effective EOs were selected and purchased from Sigma-Aldrich Corp. (St Louis, MO, USA): *thymol* (99% purity, from *thyme* EO), *menthol* (99%, from *mint*), *linalool* (97%, from *coriander*), *eucalyptol* (99%, from *eucalyptus) cinnamaldehyde* (95%, from *cinnamon*), *eugenol* (99%, from *clove*), *cuminaldehyde* (98%, from *cumin*), *(R)-(+)-Limonene* (95%, from *lemon grass*), *citral* (95%, from *citric plant*), and *citronellol* (95%, from *citric plant*).

Afterwards, disc-diffusion method assays were performed in order to elucidate the inhibitory effect of the 10 selected EOs constituents.

To do so, an *A. niger* spore suspension (prepared by flooding the culture with distilled water and filtering the solution through sterile absorbent cotton wools plugs) was spread over the entire surface of pre-poured potato dextrose agar (PDA) Petri dishes by swabbing. For each biocide compound, four solutions (with a final concentration of 100%, 10%, 1% and 0.1% w/w respectively) were prepared using ethanol as solvent. The solutions were used to impregnate paper discs (about 6 mm diameter), which were finally applied on the Petri dish as represented in Figure 13.1.

During incubation, Petri dishes were inverted to prevent condensation from falling into the medium surface, thereby resulting in heterogeneous growth of the strain. Besides, negative controls were carried out by impregnating paper discs with the same solvent employed to prepare EOs constituents solutions. Finally, the antifungal activity of each compound was monitored for a month. In order to ensure the repetitiveness of the results, each experiment was carried out in triplicates.

In the early stage, the compounds showed remarkable differences in their inhibitory activity. For instance, the growth of *A. niger* on Petri dishes containing *cinnamaldehyde* (Cn), *eugenol* (Eg), *thymol* (Th), *linalool* (Ln) and *citronellol* (Ct) discs was just barely observed after 10 days of incubation (and restricted to the area around the disc even with the lowest concentration of active compound). On the other side, the inhibitory effect of *menthol* (Me), *eucalyptol* (Ec) and *limonene* (Lm) was less intense and restricted to the PDA surface encompassing the discs loaded only with pure active compounds. In contrast, Petri dishes treated with *citral* (Ci) and *cuminaldehyde* (Cu) were almost completely covered by fungal spores. Basing on these results, the biocide effect of all compounds after 10 days of incubations was ranked: Cn>Th=Eg=Ln>Ct>Me>Ec=Lm>Ci=Cu.

After 20 days, several significant differences were observed in the inhibition activity of some of the selected compounds. Concretely, a remarkable acceleration of *A. niger* growth was observed in Petri dishes loaded with *linalool*, *citronellol, menthol, eucalyptol* and *limonene*. This phenomenon could be due to the evaporation and/or degradation of the active compound, suggesting a lower suitability of these products in comparison to *eugenol*, *thymol* and *cinnamaldehyde.*

After 30 days, only three of the ten EOs constituents were still showing remarkable inhibitory effects. The growth inhibition of *cinnamaldehyde* was limited to the area encompassing the paper disc loaded with the highest content of active compound. On the other hand, the *A. niger* growth was still inhibited in most of the PDA media treated with *eugenol* and *thymol*. Basing on the obtained results, the inhibitory effect of the three most effective active compounds has been graphically represented in Figure 13.1.

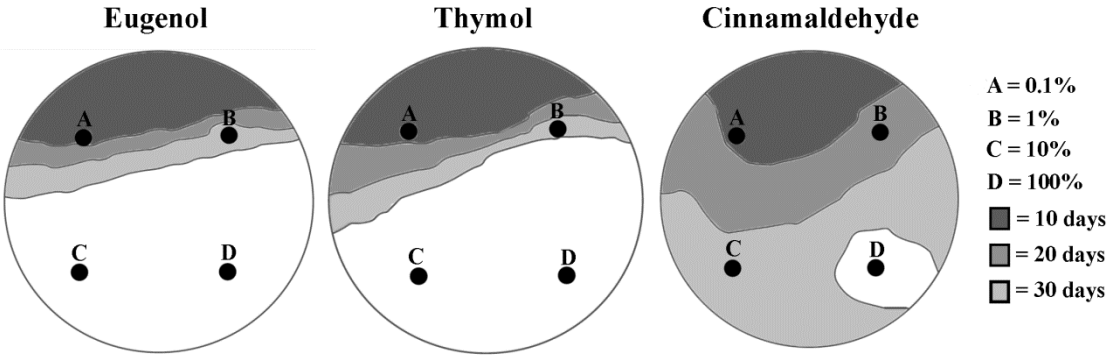


*Figure 13.1: Biocide activity of fresh eugenol, thymol and cinnamaldehyde (at different concentrations) against a wild strain of A. niger.*

The reported data are consistent with the results presented in other studies in which the biocide activity of *eugenol* [27], *thymol* [28] and *cinnamaldehyde* [29] compounds was assessed against different types of fungal and bacteria strains.

## 13.2 EOs constituents ageing and characterization

As the aim of the present study was to test of EOs as possible inhibitors of fungal growth, it was important to check the stability of the compounds. Indeed, it must be taken into account that the possible application of EOs constituents in real samples would be done in adverse conditions, being sun-light and UV-light one of the main factors that could degrade the active compounds and, thus, the anti-fungal growth capability.

According to this, *thymol, eugenol* and *cinnamaldehyde* were selected for the next set of experiments. For each compound, 3 aliquots of 5 ml were transferred to glass vials and exposed to dark, sun-light and UV-light (40 W, range of UV-light, 330–400 nm, Osram) during two months.

The samples aged on dark were used as a reference, while the ones exposed to sun-light and UV-light (which have long been known to be a catalysts for oils oxidation [30]) had the purpose of inducing regular and accelerated photo-degradation respectively.

After two months of aging, some of the samples showed slight changes in their physical properties. For example, *thymol* samples exposed to UV-light suffered a light yellowing. On the other side, *cinnamaldehyde* samples stored under UV-light conditions resulted in a strong yellowing of the solution and an evident increase of volumetric mass density (which may have been triggered by the onset of photo-oxidation reactions).

### FTIR analyses

After storage, aged samples were analyzed by means of FTIR technique with the purpose of identifying the decay products resulted from aging.

FTIR analyses were performed by means of the Jasco 6300 system (see chapter 4) in ATR mode. Starting from the characterization of *thymol* samples, the same vibrational signals were detected from the analysis of dark, sun-light and UV-light aged solutions (Figure 13.2). The main peaks detected at 593, 739, 808, 879, 946, 1050, 1088, 1154, 1233, 1290, 1340, 1382, 1421, 1458, 1519, 1585, 1619, 2872,

2926 and 2965 $cm^{-1}$, together with the broad band between 3100 and 2600 $cm^{-1}$, were consistent with the vibrational modes provided by fresh *thymol* solution.

However, by comparing the peak intensities from the three spectra, small differences were identified. For example, IR spectrum of sun-light aged *thymol* showed more intense vibrational modes at 1050 and 1088 $cm^{-1}$ than the sample stored in dark. As shown in Figure 13.2, the intensity of those signals, which according to bibliography are assigned to the out-of-plane bending of the C-H bonds [31], further increases in the spectra collected from UV-light aged *thymol.*

In contrast, UV-light spectra displayed a slight decrease in the intensity of the characteristic *thymol* signals at 808 and 1154 $cm^{-1}$ which, basing on previous works [32-33], are characteristic for O-H deformation and C-O stretching vibration.

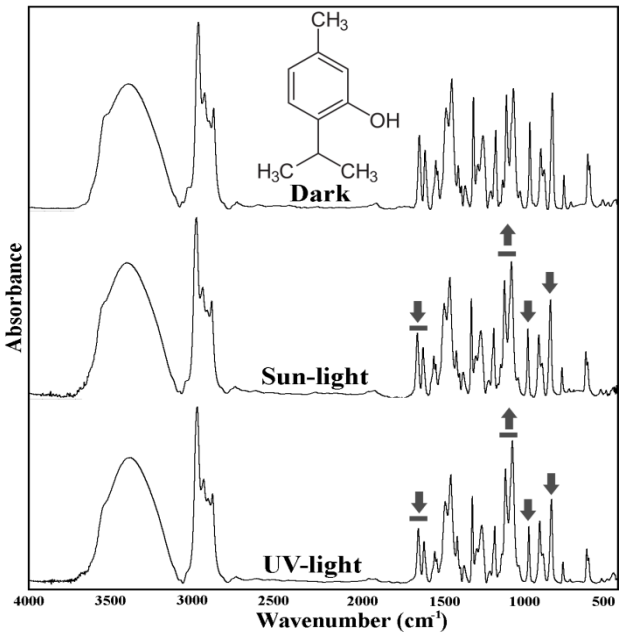


*Figure 13.2: Comparison of FTIR spectra collected from thymol solutions exposed to dark, sun-light and UV-light.*

FTIR spectra collected from aged *eugenol* solutions showed the same vibrational modes of the fresh compound (Figure 13.3, main FTIR peaks at 557, 598, 648, 747, 795, 818, 851, 914, 995, 1034, 1122, 1149, 1207, 1234, 1268, 1366, 1432, 1464, 1514, 1612, 1638, 2842, 2906, 2938, 2975, 3003, 3059, 3076 $cm^{-1}$ and a broad band at 3250-3550 $cm^{-1}$).

In this case, some divergences regarding peak intensities were also detected. For example, sun-light and UV-light aged *eugenol* exhibited more intense vibrational modes in the range between 2800 and 3550 $cm^{-1}$. Concretely, peaks detected between 2842 and 3076 $cm^{-1}$ are related to the vibration of –CH2, =CH2 and –CH3 groups, while the broad band appearing at 3250-3550 $cm^{-1}$ is due to the hydrogen-bonded O-H stretching [34]. Opposed to these, the main peak at 1514 $cm^{-1}$ (corresponding to the bending of the –OCH3 group) slight decreases its intensity when exposed to sun-light and (above all) UV-light.

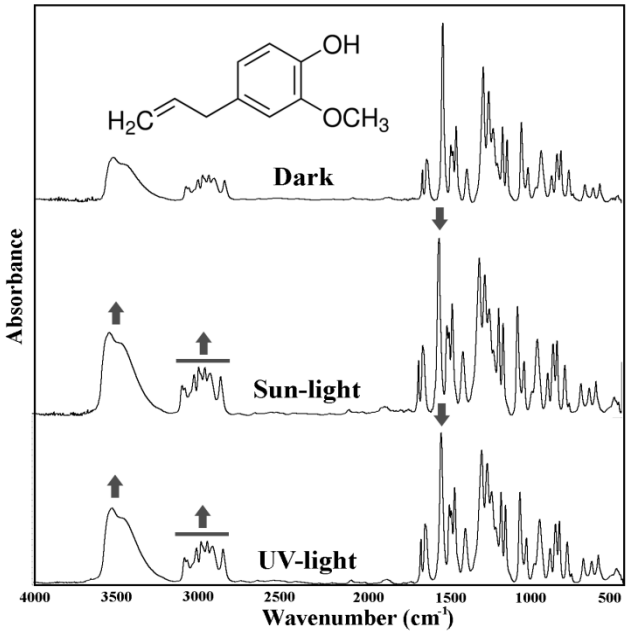


*Figure 13.3: Comparison of FTIR spectra collected from eugenol solutions exposed to dark, sun-light and UV-light.*

With regards to *cinnamaldehyde* samples, FTIR analyses collected from solutions stored under dark and sun-light conditions (Figure 13.4) showed the same vibrational modes of the fresh compound (main peaks at 494, 584, 606, 620, 689, 748, 845, 973, 1007, 1072, 1124, 1159, 1180, 1205, 1259, 1294, 1306, 1329, 1394, 1450, 1495, 1575, 1623, 1680, 2717, 2743, 2817, 2922, 3028, 3062 and 3322 $cm^{-1}$) [35-36].

In contrast, the spectra collected from UV-light aged samples displayed an increase of the characteristic peaks at 685 and 748 $cm^{-1}$, which corresponds to the vibration absorption of CH benzene ring and alkene subunit respectively [36]. In addition to those, it must be underlined the presence of an additional vibrational mode at 1715 $cm^{-1}$, combined with a strong increase in the intensity of 1495, 1450

$cm^{-1}$ peaks and the appearance of broad bands around 1000-1250 and 3250-3600 $cm^{-1}$. According to bibliography [37], most of these signals can be related to the characteristic absorption of dimeric compounds such as *truxillic* and *truxinic acids (*resulting from the photo-dimerization of *cinnamic acid* molecules*)*. Even though more analyses need to be performed for a reliable characterization of degradation products, the formation of dimeric compounds could explain the increase of volumetric mass density observed on *cinnamaldehyde* samples aged under UV-light.

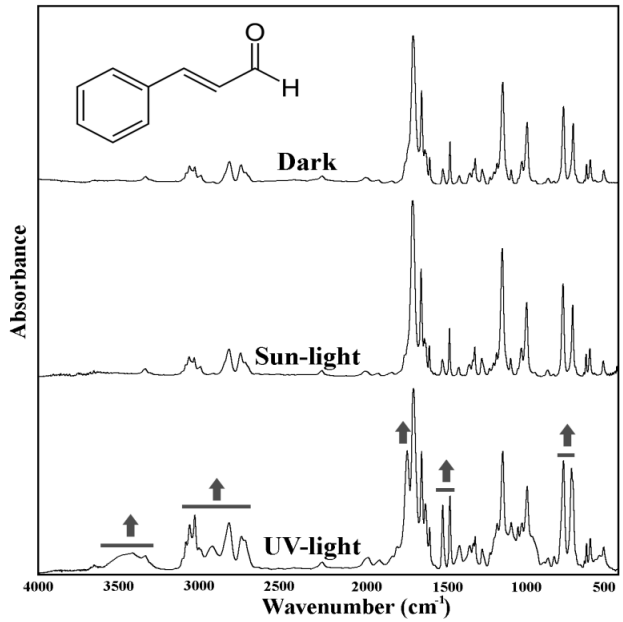


*Figure 13.4: Comparison of FTIR spectra collected from cinnamaldehyde solutions exposed to dark, sun-light and UV-light.*

## 13.3 Antifungal activity of aged EOs constituents

After confirming the onset of photo-oxidation processes, new antifungal assays were performed with the purpose of evaluating the biocide capability of EOs constituents after aging.

The evaluation was performed by using the same disc diffusion method described above. In this case, each paper disc (containing 5 µl of the compound to be tested) was placed in the middle of a PDA Petri dish previously inoculated with the *A. niger* spore suspension. Petri dishes were then inverted to prevent condensation and incubated at 25 ºC during 7 days. After incubation, the diameters of growth inhibition of each selected EOs constituent, exposed to dark, sun-light and UV-

light conditions respectively, were measured and compared. All experiments were carried out in triplicates.

The inhibition diameters of *thymol*, *eugenol* and *cinnamaldehyde* aged samples, measured after 7 days of incubation at room temperature (25 ºC), showed considerable differences on their inhibition activity.

Indeed, the inhibition diameters presented in Figure 13.5, proves that *eugenol* and *thymol* samples displayed excellent results in terms of effectiveness after aging. The diameters of growth inhibition provided by *eugenol* samples aged in sun-light (38 ± 1 mm) and UV-light (38 ± 2 mm) conditions were comparable to those displayed by samples stored in darkness (39 ± 4 mm). In the case of *thymol*, the biocide capability of sun-light (35 ± 5 mm) and UV-light (34 ± 3 mm) aged samples slightly decreases compared to reference pattern (40 ± 2 mm).

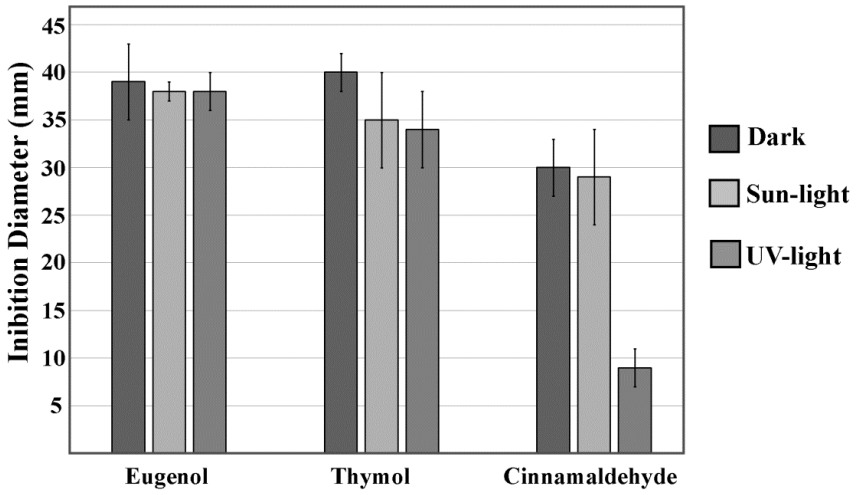


*Figure 13.5: Inhibition diameter of eugenol, thymol and cinnamaldehyde solutions after dark, sun-light and UV-light exposition.*

Finally, the degradation of *cinnamaldehyde* samples exposed to UV-light involved critical repercussions on their inhibition features. In fact, the inhibition diameter of the paper disc loaded with UV-aged *cinnamaldehyde* was only 9 ± 2 mm, against the 30 ± 3 mm and the 29 ± 5 mm obtained from solutions exposed to dark and sun-light respectively.

## 13.4 Conclusions

The aim of the present chapter was to evaluate the potential use of EOs constituents as a biological alternative for the preservation of *Cultural Heritage* materials from biodeterioration.

In the first step, disc diffusion assays were performed to compare the antifungal activity of 10 selected compounds against a wild strain of *Aspergillus niger*. The results, collected after 30 days of monitoring, allowed identifying *thymol*, *eugenol* and *cinnamaldehyde* as the most effective antifungal agents.

Afterwards, the three EOs constituents were exposed to different light condition in order to identify the possible side-effects entailed by photo-degradation processes.

According to FTIR analyses, *eugenol* and *thymol* samples did not show remarkable changes after sun-light and UV-light exposition. On the contrary, vibrational spectra collected from UV-aged *cinnamaldehyde* samples suggested the formation of degradation products, which were probably due to the onset of photo-dimerization reactions.

Then, further antifungal assays were carried out in order to check the effect of light exposition on the inhibition capability of aged EOs constituents. On the one side, the inhibition of *eugenol* and *thymol* samples after aging remained almost unchanged, suggesting their possible exploitability for long-term protection treatments. On the contrary, *cinnamaldehyde* samples exposed to UV-light showed a critical decrease of their effectiveness.

To conclude, the experimental results summarized in this chapter confirm the possible exploitability of pure *eugenol* and *thymol* as alternative green products against *Cultural Heritage* biocolonization. In this sense, further analyses will be carried out in the future aiming at evaluating their inhibition activity against several others fungal species and their possible interactions with mural paintings' materials.

## 13.5 References

**[1]** M. Maguregui, U.Knuutinen, J. Trebolazabala, H. Morillas, K. Castro, I. Martínez-Arkarazo, J.M. Madariaga (2012) Use of in situ and confocal Raman spectroscopy to study the nature and distribution of carotenoids in brown patinas from a deteriorated wall painting in Marcus Lucretius House (Pompeii). *Analytical and Bioanalytical Chemistry*, 402, 1529-1539.

**[2]** A.A. Gorbushina, J. Heyrman, T. Dornieden, M. González-Delvalle, W.E. Krumbein, L. Laiz, K. Petersen, C. Sáinz-Jiménez, J. Swings (2004) Bacterial and fungal diversity and biodeterioration problems in mural painting environments of St. Martins church (Greene–Kreiensen, Germany). *International Biodeterioration and Biodegradation*, 53, 13-24.

**[3]** O. Pepe, L. Sannino, S. Palomba, M. Anastasio, G. Blaiotta, F. Villani, G. Moschetti (2010) Heterotrophic microorganisms in deteriorated medieval wall paintings in southern Italian churches. *Microbiological Research,* 165, 21-32.

**[4]** O. Ciferri (1999) Microbial Degradation of Paintings. *Applied and Environmental Microbiology*, 65, 879-885.

**[5]** F.M. Helmi, H.R.R. Elmitwalli, M.A. Rizk, A.F. Hagrassy (2011) Antibiotic extraction as a recent biocontrol method for Aspergillus niger and Asperigullus flavus fungi in ancient Egyptian mural paintings. *Mediterranean Archaeology and Archaeometry,* 11, 1-7.

**[6]** E. Schuster, N. Dunn-Coleman, J.C. Frisvad, P.W.M. van Dijck (2002) On the safety of Aspergillus niger- a review. *Applied Microbiology and Biotechnology*, 59, 426-435.

**[7]** T.R. Jørgensen, J. Park, M. Arentshorst, A.M. van Welzen, G. Lamers, P.A. van Kuyk, R.A. Damveld, C.A.M. van den Hondel, K.F. Nielsen, J.C. Frisvad, A.F.J. Ram (2011) The molecular and genetic basis of conidial pigmentation in Aspergillus niger. *Fungal Genetics and Biology*, 48, 544-553.

**[8]** K. Sterflinger, G. Piñar (2013) Microbial deterioration of cultural heritage and works of art – tilting at winfmills?. *Applied Microbiology and Biotechnology*, 97, 9637-9646.

**[9]** H.L. Hu, J. van den Brink, B.S. Gruben, H.A.B. Wösten, J.D. Gu, R.P. de Vries (2011) Improved enzyme production by co-cultivation of Aspergillus niger and Aspergillus oryzae and with other fungi. *International Biodeterioration and Biodegradation*, 65, 248-252.

**[10]** United States Environmental Protection Agency: https://www.epa.gov/pesticides (May 9th 2017).

**[11]** European Biocidal Products Regulation: http://ec.europa.eu/health/biocides/biocidal_products_en (May 9th 2017).

**[12]** R.J.W. Lambert, P.N. Skandamis, P.J. Coote, G.J.E. Nychas (2001) A study of the minimum inhibitory concentration and mode of action of oregano essential oil, thymol and carvacrol. *Journal of Applied Microbiology*, 91, 453-462.

**[13]** A.M. Janssen, J.J.C. Scheffer, A.B. Svendsen (1987) Antimicrobial activity of essential oils: a 1976-1986 literature review. Aspects of the test methods. *Planta Medica*, 53, 395-398.

**[14]** K.A. Hammer, C.F. Carson, T.V. Riley (1999) Antimicrobial activity of essential oils and other plant extracts. *Journal of Applied Microbiology*, 86, 985-990.

**[15]** F. Bakkali, S. Averbeck, D. Averbeck, M. Idaomar (2008) Biological effects of essential oils-a review. *Food and Chemical Toxicology,* 46, 446-475.

**[16]** S. Burt (2004) Essential oils: their antibacterial properties and potential applications in foods-a review. *International Journal of Food Microbiology*, 94, 223-253.

**[17]** J.R. Calo, P.G. Crandall, C.A. O'Bryan, S.C. Ricke (2015) Essential oils as antimicrobials in food systems-a review. *Food Control*, 54, 111-119.

**[18]** A.E. Edris (2007) Pharmaceutical and therapeutic Potentials of essential oils and their individual volatile constituents: a review. *Phytotherapy*, 21, 308-323.

**[19]** W.T. Langeveld, E.J.A. Veldhuizen, S.A. Burt (2013) Synergy between essential oil components and antibiotics: a review. *Critical Reviews in Microbiology*, 40, 76-94.

**[20]** M. Stupar, M. Lj. Grbić, A. Džamić, N. Unković, M. Ristić, A. Jelikić, J. Vukojević (2014) Antifungal activity of selected essential oils and biocide benzalkonium

chloride against the fungi isolated from cultural heritage objects. *South African Journal of Botany*, 93, 118-124.

**[21]** S. Gatenby, P. Townley (2003) Preliminary research into the use of the essential oil of Melaleuca arternifolia (tea tree oil) in museum conservation. *AICCM Bulletin*, 28, 67–70.

**[22]** Y.J. Chung, K.S. Lee, S.H. Han (2003) The utilization of fungicide and insecticide from medicinal plants for conservation of cultural properties. *Proceedings of the 5th Meeting of the Indoor Air Pollution Working Group, University of East Anglia, School of Environmental Sciences, UK*.

**[23]** M.S. Rakotonirainy, B. Lavédrine (2005) Screening for antifungal activity of essential oils and related compounds to control the biocontamination in libraries and archives storage areas. *International Biodeterioration and Biodegradation*, 55, 141–147.

**[24]** S. Borrego, O. Valdés, I. Vivar, P. Lavin, P. Guiamet, P. Battistoni, S. Gómez de Saravia, P. Borges (2012) Essential Oils of Plants as Biocides against Microorganisms Isolated from Cuban and Argentine Documentary Heritage. *International Scholarly Research Network*, 826786.

**[25]** C. Turek, F.C. Stintzing (2013) Stability of Essential Oils: A review. *Comprehensive Reviews in Food Science and Food Safety*, 12, 40-53.

**[26]** V.C. Pawar, V.S. Thaker (2006) In vitro efficacy of 75 essential oils against Aspergillus niger. *Mycoses,* 49, 316-323.

**[27]** D. Campaniello, M.R. Corbo, M. Sinigaglia (2010) Antifungal Activity of Eugenol against Penicillium, Aspergillus, and Fusarium Species. *Journal of Food Protection*, 73, 1124-1128.

**[28]** M.A. Botelho, N.A.P. Noguera, G.M. Bastos, S.G.C. Fonseca, T.L.G. Lemos, F.J.A. Matos, D. Montenegro, J. Heukelbach, V.S. Rao, G.A.C. Brito (2007) Antimicrobial activity of the essential oil from Lipia sidoides, carvacrol and thymol against oral pathogens. *Brazilian Journal of Medical and Biological Research*, 40, 349-356.

**[29]** S.S. Cheng, E.H. Chang, S.T. Chang (2008) Antifungal activity of cinnamaldehyde and eugenol congeners against wood-rot fungi. *Bioresource Technology*, 99, 5145-5149.

**[30]** H. Nguyen, E.M. Campi, W.R. Jackson, A.F. Patti (2009) Effect of oxidative deterioration on flavor and aroma components of lemon oil. *Food Chemistry*, 112, 388-393.

**[31]** M. Kumar Trivedi, S. Patil, R.K. Mishra, S. Jana (2015) Structural and Physical Properties of Biofield Treated Thymol and Menthol. *Molecular Pharmaceutics and Organic Process Research*, 3: 2.

**[32]** G. Socrates (2004) Infrared and Raman Characteristic Group Frequencies: Tables and charts. *John Wiley &Sons, LTD. Chichester (UK)*, pp 366.

**[33]** I.S. Al-sheibany (2005) Qualitative and Quantitative Evaluation of some Organic Compounds in Iraqi Thyme. *National Journal of Chemistry*, 19, 366-379.

**[34]** L. Barbeş, C. Rădulescu, C. Stihi (2013) ATR-FTIR spectrometry characterization of polymeric materials. *Romanian Report in Physics*, 66, 765-777.

**[35]** O. Sirichote, K. Hansongnern, Y. Yaochuang, C. Jantaraprim (1996) Experimental and theoretical studies of vibrational frequencies of trans-cinnamaldehyde. *Journal of the Science Society of Thailand*, 22, 333-342.

**[36]** Y. Li, D. Kong, H. Wu (2013) Analysis and evaluation of essential oil components of cinnamon barks using GC-MS and FTIR spectroscopy. *Industrial Crops and Products*, 41, 269-278.

**[37]** S.D.M. Atkinson, M.J. Almond, P. Hollins, S.L. Jenkins (2003) The photodimerisation of the α- and β-forms of trans-cinnamic acid_a study of single crystals by vibrational microspectroscopy. *Spectrochimica Acta Part A*, 59, 629-635.

# CHAPTER 14:

# FINAL CONCLUSIONS

According to the analytical results summarized in this manuscript, the overall objective of this PhD work has been achieved. Indeed, innovative methodologies for the characterization and conservation of *Cultural Heritage* materials have been successfully developed and optimized.

Keeping the narrative structure followed for the drafting of this manuscript, the final conclusions derived from the study of archaeological iron artefacts will be followed by those concerning mural paintings. Furthermore, in both sections, future research works have been also outlined.

**Archaeological artefacts**

Regarding the metallic objects recovered from the archaeological site of Ereñozar (Bizkaia, Spain), the first task was to carry out an overall assessment of their chemical composition. For this purpose, portable analytical techniques were used as the base for analytical procedures that confirmed to be extremely useful, delivering extensive information regarding the alloys used to forge and decorate the objects as well as the degradation pathways threatening their preservation.

Those results, achieved by the complementary use of portable Raman and ED-XRF techniques, further demonstrate that in-situ analyses seems to be mandatory for the characterization of artefacts of cultural interests while avoiding problems related to their transportation in the laboratory.

In addition to in-situ analyses, it is important to emphasize that the study of micro-fragments by means of laboratory systems is often a necessary step to fully understand both characteristics and conservation pathologies of archaeological findings.

This consideration is supported by the results shown in chapter 6, in which the study of micro-fragments sampled from the gilded spur (*E294*) shed light on the manufacturing technique (fire gilding) used for its decoration. Moreover, laboratory studies of rust samples enabled to assess the stratigraphic distribution of reactive and stable phases as well as to provide critical information to restorers for choosing the most appropriate conservation treatment.

However, the chemical assessment of artefacts represents only one of the manifold contributions provided by the work of Conservation Scientists. In fact, as explained in chapter 1, the interdisciplinary collaboration between conservators and researchers also aims at developing innovative solutions for supporting the optimal preservation of *Cultural Heritage* materials.

In the context of archaeological artefacts, the experimental work carried out in this PhD thesis dealt with two important issues concerning the preservation of iron-based artefacts affected by chloride infiltration.

Indeed, as explained above, the presence of chlorides leads to the formation of highly reactive corrosion products (such as akaganeite) that accelerate the degradation of iron objects by promoting cracks and loss of material phenomena. Hence, it is clear that the work of conservators might be strongly benefited by the development of a rapid method to reliably evaluate the stability of artefacts' corrosion systems.

As explained in chapter 7, the assessment of the overall stability inevitably passes through the quantitative study of the iron corrosion phases composing the rust layer. Considering the limitations of the methods currently available, the first technological contribution presented in this manuscript is the development of a semi-quantification protocol based on the deconvolution of FTIR spectra.

The results obtained from the study of pure standard mixtures and real archaeological rust samples clearly proved that the proposed method represents a viable alternative to those based on X-Ray diffractograms and Raman spectra for both semi-quantification and stability evaluation of the iron phases. Furthermore, by comparing the results obtained by the laboratory FTIR system with those by transportable spectrometers, it was also proved that the novel protocol could be also applied for in-situ analyses.

Considering that the most unstable and reactive iron-phase (akaganeite) usually generates soon after the recovery of the finding from archaeological endeavours, effective dechlorination treatments need to be promptly performed in order to prevent its formation. Even though several novel and effective methods have been recently developed, their high cost makes them inaccessible for most of the conservation laboratories. For this reason, the development of innovative strategies needs to be flanked by analytical studies aimed at optimizing the most commonly used desalination treatments.

Under this requirement, the experimental study summarized in chapter 8 aimed at filling the lack of knowledge regarding the influence of several parameters on the desalination features of NaOH-based solutions. Thanks to the collected data it was statistically proved that the optimal results in terms of $Cl^-$ extraction and akaganeite stabilization are achieved by applying a 0.7 molar NaOH solution at a temperature between 65 and 75 ºC. Taking into account that most of iron objects are generally treated by using a 0.1 to 0.5 molar NaOH solution at room temperature, is therefore deduced that the data and procedure herein presented will be very helpful to conservators for increasing the efficacy of their desalination baths.

Whereas the experimental work carried out in this PhD thesis enhanced its extractive features, other aspects of NaOH solutions still need to be improved. Among them, one of the main problems is the limited ability of the alkaline bath to penetrate into the most inner layers of the artefacts under treatment.

To overcome this issue, a targeted research line has been outlined. In fact, on the wake of the excellent results summarized in chapter 8, the experimental design method will be used with the purpose of understanding the influence of several variables (such as sonication, use of surfactants and high pressure conditions) in the penetration capability of the optimized NaOH solution.

In this case, experiments need to be carried out by treating metal objects covered by compact rust layers. Furthermore, corrosion system's composition and chloride's content of the samples to be treated must be uniform in order to ensure the reliability of the results. In order to fulfil with these requirements, hundreds of nails have been already subjected to controlled aging since January 2015. The ageing process is being performed under 4 different environmental conditions: a) immersed in seawater; b) buried in a soil constantly wet by seawater; c) directly exposed to marine aerosol; d) buried near the coast line.

Once reached the desired thickness and composition of the corrosion system, nails will be subjected to the desalination treatments outlined by specific experimental designs. After treating, each nail will be cut and analyzed by means of elemental (SEM-EDS) and molecular (Raman) imaging technique with the purpose of evaluating treatment penetration. Additionally, chromatographic analyses will be performed to quantify the amount of $Cl^-$ extracted by each bath. After data interpretation, the optimal conditions to increase the penetration features of NaOH solution will be defined.

**Mural paintings**

As in the case of archaeological artefacts, mural paintings were studied by employing an analytical procedure based on the complementary use of portable and laboratory analytical techniques.

In this PhD thesis, portable molecular (Raman and FTIR) and elemental (ED-XRF and LIBS) analytical systems were successfully applied on three different case of study. The purpose was to identify original, restoration and decaying materials by avoiding extensive sampling procedure.

Starting from the paintings conserved in the church of San Martín de Tours (Gaceo, Spain), in-situ analyses underlined the presence of several pigments synthesized in the modern era. The disclosure of repainting is concordant with literature, which asserts that Gaceo murals were subjected to numerous restorations works over the past 40 years. In addition, compounds typically used during the $19^{th}$ century were also identified, suggesting that an undocumented repaint was probably carried out in the past.

Similarly, the in-situ assessment of Alaiza paintings proved the presence of both original and modern restoration materials. Furthermore, thanks to the use of

portable systems it was also possible to characterize the molecular and elemental composition of the extensive degradation processes (mainly related to soluble salts crystallization) threatening the integrity of the lower parts of the walls.

In the case of Pompeian mural painting no modern materials were detected by means of portable and hand-held analytical systems. Hence, it was deduced that no repainting was performed in the past. Additionally, in-situ analyses provided information of paramount importance for deepens the knowledge about the degradation processes of the two walls. In particular, the pathologies detected on the outdoor one, which entailed the complete loss of the paint layer, were mostly related to leaching and thermal fluctuation phenomena. The mural painting from the basement in contrast, showed deep degradation issues due to soluble salt infiltration and biological colonization.

Even though in-situ analyses provided important information to assess the state of the art of the 3 set of paintings, micro-destructive analyses were additionally carried out with the purpose of deepen the understanding of both restoration products and degradation processes.

Regarding Gaceo paintings, two fragments were collected, cross sectioned and analyzed by laboratory systems. By performing chemical imaging analyses it was definitely proved the presence of an undocumented repainting performed in the $19^{th}$ century. Among the detected degradation pathways, the most controversial phenomenon consisted in the transformation of gypsum into bassanite. As explained in chapter 7, this dehydration process, which can trigger significant deformations and fracturing of mortars, was probably favoured by the application of a protective layer of Paraloid during recent restoration treatments.

Compared to Gaceo, Alaiza and Pompeii paintings showed more extensive degradation processes that were causing irreversible damages to the artworks. In order to determine the causes leading to the onset of the detected pathologies, the laboratory analysis of mural fragments was flanked by the study of soil and water samples collected from the surroundings.

Concerning the mural paintings of Alaiza, the most problematic degradation processes were mainly located in the lower part of the walls, where massive soluble salt crystallization and mortar pulverization were precluding the irreversible lost of large painted areas. According to spectroscopic and chromatographic analyses performed by laboratory systems, it was proved that

the products used to fertilize the farmlands located in the surroundings played a primary role in the onset of the above mentioned pathologies.

With regard to Pompeian mural painting conserved in the underground basement, laboratory analyses were mainly aimed on understanding the reasons behind its heterogeneous biocolonization. Thanks to XRD and SEM-EDS techniques it was proved that the lower part of the wall (the one excavated in 2005 and interested by extensive colonization) differed from the upper part (excavated in 1988) by the presence of a thin volcanic material layer on its surface. Considering that most of the biological patinas grown over these residues, it was deduced that volcanic material played a key role on the biocolonization and further biodegradation of the mural painting.

As described in chapter 12, biological colonization can lead to the onset of several aesthetic, chemical and physical degradation processes. Despite the large number of available biocide products, doubts about the compatibility with historic materials make the number of substances suitable for the conservation of *Cultural Heritage* very restricted.

On the wake of the most recent advances in this field, the experimental work summarized in chapter 13 had the purpose of evaluating the possible use of specific essential oils constituents as alternative green products for the neutralization of biodeteriogens. Laboratory tests, carried out by disk diffusion method, proved that *thymol*, *eugenol* and *cinnamaldehyde* compounds were capable of strongly inhibiting the growth of *Aspergillus niger*, a wild fungus strain sampled from the Pompeian painting previously described.

Taking into account that their possible application on mural surfaces implies the direct exposition to the environment, the 3 compounds were also exposed to sun-light and UV-light with the purpose of evaluating the possible side effects entailed by photo-oxidation processes on their antifungal activity. The results proved that, after UV-light exposition, the degradation processes suffered by *cynnamaldehyde* samples had a critical repercussion on their antifungal activity. On the contrary, composition and properties of *eugenol* and *thymol* samples were almost not affected by aging.

Even though those results are very promising, further laboratory experiments need to be carried out to ensure the possible exploitability of *eugenol* and *thymol* for *Cultural Heritage* conservation purposes.

Under this requirement, a specific research line has been outlined for the near future. The first part of the experimental work will be focused on evaluating the inhibition activity of the two EOs constituents against several other microorganisms (fungi, algae and bacteria), focusing on those that, according to literature, most commonly colonize mural surfaces. In parallel, specific assays will be aimed at identifying the possible interaction between the active compounds and the mural surface.

The use of essential oils constituents would represents a step towards the development of novel natural and eco-compatible conservation products. However, it must be highlighted that the high volatility of these compounds makes them employable only in those cases where the colonization has already occurred.

To overcome this limitation, the final step of this research line will consist in the development of specific micro/nano sized carrying systems that leak the EOs as a function of time, providing an antifungal and antibacterial protection for long time.

In conclusion, the aim of this forthcoming project will be the development a natural green product capable of preventing the biological colonization of mural paintings and others *Cultural Heritage* assets.

# CHAPTER 15:

# SCIENTIFIC PUBLICATIONS

## 15.1 Papers in ISI journals

**[1]** M. Veneranda, M. Irazola, A. Pitarch, M. Olivares, A. Iturregui, K. Castro, J.M. Madariaga (2014) In-situ laboratory Raman analysis in the field of cultural heritage: the case of a mural painting. *Journal of Raman Spectroscopy*, 45, 228-237.

**[2]** M. Veneranda, M. Irazola, M. Díez, A. Iturregui, J. Aramendia, K. Castro, J.M. Madariaga (2014) Raman spectroscopic Study of the degradation of a middle age mural painting: the role of agricultural activities. *Journal of Raman Spectroscopy*, 45, 1110-1118.

**[3]** M. Veneranda, J. Aramenda, O. Gómez, S. Fdez-Ortiz de Vallejuelo, L. García, I. García-Camino, K. Castro, A. Azkarate, J.M. Madariaga (2016) Characterization of archaemetallurgical artefacts by means of portable Raman systems: corrosion mechanisms influenced by marine aerosol. *Journal of Raman Spectroscopy*, 48, 258-266.

**[4]** M. Veneranda, I. Costantini, S. Fdez-Ortiz de Vellejuelo, L. García, I. García, K. Castro, A. Azkarate, J.M. Madariaga (2016) Study of corrosion in archaeological

gilded irons by Raman imaging and a coupled scanning electron microscope-Raman system. *Philosophical Transaction A*, 374: 20160046.

**[5]** M. Veneranda, N. Prieto-Taboada, S. Fdez-Ortiz de Vallejuelo, M. Maguregui, H. Morillas, I. Marcaida, K. Castro, J.M. Madariaga, F.J. García-Diego, M. Osanna (2017) In-situ multianalytical approach to analyze and compare the degradation pathways jeopardizing two murals exposed to different environments (Ariadne House, Pompeii, Italy). *Spectrochimica Acta A* (under review).

**[6]** M. Veneranda, N. Prieto-Taboada, S. Fdez-Ortiz de Vallejuelo, M. Maguregui, H. Morillas, I. Marcaida, K. Castro, J.M. Madariaga, M. Osanna (2017) Biodeterioration of Pompeian mural paintings: Fungi colonization favoured by the presence of volcanic material residues. *Environmental Science and Pollution Research* (under review).

**[7]** M. Veneranda, J. Aramendia, L. Bellot-Gurlet, Ph. Colomban, K. Castro, J.M. Madariaga (2017) FTIR spectroscopic semi-quantification of iron phases: a new method to evaluate the stability of archaeological artefacts corrosion systems. *Corrosion Science* (under review).

**[8]** M. Veneranda, L. Bianco, G. Roselli, G. Di Girolami, K. Castro, J.M. Madariaga (2017) Evaluating the exploitability of several Essential Oils constituents as a novel biological treatment against Cultural Heritage biocolonization. *Analytical and Bioanalytical Chemistry* (under review).

## 15.2 Congress oral communications

**[1]** M. Veneranda, I. Costantini, J. Aramendia, N. Prieto, L. García, I. García, K. Casto, A. Azkarate, J.M. Madariaga (2015) Comparación y optimización de los tratamientos de decloruración más utilizados en el campo de la conservación de hierros arqueológicos. *MetalEspaña 2015, II Congreso de Conservación y Restauración del Patrimonio Metálico.* Segovia (Spain), 1-3 October 2015.

**[2]** M. Veneranda. L. García, L. Bellot-Gurlet, K. Castro, I. García-Camino, A. Azkarate, J.M. Madariaga (2015) Tratamiento de espectros FTIR con el programa PALME: una nueva herramienta para diagnosticar el estado de conservación de hierros arqueológicos. *MetalEspaña 2015, II Congreso de Conservación y Restauración del Patrimonio Metálico.* Segovia (Spain), 1-3 October 2015.

**[3]** M. Veneranda, I. Costantini, J. Aramendia, S. Fdez-Ortiz de Vallejuelo, L. García, I. García, K. Castro, A. Azkarate, J.M. Madariaga (2015) Raman imaging y análisis SCA (structural and chemical analyzer): herramientas analíticas aplicadas al estudio de hierros arqueológicos. *ECPC – Estudio y Conservación del Patrimonio Cultural*, Malaga (Spain), 16-19 November 2015.

**[4]** M. Veneranda, I. Costantini, L. Blanco, P. Cinaglia, G. Di Girolami, K. Castro, J.M. Madariaga (2017) Evaluating the exploitability of several Essential Oils constituents as a new biological treatment against Cultural Heritage biodeterioration. *Technart 2017, Non-destructive and microanalytical techniques in art and cultural heritage*, Bilbao (Spain) 2-6 May 2017.

## 15.3 Congress posters

**[1]** M. Veneranda, M. Irazola, M. Díez, A. Iturregui, J. Aramendia, K. Castro, J.M. Madariaga (2013) Characterization of Middle Age mural paintings: in-situ Raman spectroscopy supported by different techniques. *RAA 2013, The VII International Congress on the Application of Raman Spectroscopy in Art and Archaeology*, Ljubljana (Slovenia), 2-6 September 2013. **Awarded as best poster of the congress (2$^{nd}$ prize).**

**[2]** M. Veneranda, J. Aramendia, S. Fernández-Ortiz de Vallejuelo, L. García, I. García, M. Neira, K. Castro, J.M. Madariaga (2014) Study of the efficacy of the desalination treatment applied to an archeological artifact affected by chlorine. *VIII Congreso ibérico de Espectroscopia*, Logroño (Spain), 9-11 July 2014. **Awarded as best poster of the congress (1$^{st}$ prize).**

**[3]** M. Veneranda, I. Costantini, J. Aramendia, N. Prieto, L. García, I. García, K. Castro, A. Azkarate, J.M. Madariaga (2015) Comparativa entre las variables más efectivas para la desalinización de hierros arqueológicos afectados por cloruros. *ECPC – Estudio y Conservación del Patrimonio Cultural*, Malaga (Spain), 16-19 November 2015.

# ANNEX

## Abbreviations

**ATR:** Attenuated Total Reflectance

**DRIFT:** Diffuse Reflectance Infrared Fourier Transformed

**ED:** Energy Dispersive

**EDS:** Energy Dispersive X-Ray Spectroscopy

**EO:** Essential Oil

**FTIR:** Fourier Transform Infrared Spectroscopy

**GC:** Gas Chromatography

**ICP:** Inductively Coupled Plasma

**ITS:** Internal Transcriber Spacer

**LIBS:** Laser Induced Breakdown Spectroscopy

**LoD:** Limit of Detection

**LoQ:** Limit of Quantification

**MS:** Mass Spectrometry

**PCR:** Polimerase Chain Reaction

**PDA:** Potato Dextrose Agar

**PIXE:** Proton Induced X-Ray Emission

**SEM:** Scanning Electron Microscopy

**TIMS:** Thermal Ionization Mass Spectrometry

**XRD:** X-Ray Diffraction

**XRF:** X-Ray Fluorescence